ANALYTICAL PERFORMANCE ANALYSIS IN LASER-ASSISTED AND ULTRASONIC VIBRATION-ASSISTED MILLING

A Dissertation
Presented to
The Academic Faculty

by

Yixuan Feng

In Partial Fulfillment
of the Requirements for the Degree
Doctor of Philosophy in the
George W. Woodruff School of Mechanical Engineering

Georgia Institute of Technology
August 2019

ANALYTICAL PERFORMANCE ANALYSIS IN LASER-ASSISTED AND ULTRASONIC VIBRATION-ASSISTED MILLING

Approved by:

Dr. Steven Y. Liang, Advisor
School of Mechanical Engineering
Georgia Institute of Technology

Dr. Shreyes N. Melkote
School of Mechanical Engineering
Georgia Institute of Technology

Dr. Thomas Kurfess
School of Mechanical Engineering
Georgia Institute of Technology

Dr. Hamid Garmestani
School of Materials Science and Engineering
Georgia Institute of Technology

Dr. Christopher Saldana
School of Mechanical Engineering
Georgia Institute of Technology

Dr. Xiaohong Lu
School of Mechanical Engineering
Dalian University of Technology

Date Approved: July 22, 2019

ACKNOWLEDGEMENTS

Firstly, I would like to thank my advisor, Professor Steven Y. Liang. It has been a great learning experience to work in his group as a research assistant. I have learned the importance of being truly dedicated and thankful to my work from his enthusiasm and dedication to his work. I would also like to thank members of my committee, Professor Thomas Kurfess, Professor Christopher Saldana, Professor Shreyes N. Melkote, Professor Hamid Garmestani, and Professor Xiaohong Lu. Their time and suggestions on my thesis are greatly appreciated.

I would also like to thank the financial support provided by Metal Industries Research and Development Centre (MIRDC). Without their support on experimental measurements, completion of this thesis would not have been possible. I would like to thank Professor Tsung-Pin Hung, Yu-Ting Lu, Dr. Fu-Chuan Hsu, and Dr. Yu-Fu Lin from MIRDC. All their feedback and suggestions from the regular meetings are greatly helpful to the project progress and appreciated.

I would also like to thank previous and current members of the research group, Dr. Zhipeng Pan, Dr. Manik Rojora, Yanfei Lu, Man Zhao, Jinqiang Ning, Elham Mirkoohi, Professor Xia Ji, Professor Feng Li, and Linger Cai. It has been a great pleasure working with them. In addition, I would like to thank Camellia Henry, Sharon McKenzie, Angela Smith, and other staff in the department and university who have helped me.

Last but not least, I want to thank my wife Weiwei, my son Aden, and my parents, who have made my journey at Georgia Tech more colorful and encouraging.

TABLE OF CONTENTS

LIST OF TABLES

LIST OF FIGURES

LIST OF SYMBOLS AND ABBREVIATIONS

a_i, h_i, m_i, c_i, n_i, k_d, β_d	Johnson-Mehl-Avrami-Kolmogorov dynamic recrystallization model coefficients
A_{hp}, K_{hp}, B, n, C, m	Johnson-Cook material flow stress model coefficient
T_m	Material melting temperature
T_0	Reference temperature
Q_{act}	Activation energy
X_{drex}	Dynamic recrystallized volume fraction
d_0	Initial average grain size
d_{drex}	Recrystallized average grain size
d	Average grain size
V_f	Feed rate
RPM	Spindle speed
t_c	Chip thickness
ϕ_r	Rotation angle
w	Cutting width
d_a	Axial depth of milling
C_s	Side cutting edge angle
r_{corner}	Tool edge radius
V_r	Rotation speed
R_t	Tool radius
P_1, P_2, P_3	Force in the cutting, feed and axial direction
F_c, F_t, F_r	Force in the cutting, thrust and resultant direction
η_c	Chip flow angle

i	Inclination angle
α_r	Rake angle
T_{laser}	Laser preheating temperature
ρ	Material density
C_p	Specific heat
h	Heat transfer coefficient
q	Heat generation rate
Q	Total input power of laser
r	Radius of laser spot
α	Thermal diffusivity
ϕ	Shear angle
L_{AB}	Length of shear plane
k_{wk}	Thermal conductivity of workpiece
K_0	Modified Bessel function of the second kind or Neumann function
q_{shear}	Shearing heat source
q_{rub}	Secondary rubbing heat source
CA	Contact length
P_{cut}	Plowing force in cutting direction
γ	Heat distribution coefficient
k_t	Thermal conductivity of tool
ρ_t	Density of tool material
C_t	Specific heat of cutting tool
R	Gas constant
P_{thrust}	Normal plowing force
a	Half contact width between the tool and chip

μ	Friction coefficient
k_{AB}	Flow stress on shear plane
E	Young's modulus
v	Poisson's ratio
G_{ijk}	Plane strain Green's function
S_{ij}	Deviatoric stress
R_s	Shear yield strength
α_{ij}	Back stress
ψ	Mixed function
h_p	Plastic modulus
G	Elastic shear modulus
k	Shear flow stress
VB	Flank wear land length
$\sigma_w(x)$	Flank normal stress
$\tau_w(x)$	Flank shear stress
$q_{friction}$	Heat intensity of friction
λ	Friction angle
V_{chip}	Velocity of chip
l	Contact length between tool and chip
$q_{rubbing}$	Rubbing heat intensity
V_c	Cutting speed
α_{tool}	Wedge angle
$K_{abrasion}$	Abrasive wear coefficient
$K_{adhesion}$	Adhesive wear coefficient
$K_{diffusion}$	Diffusive wear coefficient

P_t	Hardness of tool
P_a	Hardness of abrasive particle
K, n_w, a_w, K_Q	Flank wear rate model coefficients
f_z	Feed per tooth
N_t	Number of flute
μ_c	Correction coefficient for tool tip deformation
r_t	Tool tip radius
α_e	Tool tip angle
t_{min}	Minimum cutting thickness
R_a	Arithmetic average surface roughness
L	Laser-tool distance
P	Laser power
X_n	Process parameters
K_n	Kalman gain matrix
P_n	Simulation covariance matrix
R_n	Error covariance matrix
θ_x, θ_y, θ_z	Phase angle
A_x, A_y, A_z	Vibration amplitude
ω_x, ω_y, ω_z	Angular ultrasonic vibration frequency
β	Helix angle
V_n	Resultant cutting speed
V_{ul}	Ultrasonic vibration velocity in axial direction

SUMMARY

The control of machining is critical to the quality of final product, while the evaluation of advanced manufacturing process including laser-assisted and ultrasonic vibration-assisted milling becomes more challenging. The performance of machining can be evaluated through several aspects. In situ parameters including force, temperature, and tool wear indicate if the machining is conducted within allowable range of equipment. Force and temperature in shear zone is the results of both mechanical and thermal loads during milling. Moreover, tool wear describes the gradual failure of cutting tools due to regular operation. Residual stress and surface roughness reflect the machining process and are directly related to fatigue performance and surface quality of the product. Surface roughness characterizes the surface texture in terms of deviations. Residual stress is created under mechanical load, thermal gradient, and phase change, which significantly affects the damage tolerance and fatigue performance of product. All these quantities are selected due to their importance in the evaluation of laser-assisted and ultrasonic vibration-assisted milling process.

On one hand, people are interested in knowing the performance under designed process parameters such as tool geometry, laser power, vibration amplitude, feed rate, and cutting depth. For this study, the analytical models are built to predict the milling forces, temperature field, residual stress profile of machined surface, surface roughness, and tool wear in laser-assisted and ultrasonic vibration-assisted milling. The milling configuration is treated as orthogonal cutting at each instance. All process parameters including cutting depth, cutting speed, and tool geometry are therefore transferred. The oblique cutting forces

are transferred to equivalent orthogonal cutting forces through the chip flow model. Then the forces are calculated using classic Oxley's contact mechanics theory. The shearing heat source and secondary rubbing heat source are included for machining temperature prediction. The heat source is calculated from the cutting or ploughing forces, and a mirror heat source method is applied to predict temperature rise through integration. The residual stress is predicted through the calculation of elastic stress distribution in loading process, actual stress with kinematic hardening, and the stress change during relaxation. For surface roughness, the actual tool trajectory is first predicted with the consideration of overall tool movement, elastic deformation of tool, and the tool tip profile. The tool movements include the translation in feed direction and the rotation along its axis. The elastic deformation is calculated based on the previously established milling force prediction model. The tool tip profile is predicted based on the tool tip radius and angle. The machined surface profile is simulated based on the tool trajectory with elastic recovery, which is considered through the comparison between the minimum thickness and actual cutting thickness. For tool wear, the effective force due to flank wear is calculated by integrating the stress component along the chip cross section and wear land, and the average stress on tool-workpiece interface due to flank wear is calculated based on the effective force and contact area. The average temperature along the interface is derived through imaginary heat source method with secondary and rubbing heat sources considered. The flank wear rate is then predicted considering abrasion, adhesion, and diffusion.

On the other hand, people want to know the possible combination of process parameters to achieve required target performance. Therefore, inverse analysis is proposed on milling forces, residual stress, surface roughness, and tool life, in laser-assisted milling.

The method uses the analytical model to solve the direct problem and applies a variance-based recursive method to guide the inverse analysis. For the force, the inverse analysis identifies five process parameters including feed rate, axial depth of milling, laser preheating temperature, spindle speed, and rake angle, and finds the optimal solution for target performance. For mean residual stress, three cutting parameters including depth of cut, feed per tooth, and cutting speed, and two laser parameters including laser-tool distance and laser power, are updated with respected to the minimization of resulting residual stress and measurement in each iteration. For surface roughness, the inverse analysis identifies four process parameters of feed per tooth, tool tip radius, minimum cutting thickness, and tool tip angle, and finds the optimal solution for target performance. Lastly, the iterative gradient search or variance-based recursive method is applied to solve inverse problem and update process parameters to match the tool life. Three cutting parameters including depth of cut, feed per tooth, and cutting speed, and two laser parameters including laser-tool distance and laser power, are updated in each iteration.

To accommodate the effects of laser and ultrasonic vibration, additionl factors are considered in the performance analysis including laser preheating temperature field, microstructure evolution, and tool-workpiece separation under vibration. In laser-assisted milling, the preheating temperature at top surface is predicted first by considering the heat generation from laser and convection. The heat generation rate is described by Gaussian equation. Within the material, heat conduction is considered with isothermal boundary conditions at side and bottom surfaces. The recrystallization effect and thus the grain growth are considered through calibrated models describing the dependency of strain rate, strain, and temperature on dynamic recrystallization process for specific alloys using

exponent functions. For ultrasonic vibration-assisted milling, one benefit is the frequent separation between tool and workpiece as the cutting time is reduced. In order to account for this effect, three types of tool-workpiece separation criteria are checked based on the tool center instantaneous position and velocity. Type I criterion examines the instantaneous velocity of tool center under feed movement and vibration. If the tool is moving away from workpiece, there is no contact. Type II criterion examines the position of tool center. If the tool center is far from the uncut workpiece surface, there is no contact even though the tool is getting closer. Type III criterion describes the smaller chip size due to the overlaps between current and previous tool paths as a result of vibration. If any criterion is satisfied, both mechanical and thermal stress are zero.

CHAPTER 1. INTRODUCTION

In this chapter, the motivation, objective, and overview structure of the thesis are presented.

1.1 Motivation

People have been developing advanced manufacturing technologies for years in order to obtain higher material removal rate, better surface finish, and better fatigue resistance, while keeping tool wear rate, cutting force, and temperature at a low level. In addition, the use of these technologies could enhance the machinability of some difficult-to-machine materials such as Inconel 718 and Ti-6Al-4V, which typically have high strength and cause large cutting forces, high cutting temperature, severe tool wear, and bad surface finish in conventional machining process. However, with the use of advanced technologies such as laser and ultrasonic vibration, more challenges appear for the process control. For example, under high cutting speed, the use of laser could lead to higher flank wear or even tool breakage [1] comparing with conventional milling, when inappropriate combination of cutting and laser parameters are used. The ultrasonic vibration could also speed up the tool wear rate and further lead to larger surface roughness than conventional milling [2]. Therefore, it is important to have performance analysis in laser-assisted and ultrasonic vibration-assisted milling process, including the prediction of target performances, force, temperature, residual stress, surface roughness, and tool wear, under desired process parameters, and the prediction of process parameters based on required performance. Up to now, most of the related works are done using numerical analysis or experimental investigation. The analytical approach is able to reveal the physics nature in

the process within short computation time. Therefore, analytical performance analysis in laser-assisted and ultrasonic vibration-assisted milling is presented in current study.

1.2 Research goal and objectives

In current study, performance analysis is conducted through analytical prediction. The procedure of predicting target performances under desired process parameters is defined as forward problem methodology. The procedure of predicting process parameters based on required performance is defined as inverse problem methodology. The flow chart of the proposed forward problem methodology is shown in Figure 1. Asterisk indicates step only in laser-assisted milling, while double asterisk indicates step only in ultrasonic vibration-assisted milling. At each rotation angle of milling tool, the cutting parameters and tool geometry parameters are recalculated as in equivalent orthogonal cutting. Then, the milling forces are calculated through flow stress based on mechanics of machining. The forces also result in heat sources in machining temperature prediction. And the residual stress is predicted based on mechanical stress from force and thermal stress from temperature field, followed by relaxation process. The surface roughness is calculated considering the tool deformation under forces, tool path, and the elastic recovery of machined surface. Lastly, the tool flank wear rate is decided by abrasive, adhesive, and diffusive wear based on the stress and temperature on tool-workpiece interface. For laser-assisted milling, the laser preheating temperature field is predicted which affects the flow stress and overall temperature field. In addition, the high temperature could trigger the microstructure evolution, which leads to grain growth and change of flow stress. For ultrasonic vibration-assisted milling, tool-workpiece separation criteria are examined first, and the prediction is only continued when there is contact between tool and workpiece at

the moment. For inverse problem methodology, an iterative gradient search and variance-based recursive method is applied to solve inverse problem and update process parameters to match the target performance.

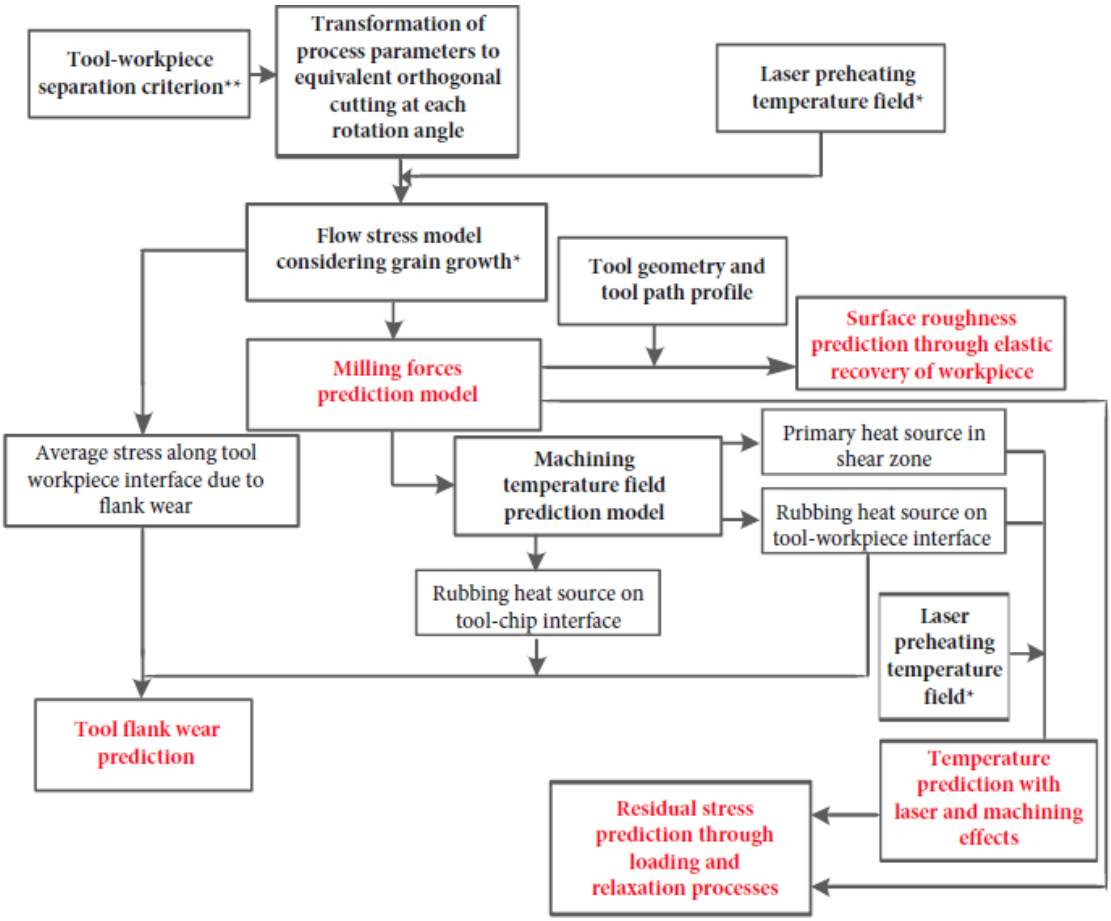

Figure 1 The flow chart of the proposed forward problem methodology

1.3 Overview of thesis

In CHAPTER 2, literature review is presented giving a comprehensive review work on the state of art research on the performance analysis in laser-assisted and ultrasonic vibration-assisted milling. In CHAPTER 3, the forward problem methodology is

introduced in laser-assisted milling including milling force, temperature, residual stress, surface roughness, and tool flank wear. In CHAPTER 4, the inverse problem methodology is introduced in laser-assisted milling including milling force, residual stress, surface roughness, and tool flank wear. In CHAPTER 5, the forward problem methodology is introduced in ultrasonic vibration-assisted milling including milling force, temperature, residual stress, surface roughness, and tool flank wear.

CHAPTER 2. LITERATURE REVIEW

In this chapter, literature review is presented giving a comprehensive review work on the state of art research on the performance analysis in laser-assisted and ultrasonic vibration-assisted milling.

2.1 Forward problem methodology in laser-assisted milling

2.1.1 Milling force and recrystallization

Superalloy like Inconel 718 is widely used in various fields of engineering due to its superior mechanical properties [3, 4]. However, it typically has poor machinability since the precipitated secondary phases within the material act as abrasive particles, which causes rapid tool wear and high machining forces [5, 6]. To improve the machinability, people have developed the technique to heat a material to make it deform more easily for a long time. Among all thermally enhanced machining methods, laser-assisted machining stands out because the temperature field is easier to control through the highly concentrated heat source [5]. With the single beam coaxial laser-assisted milling spindle used in this paper, the laser power can reach 1000W with pre-heated temperature higher than 850℃. Since one of the hot deformation behavior, dynamic recrystallization (*DRX*), will occur at high temperature [7], it is valuable to study the recrystallization effect in laser-assisted end milling.

For Inconel 718, several phases have been observed, and γ" phase is believed to be the main reason of high temperature strength [7]. Since the solvus temperature of γ" phase is 915 ℃ [5], and the pre-heated temperature in this paper is between 850℃ and 900℃, the

recrystallization effect will basically perform as the change of grain size without phase change. Marty et al. [8] first presented a recrystallization model of Inconel 718 in 1997. The spherical grains were assumed and the grain size was described as $D_0(1-X)^{1/3}$, with D_0 the initial grain size and X the recrystallized fraction. This model works most time but has less accuracy on large workpiece and partially recrystallized miocorstructure. Medeiros et al. [7] made a summary of hot deformation studies done on Inconel 718 in 2000 and proposed a model to descried the grain size d in the metadynamic recrystallization (*MDRX*) as $d = c\dot{\varepsilon}^{-p}\exp(\frac{-Q_{act}}{RT})$, where $c = 5.98\times10^{10}$ and $p = 0.028$ are constants, and Q_{act} is the activation energy of 240 *kJ/mole*. $\dot{\varepsilon}$ is strain rate, T is temperature and R is gas constant. However, in 2005, Guest et al. [9] did experiments and pointed out that this equation didn't consider the influence of time and *DRX* should be investigated first before the description of *MDRX*. At the same year, Guest et al. [10] described a new Inconel 718 microstructural evolution model containing both the normal grain growth and recrystallization. Since this model is based on the thermomechanical history produced by the finite element software package, it is then not purely analytical. More experiments were done by Thakur et al. [4] and the microstructure was described in a new way in terms of grain orientation and shape change. Wang et al. [11] used electron backscatter diffraction (*EBSD*) technique to analyze more details on the orientations of grains and subgrains. And they pointed out that the discontinuous dynamic recrystallization (*DDRX*) is the dominant deformation mechanism. Similar conclusion was made by Azarbarmas [3] several years later. Zhao et al. [12] developed state variables model to describe the flow stress behavior during *DRX*. The dynamically recrystallized grain size d_{DRX} is given by $d_{DRX} = 4.85\times10^{10}\varepsilon^{-0.41}\dot{\varepsilon}^{-0.028}\exp(\frac{-240000}{RT})$

with ε as strain. With the similar format as Medeiros et al. 's model [7], this model still has limitation when the time is taken into consideration. The modeling of laser-assisted machining has been started in recent years [6], but the models so far do not include recrystallization effect. So it is valuable to present an analytical model of milling forces prediction in laser-assisted end milling including recrystallization.

2.1.2 Preheating temperature and machining temperature

In order to improve the machinability of certain materials with high strength or hardness, people have been developing thermally enhanced machining methods for decades, among which laser-assisted machining is preferred because a highly concentrated heat source is able to control the preheating temperature field in an easier manner. Shi *et al.* [13] conducted numerical simulation on laser-assisted machining of Inconel 718, which indicated that the additional temperature increase in primary deformation zone due to laser effect would decrease the effective stress, and the reduced cutting force was mainly resulted from the thermal softening effect on the flow stress. Therefore, the study of temperature in laser-assisted machining is critical for the guidance of process. Milling process is more complex than most other machining processes in nature, and the preheating temperature of laser assisted milling process on various materials has been later investigated by different researchers. Tian *et al.* [14] proposed thermal modeling of laser-assisted milling to predict temperature field by determining spatial distribution of the laser energy and heat transfer equations including conduction, convection, and radiation. Although good agreement was found, the validation heating tests were conducted without material removal. Therefore, only the laser preheating temperature was predicted without machining induced temperature rise. Bermingham *et al.* [1] measured temperature at laser

focus and cutting tool in order to study the tool life and wear mechanisms in laser-assisted milling Ti-6Al-4V. Temperature signals were collected under different laser power and table speed, but only the laser traversed the surface of workpiece, and the temperature measured was preheating temperature instead of overall cutting temperature. Similarly, Woo and Lee [15] performed thermal analysis for the study of the machining characteristics of AISI 1045 steel and Inconel 718 in laser-assisted milling. The analysis addressed the conduction and heat generation rate due to laser, but the heat generated through machining was ignored, and only the preheating temperature was measured and studied. Up to now, a comprehensive predictive model of temperature in laser-assisted milling process addressing both laser preheating temperature and machining induced temperature rise has not been proposed.

The temperature rise due to machining cannot be ignored in temperature prediction of laser-assisted milling process, especially when the laser-cutter allowance is large enough so that there is a significant drop of temperature from laser center to shear zone. According to the study of Navas *et al.* [16], the heat generated by plastic deformation in the primary shear zone would raise the local temperature of the material already preheated by the laser by another 100-150℃ for Inconel 718, where the laser preheating temperature measured at the point nearest to the cutting zone was around 500℃. Therefore, the prediction of machining induced temperature rise needs to be considered since it could account for more than 30% of overall temperature. The study of predictive model of machining temperature in milling process can be tracked back to the year of 2000. Özel and Altan [17] predicted the temperatures in high-speed flat end milling using finite element analysis. The milling process was simplified to an orthogonal turning process assuming plane strain deformation.

The trochoidal path traveled by the tip of cutting edge was assumed to be circular under small maximum undeformed chip thickness. Then, the flow stress was calculated by a constitutional model as a function of state variables. Abukhshim *et al.* [18] summarized the analytical models in temperature predictions of metal cutting in 2006. They concluded that purely analytical approaches were severely restrictive at that time including the absence of heat source consideration and assumption of constant percentage of heat flow into chip and workpiece. Recently, Lu *et al.* [19] presented coupled thermal and mechanical analyses of micro-milling Inconel 718, where an iterative algorithm was proposed combining cutting force and temperature predictions. The cutting temperature significantly affects the shear stress which determines the cutting forces and ploughing forces, while these forces are treated as two heat sources in temperature prediction.

2.1.3 Residual stress

Residual stress is created under mechanical load, thermal gradient, and microstructure evolution, which significantly affects the damage tolerance and fatigue performance of product. Besides experimental studies [20-23] and numerical simulation [24, 25], people have been developing analytical models for residual stress prediction for decades. Ulutan *et al.* [26] proposed an analytical model for residual stress, in which the thermal and mechanical loading were computed through elastic-plastic model and relaxation process. Fergani *et al.* [27] predicted the residual stress induced thin plate deflection through the force prediction, loading, and relaxation models. Peng *et al.* [28] proposed residual stress model in micro-end-milling considering tool edge radius, material strengthening effects, and initial stress. Zhou *et al.* [29] followed a similar procedure to predict residual stress in helical end milling of nickel-aluminum bronze. Later, Huang *et*

al. [30] applied inclusion theory to consider residual stress as the misfit in elastic solid for peripheral milling. All these analytical models have reached reasonable accuracy and efficiency in the conventional milling process. However, with the development of laser-assisted milling, the effect of laser preheating temperature needs to be addressed, and the microstructure evolution triggered under high temperature in shear zone should also be considered. Both these effects are ignored in the references up to now, and a comprehensive residual stress prediction model in laser-assisted milling with laser preheating and recrystallization effects has not been proposed.

For the laser effect in laser-assisted milling, several studies have been conducted to characterize the temperature field. Tian *et al.* [14] described spatial distribution of the laser energy and applied heat transfer equations considering conduction, convection, and radiation to predict laser preheating temperature field. Bermingham *et al.* [1] collected temperature signals in laser-assisted milling of Ti-6Al-4V under different laser power and table speed. Similarly, Woo and Lee [15] performed thermal analysis addressing the conduction and heat generation rate due to laser, for the study of laser-assisted milling of AISI 1045 steel and Inconel 718. Although good agreements are found in these studies, the predictions are limited to pure thermal analysis without machining effect. Therefore, the laser preheating temperature field is combined with machining induced temperature rise in current study to calculate the thermal loads for residual stress prediction.

On the other hand, the limited availability of analytical model in laser-assisted milling is largely due to the knowledge gap on recrystallization in manufacturing under thermal-mechanical stresses. Among all recrystallization effects, *DRX* is reported to be most significant in flow stress and residual stress prediction [31-33]. The calibrated

Johnson, Mehl, Avrami and Kolomogorov-type (*JMAK*) model is applied to predict grain growth through exponent functions of strain rate, strain, and temperature during *DRX* process. The proposed predictive model then describes the observed interaction of grain size on flow stress so that recrystallization effect is accounted for through the prediction of residual stress.

2.1.4 Surface roughness

People have been studying the surface roughness after different machining processes for years, mainly in experimental investigation or by setting up mathematical model. Arunachalam *et al.* [34] measured surface roughness when facing Inconel 718 under different cutting speeds, depths of cut, and tools, and found that the geometry of insert had significant effect on surface roughness while round inserts combined with slow cutting speed as well as small depth of cut resulted in good surface finish. Ning *et al.* [35] analyzed surface roughness in high-speed milling of Inconel 718 under different cutting speed and found that the minimum surface roughness was reached when the smallest chip burrs was formed. D'Addona *et al.* [36] studied the pattern of surface roughness over time in turning of Inconel 718. The pattern was uniform throughout the process at lower speeds, and the surface roughness increased with every cut at higher cutting speed due to rapid tool wear. These experimental investigations reflected the variation of surface roughness by qualitative descriptions but failed to reveal the physics of these processes.

In addition to experiments, mathematical or statistical models are applied to the prediction or optimization of surface roughness. Response surface methodology (*RSM*) chooses several independent factors which determine the surface roughness by a nonlinear

equation. The equation is then transferred to different orders of polynomial functions, and all constant coefficients are determined by levels of independent variables as well as coding identification and evaluated by the analysis of variance (*ANOVA*). Alauddin *et al.* [37] chose cutting speed and feed as independent variables and fitted the data by both first and second order models in end milling of Inconel 718. The second-order model had adequacy in wider range of speed and feed, and the feed effect was very significant and dominant in both models. Lu *et al.* [38] followed similar steps in micro-milling of Inconel 718. Axial depth of cut was selected as an additional variable and second order model was suggested for prediction. Kasim *et al.* [39] added radial depth of cut as the fourth independent variable and found that interaction between radial depth of cut and feed rate from second order model was the most dominant factor determining surface roughness. Similar to *RSM* and *ANOVA*, Taguchi method [40-42] and neural network [43-45] are also widely used for prediction and optimization of surface roughness. Taguchi method is a design model for the selection of independent varialbles, response variables, and their interactions, which guides the orthogonal test in experiments, while neural network model builds input layer, output layer, and several hidden layers to minimize the mean square error between prediction and measurements. All these models have achieved relatively high accuracy in surface roughness prediction, but they require a large number of experiments for each certain case and again fail in revealing the physics process of surface roughness prediction. To better reflect the physics in surface finish, people have been developing analytical model of surface roughness in recent years. Muñoz-Escalona *et al.* [46] proposed a geometrical model for surface roughness prediction when face milling with square insert tools. The model was based on the geometrical analysis of tool that treated the tool profile

as the surface roughness profile, which ignored the elastic recovery of workpiece. Later, Hao *et al.* [47] developed surface roughness prediction model of ball end milling cutter. The geometrical model of the tool was built by considering tool path, cutting edge, and tool axis. The model was then corrected under the deformation caused by milling force. But the response of workpiece was still not included. Lu *et al.* [48] proposed analytical model for the prediction of surface roughness on sidewall surface in micro-milling of Inconel 718. The tool profile was predicted through a simplified two degree of freedom dynamic model, and the response of workpiece was calculated considering the minimum cutting thickness, multiple regenerative effect, and elastic recovery. In addition, Lu *et al.* [49] predicted the elastic recovery of Inconel 718 workpiece in micro-milling through the concept of minimum cutting thickness. Minimum cutting thickness is same as the smallest uncut chip thickness which indicates that only elastic deformation or plowing effect occurs when the cutting thickness is small enough so that no chip will form. The region with pure elastic deformation will recover afterwards which explains the difference between tool profile and surface profile. People have been studying minimum cutting thickness in micro-cutting for decades. Yuan *et al.* [50] studied the relationship between the cutting tool sharpness and the minimum cutting thickness and found empirical equation between minimum cutting thickness and the cutting edge radius based on measurements. The friction angle based on the force ratio also decided the minimum cutting thickness according to the model of Son *et al.* [51]. Wu *et al.* [52] calculated the minimum cutting thickness based on plastic strain gradient which was related to ductile fracture mechanics. In addition, other models [53] [54] have been proposed to calculate minimum cutting thickness with the consideration of cutting edge geometry and material properties of

workpiece. Up to now, minimum cutting thickness has been proved to be an effective way to explain the elastic recovery in micro-milling. Although this effect is not that dominant in macro-machining process like laser-assisted milling, the consideration of elastic recovery will significantly improve the accuracy of surface roughness prediction since the cutting depth is always changing with rotation angle in milling process.

2.1.5 Tool flank wear

Flank tool wear describes the gradual failure of cutting tools on tool-workpiece interface under regular operation. It occurs primarily due to the rubbing between tool and spring-backed workpiece along the flank face [55]. When this happens, some hard particles could remove tool material which causes abrasive wear or abrasion. For laser-assisted milling, high local stress and temperature on the flank face could also result in the local welded junctions between contacting surfaces, and further relative movements on tool-workpiece interface will break the junctions which may cause the transfer of material from the tool, leading to adhesive wear or adhesion. In addition, the tool materials may not be chemically stable under high temperature, and atoms could move from the tool to the workpiece, which is described as diffusion. All these wear mechanisms combined with other factors decide the process of flank tool wear. Because of the complexity of tool wear mechanisms, most of studies on flank tool wear are purely experimental [14, 56-59], based on statistical analysis [60-63] or simulation [64]. All these methods are time-consuming and do not reveal the physics in flank tool wear mechanisms. Predictive analytical model is physics-based method which normally provides fast and credible results. Zhang *et al.* [65] proposed a flank wear model based on the prediction of the cutting force and the energy consumption. The wear volume of the tool edge was directly related to the

accumulated energy intensity, which was basically calculated by cutting force and travelling distance. The model successfully described the flank tool wear due to mechanical loads or abrasion, but ignored the adhesion and diffusion. Therefore, it cannot be directly applied in laser-assisted milling. Huang *et al.* [55, 66, 67] proposed the tool wear prediction model in hard turning of Cubic Boron Nitride cutters, which considered abrasion, adhesion, and diffusion. This model is applied as the fundamental algorithm of the current predictive model, while the effects of rake angle and microstructure evolution that are ignored in Huang's model, and the laser effect as well as milling configuration required by laser-assisted milling, are added based on several previous established models. Up to now, this is the first comprehensive analytical predictive model of flank tool wear in laser-assisted milling process.

2.2 Inverse problem methodology in laser-assisted milling

The inverse analysis so far has been focusing on determining model coefficients that are hard to be defined in analytical model or material properties that are hard to be measured in experiments. Edouard *et al*. [68] used inverse analysis to determine nine cutting coefficients for two different cutting forces models. Their results were validated under different combinations of axial depth of cut, radial depth of cut, feed per tooth, and spindle speed, but these process parameters were not involved in the inverse analysis. Solidônio *et al.* [69] predicted the heat flux in a thermal model of the assembly tool-tool holder under four different inverse analysis methods. The direct problem was solved by an irregular finite volume mesh. Marcelo *et al.* [70] estimated the heat flux and the temperature field at the cutting interface of the tool in turning process. The direct problem was solved by algorithm implemented in C++. In addition, there are several other

researchers applying inverse analysis on coefficients of constitutive equations. Pujana *et al.* [71] identified the constitutive equations of flow stress in orthogonal cutting and used finite element method to evaluate the results. Cutting force, feed force, average temperature, and chip thickness were compared to experiments with an average error of 30%. Agmell *et al.* [72] determined five coefficients in the Johnson-Cook constitutive model in orthogonal cutting. The inverse analysis was performed using a Kalman filter. The primary cutting force and chip compression ratio were chosen to be the target performances and less than 2% errors were gained in all cases. Rodolfo *et al.* [73] identified five material parameters in Johnson-Cook jaw and Coulomb friction coefficient at the tool-chip interface in orthogonal cutting. The direct analysis was conducted by finite element simulation and the inverse analysis was done by a Multi Island Genetic Algorithm. The target performances were cutting force, thrust force, and temperature. The direct problem was solved 140 times in batch mode and huge errors of more than 50% were found in several cases. Sampsa *et al.* [74] also used the finite element method and inverse analysis to predict seven Johnson-Cook model parameters with four target performances including cutting force, tangential force, resultant force, and cutting temperature. Five different inverse analysis methods were compared and discussed. Denkena *et al.* [75] used Oxley's predictive machining theory to solve the direct problem in orthogonal milling and applied a particle swarm optimization algorithm to identify the ideal process parameters. The position and velocity of each particle of the swarm is updated within the problem space until the best position is found or the preset step limit is reached. The constitutive parameters of the Johnson-Cook's flow stress model were determined with a good agreement of cutting force. Martin [76] proposed a new method to identify five parameters

of the Johnson-Cook law with a small number of finite element simulations. Chen *et al.* [77] chose cutting force and chip thickness as targets and optimized the inverse analysis of determining Al6063 constitutive model coefficients. Cui *et al.* [78] proposed a new gradient-based inversion method with the relaxation factor updated in each loop to guarantee both efficiency and convergence. Xie *et al.* [79] applied Levenberg-Marquardt method for inverse analysis. The core of the algorithm is sensitivity coefficient matrix which takes the derivative of target performance with respect to each process parameter. Other inverse analysis techniques [80] [81] have also been developed for material properties or plasticity constants.

In current study, iterative gradient search method is used on force, residual stress, surface roughness, and tool life in laser-assisted milling. This method guesses the process parameters based on the difference between predicted target performance and experimental measurement. Ning *et al.* [82] determined the Johnson-Cook model constants by searching cutting force and thrust force in orthogonal machining of ultra-fine-grained titanium. Mirkoohi *et al.* [83] determined optimal combination of depth of cut and cutting velocity to match desirable forces in the machining of Ti-6Al-4V. This procedure has also been widely applied in inverse analysis of hydraulic parameters [84], material properties [79, 85], and torque [86].

2.3 Forward problem methodology in ultrasonic vibration-assisted milling

Non-conventional milling has been developed for years in order to reach high precision, extend tool life while keep the material removal rate. Ultrasonic vibration-assisted milling is a newly developed non-conventional milling process to achieve these

targets in a more ecofriendly manner comparing to laser-assisted or electrical discharge milling. Micro-scale high frequency vibration with small amplitude is applied on the tool or workpiece to realize the tool-workpiece separation during the milling process. Several research studies have concluded that the tool-workpiece separation in ultrasonic vibration-assisted milling is the main reason for several benefits including improved surface quality [49], lower machining forces, and extended tool life [87]. This tool-workpiece interaction is microscopically non-monotonic which facilitates chip separation and therefore reduces machining forces. In addition, the frequent separation reduces the deformation zone of workpiece during milling which is the main reason for improved surface finish.

2.3.1 Milling force

Several experimental investigations and statistical analysis have been conducted on milling force during ultrasonic vibration-assisted milling. Hsu *et al.* [88] analyzed the effects of milling parameters on cutting forces in ultrasonic vibration-assisted milling of Inconel 718 and found that depth of cut was the dominant factor. Ibrahim *et al.* [89] studied the cutting force reduction on Aluminium Al6061, and a 32% reduction was recorded on mean forces while peak forces were at same level for conventional and ultrasonic vibration-assisted milling. Similarly, Halim *et al.* [2] recorded a 10% reduction on maximum machining force in feed direction for ultrasonic vibration-assisted milling of carbon fiber reinforced plastic. These studies reflect the benefits of ultrasonic vibration-assisted milling, but the quantitative conclusions are limited to specific material and process parameter combinations, and are unable to reveal the physics nature analytically.

Up to now, there are few analytical models proposed for force prediction in ultrasonic vibration-assisted milling. Verma *et al.* [90] predicted static machining force in axial ultrasonic vibration-assisted milling. The instantaneous chip thickness is calculated based on the frequency and maximum velocity of vibration, and the mean cutting force for the specific tool angular position is derived from contact ratio and shear flow stress based on Johnson–Cook model. This method is able to calculate mean oblique cutting forces accurately through mechanics of machining. However, the tool-workpiece separation criterion in axial direction is relatively easy to decide, and the dynamics of moving tool or workpiece is simplified as a contact ratio. In current study, an analytical force predictive model is proposed which is able to characterize vibration in three directions and decide three types of tool-workpiece separation criterions.

2.3.2 Temperature

Machining temperature is one of the key factors for process control as it can significantly influence tool wear rate and residual thermal stresses. Therefore, several investigations have been conducted to characterize temperature during ultrasonic vibration-assisted machining. Halim *et al.* [2] recorded maximum machining temperature during ultrasonic vibration-assisted and conventional milling of carbon fiber reinforced plastic. The machining temperature recorded in ultrasonic vibration-assisted milling was 15% lower when compared with conventional milling mainly due to reduction of cutting forces. Abbasi *et al.* [91] conducted ultrasonic vibration-assisted turning of AISI 4140 hardened steel. The maximum cutting temperature dropped over 30% when the vibration was applied, and the increase in vibration amplitude would further decrease cutting temperature, since the increase of amplitude would increase the separation time and

decrease total cutting time in each cycle. These experimental studies show the effects of ultrasonic vibration on machining temperature, but have limited application as the quantitative conclusions are only applicable to specific workpiece material and tool studied.

In order to reveal the physics behind machining temperature during ultrasonic vibration-assisted milling. The tool-workpiece separation needs to be first described analytically. Overcash *et al.* [92] modeled dynamic tool tip temperature during ultrasonic vibration-assisted turning. The vibrated tool movement is described as a triangular function with different velocity in extension and retraction processes. The tool will separate from workpiece due to a higher linear velocity in retraction. In addition, contact is not reinitiated until some finite time after the beginning of the next vibration cycle when the tool is extending and chasing the workpiece. The model is able to describe these two separation criteria accurately. However, the tool trajectory is more complex in milling situation, and the thermal loads are considered through numerical simulation. Therefore, the prediction of temperature in their work is not purely analytical. Later, Khajehzadeh *et al.* [93] proposed theoretical model of tool temperature in ultrasonic vibration-assisted turning. The tool position is the superposition of linear feed movement and sinusoid vibration movement. The primary heat source in shear zone and secondary heat source at tool-chip interface are considered. However, the rubbing heat source on tool-workpiece interface is ignored. Up to now, there are few analytical model proposed for temperature prediction in milling with ultrasonic vibration assistance in any direction.

2.3.3 Residual stress

Residual stress is another key factor that can significantly influence fatigue performance of the product. Therefore, several investigations have been conducted to characterize residual stress during ultrasonic vibration-assisted machining. Nestler and Schubert [94] measured residual stress in surface layer after ultrasonic vibration-assisted turning of aluminium matrix composite with vibration in different direction and amplitude. All values are compressive with higher amplitude leading to more compressive residual stress as temperature is reduced in the chip formation zone. In addition, much higher compressive residual stresses are recorded when the vibration is applied in depth direction as it has a similar effect like shot peening. Sharma and Pandey [95] later summarized studies on ultrasonic vibration-assisted turning and concluded that it is an effective method to enhance the fatigue life by inducing compressive residual stress through vibro-impacts. This finding is further confirmed by Zhang *et al.* [96] as in their turning experiments on Ti-6Al-4V alloy. The original tensile residual stress in conventional machining becomes compressive with the vibration applied. And the magnitude of the compressive residual stress increases as the vibration amplitude increases. For ultrasonic vibration-assisted milling process, Lu *et al.* [97] and Hu *et al.* [98] summarized the effects of different cutting and vibration parameters on residual stress using numerical simulation. With the increase of spindle speed, more compressive residual stress is predicted. With higher vibration frequency, both the milling force and temperature decrease, which lead to residual stress with smaller magnitude. Ren *et al.* [99] measured residual stress after ultrasonic vibration-assisted milling on Ti-6Al-4V Alloy and found that the residual stress would move to tensile direction under higher feed rate. These experimental studies show the effects of ultrasonic vibration on residual stress, but have limited application as the quantitative

conclusions are only applicable to specific workpiece material and tool studied. Up to now, residual stress after ultrasonic vibration-assisted milling has not been predicted through analytical model thus not revealing the physics nature.

2.3.4 Surface roughness

Surface roughness is an important indicator of machined surface quality. With the development of vibration-assisted machining and milling, people have been investigating the effects of vibration on surface roughness for years. Abdur-Rasheed [100] summarized the measurements on machined surface after vibration-assisted machining for various workpiece and tool combinations. The surface roughness drops for all cases when comparing with conventional orthogonal cutting with a decrease percentage varying from 40 to 70%. Razfar *et al.* [101] measured surface roughness of AISI 1020 steel after conventional and ultrasonic vibration-assisted milling when the vibration was applied in feed direction. Again, the surface roughness is improved in all vibration cases by 12.9% in average. In addition, the cutting parameters have similar effects on surface roughness, as increasing feed or spindle speed will result in higher surface roughness after both conventional and ultrasonic vibration-assisted milling. The depth of milling has insignificant effect on surface roughness. Besides cutting parameters, tool geometry including tool radius and tool edge radius has a more dominant effect as confirmed by Xiao *et al.* [102] and Hsu *et al.* [88]. In order to maximize the benefit of ultrasonic vibration-assisted milling in turns of reduced surface roughness, the direction of ultrasonic vibration being applied with respect to the workpiece needs to be correctly chosen as it will also influence the resultant surface roughness. According to the measurements obtained by Halim *et al.* [2], the surface roughness was higher in ultrasonic vibration-assisted milling

when the vibration was applied in axial direction. In addition, Ko *et al.* [103, 104] and Chen *et al.* [49] compared machined surface quality after feed directional and cross-feed directional vibration-assisted milling with conventional milling. A better surface quality was reached in feed directional ultrasonic vibration-assisted milling, while the surface roughness became higher in some cases after cross-feed directional vibration-assisted milling. As shown in Figure 2, with the vibration in the same direction as feed movement, the uncut material area due to gap between tool edges is smaller. Gao and Sun [105] did analytical predictive modeling of surface roughness for two-dimensional vibration-assisted machining based on kinematics and tool geometry analysis, but the effects of forces and workpiece recovery are ignored. In current study, an analytical model of surface roughness on side wall in feed directional ultrasonic vibration-assisted milling is proposed.

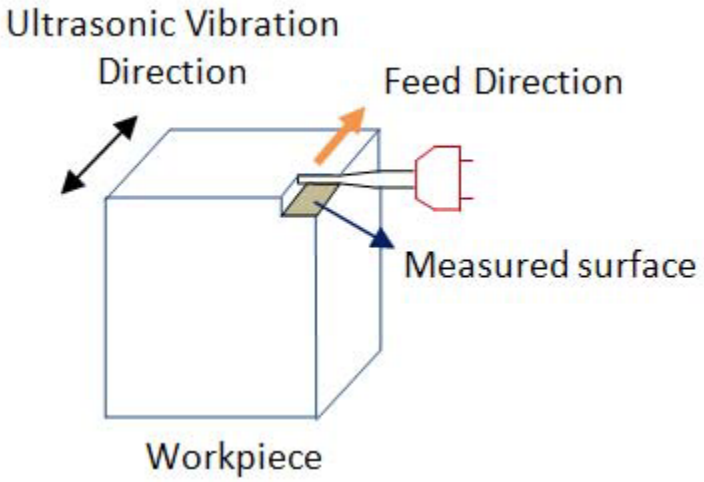

Figure 2 Feed directional ultrasonic vibration-assisted milling [104]

2.3.5 Tool flank wear

Tool wear is one of the most important factor that needs to be considered during a manufacturing process. People have been developing advanced machining process for a

long time in order to limit the tool wear rate and extend the tool life. Ultrasonic vibration machining is one of the newly developed technique that generates discontinuous and smaller chips than conventional machining by applying micro-scale high frequency vibration with small amplitude on either workpiece or tool. Many studies so far have revealed the effect of ultrasonic vibration on tool wear through experimental investigation or numerical simulation. Nath *et al.* [106] measured tool flank wear during ultrasonic vibration turning on low alloy steel with CBN tools. Both flank wear and flank wear rate are much lower for ultrasonic vibration turning under various combinations of cutting parameters. Hsu *et al.* [88] recorded tool wear in ultrasonic vibration milling of Inconel 718 with tungsten carbide tools. Through the analysis of variance, the type of cutting tool is found to have the most significant effect on flank wear followed by vibration frequency, feed rate, and depth of cut. Li *et al.* [107] also examined the tool wear on tungsten carbide tool and concluded that the ultrasonic vibration enhances the abrasive resistance of the tool due to accelerated heat transfer. Similar conclusion is later made by Ibrahim *et al.* [108]. In addition, they pointed out that the reduced contact time in vibration-assisted milling also contributes to less tool wear due to more available time for stress release on tool and less available time for wear reactions such as graphitization. Several other review studies [49, 87, 109-111] have concluded that ultrasonic vibration machining is able to extend tool life and limit tool wear rate in general. However, exception is also observed by Halim *et al.* [2] during ultrasonic vibration-assisted milling using polycrystalline diamond tool. The tool for ultrasonic vibration-assisted milling worn out faster than conventional milling. The z-direction oscillation of the cutting tool creates more interaction and contact length between the tool and the workpiece thus increase the tool wear of the cutting tool. Therefore, the

usage of vibration is not always leading to low tool flank wear, and an optimal combination of vibration frequency and amplitude is desirable for different material and cutting parameters. However, the experimental studies and numerical simulations have limited application as the quantitative conclusions are only applicable to specific workpiece material and tool studied. And a comprehensive analytical predictive model has not been proposed for tool wear rate in ultrasonic vibration-assisted milling. In current study, an analytical tool wear rate predictive model is proposed which is applicable for vibration in three directions based on three types of tool-workpiece separation criteria.

CHAPTER 3. FORWARD PROBLEM METHODOLOGY IN LASER-ASSISTED MILLING

3.1 Milling force

The 3D oblique cutting is transferred to equivalent 2D orthogonal cutting at each rotation angle. Then based on modified Oxley's model, the equivalent 2D cutting forces can be calculated. These two forces are in cutting and radial directions in 3D. The axial force is calculated according to 3D geometry. And three milling forces are transferred into Cartesian coordinates to match up with experiment measurements. In the modified Oxley's model, the flow stress in the chip is given by the Johnson-Cook flow stress model. Instead of assuming all Johnson-Cook parameters to be constants, one Johnson-Cook parameter becomes grain size dependent through Hall-Petch equation so that the recrystallization effect is taken into consideration. The Johnson-Mehl-Avrami-Kolmogorov (*JMAK*) model calculates the recrystallized volume fraction as a function of strain, strain rate, and temperature.

3.1.1 Milling force modeling and its equivalent orthogonal cutting model

Due to the geometry of milling tool, the chips created during cutting do not remain the same thickness. So for the equivalent orthogonal cutting model, the chip thickness will vary with rotation angle. The average chip thickness is given as

$$\overline{t_c} = \frac{1}{2}\frac{V_f}{RPM} \tag{1}$$

where $\overline{t_c}$ is the average chip thickness, Vf is feed rate, and RPM is the spindle speed. Then the instantaneous equivalent chip thickness is

$$t_c(\phi_r) = \sqrt{2} \times \overline{t_c} \times \sin(\phi_r) \tag{2}$$

where $\phi_r = 2\pi \times RPM \times t$ is the rotation angle at given time t. As shown in Figure 3, the equivalent chip thickness is

$$t_c^* = t_c(\phi_r) \times \cos C_s^* \tag{3}$$

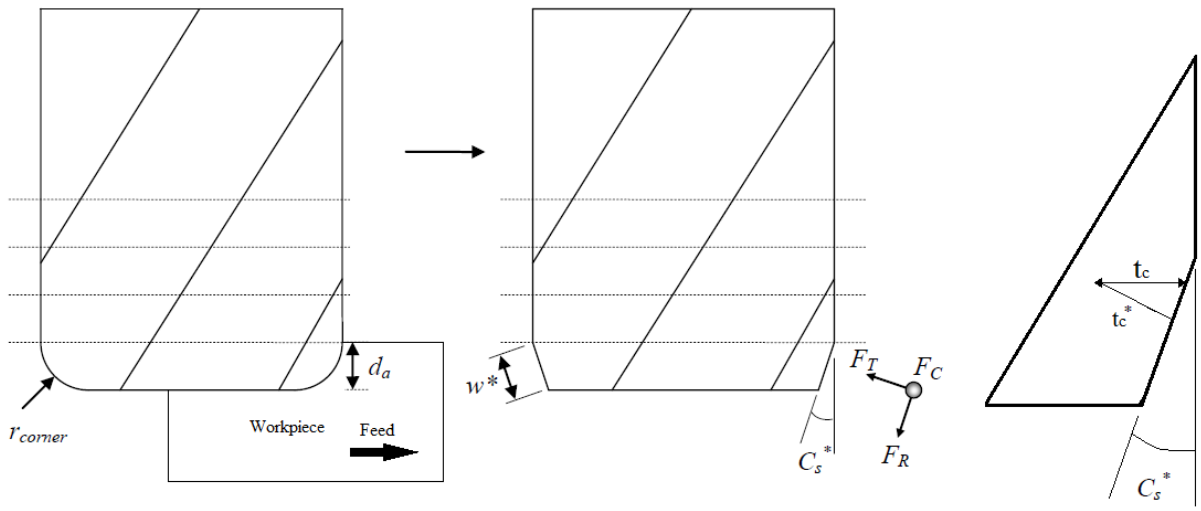

(a) (b) (c)

Figure 3 Transformation from milling to equivalent orthogonal cutting (a) Milling configuration with instantaneous axial depth of milling d_a and tool edge radius r_{corner} (b) Equivalent orthogonal cutting with equivalent side cutting edge angle C_s^* and equivalent cutting width w^*, the tangential cutting force is perpendicular to cutting edge instead of machined surface (c) Transformation of cutting depth [112]

The axial depth of cut can be treated as cutting width in equivalent 2D model as

$$w^* = \frac{d_a}{\cos(C_s^*)} \tag{4}$$

The equivalent cutting speed is a function of rotation angle as

$$V(\phi) = \sqrt{V_f^{\,2} + V_r^{\,2} + 2V_f V_r \cos\phi_r} \tag{5}$$

where $V_r = 2\pi R \times RPM$ is the rotation speed, R_t is the tool radius. Based on the results of Equations (3)-(5), the cutting force F_c and thrust force F_t are calculated in modified Oxley's model [113]. Then the resultant force in third direction can be calculated as

$$F_r = \frac{F_c\left(\sin i^* - \cos i^* \sin \alpha_r^{\,*} \tan \eta_c^{\,*}\right) - F_t \cos \alpha_r^{\,*} \tan \eta_c^{\,*}}{\sin i^* \sin \alpha_r^{\,*} \tan \eta_c^{\,*} + \cos i^*} \tag{6}$$

Since the side cutting edge angle is not zero, F_t and F_r will no longer act in the feed and axial directions. So these three forces are redefined as P_1, P_2 and P_3 where they act in the cutting, feed, and axial direction.

$$\begin{aligned} P_1 &= F_c \\ P_2 &= -F_t \cos\left(C_S^*\right) - F_r \sin\left(C_S^*\right) \\ P_3 &= F_t \sin\left(C_S^*\right) - F_r \cos\left(C_S^*\right) \end{aligned} \tag{7}$$

The positive directions P_1, P_2 and P_3 are defined as the cutting, positive feed, and facing workpiece directions. Since the tool used in experiments has single flute, the forces transferred into Cartesian coordinates are

$$
\begin{aligned}
F_X(\phi_r) &= P_1\cos(\phi_r) + P_2\sin(\phi_r) \\
F_Y(\phi_r) &= -P_1\sin(\phi_r) - P_2\cos(\phi_r) \\
F_Z(\phi_r) &= -P_3
\end{aligned} \tag{8}
$$

The forces calculated in three directions from Equation (8) when $0^o \le \phi_r \le 180^o$ are compared with experiment measurements.

3.1.2 Recrystallization effect

In the modified Oxley's model, the flow stress in the chip is given by the Johnson-Cook flow stress model. The traditional model assumes all Johnson-Cook parameters to be constants, which does not take the recrystallization effect into consideration. However at higher temperature, the augmented grain size will reduce the flow stress. For simplification, only the initial yield stress term is considered varying with grain size. The relationship is described by the Hall-Petch equation

$$
A = A_{hp} + K_{hp} d^{-0.5} \tag{9}
$$

where d is the average grain size. A_{hp} and K_{hp} are material constants. Then the modified Johnson-Cook flow stress model becomes

$$
\sigma = (A_{hp} + K_{hp} d^{-0.5} + B\bar{\varepsilon}^n)(1 + C\ln\frac{\dot{\bar{\varepsilon}}}{\dot{\varepsilon}_0})\{1 - (\frac{T - T_0}{T_m - T_0})^m\} \tag{10}
$$

where B, C, m and n are still material constants, $\bar{\varepsilon}$ is the plastic strain, $\dot{\bar{\varepsilon}}$ is the plastic strain rate, $\dot{\varepsilon}_0$ is the reference strain rate, selected to be 1 s^{-1} for this paper. T_m is the melting

temperature of Inconel 718. T_0 is the environment temperature, which is the laser preheated temperature. T is the temperature of chip or shear plane based on which flow stress is calculated.

To decide the grain size, the *JMAK* model [114] is used to describe the dynamic recrystallization process of crystalline material. Based on the assumption that nucleation and grain growth are randomly distributed, the average grain size d could then be expressed as

$$d = d_{drex} X_{drex} + d_0 (1 - X_{drex}) \tag{11}$$

where d_0 is the initial average grain size, d_{drex} is the dynamically recrystallized average grain size and X_{drex} is the recrystallized volume fraction.

When $\bar{\varepsilon}$ is larger than $a_2 \varepsilon_p$, the dynamic recrystallization will occur. ε_p is the peak strain as

$$\varepsilon_p = a_1 d_o^{\,h_1} \dot{\bar{\varepsilon}}_0^{\,m_1} \exp(Q_{act} m_1 / RT) + c_1 \tag{12}$$

where R is the gas constant, Q_{act} is the activation energy, a_1, h_1, m_1 and c_1 are material constants. The recrystallized volume fraction is defined with the Avrami equation as

$$X_{drex} = 1 - \exp\left[-\beta_d \left(\frac{\bar{\varepsilon} - a_{10} \varepsilon_p}{\varepsilon_{0.5}} \right)^{k_d} \right] \tag{13}$$

where β_d , a_{10} and k_d are material constants, $\varepsilon_{0.5}$ is the strain that gives X_{drex} =0.5, which is calculated by

$$\varepsilon_{0.5} = a_5 d_0^{h_5} \bar{\varepsilon}^{n_5} \dot{\bar{\varepsilon}}^{m_5} \exp(Q_{act} m_5 / RT) + c_5 \tag{14}$$

where a_5, h_5, n_5, m_5 and c_5 are material constants, the dynamically recrystallized average grain size d_{drex} is given by

$$d_{drex} = a_8 d_0^{h_8} \bar{\varepsilon}^{n_8} \dot{\bar{\varepsilon}}^{m_8} \exp(Q_{act} m_8 / RT) + c_8 \tag{15}$$

where a_8, h_8, n_8, m_8 and c_8 are material constants, the results from Equations (13) and (15) provide the average grain size in Equation (11). Then the modified Johnson-Cook flow stress model in Equation (10) is applied in modified Oxley's model to calculate equivalent orthogonal forces. Experiments are conducted on Inconel 718. The modified Johnson-Cook flow stress model parameters of Inconel 718 are obtained from Jafarian *et al.* [115] and listed in Table 1. The *JMAK* model parameters are obtained from Huang *et al.* [116], Reyes *et al.* [117] and Loyda [118] and listed in Table 2. The initial grain size d_0 is assumed to be 10 μm.

Table 1 Modified Johnson-Cook model parameters for Inconel 718 [115]

A_{hp}(MPa)	$K_{hp}(MPa\sqrt{\mu m})$	B(MPa)	C	m	n	T_m(℃)	$\dot{\varepsilon}_0$ (s^{-1})
378	298.4	1370	0.02	1.03	0.164	1300	1

Table 2 Inconel 718 material constants of *JMAK* model [116-118]

Peak strain	$a_1 d_0^{h1}$	m_1	$Q_{act} m_1 (J/mol)$	c_1		
	0.4659×10^{-2}	0.1238	49520	0		
DRx kinematics	β_d	k_d	a_{10}	a_2		
	0.693	2	0.8	0.8		
Required strain	a_5	h_5	n_5	m_5	$Q_{act} m_5 (J/mol)$	c_5
	5.043×10^{-9}	0	-1.42	-0.408	196000	0
DRx grain size	a_8	h_8	n_8	m_8	$Q_{act} m_8 (J/mol)$	c_8
	4.85×10^{10}	0	-0.4	-0.028	-240000	0

3.1.3 Experimental validation

The single beam coaxial laser-assisted milling spindle used is shown in Figure 4. A 1000W laser source as well as a water-cooling system was connected to the milling spindle. A *TiSiN* coated tungsten carbide milling tool with single flute was installed. The milling tool has a rake angle of 35°, 6mm diameter with 0.1mm nose radius. The measurement system includes 4-component dynamometer (Kistler: Type-9272), dynamometer amplifier (Kistler: Type-5019A), triaxial accelerometer (Kistler: Type-8763-BB), accelerometer amplifier (Kistler: Type -5070) and data acquisition module (National Instrument: USB DAQ-6212). The half slot climb milling was conducted under five different sets of cutting parameters as listed in Table 3. The spindle speed was set to be 3000 rpm. 30 periods were evenly selected among 10 seconds data and averaged to calculate the forces. The forces measured within ±40% of the biggest peak were averaged as shown in Figure 5.

Figure 4 The single beam coaxial laser-assisted milling spindle

Table 3 Cutting parameters of experiments

Experiment number	Feed rate (*mm/min*)	Axial depth of milling(*mm*)
1	200	0.1
2	200	0.15
3	200	0.2
4	300	0.1
5	300	0.15

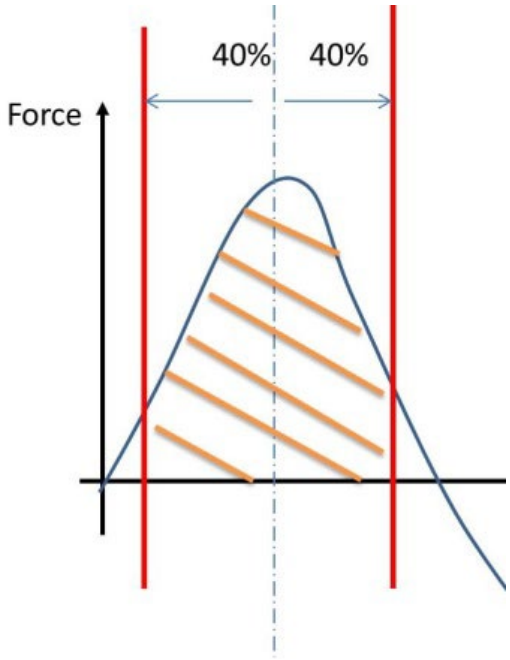

Figure 5 The forces measured within ±40% of the biggest peak

3.1.4 Results

The force signals predicted from analytical model are shown in Figure 6. Because it is the half slot milling with single flute tool, the force is constant zero between 0° and 90°. *Fy* and *Fz* will sharply increase to the peak value then gradually return. *Fx* will slowly increase and back to zero on the second half of the period. When the feed rate is fixed (200 *mm/min*), the forces are increasing with an increased axial depth of milling from 0.1*mm* in case 1 to 0.2*mm* in case 3. And an increased feed rate from 200 *mm/min* to 300 *mm/min* can also lead to larger cutting forces with constant axial cutting depth of 0.1*mm* in case 1 and case 4, 0.15*mm* in case 2 and case 5. The average forces in three directions were calculated in models with and without recrystallization effect consideration, based on the method in Figure 5. Due to the grain growth, the flow stress will decrease and the machinability is improved. The forces predicted in model including grain growth are therefore smaller.

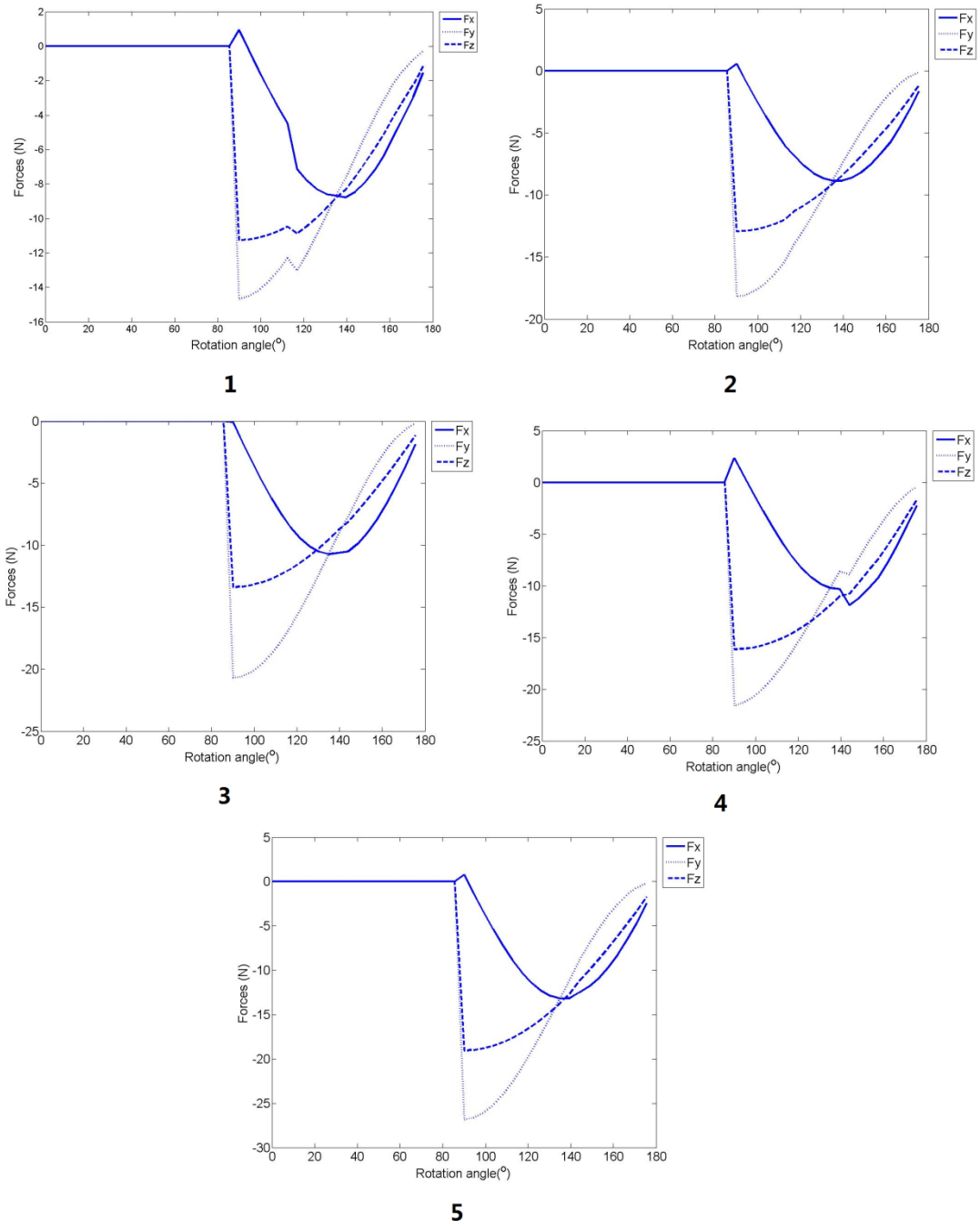

Figure 6 The force signals predicted from analytical model

Figure 7 shows the comparison of *Fx* between experiment measurements and analytical predictions. Both models could predict the trend of *Fx* with varying feed rate or axial depth of milling. But it is obvious that the original model fails in the prediction since

the values are about twice of the measurements in each case. For the new analytical model including recrystallization, the predicted forces are much more accurate. The analytical results are still larger than experiment measurements except case 3, but the maximum error has been much improved. The maximum error for new model is 19.8% in case 5, 137% in case 1 for old model.

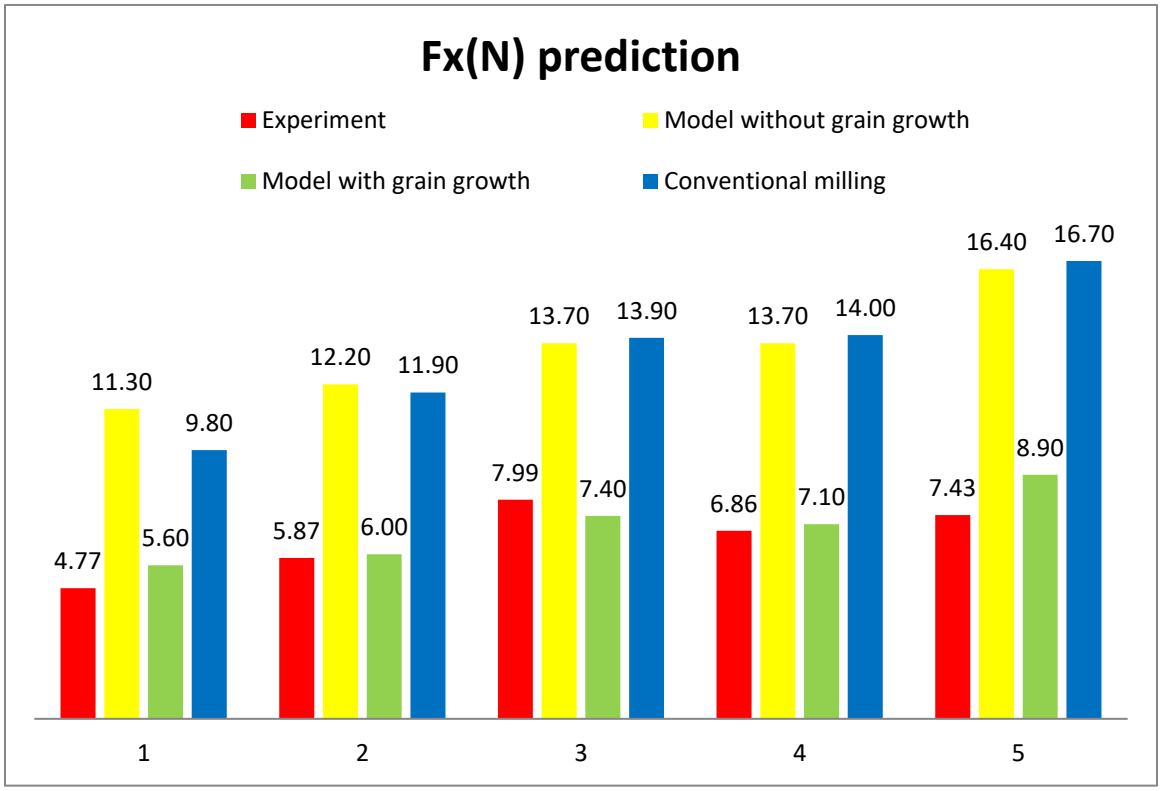

Figure 7 Comparison of *Fx*

Figure 8 shows the comparison of *Fy* between experiment measurements and analytical predictions. The new analytical model does not provide a better prediction in y direction since the actual measurements are much larger in most cases. However, the error introduced in *Fy* is more on the experiment side. The most chatter occurred during milling process was in *y* direction. Although the noise signal was filtered, the experiment

measurements in *y* direction are still larger than expected. The analytical model prediction matches with theory, but the experiment measurements get much larger forces in case 2 and case 5. Therefore, it is hard to quantify the improvement of new model in *Fy* prediction before better experiment measurements are obtained.

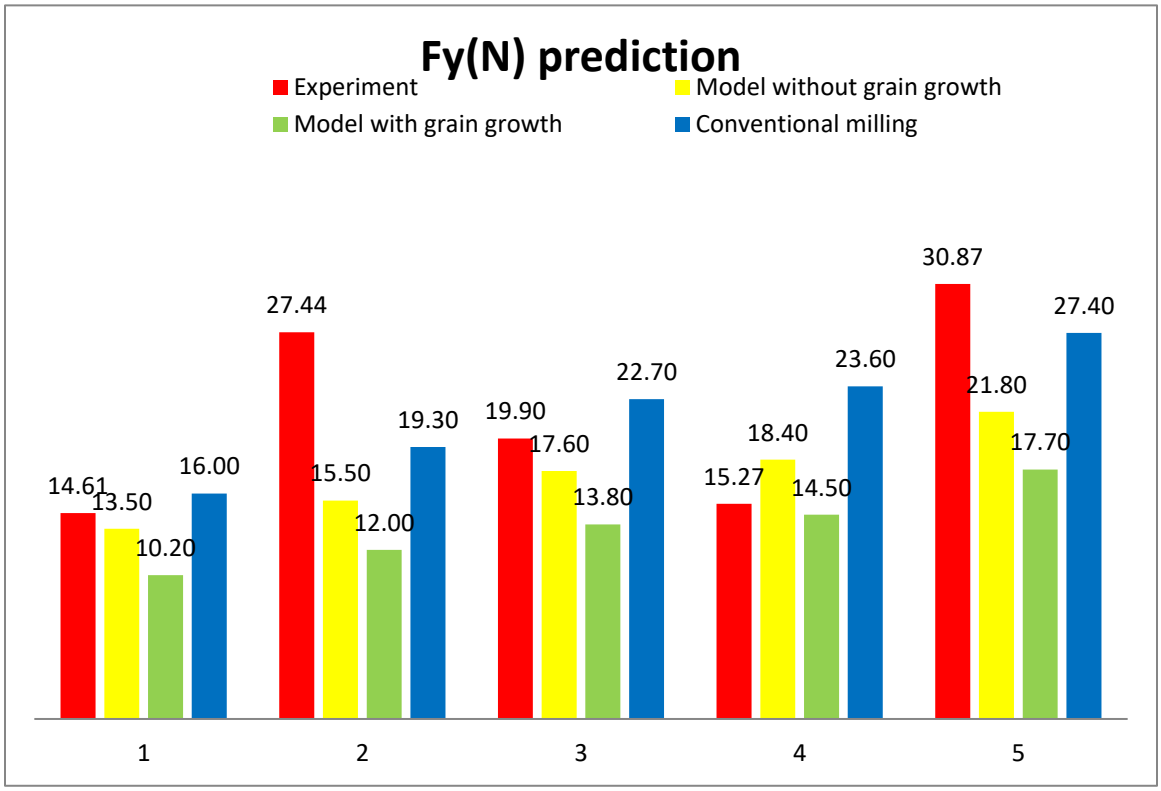

Figure 8 Comparison of *Fy*

Figure 9 shows the comparison of *Fz* between experiment measurements and analytical predictions. Again, the force measured in case 3 is smaller than expected since an increased axial cutting depth from case 2 to case 3 gives a decreased force from 11.71*N* to 9.71*N*. But similar to *Fx*, the new model with grain growth provides results much more closer to the experiment measurements. The maximum error for new model is 19.2% in case 4, 45.9% in case 4 for old model.

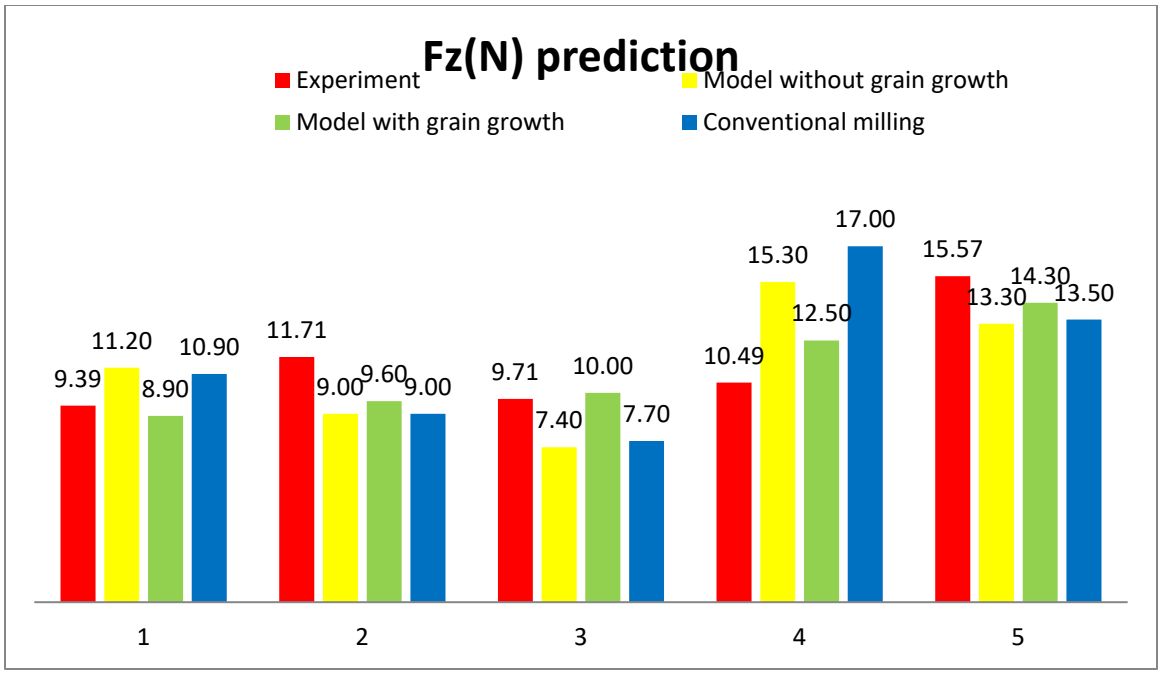

Figure 9 Comparison of *Fz*

Overall, this analytical model of milling forces prediction in laser-assisted end milling of Inconel 718 including recrystallization could provide better results in *x* and *z* directions, compared with original model without grain growth consideration. In addition, the predicted forces under conventional milling are also included to show the reduction of force in laser-assisted milling.

3.2 Temperature

The laser-assisted milling is a complex machining process including the preheating of material ahead of tool tip by laser followed by the chip removal through the contact between tool tip and workpiece. Since the milling process is treated as equivalent orthogonal cutting process at each instance, plain strain condition is assumed, and heat transfer only occurs in cutting direction indicated by X and depth direction indicated by Z. The coordinate system is defined as in Figure 10.

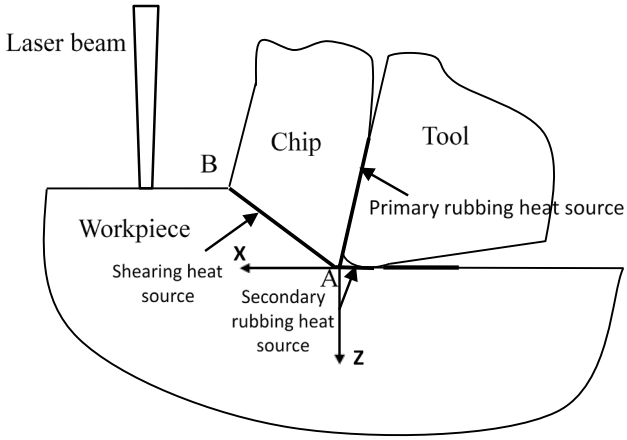

Figure 10 Coordinate system and heat sources of the predictive model

3.2.1 Temperature rise due to laser preheating

The laser preheating temperature field is calculated considering heat generation by laser power at top surface of workpiece, convection between workpiece and environment at top surface, conduction within workpiece, and isothermal boundary conditions at both sides and bottom. The temperature increase rate at top surface is described by

$$\Delta T_{\text{laser}}(x,0) = \frac{q(x) - h(T_{\text{laser}}(x,0) - T_0)}{\rho c_{\text{p}}} \tag{16}$$

where T_{laser} is the laser preheating temperature, ρ is the material density, c_{p} is specific heat, h is the heat transfer coefficient, T_0 is the environment temperature, $q(x)$ is the heat generation rate due to laser power described by the Gaussian equation as

$$q(x) = \frac{2Q}{\pi r^2} \exp(-\frac{2x^2}{r^2}) \tag{17}$$

where Q is the total input power of laser, r is the radius of laser spot. Within the workpiece, heat conduction is the dominant effect with the governing equation of

$$\Delta T_{\text{laser}}(x,z) = \alpha \nabla^2 T_{\text{laser}}(x,z) - V_{\text{f}} \frac{\partial T_{\text{laser}}(x,z)}{\partial x} \tag{18}$$

where α is thermal diffusivity and V_{f} is the moving speed of laser spot or the feed speed. The first term on the right describes the two dimensional heat conduction, while the second term considers the effect of moving laser beam in cutting direction [119]. At side or bottom boundaries, isothermal condition is assumed in cutting direction. Therefore, heat conduction is only considered in Z direction as

$$\Delta T_{\text{laser}}(x,z) = \alpha \frac{\partial^2 T_{\text{laser}}(x,z)}{\partial z^2} \tag{19}$$

The workpiece is assumed to have same temperature as the environment as intial condition, which is 25℃ in current study.

3.2.2 Machining induced temperature increase

As shown in Figure 10, three main heat sources contribute to the machining induced temperature rise. The plastic deformation in shear zone leads to the shearing heat source, while the friction on tool-chip interface and tool-workpiece interface induces two rubbing heat sources. The primary rubbing heat source is ignored because it mainly contributes to the temperature rise in chip instead of workpiece. Shearing heat source denoted by shear plane heat density q_{shear} is calculated from F_{c} and F_{t} by

$$q_{\text{shear}} = \frac{\left(F_{\text{c}} \cos\phi - F_{\text{t}} \sin\phi\right)\left(V(\phi_r) \cos\alpha_r^{*} / \cos\left(\phi - \alpha_r^{*}\right)\right)}{t_{\text{c}}^{*} \cdot w^{*} \cdot \csc\varphi} \tag{20}$$

where ϕ is the shear angle, α_r^* is the equivalent rake angle. A mirror heat source method is applied as shown in Figure 11, when the moving heat sources and adiabatic uncut workpiece surface are assumed. In Figure 11(a), a point on workpiece M(X, Z) is under a temperature rise from shearing heat source as well as its mirror heat source. The temperature rise at point M is calculated by

$$\Delta T_{\text{wk-shear}}(X,Z)=\frac{q_{\text{shear}}}{2\pi k_{\text{wk}}}\int_0^{L_{\text{AB}}} e^{-\frac{(X-l_i\sin\varphi)V(\phi)}{2\alpha}}\left\{K_0\left[\frac{V(\phi)}{2\alpha}\sqrt{\left(X-l_i\cos\varphi\right)^2+\left(Z+l_i\sin\varphi\right)^2}\right]+K_0\left[\frac{V}{2\alpha}\sqrt{\left(X-l_i\cos\varphi\right)^2+\left(2t_{\text{c}}^{*}-l_i\sin\varphi+Z\right)^2}\right]\right\}dl_i \tag{21}$$

where $L_{\text{AB}}=\dfrac{t_{\text{c}}^{*}}{\sin\varphi}$ is the length of shear plane, k_{wk} is the thermal conductivity of workpiece, and K_0 is the modified Bessel function of the second kind or Neumann function. The secondary rubbing heat source density q_{rub} comes from P_{cut} by

$$q_{\text{rub}}=\frac{P_{\text{cut}}V(\phi)}{w^{*}\cdot CA} \tag{22}$$

where CA is the contact length, P_{cut} is the plowing force in cutting direction which is also calculated from force predictive model. As shown in Figure 11(b), the secondary heat on tool-workpiece interface from rubbing is treated as a moving heat source along X direction. The temperature rise due to the rubbing is calculated as

$$\Delta T_{\text{wk-rub}}(X,Z)=\frac{q_{\text{rub}}}{\pi k_{\text{wk}}}\int_0^{CA}\gamma e^{-\frac{(-X-x_i)V(\phi)}{2\alpha}}\left\{K_0\left(\frac{V(\phi)}{2\alpha}\sqrt{\left(X+x_i\right)^2+Z^2}\right)\right\}dx_i \tag{23}$$

where γ is a heat distribution coefficient defined as

$$\gamma = \frac{\sqrt{k_{\mathrm{wk}} \rho C_{\mathrm{p}}}}{\sqrt{k_{\mathrm{wk}} \rho C_{\mathrm{p}}} + \sqrt{k_{\mathrm{t}} \rho_{\mathrm{t}} C_{\mathrm{t}}}} \tag{24}$$

where k_t, ρ_t, and C_t are the thermal conductivity, density, and specific heat of cutting tool. Therefore, the temperature rise of any point on the workpiece M(X, Z) is calculated as the summation of two machining induced temperature rise sources in addition to laser preheating temperature rise

$$\Delta T(X,Z) = \Delta T_{\text{wk-shear}}(X,Z) + \Delta T_{\text{wk-rub}}(X,Z) + \Delta T_{\text{laser}}(X,Z) \tag{25}$$

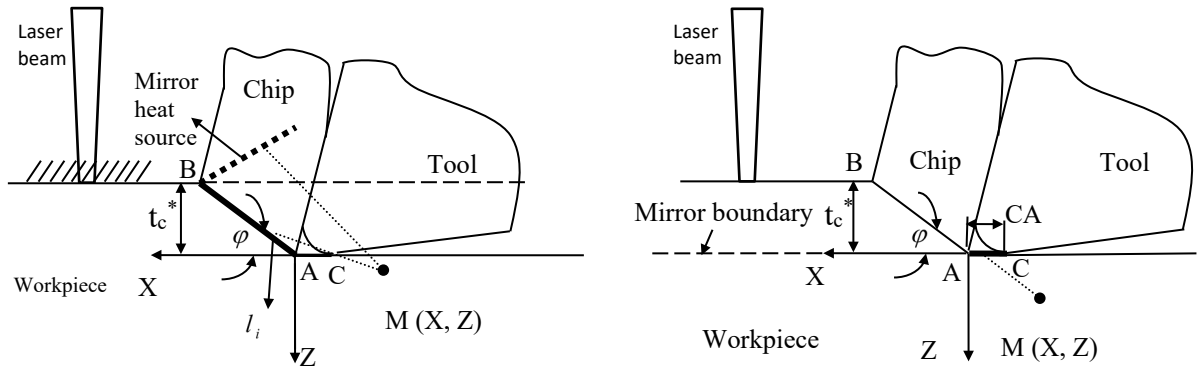

(a) (b)

Figure 11 Schematic of (a) shearing heat source and (b) rubbing heat source for machining temperature prediction [120]

3.2.3 Experimental validation and results

In order to validate the proposed predictive model, experimental measurements are collected during laser-assisted milling of Si_3N_4 [121] and Ti-6Al-4V [122].

3.2.3.1 Silicon nitride ceramics (Si_3N_4)

The laser-assisted milling is conducted on a CNC machine (Haas Automation Inc.). A diode laser (Visotek Inc., DFL500) in continuous wave mode is used to generate a high-power laser beam. The surface temperature of the workpiece is measured through an infrared pyrometer (Williamson Inc., Model 91-20-C-23D) with a range from 475 to 1,750°C. The dimensions of Si_3N_4 specimens are 4.3×5.3×48*mm*. The axial depth of cut is 1*mm*, the feed speed is 6*mm/min*, and the laser-cutter allowance or the distance between laser beam spot and tool tip is about 3*mm*. The pyrometer measures the temperature at about 0.2*mm* below the machined surface corresponding to the laser beam spot. Measurements from five experiments are compared with two variables including diameter of laser spot and laser power. For the first three experiments, the diameter of laser spot is a constant of 3.3*mm* with three levels of laser power 300, 340, and 410*W*. The other two experiments have a constant laser power of 340*W* with different diameters of laser spots of 1.8 and 2.6*mm*. The predictive model introduces a constitutive model for flow stress [123] following the form of

$$\sigma = \sigma_0 \{1 + (\frac{\varepsilon}{\varepsilon_0})^n\} \{\frac{\dot{\varepsilon}}{\dot{\varepsilon}_0} \cdot exp(\frac{Q_{\text{act}}}{RT})\}^m \tag{26}$$

where σ_0 is the yield stress measured at $\dot{\varepsilon} = 1 \times 10^{-8} s^{-1}$, Q_{act} is the activation energy, and R is the universal gas constant. All the material constants are listed in Table 4.

Table 4 Constitutive model parameters for Si_3N_4 and Ti-6Al-4V

Si_3N_4	σ_0(MPa)	Q(KJ/mol)	R(J/mol·K)	ε_0	m	n	T(℃)	$\dot{\varepsilon}_0$ (s^{-1})
	25	800	8.31447	0.3	0.061	0.4	1400	1
Ti-6Al-4V	A(MPa)	B(MPa)	C	m	n	T_m(℃)	$\dot{\varepsilon}_0$ (s^{-1})	
	997.9	653.1	0.0198	0.7	0.45	1668	1	

As shown in Figure 12, the temperature distribution from the predictive model is able to show both the machining induced temperature rise and overall temperature including laser effect, when the laser power is 340W and laser spot dimeter is 3.3mm. The machining induced temperature rise is negligible for Si_3N_4, because the maximum temperature rise at tool tip is only 10.04℃ at machined surface as shown in Figure 12(a). The overall maximum temperature occurs at 3mm ahead of tool tip due to laser-cutter allowance as shown in Figure 12(b). The temperature distribution at depth of 0.2mm below machined surface is compared with experimental measurements as listed in Table 5. The temperature below laser spot increases with a larger laser power or a smaller laser spot diameter, which matches the prediction of proposed model. Good agreements are found for the maximum temperature prediction between experimental measurements and the predictive model with average difference of 3.25% and maximum difference of 7.08%. The prediction process is done within 3.1s for all cases.

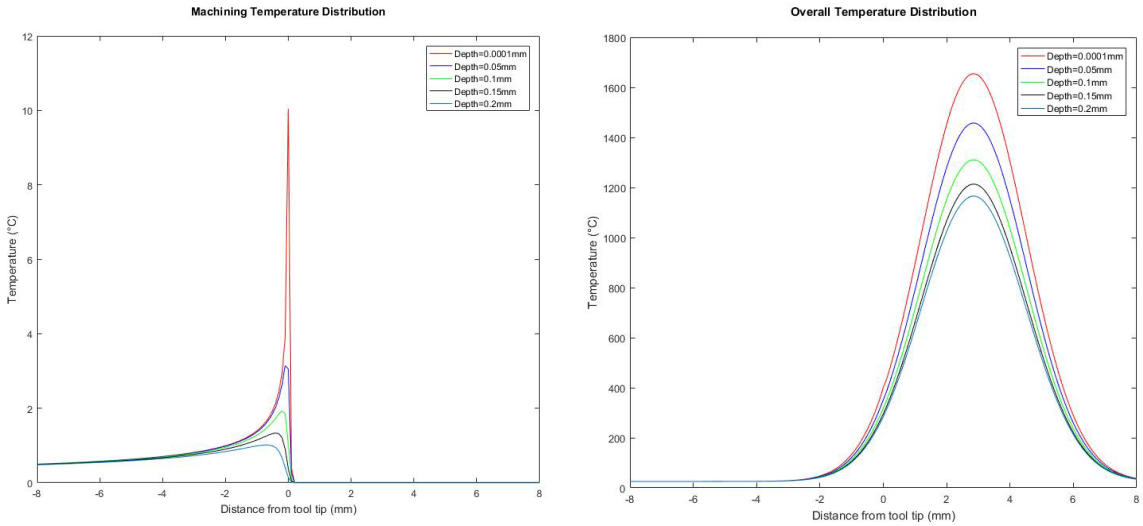

(a) (b)

Figure 12 Temperature field prediction of Si_3N_4 with laser power of 340*W* and laser spot diameter 3.3*mm* (a) Machining induced temperature rise and (b) Overall temperature distribution

Table 5 Temperature comparison for Si_3N_4 at 0.2*mm* below machined surface under laser beam spot

Laser power (*W*)	Diameter of laser spot (*mm*)	Temperature measured from experiment (℃)	Temperature from the predictive model (℃)	Percentage difference (%)	Computation time (*s*)
300	3.3	About 1,000	1,031.00	3.10	3.09
340	3.3	About 1,130	1,165.13	3.11	2.94
410	3.3	About 1,230	1,246.37	1.33	2.91
340	1.8	About 1,600	1,713.27	7.08	2.92
340	2.6	About 1,320	1,341.21	1.61	2.91

3.2.3.2 Ti-6Al-4V

The experiments are conducted on a 5hp Hafco Metal Master mill with model BM-62VE under dry conditions. The cutter is 490-040C40-0M type with a diameter of 40*mm* and four carbide inserts. The tool has a primary rake angle of 30° and clearance angle of

6°. A continuous-wave Nd:YAG laser with wavelength 1.064μm and maximum power 2.5kW is used. The diameter of laser spot is 5mm, and the feed rate is 0.1$mm/tooth$. A Maurer model QKTR 1075 two-colour optical pyrometer and an infrared thermal camera of ThermoVision® model A40 are applied to measure the surface temperature at the laser spot. The measurement range for the pyrometer is between 800 and 2,500℃ and for the infrared thermal camera is up to 2,000℃. The flow stress constitutive model for Ti-6Al-4V applied in the predictive model follows the equation of

$$\sigma = (A + B\bar{\varepsilon}^{n})(1 + C\ln\frac{\dot{\bar{\varepsilon}}}{\dot{\bar{\varepsilon}}_0})\{1 - (\frac{T - T_0}{T_{\mathrm{m}} - T_0})^{m}\} \tag{27}$$

where T_{m} is the melting temperature and T_0 is the environment temperature. All the material constants are listed in Table 4.

The first measurement is collected at laser spot at cutting speed of 190m/min, axial depth of cut of 1.5mm, feed speed of 600mm/min, laser-cutter allowance of 28.5mm, and laser power of 1,250W. The temperature distribution from the predictive model is shown in Figure 13. At the center of the laser spot at machined surface, a constant value of 1,550℃ is recorded after the laser beam fully interacting with the workpiece. The maximum temperature at surface from the predictive model is 1,633.39℃. The difference is 5.38% and the computation time is 6.73s.

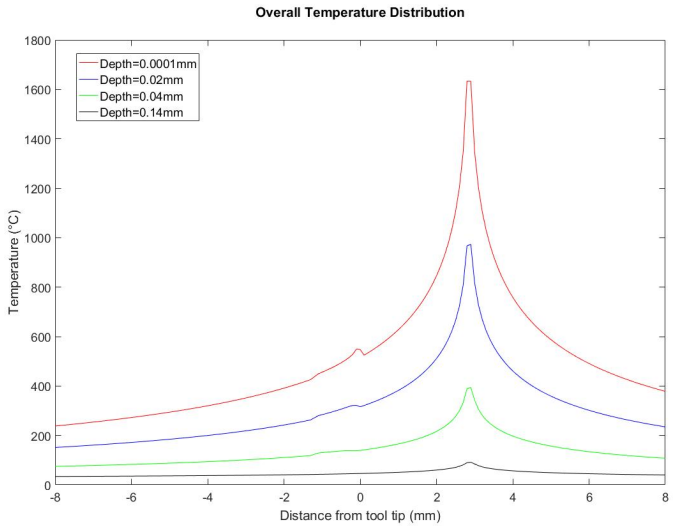

Figure 13 Temperature field prediction of Ti-6Al-4V with laser power of 1250*W*, cutting speed of 190*m/min*, axial depth of cut of 1.5*mm*, and laser-cutter allowance of 28.5*mm*. The highest point in red curve corresponding to workpiece surface is compared with experimental measurement at the center of the laser spot at machined surface

In order to check the variation of surface temperature near the cutting zone, infrared thermal camera with different set up range from 0℃ to about 500℃ is applied to record the temperature in the middle of the radial depth of cut going through both the laser spot and the cutting zone. The cutting speed is 130*m/min*, axial depth of cut is 1*mm*, feed speed is 400*mm/min*, laser-cutter allowance is 43.5*mm*, and laser power is 510*W*. The profile of temperature distribution by connecting measured points from experiments is shown in Figure 14. The temperature at the laser spot is cut off because the upper limit of measurement range is reached. Since the laser-cutter allowance is larger and the laser power is lower, the machining induced temperature rise cannot be ignored at the cutting zone. The temperature in front of the cutting zone is 250℃, while the temperature at the cutting zone is about 300℃, which indicates that the contribution of the machining process to the temperature increase at the cutting zone is about 50℃. Under same conditions, the

predicted temperature profiles from proposed analytical model at different depths are shown in Figure 15. From Figure 15(a), the maximum temperature rise at surface is 274.89℃, while the corresponding laser preheating temperature is 173.65℃ from Figure 15(b). Therefore, the machining induced temperature rise has a more significant effect at the cutting zone than laser. By comparing overall temperature distribution from Figure 15(c) to Figure 14, as shown in Figure 16, the temperature in front of the cutting zone from the predictive model is 237.18℃ with 5.13% difference from experiments. The predicted temperature at the cutting zone is 448.54℃, which is much higher than the experimental measurement. The main reason is the lack of measurement points at the cutting zone. As seen in Figure 14, there are only two data points connected by a smooth curve. However, in the profile from the predictive model, there is a rapid rise of temperature over 200℃ followed by a sudden drop within $0.2mm$ at the cutting zone. The density of measurement points at the cutting zone is unable to capture this trend. Overall, the predictive model catches the temperature distribution measured by experiments except for extreme points at the laser spot and the cutting zone due to the lack of measurements. The computation time is $14.67s$.

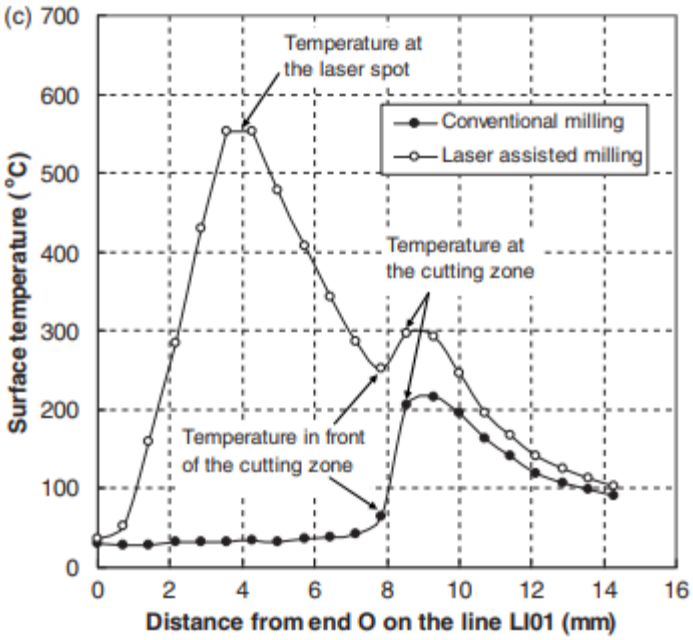

Figure 14 Variation of surface temperature on the line L101 which goes through the laser spot and the cutting zone from experimental measurements [122]

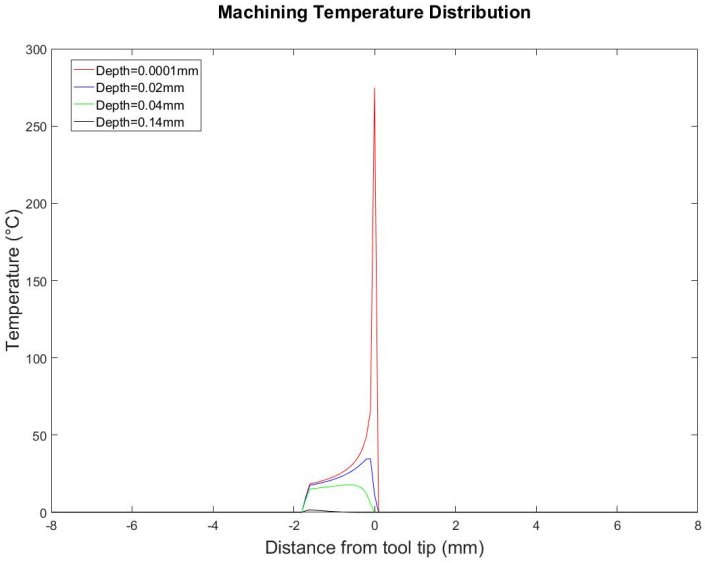

(a)

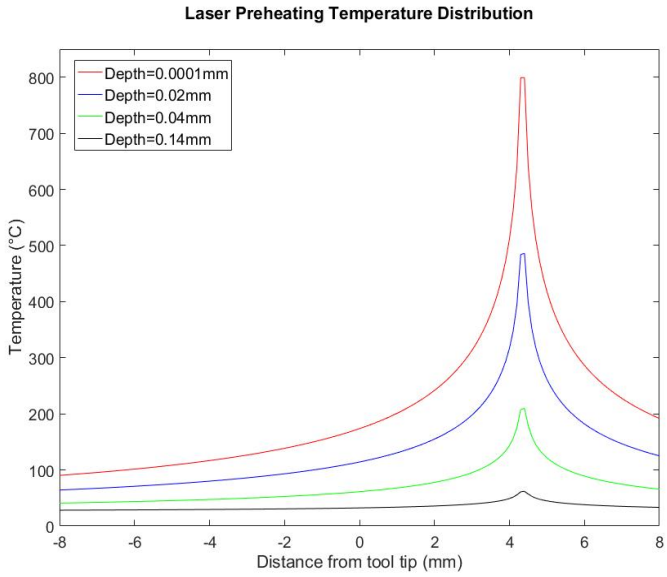

(b)

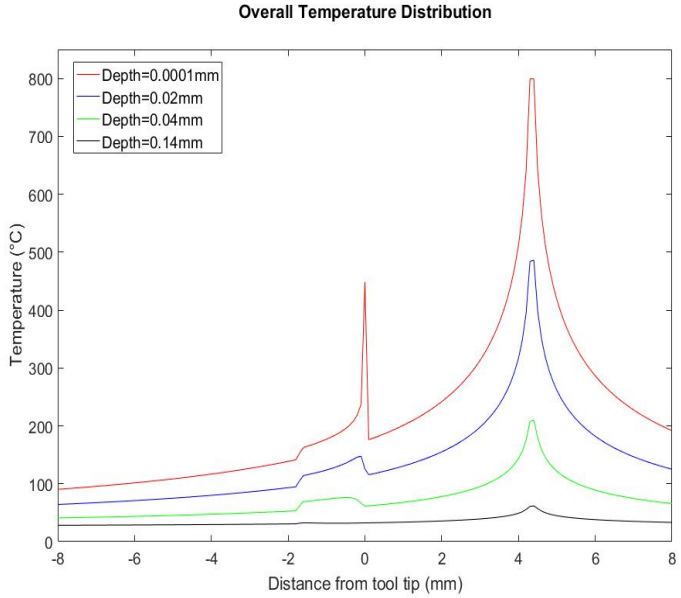

(c)

Figure 15 Temperature field prediction of Ti-6Al-4V with laser power of 510*W*, cutting speed of 130*m/min*, axial depth of cut of 1*mm*, and laser-cutter allowance of 43.5*mm* (a) Machining induced temperature rise (b) Laser preheating temperature field, and (c) Overall temperature distribution

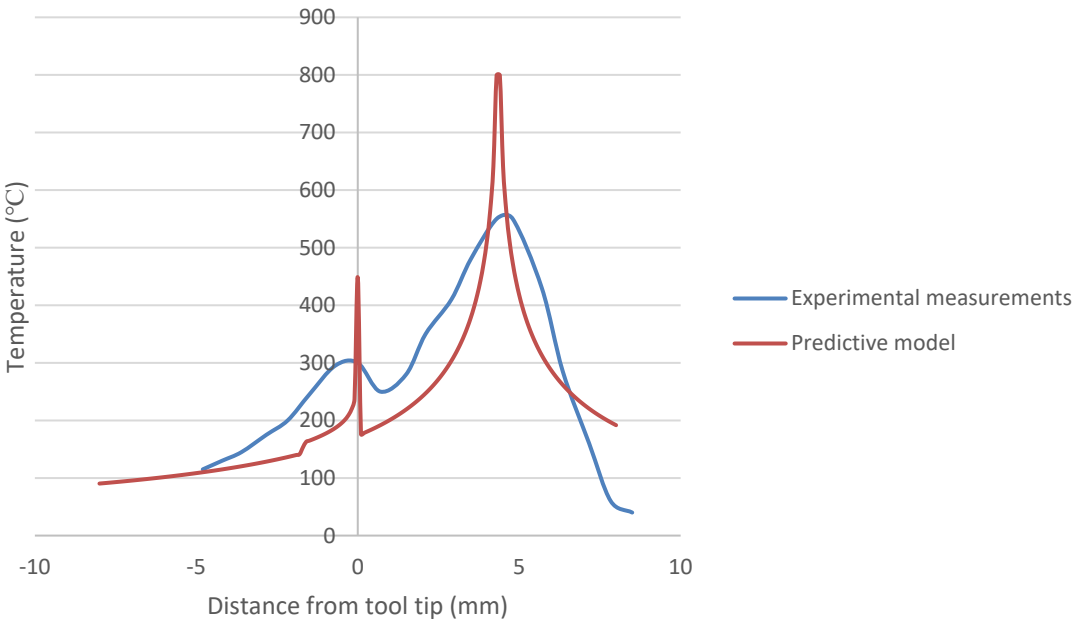

Figure 16 Comparison between experimental measurements and predictive model. The predicted temperature profile is from the red curve in Figure 15(c), while experimental measurements are from the line L101 shown in Figure 14

3.3 Residual stress

The overall process of the residual stress predictive model is summarized in Figure 17. The laser preheating temperature field is calculated based on the heat source distribution prediction through the laser total power input and the temperature rise considering conduction and convection [119] as introduced in 3.2.1. The oblique milling process is transferred to equivalent orthogonal cutting process at each rotation angle to predict the flow stress dependent on *DRX* process [124, 125] as introduced in 3.1.1 and 3.1.2. The flow stress is used to predict the cutting forces [126, 127], and the laser preheating temperature is embedded in machining temperature predictive model [120] as introduced in 3.2.2. The residual stress is then predicted through loading and relaxation processes [128]. The model is validated through the comparison with results from

experimental studies of laser-assisted milling of silicon nitride ceramics (Si_3N_4) [121, 123] and Ti-6Al-4V alloy [129, 130].

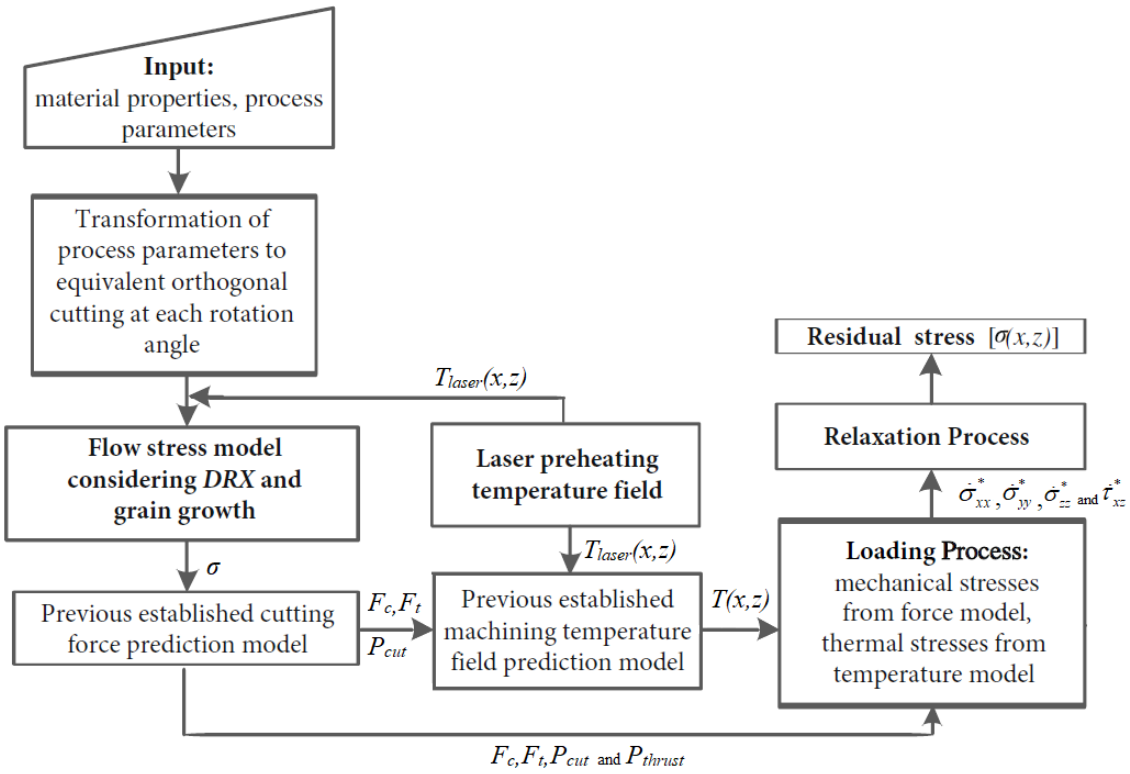

Figure 17 Overall flow chart of residual stress predictive model

3.3.1 Elastic loading process considering mechanical and thermal stresses

The loading process is first predicted by assuming only elastic deformation. A rolling contact between a cylinder and a semi-infinite plane is assumed between tool and workpiece. The mechanical loads are the shear stress on shear plane based on two cutting forces and the friction between tool nose and machined surface based on two plowing forces as shown in Figure 18. Thermal loads include thermal stresses in cutting and depth directions, surface tension and hydrostatic pressure according to the overall temperature field considering both machining and laser preheating effects. The area of interest is

defined within $-a<x<a$, where Hertzian rolling contact is assumed, and normal stress $p(s)$ and tangential stress $q(s)$ are calculated at $x=s$ shown in Figure 19. The mechanical stresses are then calculated by integration as

$$\begin{aligned}
\sigma_x &= -\frac{2z}{\pi}\int_{-a}^{a}\frac{p(s)(x-s)^2}{\left[(x-s)^2+z^2\right]^2}ds - \frac{2}{\pi}\int_{-a}^{a}\frac{q(s)(x-s)^3}{\left[(x-s)^2+z^2\right]^2}ds \\
\sigma_z &= -\frac{2z^3}{\pi}\int_{-a}^{a}\frac{p(s)}{\left[(x-s)^2+z^2\right]^2}ds - \frac{2z^2}{\pi}\int_{-a}^{a}\frac{q(s)(x-s)}{\left[(x-s)^2+z^2\right]^2}ds \\
\tau_{xz} &= -\frac{2z^2}{\pi}\int_{-a}^{a}\frac{p(s)(x-s)}{\left[(x-s)^2+z^2\right]^2}ds - \frac{2z}{\pi}\int_{-a}^{a}\frac{q(s)(x-s)^2}{\left[(x-s)^2+z^2\right]^2}ds
\end{aligned} \tag{28}$$

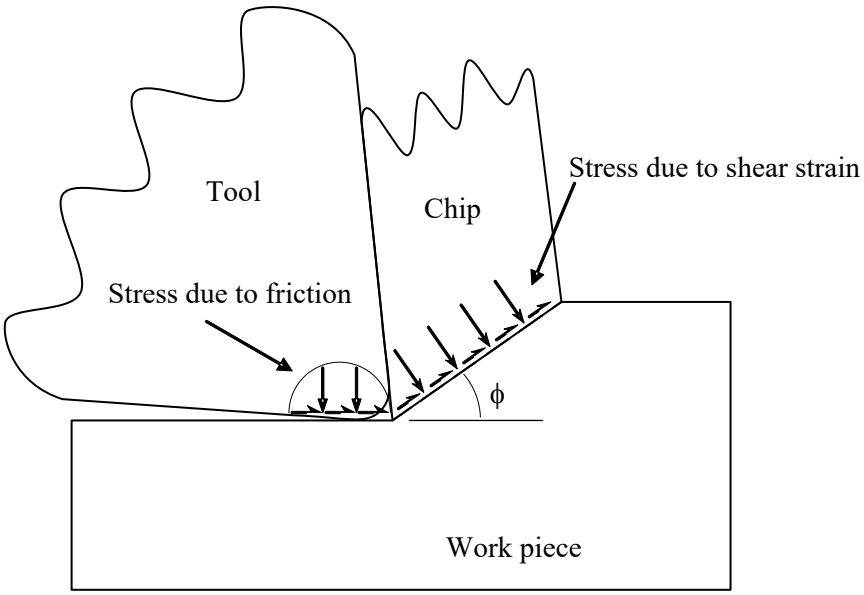

Figure 18 Stress sources for mechanical load

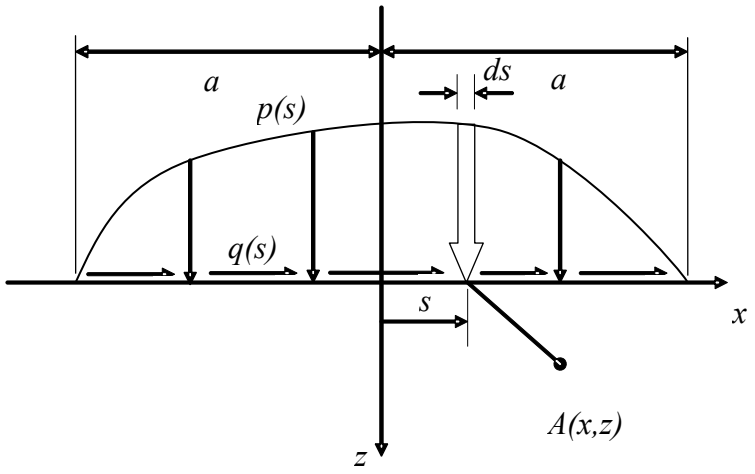

Figure 19 Schematic of stress distribution

The same integration process is repeated twice for two stress sources. At tool-workpiece interface, normal stress $p(s)$ is $p_{tool-edge}$ calculated by

$$p_{tool-edge} = \frac{2P_{thrust}}{\pi(wa)} \tag{29}$$

where P_{thrust} is the normal plowing force, w is the cutting width, a is the half contact width between the tool and chip. Tangential stress $q(s)$ is $\tau_{tool-edge}$ calculated by

$$\tau_{tool-edge} = \mu\left(\frac{P_{cut}}{w \cdot CA}\right) \tag{30}$$

where P_{cut} is the cutting plowing force, μ is the friction coefficient, CA is the contact width.

At the shear zone, normal stress $p(s)$ from shear strain is P_s given by

$$p_s = \frac{F_c \sin\phi + F_t \cos\phi}{L_{AB} w} \tag{31}$$

where F_c and F_t are chip formation forces in cutting and axial directions, ϕ is shear angle, L_{AB} is shear length. Tangential stress *q(s)* from shear strain is q_s given by

$$q_s = k_{AB} \tag{32}$$

where k_{AB} is the flow stress on shear plane. Then the overall mechanical stress are the summation of two integrations as

$$\left[\sigma_{total}^{mech}\right] = \left[\sigma_{shear\_X-Z}\right] + \left[\sigma_{tooledge\_X-Z}\right] \tag{33}$$

where $\left[\sigma_{tooledge\_X-Z}\right]$ is calculated by directly substituting Equations (29) and (30) into (28), $\left[\sigma_{shear\_X-Z}\right]$ is calculated after transformation as

$$\left[\sigma_{shear\_X-Z}\right] = [Q]\begin{bmatrix} \sigma_{X'} & \tau_{X'Z'} \\ \tau_{X'Z'} & \sigma_{Z'} \end{bmatrix}\left[Q^T\right] \tag{34}$$

where $\begin{bmatrix} \sigma_{X'} & \tau_{X'Z'} \\ \tau_{X'Z'} & \sigma_{Z'} \end{bmatrix}$ is calculated by substituting Equations (31) and (32) into (28), $[Q]$ is coordinate transformation matrix defined as

$$[Q] = \begin{bmatrix} \cos\phi & \sin\phi \\ -\sin\phi & \cos\phi \end{bmatrix} \tag{35}$$

Besides mechanical loads, stresses induced from thermal loads are calculated based on the overall temperature field. Thermal loads include thermal stress in cutting direction $X=-\left(\alpha E/\left(1-2\upsilon\right)\right)\left(\delta T/\delta x\right)$ and depth direction $Z=-\left(\alpha E/\left(1-2\upsilon\right)\right)\left(\delta T/\delta z\right)$, surface tension $\alpha ET\left(x,z=0\right)/\left(1-2\upsilon\right)$, and hydrostatic pressure $\alpha ET/\left(1-2\upsilon\right)$, where E is the Young's modulus, υ is the Poisson's ratio, α is the thermal expansion coefficient calculated by $\alpha=\frac{K}{\rho C_p}$ in which K, ρ, and C_p are thermal conductivity, density, and specific heat. During the heating and machining, these material constants are assumed unchanged. The overall thermal stress at any point *(x,z)* is the superposition of three individual stress sources as

$$\begin{aligned}
&\sigma_{xx}^{therm}\left(x,z\right)=-\frac{\alpha E}{1-2\upsilon}\int_0^\infty\int_{-\infty}^\infty\left(G_{xh}\frac{\partial T}{\partial x}\left(x,z\right)+G_{xv}\frac{\partial T}{\partial x}\left(x,z\right)\right)dxdz\\
&+\frac{2z}{\pi}\int_{-\infty}^\infty\frac{p(t)\left(t-x\right)^2}{\left(\left(t-x\right)^2+z^2\right)^2}dt-\frac{\alpha ET\left(x,z\right)}{1-2\upsilon}\\
&\sigma_{zz}^{therm}\left(x,z\right)=-\frac{\alpha E}{1-2\upsilon}\int_0^\infty\int_{-\infty}^\infty\left(G_{zh}\frac{\partial T}{\partial x}\left(x,z\right)+G_{zv}\frac{\partial T}{\partial x}\left(x,z\right)\right)dxdz\\
&+\frac{2z^3}{\pi}\int_{-\infty}^\infty\frac{p(t)}{\left(\left(t-x\right)^2+z^2\right)^2}dt-\frac{\alpha ET\left(x,z\right)}{1-2\upsilon}\\
&\tau_{xz}^{therm}\left(x,z\right)=-\frac{\alpha E}{1-2\upsilon}\int_0^\infty\int_{-\infty}^\infty\left(G_{xzh}\frac{\partial T}{\partial x}\left(x,z\right)+G_{xzv}\frac{\partial T}{\partial x}\left(x,z\right)\right)dxdz\\
&+\frac{2z^2}{\pi}\int_{-\infty}^\infty\frac{p(t)\left(x-t\right)}{\left(\left(t-x\right)^2+z^2\right)^2}dt\\
&p\left(t\right)=\frac{\alpha ET\left(x,z=0\right)}{1-2\upsilon}
\end{aligned}\tag{36}$$

where G_{xh}, G_{xv}, G_{zh}, G_{zv}, G_{xzh}, and G_{xzv} are the plane strain Green's functions. The overall elastic stresses is calculated by adding mechanical and thermal stresses as

$$\left[\sigma_{total}\right]=\left[\sigma_{total}^{mech}\right]+\left[\sigma_{total}^{thermal}\right]\tag{37}$$

$$\left[\sigma_{total}^{therm}\right]=\begin{bmatrix}\sigma_{xx}^{thermal} & & \\ & \sigma_{zz}^{thermal} & \\ & & \tau_{xz}^{thermal}\end{bmatrix}$$

3.3.2 Kinematic hardening and relaxation process

In real laser-assisted milling process, the shear strain and stress always surpass the yielding point together with plastic deformation. The actual loading process is predicted based on elastic stresses, by checking von Mises yield criterion at each position to decide whether the yielding happens. The effective strain and strain rate in von Mises yield criterion are defined as

$$\begin{aligned}\varepsilon_{eff}^{p}&=\frac{\sqrt{2}}{3}\sqrt{\left(\varepsilon_{xx}^{p}-\varepsilon_{yy}^{p}\right)^{2}+\left(\varepsilon_{yy}^{p}-\varepsilon_{zz}^{p}\right)^{2}+\left(\varepsilon_{zz}^{p}-\varepsilon_{xx}^{p}\right)^{2}+6\left(\varepsilon_{xz}^{p}\right)^{2}}\\ \overset{\bullet}{\varepsilon}_{eff}^{p}&=\sqrt{\frac{2}{3}}\sqrt{\left(\overset{\bullet}{\varepsilon}_{xx}^{p}\right)^{2}+\left(\overset{\bullet}{\varepsilon}_{yy}^{p}\right)^{2}+\left(\overset{\bullet}{\varepsilon}_{zz}^{p}\right)^{2}+2\left(\overset{\bullet}{\varepsilon}_{xz}^{p}\right)^{2}}\end{aligned} \tag{38}$$

The yielding criterion based on kinematic hardening is denoted as

$$F=\frac{3}{2}\left(S_{ij}-\alpha_{ij}\right)\left(S_{ij}-\alpha_{ij}\right)-R_{s}^{2}=0 \tag{39}$$

where $S_{ij}=\sigma_{ij}-\left(\sigma_{kk}/3\right)\delta_{ij}$ is the deviatoric stress, R_s is the shear yield strength, $\alpha_{ij}=\left\langle S_{kl}n_{kl}\right\rangle n_{ij}$ is the back stress, where $\langle\ \rangle$ is MacCauley symbol defined as $\left\langle x\right\rangle=0.5\left(x+\left|x\right|\right)$, $n_{ij}=\dfrac{S_{ij}-\alpha_{ij}}{\sqrt{2}k}$, where k is the average flow stress. After the yielding

occurs, the strain rate in feed direction is zero due to plane strain condition, and the strain rate in cutting direction is represented by real stresses, or elastic stresses through mixed function as

$$\begin{aligned}\dot{\varepsilon}_{xx} &= \frac{1}{E}\left[\dot{\sigma}_{xx} - \nu\left(\dot{\sigma}_{yy} + \dot{\sigma}_{zz}^{*}\right)\right] + \alpha\Delta T + \frac{1}{h}\left(\dot{\sigma}_{xx}n_{xx} + \dot{\sigma}_{yy}n_{yy} + \dot{\sigma}_{zz}^{*}n_{zz} + 2\dot{\tau}_{xz}^{*}n_{xz}\right)n_{xx} \\ &= \Psi\left(\frac{1}{E}\left[\dot{\sigma}_{xx}^{*} - \nu\left(\dot{\sigma}_{yy} + \dot{\sigma}_{zz}^{*}\right)\right] + \alpha\Delta T + \frac{1}{h}\left(\dot{\sigma}_{xx}^{*}n_{xx} + \dot{\sigma}_{yy}n_{yy} + \dot{\sigma}_{zz}^{*}n_{zz} + 2\dot{\tau}_{xz}^{*}n_{xz}\right)n_{xx}\right)\end{aligned} \tag{40}$$

$$\dot{\varepsilon}_{yy} = \frac{1}{E}\left[\dot{\sigma}_{yy} - \nu\left(\dot{\sigma}_{xx} + \dot{\sigma}_{zz}^{*}\right)\right] + \alpha\Delta T + \frac{1}{h}\left(\dot{\sigma}_{xx}n_{xx} + \dot{\sigma}_{yy}n_{yy} + \dot{\sigma}_{zz}^{*}n_{zz} + 2\dot{\tau}_{xz}^{*}n_{xz}\right)n_{yy} = 0$$

where $\dot{\sigma}_{xx}^{*}$, $\dot{\sigma}_{yy}^{*}$, $\dot{\sigma}_{zz}^{*}$ and $\dot{\tau}_{xz}^{*}$ are stress calculated under elastic loading from Equation (37). Ψ is a mixed function introduced from McDowell algorithm defined as

$$\Psi = 1 - \exp\left(-\kappa\frac{3}{2}\frac{h_p}{G}\right) \tag{41}$$

where κ=0.15 is an algorithm constant [128], h_p is plastic modulus, G is elastic shear modulus. When Ψ equals to one, no yielding happens, and real stresses are just elastic stresses. When Ψ equals to zero, it indicates perfect plasticity, and strain rate is also zero. Ψ is always between one and zero. When unloading process starts, the stress release is assumed to be fully elastic. When F $\leq$0 and $dS_{ij}n_{ij} \geq 0$, the relaxation process is described by the general Hook's law as

$$\begin{cases} \Delta\sigma_{xx} = \dfrac{E\Delta\varepsilon_{xx} + (1+\nu)(\Delta\sigma_{zz}\nu - E\alpha\Delta T)}{(1-\nu^2)} \\ \Delta\sigma_{yy} = \dfrac{\nu E\Delta\varepsilon_{xx} + (1+\nu)(\Delta\sigma_{zz}\nu - E\alpha\Delta T)}{(1-\nu^2)} \end{cases} \tag{42}$$

When F > 0, the released stress is calculated as

$$\begin{cases} \Delta\sigma_{yy} = \dfrac{\left(-\dfrac{\upsilon}{E} + \dfrac{1}{h}n_{xx}n_{yy}\right)(C - \alpha\Delta T) - \left(\dfrac{1}{E} + \dfrac{1}{h}n_{xx}n_{xx}\right)(D - \alpha\Delta T)}{\left[\left(-\dfrac{\upsilon}{E} + \dfrac{1}{h}n_{xx}n_{yy}\right)^2 - \left(\dfrac{1}{E} + \dfrac{1}{h}n_{xx}n_{xx}\right)\left(\dfrac{1}{E} + \dfrac{1}{h}n_{yy}n_{yy}\right)\right]} \\ \Delta\sigma_{xx} = \dfrac{D - \left(\dfrac{1}{E} + \dfrac{1}{h}n_{yy}n_{yy}\right)\Delta\sigma_{yy} - \alpha\Delta T}{-\dfrac{\upsilon}{E} + \dfrac{1}{h}n_{xx}n_{yy}} \end{cases} \tag{43}$$

$$\begin{cases} C = \Delta\varepsilon_{xx} + \left(\dfrac{\upsilon}{E} - \dfrac{1}{h}n_{xx}n_{zz}\right)\Delta\sigma_{zz}^{*} - \dfrac{2}{h}\Delta\tau_{xz}^{*}n_{xz}n_{xx} \\ D = \left(\dfrac{\upsilon}{E} - \dfrac{1}{h}n_{zz}n_{yy}\right)\Delta\sigma_{zz}^{*} - \dfrac{2}{h}\Delta\tau_{xz}^{*}n_{xz}n_{yy} \end{cases}$$

The residual stresses in cutting and feed directions are then calculated as the remaining stresses after relaxation.

3.3.3 Experimental validation and results

In order to validate the proposed predictive model, experimental measurements are collected during laser-assisted milling of Si_3N_4 [121] and Ti-6Al-4V [129, 130].

3.3.3.1 Silicon nitride ceramics (Si_3N_4)

Experiments are conducted under same conditions as in 3.2.3.1. Surface residual stresses in two directions are measured under three levels of laser power as shown in Figure 20.

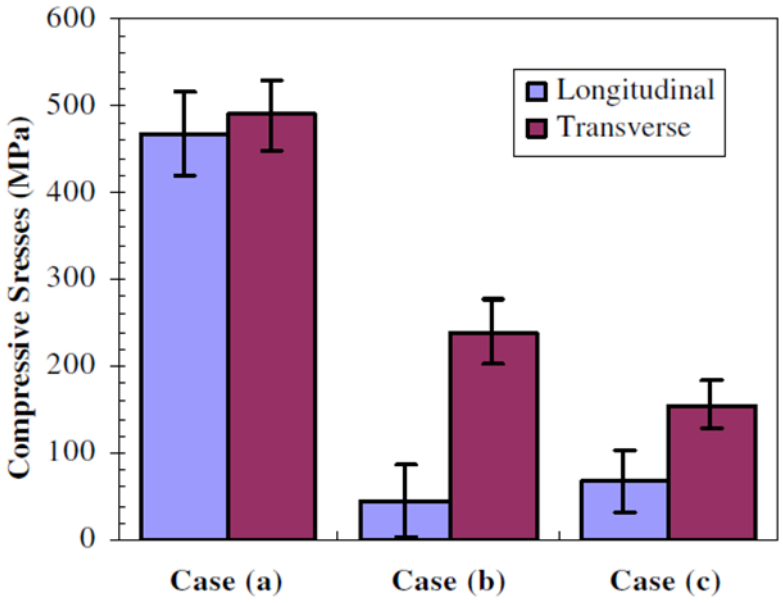

Figure 20 Surface residual stress under different operating temperatures (D=3.6mm, V_f=6.0mm/min, V_r=1.0m/s, d_a=0.2mm; case (a), P=300W; case (b), P=410W; case (c), P=470W) [121]

The predicted surface residual stresses are compared with experimental measurements from Figure 20 as listed in Table 6. Good agreements are found in all cases except the residual stress in feed direction in case (b), where the experiment measurement is much smaller than expected. The prediction catches the trend of more tensile residual stress under higher temperature or larger laser power, and the average error is 13.30% after eliminating the Y direction measurement in case (b). Table 6 also includes the prediction under conventional milling, which confirms that more tensile residual stresses are present when laser power is high (410 or 470W). In addition, when the temperature is above the softening point of Si_3N_4 glassy phase under laser preheating, larger micro-plastic

deformation is produced by the mechanical loading in cutting or transverse direction than feed or longitudinal direction. Therefore, higher compressive residual stresses are observed in cutting direction for all cases, but the difference of surface residual stresses between two directions is smaller for conventional milling due to lower temperature.

Table 6 Surface residual stress prediction for Si_3N_4 under three levels of laser power

	Predictive model		Experiments	
	σ_{yy} (Mpa) Longitudinal	σ_{xx} (Mpa) Transverse	σ_{yy} (Mpa) Longitudina	σ_{xx} (Mpa) Transverse
Case (a) *P*=300 W	391.49	497.51	470	490
Case (b) *P*=410 W	180.91	237.82	45	240
Case (c) *P*=470 W	88.85	180.63	70	150
Convention al milling	296.94	335.37		

3.3.3.2 Ti-6Al-4V

The experiments are conducted on a vertical milling center with a controller. The spindle rotation speed is 1253*RPM*. A laser system is used with a power of 185*W*. The laser spot size is 2.5*mm* x 3.6*mm* in an elliptical shape with a Gaussian power distribution and the tool laser allowance is 3.5*mm*. Young's modulus of E=110*GPa* and Poisson's ratio ν=0.36 are used to calculate the residual stress. Depth profiles for the residual stresses were measured by chemically etching successive layers of the material by electro-polishing. The tool has a diameter of 19.05*mm*, rake angle of 15°, and nose radius of 0.8*mm*. The cutting speed is 75*m/min*, the feed per tooth is 0.1*mm/tooth*, the depth of cut is 1*mm*, and the width of cut is 3*mm*. Two types of Ti-6Al-4V, grade 5 and ELI (Grade 23) are milled under same conditions. The flow stress constitutive model for both types of Ti-6Al-4V applied in

predictive model follows Equation (10). All the material constants are listed in Table 7. d_0 is decided to be $10\mu m$.

Table 7 Constitutive model parameters for two types of Ti-6Al-4V

	A_{hp}(MPa)	$K_{hp}(MPa\sqrt{\mu m})$	B(MPa)	C	m	n	T_m(℃)	$\dot{\varepsilon}_0$ (s^{-1})
Grade 5	803.22	401.61	653.1	0.015	0.6	0.45	1668	1
ELI	803.22	401.61	653.1	0.025	0.8	0.45	1630	1

The predictions as well as experimental measurements of residual stress in laser assisted milling of Ti-6Al-4V grade 5 are shown in Figure 21. Measurements are collected up to $200\mu m$ depth with even distribution for every $50\mu m$. As shown in Figure 21(a), in cutting direction, a close match is found for the first four measurements with an average error of 24.72%. The relative percentage error is large for residual stress at $200\mu m$, because the actual measurement is close to zero. In feed direction, the prediction is close to experimental measurements with an average error of 11.21% in first four points as shown in Figure 21(b). The residual stress profiles are also predicted under conventional milling in both directions, and more compressive stress distributions are observed.

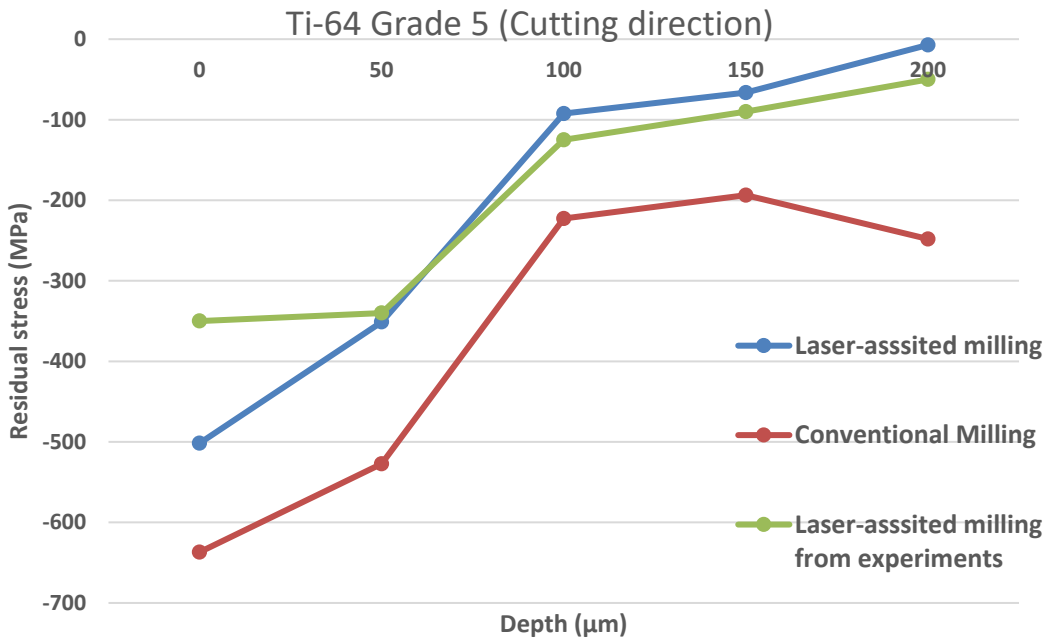

(a)

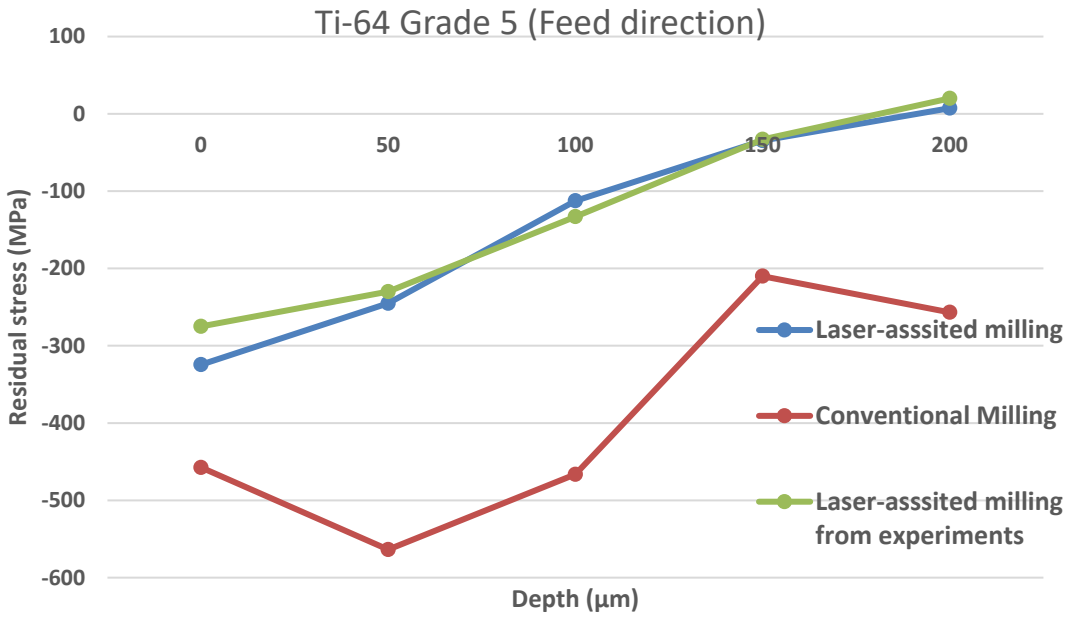

(b)

Figure 21 Residual stress comparison for Ti-64 grade 5 in (a) Cutting direction and (b) Feed direction

The predictions as well as experimental measurements of residual stress in laser assisted milling of Ti-6Al-4V ELI are shown in Figure 22. The predictive model is able to show the trend of measured residual stress profile during laser-assisted milling. The average error is 23.88%, and the maximum error is 36.49% at $50\mu m$ due to an extreme compressive measurement as shown in Figure 22(a). In Figure 22(b), the experiments show minimal residual stress below $150\mu m$, which bring huge relative errors comparing to predictions, even though the absolute differences are small. For measurements above $100\mu m$, the average error is 27.29%. Again, residual stress profiles under same other cutting conditions but conventional milling are predicted, and all 10 data points have shifts toward compressive direction.

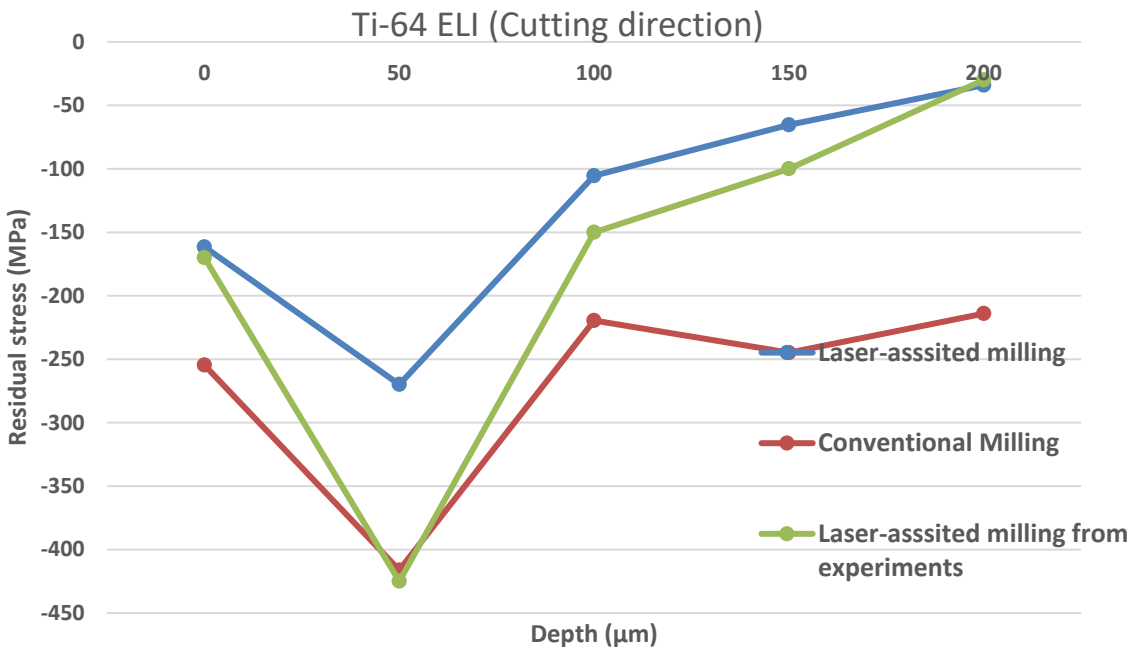

(a)

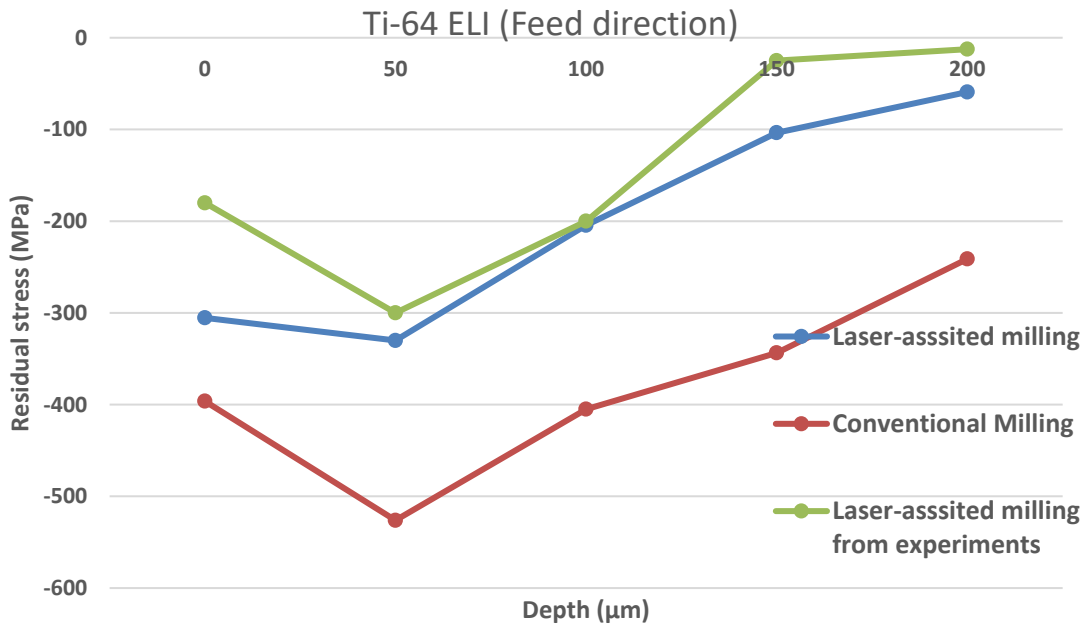

(b)

Figure 22 Residual stress comparison for Ti-64 ELI in (a) Cutting direction and (b) Feed direction

3.4 Tool flank wear

Several researches have been reported related to the analysis of tool wear in laser-assisted milling. Bermingham *et al.* [1] found that the effectiveness of laser-assisted milling in terms of extending tool life compared to conventional machining processes depended strongly on the cutting conditions. At lower cutting speed, the effect of laser is insignificant, while at higher cutting speed, the laser preheating temperature will harm the tool life by overheating. Therefore, an optimal range of parameters need to be selected. Brecher *et al.* [57] also concluded that, relative to conventional machining processes, laser-assisted milling was found to increase tool life at some cutting speeds and decrease tool life at other speeds. These experimental investigations provide a general idea about the effects of cutting and laser parameters on tool wear but are limited to specific tool and

workpiece. With the sensitivity analysis conducted in current study, the proposed analytical approach is able to guide the selection of parameters quantitatively for wider range of tool and workpiece material. As shown in Figure 23, for the flank tool wear predictive model, the initial temperature is decided by the laser preheating temperature field, which is first calculated according to the heat source distribution and the temperature rise considering conduction and convection [119], and then averaged along the tool-workpiece interface. Then, the oblique milling process is transferred to equivalent orthogonal cutting process at each rotation angle to predict the flow stress dependent on *DRX* process [124, 125]. The flow stress is used to predict the cutting forces [126, 127] and the average stress on tool-workpiece interface due to flank wear [131]. The average temperature is calculated on cutting tool along the tool-workpiece interface, by considering rubbing and secondary heat sources based on cutting forces, following a similar procedure of workpiece machining temperature predictive model [120]. The flank wear rate is then predicted considering abrasion, adhesion, and diffusion, which are dependent on average stress and temperature on flank wear land (*VB*). The proposed model is validated through experimental measurements on the laser-assisted milling of K24 nickel-based superalloy [132]. In addition, the effects of feed rate, axial depth of milling, cutting speed, laser power, and laser-tool distance on tool life are studied through sensitivity analysis.

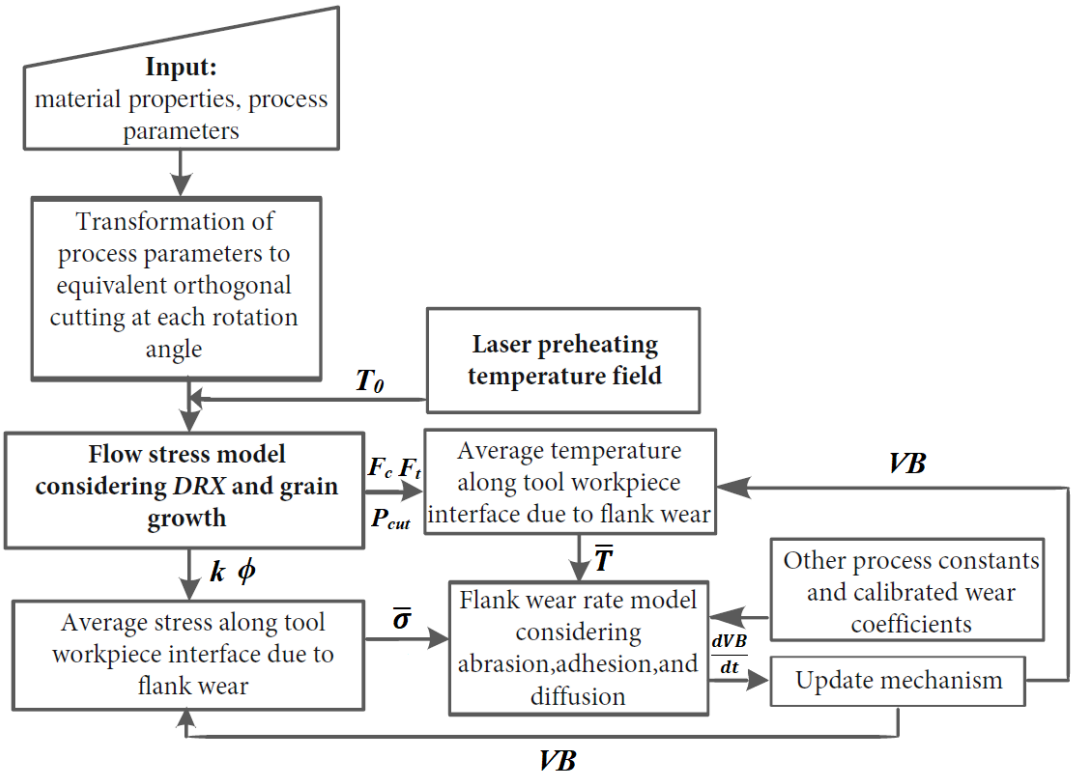

Figure 23 Overall flow chart of tool wear predictive model

3.4.1 Average stress on tool-workpiece interface due to flank wear

After the preheating temperature being predicted, the cutting forces are calculated through the transformation of milling process parameters and flow stress model [133] controlled by *DRX* and grain growth. The geometry parameters of milling tool are transferred as well [126], and the preheating temperature is utilized to predict the flow stress that gives cutting force F_c, tangential force F_t and plowing force P_{cut} [133]. As shown in Figure 23, the flow stress calculated based on laser preheating temperature field and recrystallization effect is used to calculate the average stress on tool-workpiece interface due to flank wear. Forces predicted from previous established cutting force predictive model [126] are used to derive heat sources in temperature prediction of cutting tool on

tool-workpiece interface, following a similar procedure as in previous established machining temperature field predictive model [120] in addition to laser preheating temperature field. The transformation of milling parameters, the flow stress model, and the cutting forces prediction have already been introduced [126, 133] and therefore not repeated. The prediction of stress and temperature on tool-workpiece interface as well as flank tool wear rate is based on the procedure proposed by Huang [55] and adjusted for laser-assisted milling.

The proposed model assumes that the flank tool wear is at steady state region, and the flank wear land length (*VB*) after break-in period is known. The average stress on tool-workpiece interface due to flank wear $\bar{\sigma}$ is calculated as

$$\bar{\sigma} = \frac{F_{wcutting}}{wVB} \tag{44}$$

where w is the cutting width and $F_{wcutting}$ is the effective force in cutting direction due to flank wear. As shown in Figure 24, $F_{wcutting}$ is calculated through the summation of wear force components in each segment along the machined surface profile ABD, when AC is the profile in last revolution and AD is for current revolution. The area ABDC is basically the cross-section shape of the chip if d is the cutting depth and r is the tool tip radius.

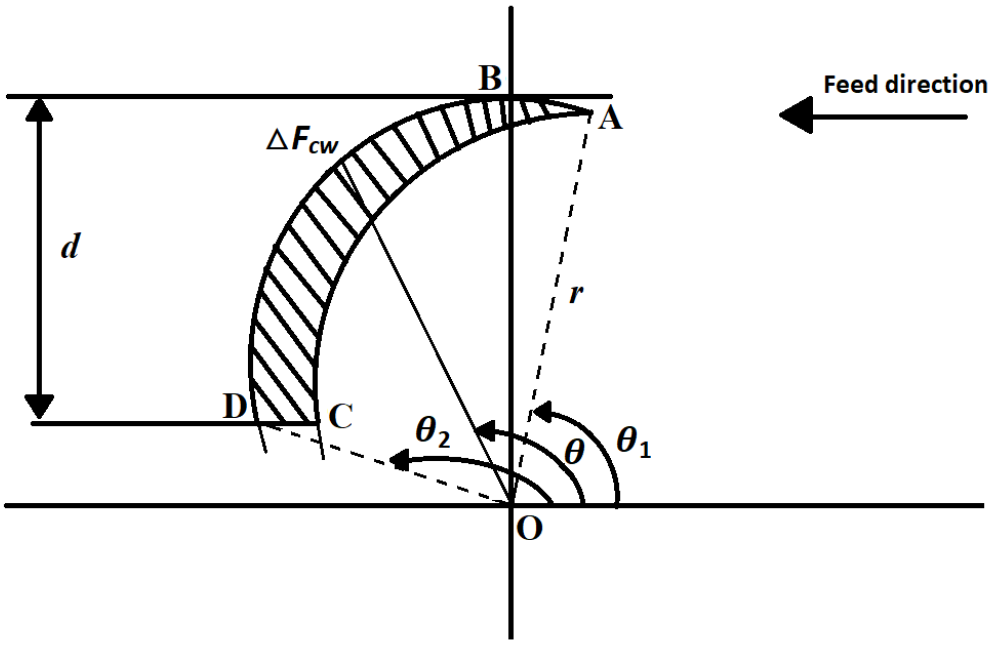

Figure 24 Cutting geometric model under equivalent orthogonal cutting

The integration is made between two angles $\theta_1$and $\theta_2$corresponding to ends of arc ABD and along the wear land as

$$F_{wcutting} = \sum_{ABD} \Delta F_{cw} = \int_{\theta_1}^{\theta_2} \int_{0}^{VB} r\tau_w(x)dxd\theta \tag{45}$$

where $\tau_w(x)$ is flank shear stress component computed from Waldorf's worn tool force model. The distribution of $\tau_w(x)$ is separated by a critical wear land width VB^*. Purely elastic contact is assumed within the distance of VB^* from the back of the wear land as shown in Figure 25. Plastic flow is present at the front edge of the wear land beyond VB^*. When $VB<VB^*$, the flank normal stress $\sigma_w(x)$ is described by a parabolic function as

$$\sigma_w(x) = \sigma_0 (\frac{VB - x}{VB})^2 \tag{46}$$

where $\sigma_0 = k\left[1 + \frac{\pi}{2} - 2\phi + 2\beta + \sin(2\beta - 2\phi)\right]$ and $\beta = \frac{\cos^{-1} 1}{2} + \phi$. Shear flow stress k and shear angle ϕ are calculated from the shear flow stress model.

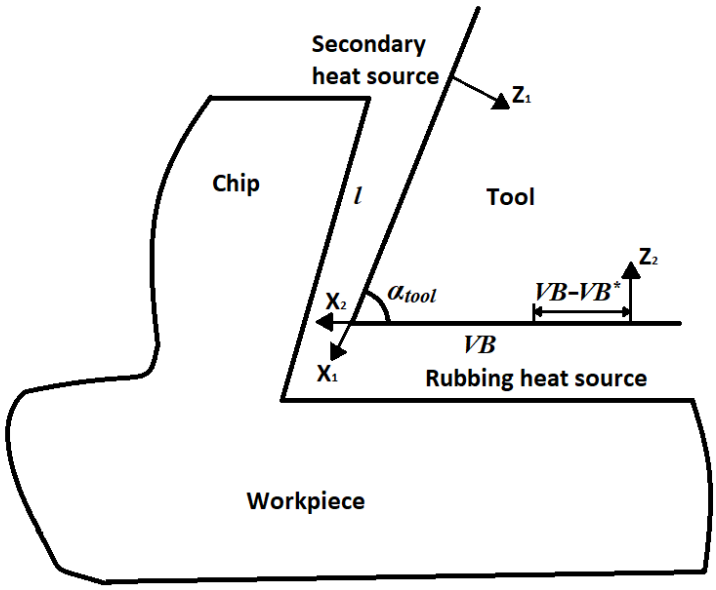

Figure 25 Heat sources and associated coordinate systems in temperature prediction

Flank shear stress $\tau_w(x)$ [131] is modeled as

$$\tau_w(x) = \begin{cases} \tau_0, for\ \ 0 < x < VB(1 - \sqrt{\frac{\tau_0}{\sigma_0}}) \\ \mu\sigma_w(x), for\ VB(1 - \sqrt{\frac{\tau_0}{\sigma_0}}) < x < VB \end{cases} \tag{47}$$

where $\tau_0 = k\cos(2\beta - 2\phi)$. If $VB > VB^*$, $\tau_w(x)$ becomes

$$\tau_w(x) = \begin{cases} \tau_0, for\ 0 < x < VB - VB^* \sqrt{\frac{\tau_0}{\sigma_0}} \\ \mu\sigma_w(x), for\ VB - VB^* \sqrt{\frac{\tau_0}{\sigma_0}} < x < VB \end{cases} \quad (48)$$

where $\sigma_w(x) = \begin{cases} \sigma_0, for\ 0 < x < VB - VB^* \\ \sigma_0 (\frac{VB - x}{VB^*})^2, for\ VB - VB^* < x < VB \end{cases}$, $\tau_0 = k$, and

$\sigma_0 = k\left[1 + \frac{\pi}{2} + \cos^{-1} 1 + \sin(\cos^{-1} 1)\right]$.

3.4.2 Temperature prediction of cutting tool on tool-workpiece interface

Besides laser effect, the temperature of the tool increases under the friction between tool and chip, and rubbing between tool and machined surface, which are considered as secondary heat source and rubbing heat source respectively as shown in Figure 25. The coordinate systems are built along the interface for both heat sources, with X direction toward tool tip and Z direction perpendicular to the interface toward tool. Without tool wear, the tool-chip and tool-workpiece interfaces are considered insulated boundary condition, where the imaginary heat source method is applied to predict the temperature [120]. When the tool wear is present, the material transfers from the tool as the wear land expands, but the temperature rises on both sides of the interface are still the same, and the adiabatic boundary conditions still hold. Therefore, the same procedure is used, and the temperature rise of tool due to secondary heat source is calculated as

$$T_{tool-friction}(X_1,Y_1,Z_1)=\frac{1}{2\pi k_t}\int_0^l(1-\gamma)q_{friction}dx_1\int_{-\frac{w}{2}}^{\frac{w}{2}}(\frac{1}{R_1}+\frac{1}{R_1'})dy_1 \tag{49}$$

where $R_1=\sqrt{(X_1-x_1)^2+(Y_1-y_1)^2+Z_1^2}$, $R_1'=\sqrt{(X_1-2l+x_1)^2+(Y_1-y_1)^2+Z_1^2}$. The heat intensity of friction $q_{friction}$ is derived based on cutting forces as

$$q_{friction}=\frac{\sqrt{F_c^2+F_t^2}\sin(\lambda)V_{chip}}{wl} \tag{50}$$

where λ is the friction angle, V_{chip} is the velocity of chip, l is the contact length between tool and chip. These three parameters are calculated from the flow stress model. $\sqrt{F_c^2+F_t^2}\sin(\lambda)$ gives the friction along the interface. When the heat source is considered uniform, the total power over the contact area becomes the heat intensity. γ is the heat partition ratio of the heat source going to chip or workpiece. An approximate value for the partition ratio based on material properties of the tool and the workpiece is decided by

$$\gamma=\frac{\sqrt{k_{wk}\rho_{wk}C_p}}{\sqrt{k_{wk}\rho_{wk}C_p}+\sqrt{k_t\rho_tC_t}} \tag{51}$$

where k_{wk} is the thermal conductivity of the workpiece material, k_t, ρ_t, and C_t are the thermal conductivity, density, and specific heat of the tool material respectively. Similarly, the temperature rise at any point on the tool due to rubbing heat source is

$$T_{tool-rubbing}(X_2,Y_2,Z_2)=\frac{1}{2\pi k_t}\int_0^{VB}(1-\gamma)q_{rubbing}dx_2\int_{-\frac{w}{2}}^{\frac{w}{2}}(\frac{1}{R_2}+\frac{1}{R_2'})dy_2 \quad (52)$$

where $R_2=\sqrt{(X_2-x_2)^2+(Y_2-y_2)^2+Z_2^{\,2}}$ and $R_2'=\sqrt{(X_2-2VB+x_2)^2+(Y_2-y_2)^2+Z_2^{\,2}}$. The rubbing heat intensity $q_{rubbing}$ is

$$q_{rubbing}=\frac{P_{cut}\tan(\lambda)V_c}{wVB} \quad (53)$$

where V_c is the cutting speed. The overall temperature rise at any point on flank face $T_{tool-flank}(X_2,0,0)$ is mainly the summation of Equations (49) and (52), after the coordinate transformation of secondary heat source from coordinates $X_1Y_1Z_1$ to $X_2Y_2Z_2$ as shown in Equation (54),

$$T_{tool-flank}(X_2,0,0)=T_{tool-friction}(l-(VB-X_2)\cos\alpha_{tool},0,(VB-X_2)\sin\alpha_{tool})+T_{tool-rubbing}(X_2,0,0) \quad (54)$$

where α_{tool} is the wedge angle. The average temperature of the tool along the tool-workpiece interface is calculated by averaging the temperature predictions along the worn tool flank face in addition to laser preheating temperature as

$$\overline{T}=\frac{1}{VB}\int_0^{VB}(T_{tool-flank}(X_2,0,0))dX_2+T_0 \quad (55)$$

3.4.3 Flank tool wear rate prediction and update mechanism

The proposed flank tool wear rate model assumes that the length of flank wear land after break-in period is known, and the flank wear is then predicted based on wear rate and a predefined time interval. For abrasive wear, the volume loss is calculated through an empirical equation dependent on sliding distance, the normal load, the average roughness angle of the abrasive particle, and hardness of both the tool P_t and the abrasive particle P_a. The normal load is predicted based on $\bar{\sigma}$, and all the other unknown parameters are simplified as the dimensionless abrasive wear coefficient $K_{abrasion}$. For the prediction of adhesive wear, the actual contact area along the interface is made up of asperities with plastic deformation under high temperature and high stress. The adhesion forms micro-welds which support partial normal force decided by $\bar{\sigma}$ similar to abrasive wear. However, the hardness of asperity is strongly dependent on the temperature which cannot be assumed as constant as P_t or P_a. An exponential function is introduced instead based on $\bar{T}$. Other parameters are simplified as the adhesive wear coefficient $K_{adhesion}$ with a unit of m^3/N. Diffusive wear is caused by the diffusion of binder material under high temperature. The volume loss is mainly dependent on the average flux rate of atoms instead of forces, and the coefficient of diffusion is an exponential function of $\bar{T}$. The diffusive wear coefficient $K_{diffusion}$ has a unit of $m/\sqrt{s}$. The further detailed physics interpretation of each wear type has been proposed by Huang [55] and not repeated in proposed model since only the simplified model coefficients are applied. The overall flank wear rate is expressed as

$$\frac{dVB}{dt} = \frac{2}{VB}\left\{ K_{abrasion} K \left(\frac{P_a^{n_w - 1}}{P_t^{n_w}}\right) V_c VB\bar{\sigma} + K_{adhesion} e^{a_w \bar{T}} V_c \bar{\sigma} + K_{diffusion} \sqrt{V_c VB} e^{-\frac{K_Q}{\bar{T}+273}} \right\} \quad (56)$$

where the coefficients K, n_w, a_w, and K_Q are assumed to be constants together with three wear coefficients. These model coefficients are only dependent on the different combinations of tool and workpiece, and are decided through inverse analysis in current study. Due to the multiple-solution issue in inverse analysis, the decided coefficients are only from fitting of data and may not be the true values based on physical interpretation. The exact coefficients can be calculated based on measurements under non-machining conditions.

Although the tool wear rate is calculated based on an orthogonal cutting configuration, the cutting and tool geometry parameters are updated with rotation angle. Therefore, the proposed model is applicable for a three-dimensional milling. Once the average tool wear rate within one tool revolution is calculated, it is assumed to be constant within a predefined time interval Δt, so that VB is calculated for the prediction of wear rate during next interval until the end of steady wear period as shown in Figure 23.

3.4.4 Experimental validation and results

The proposed flank tool wear predictive model is validated through comparison of the experimental measurements from Kong *et al.* [132]. In their work, laser-assisted milling and conventional milling are conducted on a nickel-based superalloy (K24). All experiments are under dry conditions. Three types of tungsten carbide tools are used with details summarized in Table 8. The cutting speed is 30*m/min*, feed rate is 0.1*mm/rev*, and axial depth of milling is 0.2*mm*. Measured flank wear progressions for laser-assisted and conventional milling of three different tools as a function of the cutting time are shown in Figure 26. It is obvious that the average wear rate is smaller when the laser is applied for

all three tools. The average machined times are 17.3 and 31.4*min* for conventional and laser-assisted milling when the wear criterion is reached.

Table 8 Summary of cutting tools used in milling tests [132]

Tools	Coatings	Subtract	Depth of coatings (μm)	Relief angle(°)	Cutting edge angle (°)
A	TiAlN	P10	4	21	90
B	Ti(CN)/Al_2O_3/TiN	M30	9	21	90
C	TiCN	P10	3	21	90

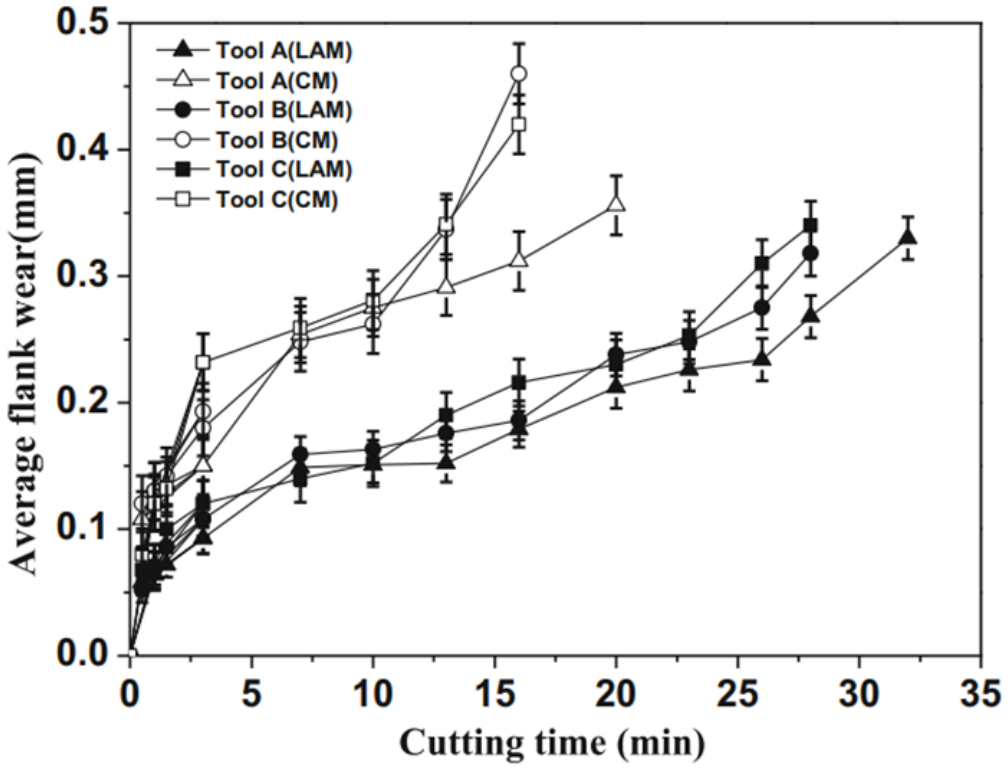

Figure 26 Measured flank wear progressions for laser-assisted (LAM) and conventional milling (CM) of three different tools as a function of the cutting time [132]

The progression curve is roughly divided into three stages. For the initial wear stage and rapid wear stage near tool failure, the tool flank wear rate is high and changes dramatically. For the second or the steady state wear region, the curve can be regarded as a line, and the wear rate is almost constant. Since the predictive model is only valid within steady state wear region, the start and end points of the region are decided. Six data points between cutting time of 7.25 and 23min for laser-assisted milling, and four data points between cutting time of 3 and 12.75min for conventional milling shown in Figure 26 are considered within steady stage and therefore compared with predictions from analytical model as shown in Figure 27. The time interval Δt is 0.25min, and the average computation time is 120s for laser-assisted milling and 78s for conventional milling.

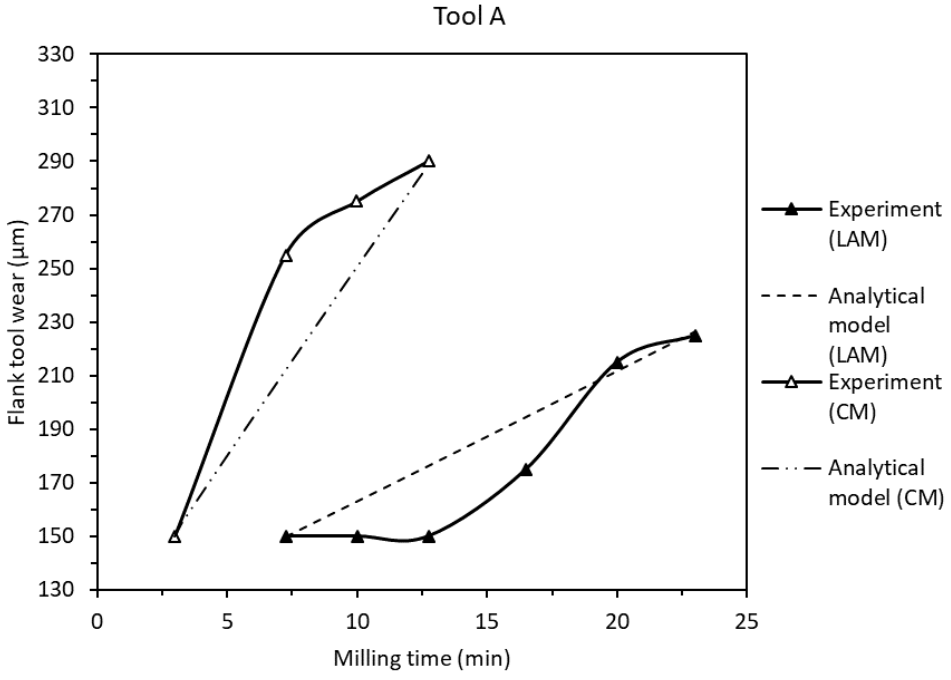

(a)

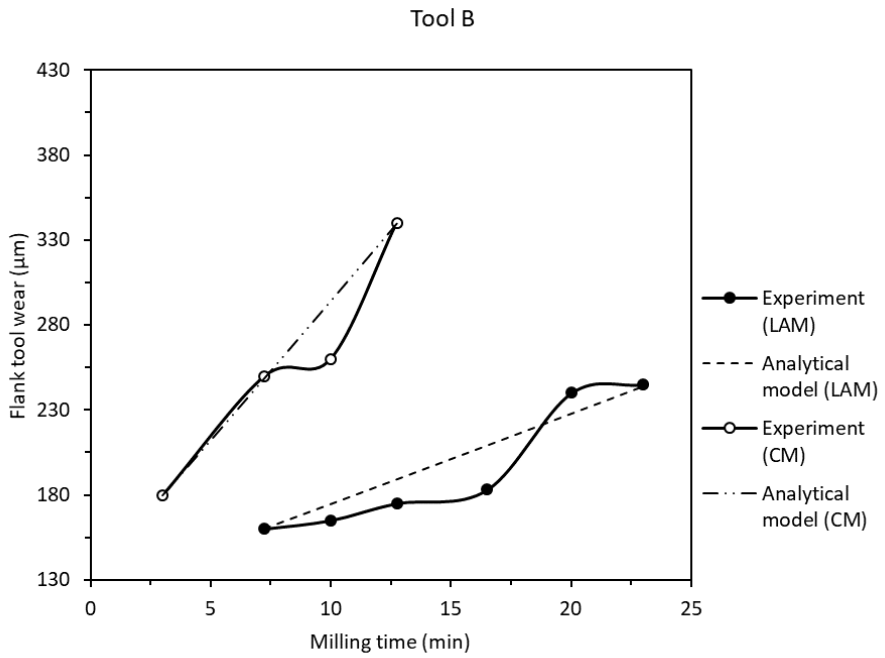

(b)

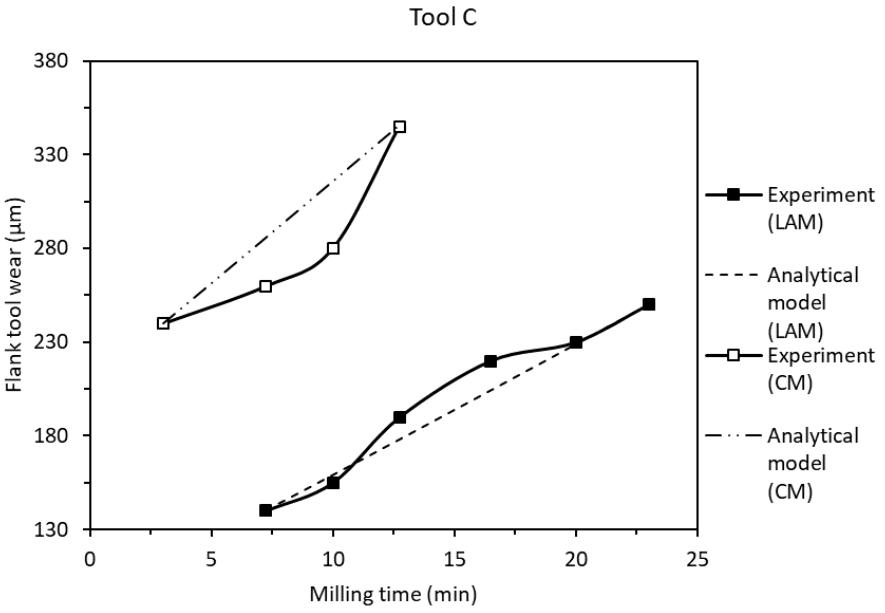

(c)

Figure 27 The comparison of wear progressions for laser-assisted (LAM) and conventional milling (CM) of (a) tool A, (b) tool B, and (c) tool C

It can be shown from Figure 27 that the predicted flank wear increases linearly with increasing time, which matches the feature of steady state wear region [56]. However, the measured flank wear growth is nonlinear within some portions as the steady state region cannot be always clearly defined in real data. Many factors such as tool chatter may result in unsteady wear. The measured wear length at the beginning of manually selected steady stage is chosen as initial *VB* in the algorithm, and the predictive model is able to match the final wear length in all six cases with a maximum error of 0.69%. For tool A, the flank wear increases from 150μm to 225μm in laser-assisted milling and from 150μm to 290μm in conventional milling. The predicted average wear rate is 4.86$\mu m/min$ with laser and 14.78$\mu m/min$ without laser, and the average difference of *VB* between measurements and predictions is 7.97% among five data points for laser-assisted milling and 8.65% among three data points for conventional milling, since the first data point is always same. For tool B, the flank wear increases from 160μm to 245μm in laser-assisted milling and from 180μm to 340μm in conventional milling. The predicted average wear rate is 5.33$\mu m/min$ with laser and 16.40$\mu m/min$ without laser, and the average difference of *VB* is 6.70% for laser-assisted milling and 4.55% for conventional milling. For tool C, the flank wear increases from 140μm to 250μm in laser-assisted milling and from 240μm to 345μm in conventional milling. The predicted average wear rate is 6.98$\mu m/min$ with laser and 10.86$\mu m/min$ without laser, and the average difference of *VB* is 3.34% and 7.66% respectively. Under the same cutting and laser conditions, tool B has a higher wear rate than tool A, and both of them are largely effected by laser since the wear rate reduces over 67% when the laser is applied. Tool C has a higher wear land length after break-in period, and the tool wear rate only decreases by 36% in laser-assisted milling. Overall, the

proposed flank tool wear model is able to predict the wear progressions in less than two minutes with high accuracy of 6.48% error in average.

3.4.5 Sensitivity analysis

In order to appreciate the proposed predictive model, sensitivity analysis is conducted to estimate tool life under the effects of different cutting and laser parameters. The tool parameters are the same as tool C, and other parameters are fixed as in experiments of Kong *et al.* [132]. Tool flank wear land after the break-in period is assumed as 150μm, and the tool life criterion is set as 300μm flank wear land. The time interval is taken as 0.5min, and the upper limit is 100min, to have a good balance of accuracy and computation time. The effects of cutting speed, feed rate, and axial depth of milling on tool life are shown in Figure 28. It can be seen that cutting speed has the most significant influence on tool life, followed by feed rate and axial depth of milling, which agrees with the conclusions by Kumar *et al.* [134].

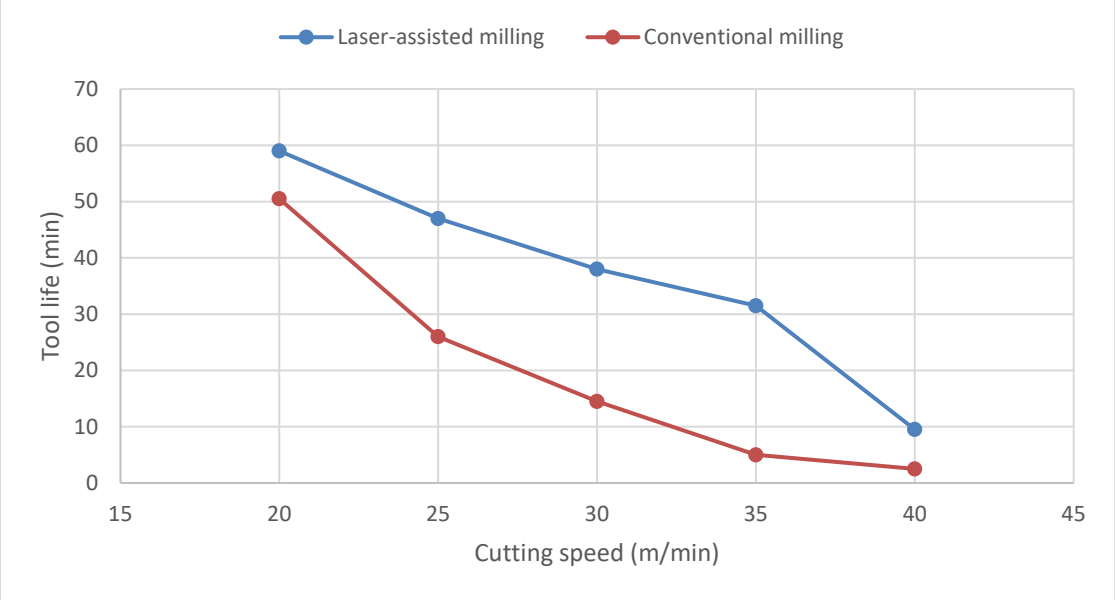

(a)

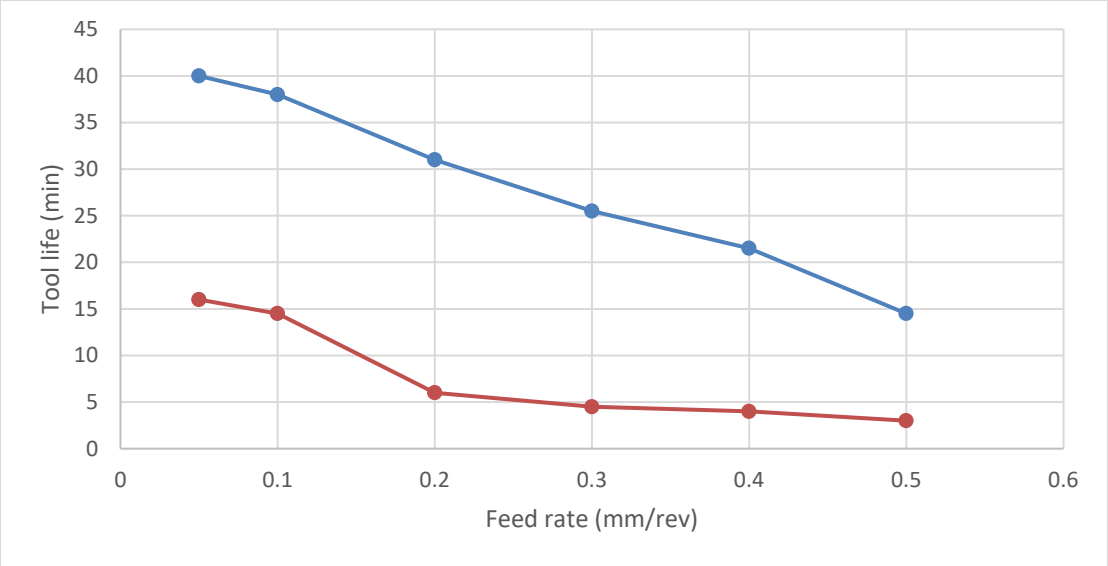

(b)

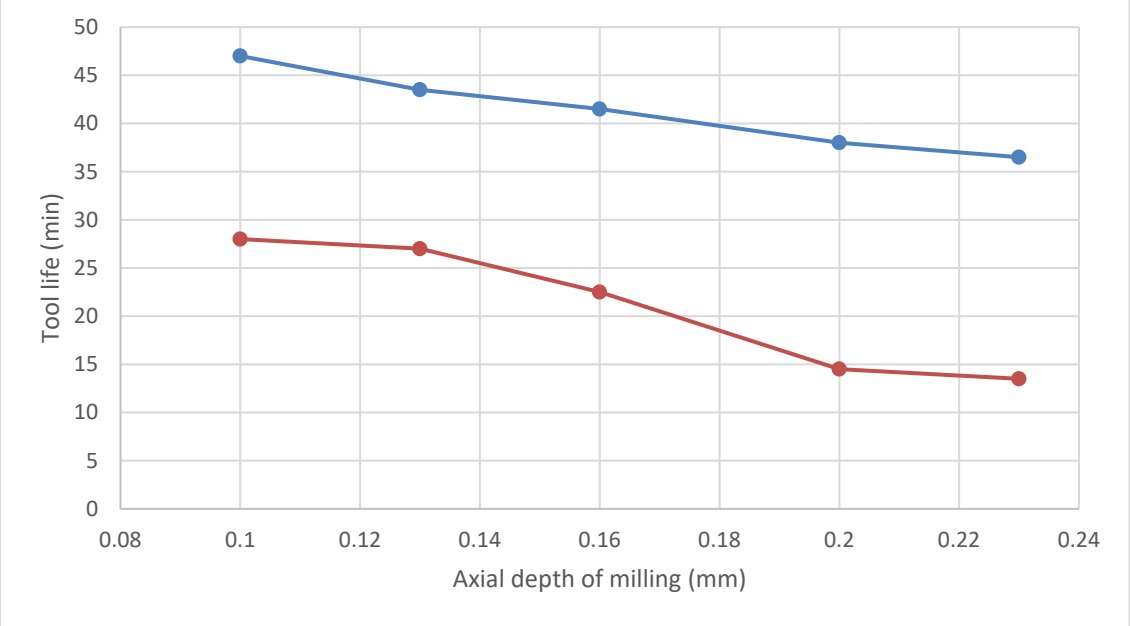

(c)

Figure 28 The change of tool life based on flank wear criterion under the effect of different cutting parameters (a) Cutting speed when feed rate is 0.1mm/rev and axial depth of milling is 0.2mm. (b) Feed rate when cutting speed is 30m/min and axial depth of milling is 0.2*mm*. (c) Axial depth of milling when cutting speed is 30*m/min* and feed rate is 0.1*mm/rev*. The laser parameters are fixed at laser power of 600*W* and laser-tool distance of 2.85*mm*.

The laser parameters also have significant effects on tool life [135]. The laser-tool distance is defined as the distance between laser beam center and the tool tip. Although the laser preheating temperature will reduce the tool wear in general, optimum laser parameters need to be picked to avoid tempering effect [135]. The estimated tool life under various laser power and laser-tool distance is listed in Table 9. Either the laser parameter being too large or too small will harm the tool life. Low laser power or long laser-tool distance will diminish the preheating effect, increase the cutting forces, and enhance the abrasive wear. On the other hand, high laser power or short laser-tool could significantly increase the local temperature, leading to severe adhesive and diffusive wear. A bad combination of laser parameters could even result in shorter tool life than conventional milling as the experiments in Bermingham *et al.* [1]. According to the sensitivity analysis, the optimal laser power is between 400 and 500W, since the tool life has reached the upper limit of 100min decided by the algorithm to save computation time. The optimal laser-tool distance is around 3.2mm as the tool life is also greater than 100min.

Table 9 The change of tool life based on flank wear criterion under the effect of different laser parameters. The cutting parameters are fixed at cutting speed of 30m/min, feed rate of 0.1mm/rev, and axial depth of milling of 0.2mm

Laser-tool distance of 2.85mm		Laser power of 600W	
Laser power (W)	Tool life (min)	Laser-tool distance (mm)	Tool life (min)
0	14.5	2.5	0.5
300	87	2.85	38
400	>100	3.2	>100
500	>100	3.6	20
600	38		
700	5		

3.5 Surface roughness

The proposed model predicts the overall movement of the milling tool and the tool profile based on geometry. The deformation of the cutting tool is also included according to the previously established prediction model of milling forces [136]. The profile of machined surface is then predicted based on the actual tool movement and the elastic recovery of Inconel 718. Experiments are conducted on one workpiece when the laser is off and three workpieces when the laser is on, with seven different experimental conditions including four axial depths of milling and two feed rates. The experimental measurements are compared with predicted surface roughness to verify the validation of the proposed model.

3.5.1 Analytical modeling of surface roughness

The laser-assisted milling is a complex machining process including the preheating of material ahead of tool tip by laser followed by the chip removal through the contact between tool tip and workpiece. The surface roughness is generated by the machined surface profile after material removal. The proposed model predicts surface roughness based on the actual trajectory of milling tool and the elastic recovery of machined surface. The overall movement of the milling tool is modeled first with the consideration of feed rate and tool diameter. Then the elastic deformation of milling tool due to cutting force in feed direction is calculated. The path of cutting edge is defined as the trochoidal trajectory, and the passes are performed as a single groove in the half-slot milling. Since the trajectory of milling tool highly depends on the tool tip geometry, the profile of tool tip is also included based on the tool tip radius and angle. The actual movement of any point on tool

tip is predicted from the summation of three components. Ideally, the surface finish is fully decided by the trajectory of milling tool. However, the elastic recovery of Inconel 718 decreases the material removal rate and increases the surface roughness. This process is described by the minimum chip thickness. The concept of minimum chip thickness states that the workpiece material will be removed as chip only if the uncut chip thickness is larger than a critical thickness. If the actual milling thickness is small enough, ploughing effect dominates the process, and only elastic deformation will take place. The surface roughness is then calculated according to the weighted average depth of the machined surface profile based on the length of each segment in feed direction.

3.5.1.1 Overall movement of milling tool

The movement of milling tool includes the translation in feed direction and the rotation along center axis. The translation is represented by feed per tooth f_z. If the milling tool rotates by one round, it will move in feed direction by $N_t f_z$, where N_t is the total number of flute. The coordinates of any cutting edge characterized by x_f, y_f, z_f are calculated by

$$\begin{cases} x_f = f_z \dfrac{N_t \phi_r + 2\pi(k-1)}{2\pi} + R_t \sin\phi_r \\ y_f = R_t \cos\phi_r \\ z_f = 0 \end{cases} \tag{57}$$

where ϕ_r is the rotation angle, k is the number of flute or cutting edge being calculated, and R_t is the tool radius. x_f indicates feed direction, y_f indicates cutting direction ,*and* z_f indicates axial direction. For the laser-assisted end milling, the milling tool is one flute.

The surface roughness is predicted at ϕ_r=90°, and a total of five revolutions is simulated. Therefore, the simplified function of tool movement is shown in Figure 29 as

$$\begin{cases} x_f = f_z(\frac{N_t}{4}+n)+R_t \\ y_f = 0 \\ z_f = 0 \end{cases} \tag{58}$$

where n=1:5 is the number of revolution.

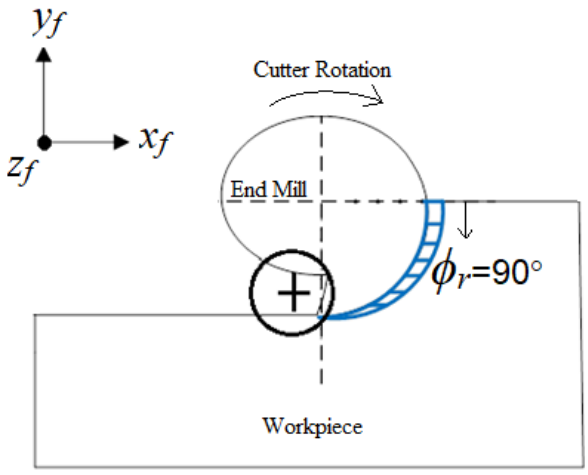

Figure 29 Schematic diagram of overall movement of milling tool at rotation angle of 90°. Cross indicates the laser's instantaneous center location with a radius of 0.35mm

3.5.1.2 Elastic deformation of cutting tool

Based on the previously established milling force prediction model [136], the contact force between workpiece and milling tool is mainly in feed direction. The model is based on the assumption that the milling process is stable, and the temperature as well as strain is evenly distributed on shear plane. The single beam coaxial laser-assisted milling spindle has high dynamic stability with fine adjustment of laser path, which justify the use of force

prediction model. The oblique cutting is transferred to equivalent orthogonal cutting at each rotation angle. For the equivalent orthogonal cutting at each instant, the plane strain condition is assumed, meaning that the plastic strain only occurs in a plane perpendicular to cutting edge. The milling force F is calculated through an iterative process for equivalence between shear stress on shear plane and mean chip flow stress. The elastic deformation of milling tool is assumed, and the deformation in feed direction x_e is calculated as

$$x_e = \frac{\mu_c F}{E} \tag{59}$$

where E is the Young's modulus of tool material and μ_c is a correction coefficient for tool tip deformation since the elastic deformation is nonlinear. μ_c is decided to be 1.181 based on the stress-strain curve of tungsten carbide in elastic region and geometry of tool [137].

3.5.1.3 *Geometry of tool tip*

To increase the accuracy of prediction, the tool tip geometry needs to be described. The coordinate system is defined in Figure 30, where r_t is the tool tip radius, α_e is the tool tip angle. The origin of the coordinate is the point on the edge which is on the same horizontal level of tool tip center. x_p indicates feed direction, y_p indicates cutting direction ,*and* z_p indicates axial direction. The exact position of a point is represented by angle α, and its coordinates are calculated by

$$x_p = \begin{cases} r_t \sin\phi_r(\cos\alpha - 1), \dfrac{3\pi}{2} - \alpha_e \le \alpha \le 2\pi \\ \sin\phi_r \left(-r_t + \left| \dfrac{r_t}{\cos(\dfrac{3\pi}{2} - \alpha_e - \alpha)} \right| \cos\alpha \right), \pi \le \alpha \le \dfrac{3\pi}{2} - \alpha_e \end{cases}$$

$$y_p = \begin{cases} r_t \cos\phi_r(\cos\alpha - 1), \dfrac{3\pi}{2} - \alpha_e \le \alpha \le 2\pi \\ \cos\phi_r \left(-r_t + \left| \dfrac{r_t}{\cos(\dfrac{3\pi}{2} - \alpha_e - \alpha)} \right| \cos\alpha \right), \pi \le \alpha \le \dfrac{3\pi}{2} - \alpha_e \end{cases} \tag{60}$$

$$z_p = \begin{cases} r_t \sin\alpha, \dfrac{3\pi}{2} - \alpha_e \le \alpha \le 2\pi \\ \left| \dfrac{r_t}{\cos(\dfrac{3\pi}{2} - \alpha_e - \alpha)} \right| \sin\alpha, \pi \le \alpha \le \dfrac{3\pi}{2} - \alpha_e \end{cases}$$

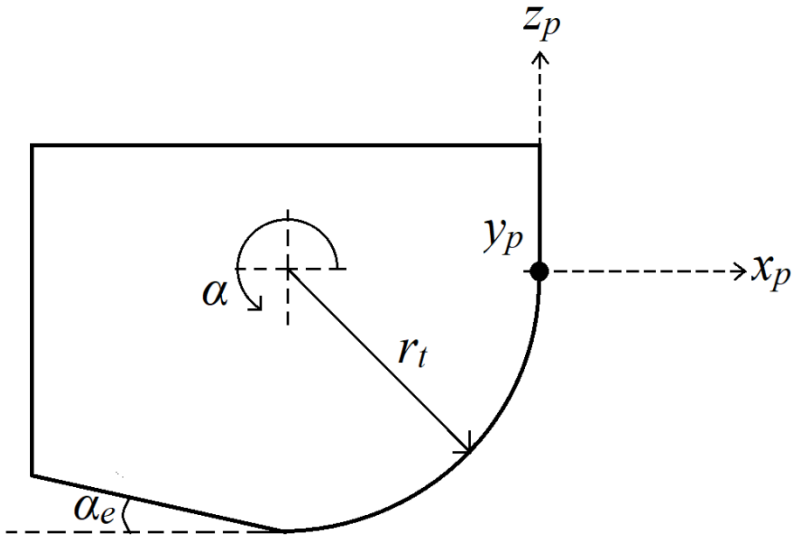

Figure 30 Coordinate system of tool tip

Since rotation angle ϕ_r=90° in the case study, y_p is always zero. Therefore, the actual coordinate of a point on milling tool is calculated as a function of α by the summation of three components as

$$\begin{cases} x = x_f + x_e + x_p \\ y = y_f + y_p = 0 \\ z = z_f + z_p \end{cases} \tag{61}$$

The tool trajectory is then represented as a curve in x-z plane.

3.5.1.4 *Machined surface profile with elastic recovery*

The machined surface profile is illustrated in Figure 31. Ideally, the surface profile will follow the tool trajectory described as functions of x and z as in Equation (61). Based on this assumption, the surface roughness is generated solely due to the gap between tool profiles in adjunct revolutions. As shown in Figure 31, for the tool profiles in i^{th} and $(i+1)^{th}$ revolutions, the ideal surface profile is from the gap X_i as the dashed line. However, in the $(i+1)^{th}$ revolution, the actual cutting thickness at some points is so small that only ploughing happens. Part of the material is under elastic deformation and recovers after the contact with milling tool as shown in Figure 31 as the dashed area. The actual surface roughness is then described by the solid line and calculated as the average height of the gap area with length X_i, between 0 and Z_{max}.

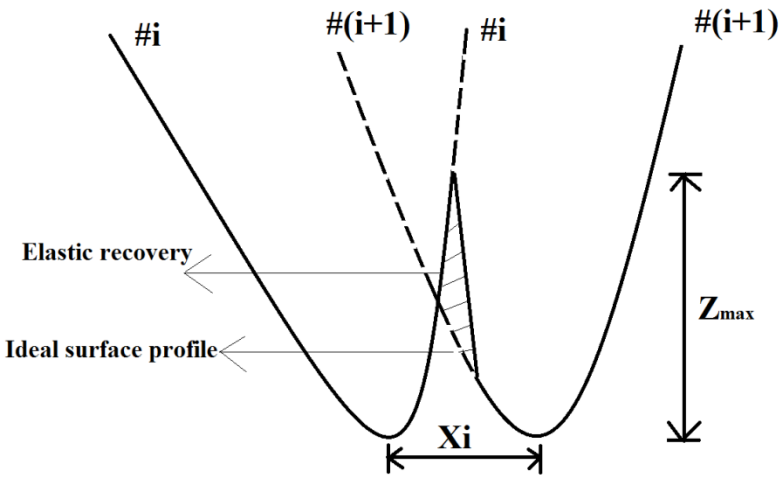

Figure 31 Minimum chip thickness and calculation of surface roughness on machined surface

The elastic recovery is described by the minimum cutting thickness $t_{\min}$, which depends on the radius of cutting edge, material tensile reference stress, and flow stress at fracture [138]. The flow stress can then be predicted theoretically through the stress intensity factor and material properties. For this study, $t_{\min}$ is directly determined through the inverse analysis of experimental measurements. In the laser-assisted end milling of Inconel 718, $t_{\min}$ =0.4μm when the laser is off, and $t_{\min}$ =0.1μm when the laser is on. The actual cutting thickness t_c in i^{th} revolution is defined as the radial distance between two points on the tool tip with same angular position from current and previous revolution, calculated as

$$t_c = \sqrt{(x^i - x_o^{i-1})^2 + (z^i - z_o^{i-1})^2} - r_t \tag{62}$$

where x^i and z^i are the coordinates of any point on the tool tip in i^{th} revolution, x_o^{i-1} and z_o^{i-1} are the coordinates of tool tip center in $(i\text{-}1)^{\text{th}}$ revolution. Therefore, when $t_c \geq t_{\min}$, only plastic deformation occurs with shearing. The material is removed as chip flow, and the

machined surface profile is same as the tool trajectory. When $t_c < t_{\min}$, only elastic deformation occurs with ploughing, and no chip forms. The material returns to its original state afterwards, and the machined surface profile is modified by recovering part of the material until the thickness calculated by Equation (62) is same as $t_{\min}$. The machined surface profile is then predicted, and the arithmetic average surface roughness R_a is defined as

$$R_{\mathrm{a}} = \frac{\sum_i X_i \overline{Z_i}}{\sum_i X_i} \tag{63}$$

where i is the number of revolution, X_i is the length of each gap between two revolutions in feed direction shown in Figure 31, and $\overline{Z_i}$ is the arithmetical mean deviation between 0 and Z_{max} in each section, which is also the surface roughness in that section, when the mean line is chosen as reference. The surface roughness R_a from Equation (63) gives the weighted average of all surface roughness over revolutions.

3.5.2 Experimental validation

The experiments are conducted under the single beam coaxial laser-assisted milling spindle as same as in 3.1.3. The overall dimension of workpiece is 12*cm*×18*cm*×15*mm*. The workpiece material is Inconel 718, and the milling tool is made of TiSiN-coated tungsten carbide with a single tooth (JSK, AA130-0600, Taiwan). The radius of the tool, *R,* is 3*mm*, the rake angle is 20.2°, and the edge radius is 0.1 mm. The tool tip radius r_t is 0.2*mm*, and the tool tip angle α_e is 2.2°. The mechanical and thermal properties of both

materials are listed in Table 10. Cutting parameters are listed in Table 11. The spindle speed is 3000*rpm*, and the radial depth of cut is 3*mm* for half-slot milling. The laser beam spot has a radius of 0.7*mm* with the center 3*mm* ahead of the tool tip. The laser pre-heating temperature is measured through the thermal couples and averaged to 850℃. Six sets of experiments are conducted as shown in Figure 32. For experiments A1 to A3, the feed rate is 100*mm/min* with axial depth of cut of 0.1*mm*, 0.15*mm*, and 0.2*mm*. Experiments B1 to B3 have same distribution of preset axial depth of milling but with a feed rate of 150*mm/min*. The laser beam and milling tool move in direct direction in each slot with a total length of 63*mm*. The surface roughness is measured by Mitutoyo SJ-410 shown in Figure 33. It has a measuring range of 8μm with high resolution of 0.0001μm. For each machined surface, the measurements are repeated at three points P1, P2, and P3 shown in Figure 32, where P1 is at the beginning of milling path, P2 is in the middle, P3 is near the end of path. Due to the instability of laser-assisted milling, same experiments are repeated on three identical workpieces for credibility. The conventional milling is conducted under the same cutting parameters for comparison. For each laser-assisted milling condition, the experiment is repeated twice under the same cutting parameters, except for A1, five times, and B3, three times, since the initial measurements have large deviations in these two groups. An additional set of experiments A4 with feed rate of 100*mm/min* and preset axial depth of cut of 0.3*mm* are conducted only in laser-assisted milling as supplement. After the elimination of deviated values, the total number of measurements from each group is listed in Table 11.

Table 10 The mechanical and thermal properties of Inconel 718 and tungsten carbide

Properties	Inconel 718	Tungsten carbide
Young's modulus	-74.35T + 214790 *MPa*	560000 *MPa*
Poisson's ratio	0.3	0.3
Thermal expansion	$10^{-5}\ e^{0.0004T}$ /℃	
Thermal conductivity	$11.367\ e^{0.0009T}$ W/m · k	84.02 W/m · k
Heat capacity	$418.63\ e^{0.0433T}$ *J/(Kg·℃)*	500 *J/(Kg·℃)*
Emissivity	0.8	
Density	8.19 g/cm³	15.8 g/cm³

Table 11 Experimental cutting parameters

Experiment	Feed rate (*mm/min*)	Preset axial depth of milling (*mm*)	Rotation speed (*rpm*)	Radial depth of milling (*mm*)	Number of measurements	
					Conventional milling	Laser-assisted milling
A1	100	0.1	3000	3	3	14
A2		0.15			3	6
A3		0.2			2	6
A4		0.3			0	3
B1	150	0.1			3	6
B2		0.15			2	5
B3		0.2			3	8

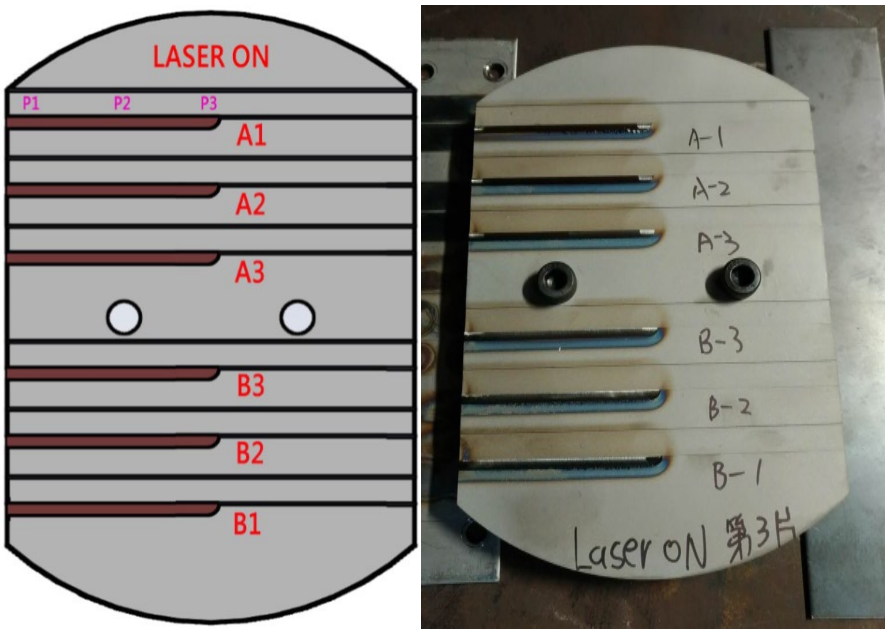

(a) (b)

Figure 32 (a) Schematic plot of six sets of experiments conducted on one Inconel 718 workpiece (b) Actual workpiece after laser-assisted milling with an overall dimension of 12*cm*×18*cm*×15*mm*

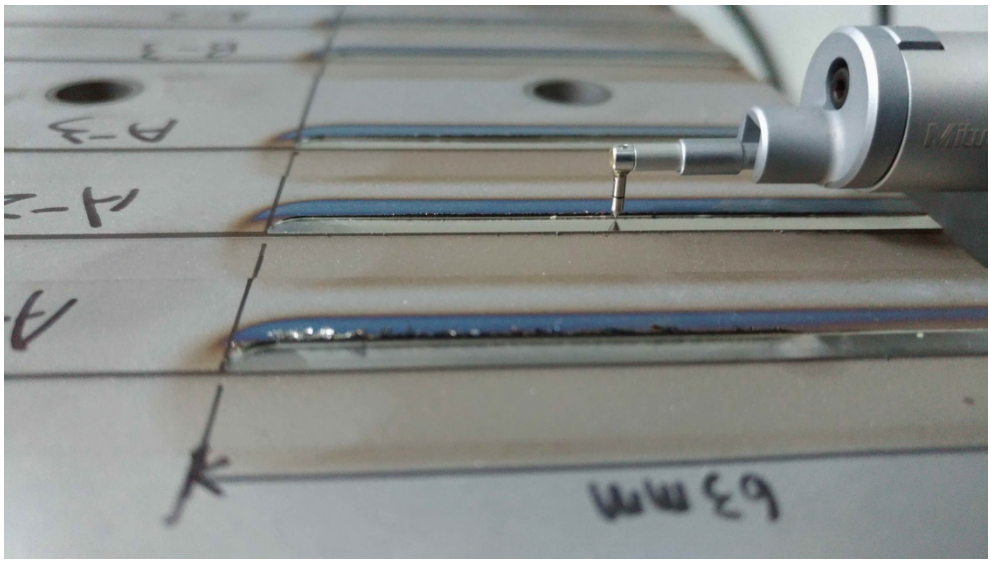

Figure 33 Surface roughness measurement equipment Mitutoyo SJ-410

3.5.3 Results

Due to the tool vibration and elongation of tool under temperature rise, the actual axial depth of cut is off from the preset value in some measurements. Therefore, the actual axial depth of cut is also measured for all experiments by Mitutoyo 1μm dial test indicator. Based on the tests in proposed analytical model, surface roughness is not sensitive to axial depth of milling with variance less than 1%. Therefore, all experiments are divided into four groups for comparison. Group A has experiments with feed rate of 100 *mm/min*, while group B has experiments with feed rate of 150 *mm/min*. All experimental measurements as well as average surface roughness in both conventional and laser-assisted milling are plotted in Figure 34.

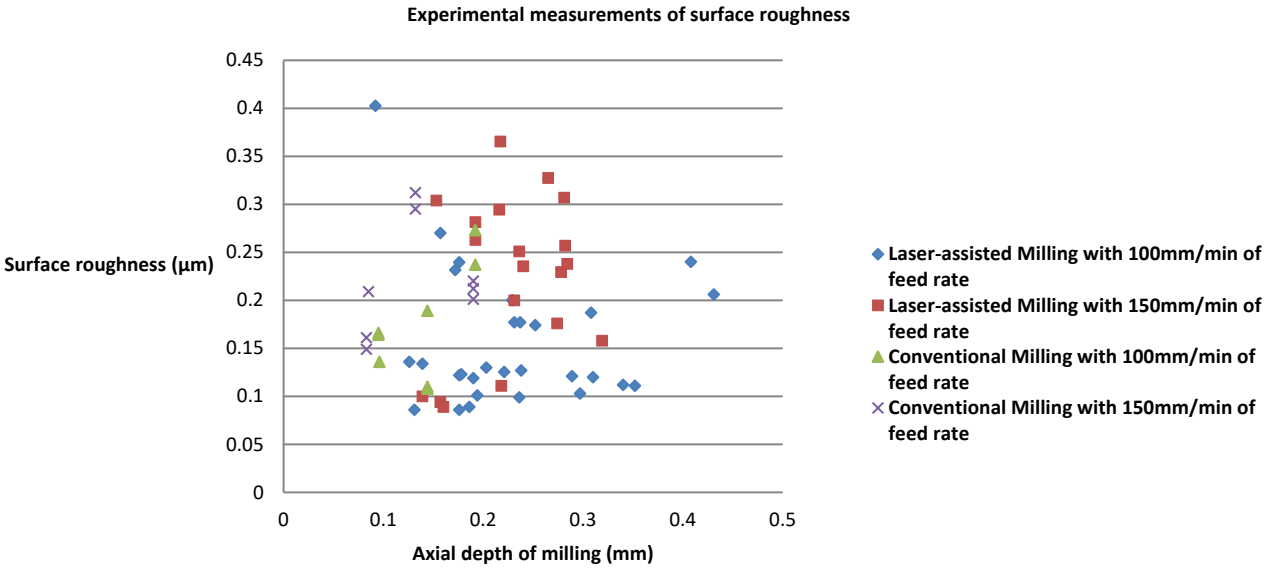

(a)

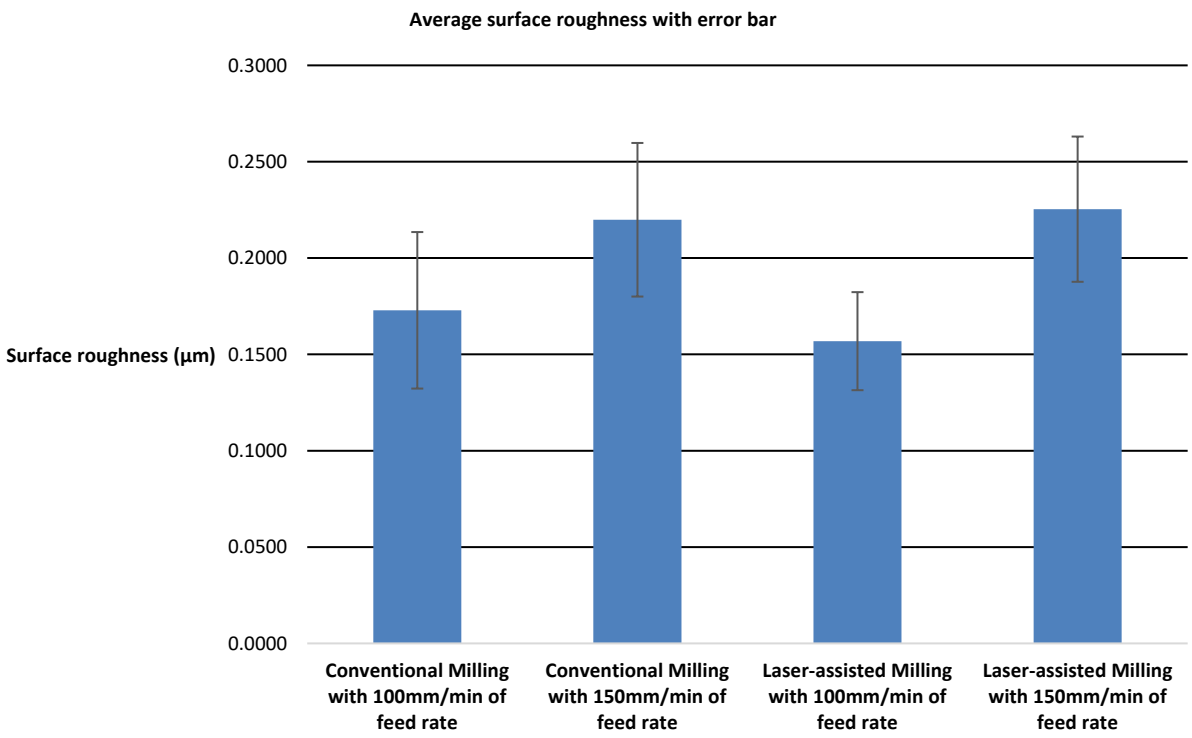

(b)

Figure 34 Experimental measurements of surface roughness (a) Scattered plot of all measurements (b) Average surface roughness in each group with error bar representing 95% confidence intervals

Five revolutions of milling process are simulated in the proposed analytical model. When the feed rate is 100*mm/min*, the resultant tool profile in light line and machined surface profile in dark line are shown in both conventional and laser-assisted milling in Figure 35. It shows that the elastic recovery takes place during conventional milling process, while the same effect is almost invisible in laser-assisted milling. The difference results in a larger surface roughness of 0.1725μm in conventional milling and a better surface finish of 0.1523μm surface roughness in laser-assisted milling.

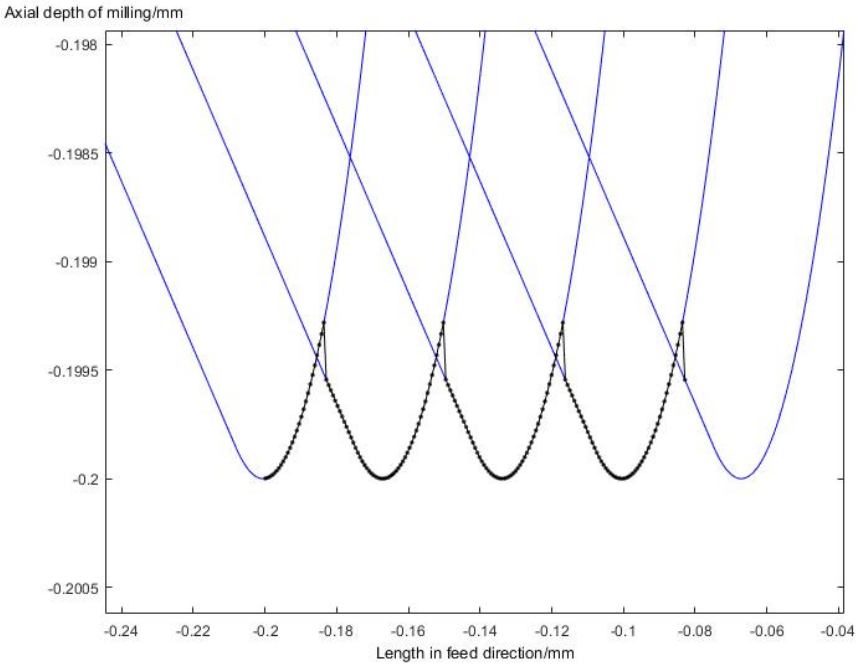

(a)

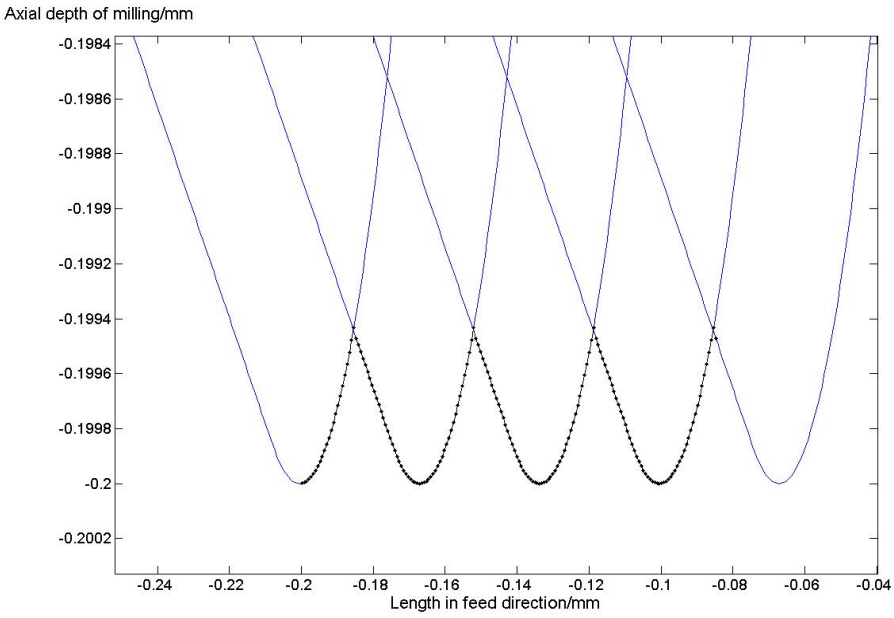

(b)

Figure 35 Analytical prediction of machined surface profile when feed rate is 100mm/min for (a) conventional milling and (b) laser-assisted milling

When the feed rate is 150*mm/min*, the resultant tool profile in light line and machined surface profile in dark line are shown in both conventional and laser-assisted milling in Figure 36. Because tool moves fast in feed direction, there is a large gap between tool profiles in two revolutions, which results in a larger surface roughness. The elastic recovery effect is still visible in conventional milling, which is less obvious than that of the previous case, and it also shows minor effect for laser-assisted milling. The surface roughness for conventional milling is 0.2788μm and for laser-assisted milling is 0.2715μm.

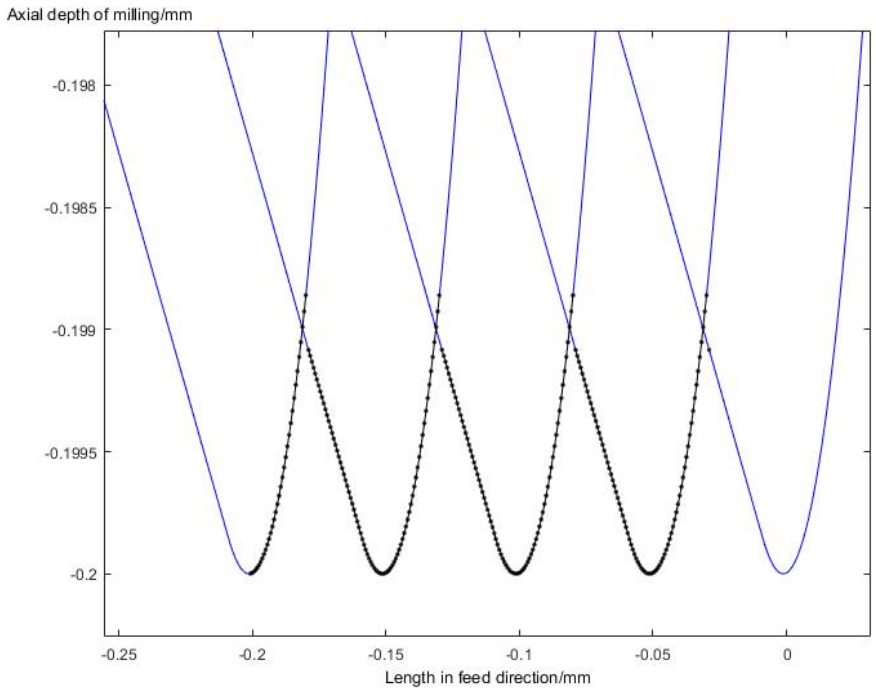

(a)

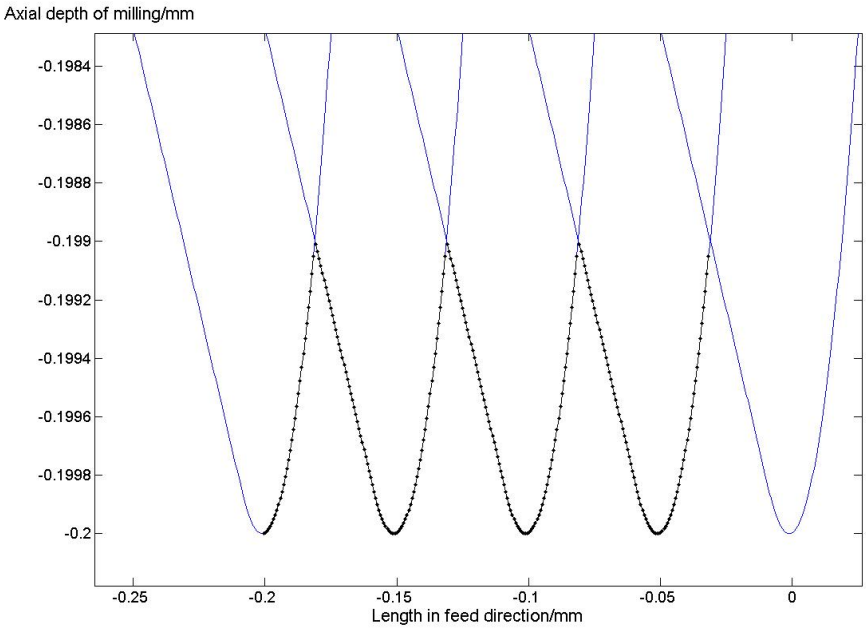

(b)

Figure 36 Analytical prediction of machined surface profile when feed rate is 150mm/min for (a) conventional milling and (b) laser-assisted milling

The comparison between experimental measurements and analytical predictions is shown in Table 12. The resultant surface roughness from experiments is the average of all measurements from Figure 34(a) in each group. The proposed model is accurate with maximum error less than 27%, and the prediction is more accurate in lower feed rate case with errors less than 3%. The softening effect of laser normally leads to better surface finish. However, when the tool is moving faster in feed direction, the tool vibration and the elongation of tool under temperature rise due to laser will harm the quality of surface finish as indicated in the experimental measurements in Table 12.

Table 12 Comparison of surface roughness

Surface roughness (μm)	Experimental Measurements	Analytical model	Error(%)
Conventional Milling with 100mm/min of feed rate	0.1729	0.1725	0.22
Conventional Milling with 150mm/min of feed rate	0.2199	0.2788	26.80
Laser-assisted Milling with 100mm/min of feed rate	0.1569	0.1523	2.91
Laser-assisted Milling with 150mm/min of feed rate	0.2254	0.2715	20.47

In order to demonstrate the accuracy of proposed model, the standard deviation of surface roughness in each category is calculated and compared with standard error of the mean listed in Table 12. For the laser-assisted milling, the standard deviation is 6.99% and the error is 2.91% when feed rate is 100*mm/min*, 8.38% of standard deviation and 20.47% of error when feed rate is 150*mm/min.* For the conventional milling, the standard deviation is 5.86% and the error is 0.22% when feed rate is 100*mm/min*, 5.75% of standard deviation and 26.80% of error when feed rate is 150*mm/min.* The deviations in low feed rate groups are less than the differences between experimental measurements and analytical predictions, which means that the proposed model is accurate enough that the error of predicted value is less than deviation from repeated measurements. While the accuracy of the model needs improvement when the feed rate is high, by considering the more significant tool vibration effect.

3.6 Conclusion

In CHAPTER 3, the forward problem methodology is presented for force, temperature, residual stress, tool wear, and surface roughness prediction in laser-assisted milling. The 3D oblique milling configuration is transferred to equivalent orthogonal cutting configuration through the chip flow model. Then the forces are calculated using classic Oxley's contact mechanics theory and back to 3D. Due to the temperature during laser-assisted milling, only the grain growth needs to be considered without phase change. The Hall-Petch equation is used to define a modified Johnson-Cook model parameter. And *JMAK* model is used to predict grain size during *DRx*. Five experiments are conducted through the single beam coaxial laser-assisted milling spindle. Periodic force signals are collected in each direction and noise signal is filtered. Data around biggest peak is averaged as experiment measurements. And analytical results from both models with and without recrystallization are provided. Overall, the proposed model provides more accurate results in *Fx* and *Fz* prediction. The maximum error is reduced to less than 20%.

For temperature prediction, the laser preheating temperature field is predicted in cutting and depth directions. The top surface is predicted first by considering the heat generation from laser and convection. The heat generation rate is described by Gaussian equation. Within the material, heat conduction is considered with isothermal boundary conditions at side and bottom surfaces. The machining temperature is considered by transferring the milling configuration to orthogonal cutting at each instance. The shearing heat source and secondary rubbing heat source are included for machining temperature prediction. The heat source is calculated from the cutting or ploughing forces, and a mirror heat source method is applied to predict temperature rise through integration. The proposed

model is validated through experimental measurements on Si_3N_4 and Ti-6Al-4V. The following conclusions are summarized:

- The machining induced temperature rise is negligible comparing to laser preheating temperature under certain combination of material and process parameters. The temperature will then only depend on laser configuration which increases with a larger laser power or a smaller laser spot diameter.
- The machining induced temperature rise cannot be ignored under certain cases especially at the cutting zone, when the laser power is low or the laser-cutter allowance is large.
- The proposed predictive model matches the experimental measurements with less than 7.1% difference at the laser spot and 5.2% difference in front of the cutting zone. A good agreement is also found between the profiles of temperature distribution from experiments and the predictive model.

The residual stress is predicted through the calculation of elastic stress distribution in loading process, actual stress with kinematic hardening, and the stress change during relaxation. The proposed model is also validated through experimental measurements on the laser-assisted milling of Si_3N_4 and Ti-6Al-4V. The following conclusions are summarized:

- With the increase of laser power, the increased temperature around the shear zone will soften the material, which leads to less compressive residual stress at surface.
- The conventional milling only has machining induced temperature rise, which hardens the material more than laser-assisted milling, and the residual stress profiles are more compressive.

- The proposed predictive model matches the trends of experimental measurements with agreement to an average error less than 30% in all cases.

For tool flank wear, the flow stress is related to the flank shear stress component according to Waldorf's worn tool force model. The effective force due to flank wear is then calculated by integrating the stress component along the chip cross section and wear land. The average stress on tool-workpiece interface due to flank wear is calculated based on the effective force and contact area. The average temperature along the interface is derived through imaginary heat source method with secondary and rubbing heat sources considered. The flank wear rate prediction considers abrasion, adhesion, and diffusion. The proposed model is validated through experimental measurements on the laser-assisted milling of K24 nickel-based superalloy, and a sensitivity analysis is conducted. The following conclusions are summarized:

- The proposed predictive model is able to match the wear progressions during steady state wear region in less than two minutes with high accuracy of 6.48% error in average.
- Cutting speed has the most significant influence on tool life, followed by feed rate and axial depth of milling.
- Either the laser parameter being too large or too small will harm the tool life. Optimum laser parameters will significantly reduce the tool wear rate.

For surface roughness, the actual tool trajectory is first predicted with the consideration of overall tool movement, elastic deformation of tool, and the tool tip profile. The tool movements include the translation in feed direction and the rotation along its axis. The elastic deformation is calculated based on the previously established milling force

prediction model. The tool tip profile is predicted based on the tool tip radius and angle. The ideal machined surface profile is the same as the tool trajectory. However, since the actual cutting thickness is smaller than the minimum cutting thickness at some locations, ploughing occurs in place of chip flow. The elastic recovery is considered through the comparison between the minimum thickness and actual cutting thickness. Experiments are conducted in both conventional and laser-assisted milling under seven different sets of cutting parameters. Since surface roughness is not sensitive to axial depth of milling, the measurements are classified based on feed rate. Through the comparison between the analytical predictions and experimental measurements, the following conclusions are summarized

- Feed rate has critical influence on the surface roughness, while axial depth of milling has minor effect.
- The laser-assisted milling achieves better surface finish. However, when the tool moves faster in feed direction, the tool vibration and the elongation of tool under temperature rise due to laser will harm the quality of surface finish.
- The proposed model has high accuracy with maximum error less than 27%, and it is more accurate for lower feed rate with error less than 3%, since there is less tool vibration.

The proposed analytical models in this chapter are valuable for providing a fast, credible, and physics-based method for the prediction of five target performances in laser-assisted milling of various materials.

CHAPTER 4. INVERSE PROBLEM METHODOLOGY IN LASER-ASSISTED MILLING

4.1 Performance driven optimization

The Kalman filter is a popular iterative gradient search method in inverse analysis method to meet the requirement of target performance through identification of process parameters. The proposed iterative gradient search method matches milling force, residual stress, surface roughness, and tool life in laser-assisted milling by determining several cutting and laser parameters. For example, tool life is decided as the cutting time when the flank wear limit of the tool is reached. Optimal combination of three cutting parameters including depth of cut d_a, feed per tooth f_z, and cutting speed V_r, and two laser parameters including laser-tool distance L and laser power P is searched to meet the tool life requirement. Laser power P is considered as the total input power Q in Equation (17). The process parameters after n^{th} loop are represented as a vector of

$$X_n = (d_a^n, f_z^n, V_r^n, L^n, P^n)^T \tag{64}$$

The very first process parameters vector X_0 is based on the initial guesses. The process parameters are updated following

$$X_{n+1} = X_n + K_n(T_{tool}^{\exp} - T_{tool}^n) \tag{65}$$

where $T_{tool}^{\exp}$ is the measured tool life from experiments, X_n and X_{n+1} are the process parameters in current and next iteration, T_{tool}^{n} is the tool life calculated based on X_n, and K_n is the Kalman gain matrix, which is also updated by iteration as

$$K_n = P_n \left(\frac{\Delta T_{tool}^{n-1}}{\Delta X_{n-1}} \right)^T R^{-1} \tag{66}$$

where P_n is the simulation covariance matrix, $\left(\frac{\Delta T_{tool}^{n-1}}{\Delta X_{n-1}} \right)$ is the derivative matrix capturing the gradients of T_{tool}^{n} with respect to the each process parameter. The initial differences ΔX_0 and ΔT_{tool}^{0} are assumed to be equal to X_0 and T_{tool}^{0}. R_n is the error covariance matrix defined as

$$R_n = \left(T_{tool}^{\exp^2} \right) \tag{67}$$

The derivative matrix is calculated as

$$\left(\frac{\Delta T_{tool}^{n-1}}{\Delta X_{n-1}} \right) = \left(\frac{T_{tool}^{n} - T_{tool}^{n-1}}{d_a^n - d_a^{n-1}}, \frac{T_{tool}^{n} - T_{tool}^{n-1}}{f_z^n - f_z^{n-1}}, \frac{T_{tool}^{n} - T_{tool}^{n-1}}{V_r^n - V_r^{n-1}}, \frac{T_{tool}^{n} - T_{tool}^{n-1}}{L^n - L^{n-1}}, \frac{T_{tool}^{n} - T_{tool}^{n-1}}{P^n - P^{n-1}} \right) \tag{68}$$

All parameters in first loop are assumed to be zero, and the initial simulation covariance matrix is

$$P_0 = \begin{pmatrix} (\Delta d_a)^2 & 0 & 0 & 0 & 0 \\ 0 & (\Delta f_z)^2 & 0 & 0 & 0 \\ 0 & 0 & (\Delta V_r)^2 & 0 & 0 \\ 0 & 0 & 0 & (\Delta L)^2 & 0 \\ 0 & 0 & 0 & 0 & (\Delta P)^2 \end{pmatrix} \tag{69}$$

where $\Delta d_a, \Delta f_z, \Delta V_r, \Delta L,$ and ΔP are the expected variance ranges of each process parameter. The simulation covariance matrix is updated as

$$P_n = P_{n-1} - P_{n-1}\left(\frac{\Delta T_{tool}^{n-1}}{\Delta X_{n-1}}\right)^T \left(\frac{\Delta T_{tool}^{n-1}}{\Delta X_{n-1}} P_{n-1} \left(\frac{\Delta T_{tool}^{n-1}}{\Delta X_{n-1}}\right)^T + R_n\right)^{-1} \times \frac{\Delta T_{tool}^{n-1}}{\Delta X_{n-1}} P_{n-1} \tag{70}$$

Both forward and inverse problems are solved analytically and combined in the one iterative predictive model with details of procedure summarized in Figure 37.

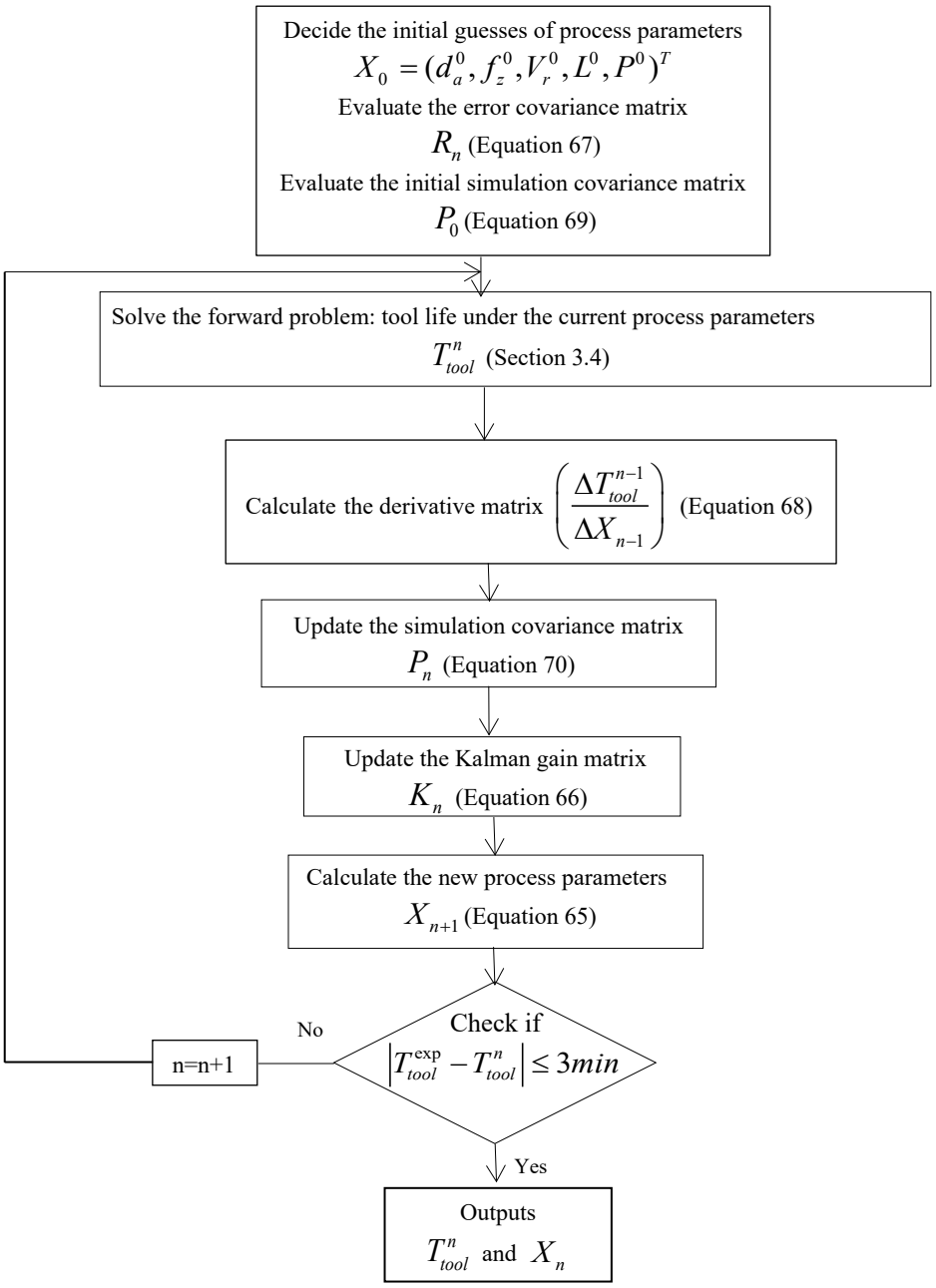

Figure 37 Flow chart of the inverse analysis process

4.2 Milling force

Force signals were collected under four different cutting conditions as in 3.1.3. The five process parameters were feed rate, axial depth of milling, laser preheating temperature,

spindle speed, and cutter rake angle. For the experiments, the laser preheating temperature was average to 850 ℃, the spindle speed was set to 3000 rpm, the cutter rake angle was 35°, and the feed rate and axial depth of milling varied according to Table 13. The initial guesses of X_1 were based on the experiment values. In each loop, both direct and inverse analyses were conducted once, and the resultant force predicted was compared to the experimental measurement. The final process parameters predicted are listed in Table 14, and the resultant forces as well as the percentage errors are listed in Table 15.

Table 13 Cutting parameters of experiments

Experiment number	Feed rate (*mm/min*)	Axial depth of milling(*mm*)
1	200	0.1
2	200	0.2
3	300	0.1
4	300	0.15

Table 14 Comparison of process parameters from experiments and inverse analysis

Experiment number		Feed rate (mm/s)	Axial depth of milling (mm)	Laser preheating temperature(℃)	Spindle speed (rpm)	Cutter rake angle(°)
1	Optimal solution	3.908159	0.112568	1041.519	3254.728	39.063
	Experiment	3.33	0.1	850	3000	35
2	Optimal solution	4.536662	0.158558	1196.044	3902.204	47.23546
	Experiment	3.33	0.2	850	3000	35
3	Optimal solution	5.627785	0.105203	957.1991	3365.233	39.06187
	Optimal solution	5.172909	0.141804	880.8117	3069.678	35.21963
	Experiment	5	0.1	850	3000	35
4	Optimal solution	6.819174	0.210865	1158.594	4107.516	48.19985
	Experiment	5	0.15	850	3000	35

Table 15 Resultant force from experiments and inverse analysis

	Feed rate (mm/min)	Axial depth of milling(mm)	Force (N) Experiment	Force (N) Inverse analysis	Error%
1	200	0.1	18.00968	17.69383	1.753
2	200	0.2	23.54006	21.8458	7.19716
3	300	0.1	19.75426	19.02617	0.03686
4	300	0.15	35.36364	35.375633	0.0339

For the 1st experiment, the feed rate was 200 *mm/min*, and the axial depth of milling was 0.1 *mm*. The resultant force measured from experiment was 18.01 *N*. The initial guess was $X_1 = [3, 0.08, 800, 2500, 30]^T$ and the optimal solution was 17.694 *N* at loop #81. From Figure 38, it could be seen that the resultant force from inverse analysis was oscillating around 6 *N* for the first 50 loops, and then it found the right direction, jumped to over 14 *N*, and got closer to the experimental measurement loop by loop.

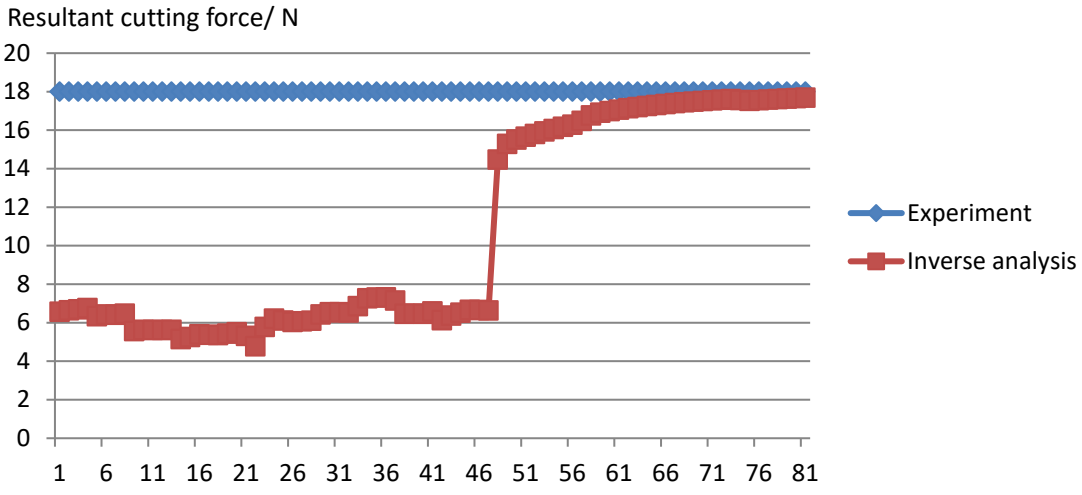

Figure 38 Resultant forces from experiment and inverse analysis under a feed rate of 200 mm/min, an axial depth of milling of 0.1mm

For the 2nd experiment, the feed rate was 200 *mm/min*, and the axial depth of milling was 0.2 *mm*. The resultant force measured from experiment was 23.54 *N*. The initial guess was $X_1 = [3.7, 0.1, 1000, 3200, 38]^T$ and the optimal solution was 21.846 *N* at loop #38. Because of a better initial guess, the optimal solution was found with a less number of loops. The resultant force from inverse analysis increased rapidly for the first five loops and got slowly closer to the experimental measurement as shown in Figure 39.

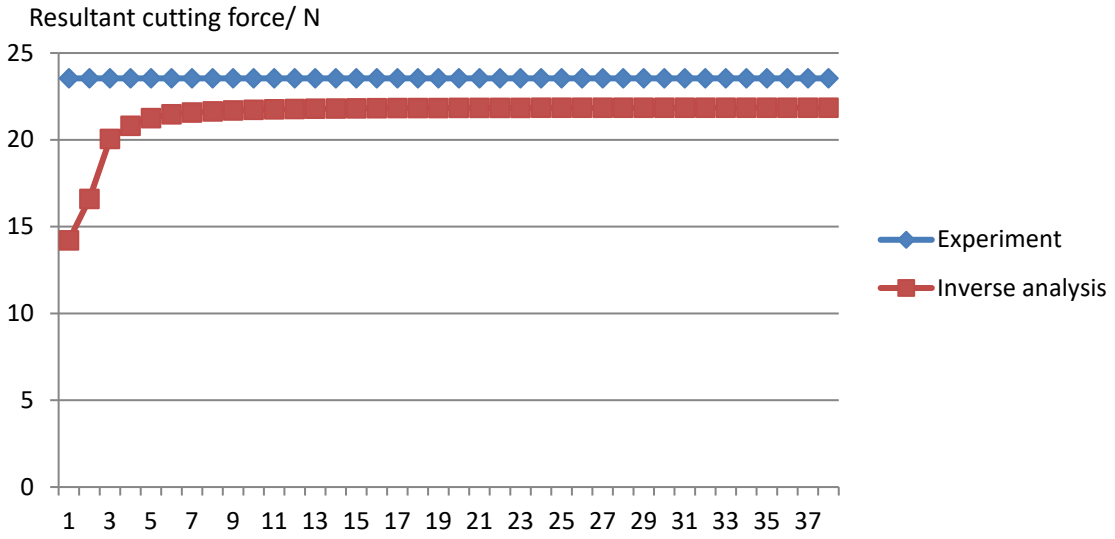

Figure 39 Resultant forces from experiment and inverse analysis under a feed rate of 200 mm/min, an axial depth of milling of 0.2mm

For the 3nd experiment, the feed rate was 300 *mm/min*, and the axial depth of milling was 0.1 *mm*. The resultant force measured from experiment was 19.75 *N*. The initial guess was $X_1 = [5, 0.15, 850, 3000, 35]^T$. The optimal solution was 19.03 *N* at loop #500. From Figure 40, the predicted force went to the wrong direction two or three times during the process but got a pretty close result at the end.

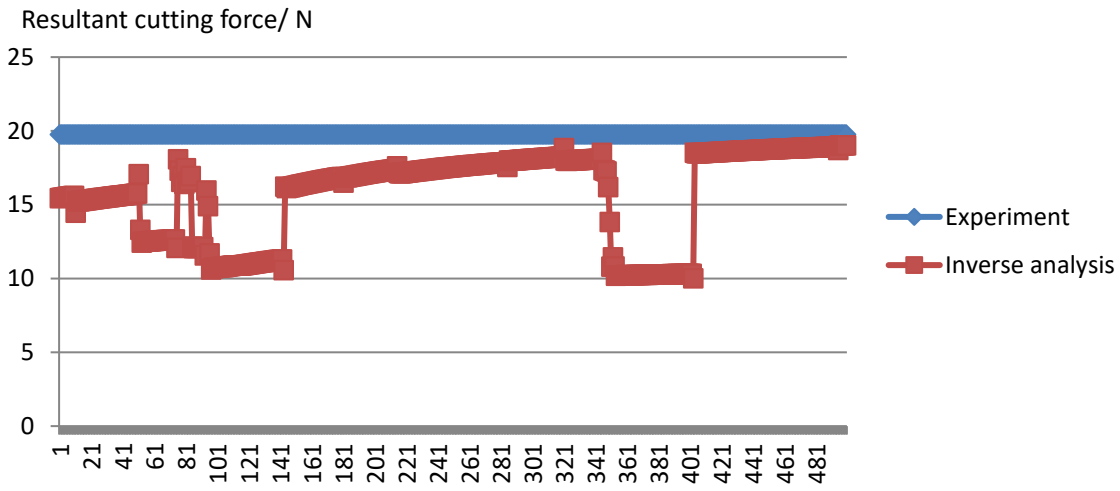

Figure 40 Resultant forces from experiment and inverse analysis under a feed rate of 300mm/min, an axial depth of milling of 0.1mm

For the 4th experiment, the feed rate was 300 *mm/min*, and the axial depth of milling was 0.15 *mm*. The resultant force measured from experiment was 35.36 *N*. The initial guess was $X_1 = [5, 0.15, 850, 3000, 35]^T$ and the optimal solution was 35.38 *N* at loop #14. As shown in Figure 41, the force predicted from inverse analysis was able to catch the experimental measurement in the first three loops. Then it was looking for the optimal solution around the reference value and found a good agreement in 15 loops.

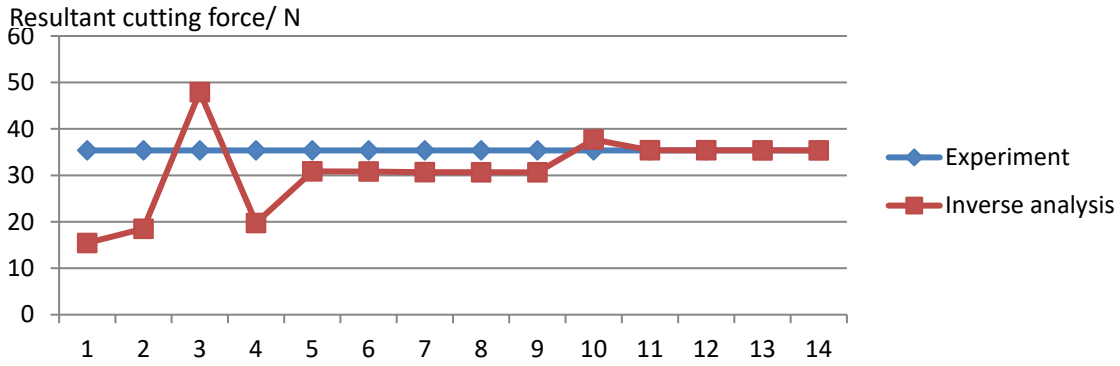

Figure 41 Resultant forces from experiment and inverse analysis under a feed rate of 300mm/min, an axial depth of milling of 0.15mm

4.3 Residual stress

Depth of cut d_a, feed per tooth f_z, cutting speed V_r, laser-tool distance L, and laser power P are updated to match the residual stress measurements from 3.3.3.2. For Ti-6Al-4V grade 5, the measured mean residual stress as well as prediction from inverse analysis in laser-assisted milling are shown in Figure 42. Measurements are collected every $50\mu m$ up to $200\mu m$ depth and averaged for mean residual stress. The initial guesses for inverse analysis are cutting depth of $1mm$, feed per tooth of $0.22mm/s$, cutting speed of $2.75m/s$, laser-tool distance of $7.7mm$, and laser power of $1034W$. In machining direction, the mean residual stress from experiments is $191MPa$ in compression, and the prediction through inverse analysis is $-182.72MPa$. A close match is found after 44 iterations with a percentage difference of 4.33% as listed in Table 16. In feed direction, the mean residual stress from experiments is $130.2MPa$ in compression, and the prediction through inverse analysis is $-132.80MPa$ with a percentage difference of 1.99%. The process parameters in final iteration are cutting depth of $0.79mm$, feed per tooth of $0.11mm/s$, cutting speed of $1.62m/s$, laser-tool distance of $6.03mm$, and laser power of $816.6W$. As observed in Figure 42, the proposed algorithm is able to jump out of local extreme several times throughout the inverse analysis until the stopping criteria are reached.

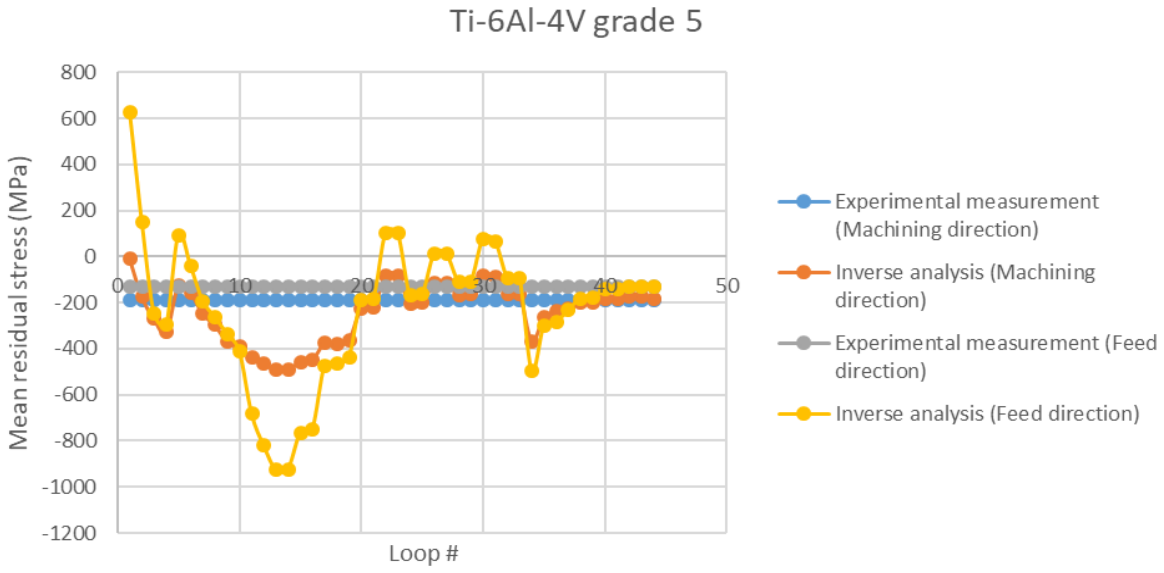

Figure 42 Estimation of mean residual stress via inverse analysis on Ti-6Al-4V grade 5

Table 16 Comparison of mean residual stress between experimental measurements and predictions through inverse analysis

	Ti-6Al-4V Grade 5		
	Measured mean residual stress (*MPa*)	Prediction from inverse analysis (*MPa*)	Percentage difference (*%*)
Machining direction	-191	-182.72	4.33
Feed direction	-130.2	-132.80	1.99
	Ti-6Al-4V ELI		
	Measured mean residual stress (*MPa*)	Prediction from inverse analysis (*MPa*)	Percentage difference (*%*)
Machining direction	-175	-171.50	2.00
Feed direction	-143.5	-146.68	2.21

The measured mean residual stress as well as prediction from inverse analysis in laser-assisted milling of Ti-6Al-4V ELI are shown in Figure 43. The initial guesses for inverse analysis are cutting depth of 1*mm*, feed per tooth of 0.1*mm/s*, cutting speed of

1.25*m/s*, laser-tool distance of 3.5*mm*, and laser power of 70*W*. In machining direction, the mean residual stress from experiments is 175*MPa* in compression, and the prediction through inverse analysis is -171.5*MPa*. A close match is found after 27 iterations with a percentage difference of 2% as listed in Table 16. In feed direction, the mean residual stress from experiments is 143.5*MPa* in compression, and the prediction through inverse analysis is -146.68*MPa* with a percentage difference of 2.21%. The process parameters in final iteration are cutting depth of 0.51*mm*, feed per tooth of 0.06*mm/s*, cutting speed of 0.74*m/s*, laser-tool distance of 1.78*mm*, and laser power of 237.37*W*. Again, the proposed inverse analysis method is able to reach both high computational efficiency and accuracy.

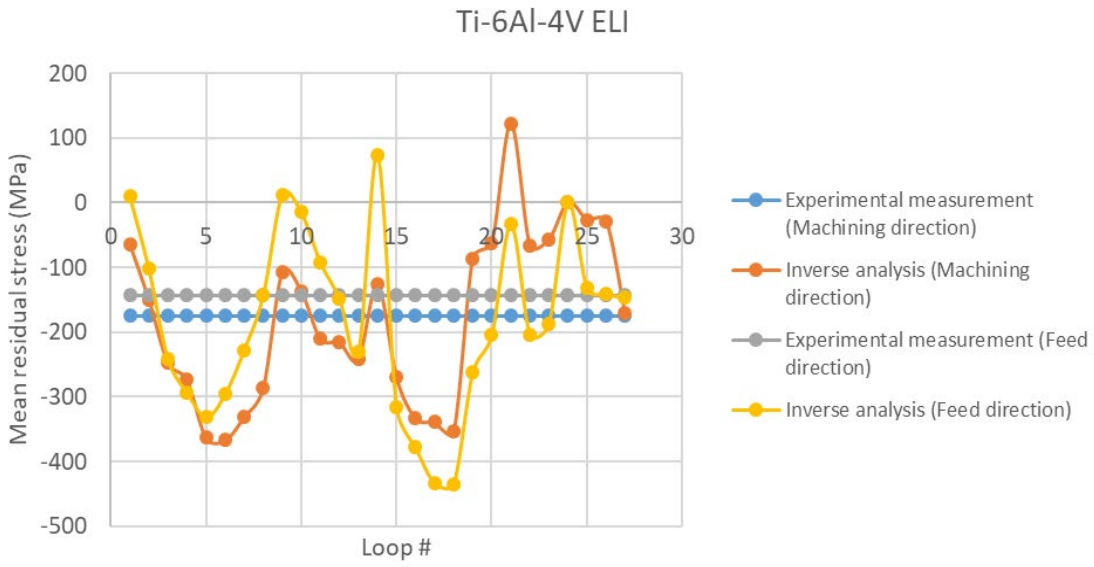

Figure 43 Estimation of mean residual stress via inverse analysis on Ti-6Al-4V ELI

When comparing the process parameters in final loop to initial guesses and experimental values, it is observed that although the process parameters are relatively close to initial guesses, they may be very different than experimental process parameters since the mean residual stress solutions may not be unique. In addition, the model-predicted residual stresses under experimental process parameters have been calculated by solving

forward problem only [139] as in 3.3.3.2. The percentage errors for Ti-6Al-4V grade 5 and ELI are higher than 10% in both directions, which also indicates that the proposed inverse analysis method is highly accurate as the errors are mainly from the forward model.

4.4 Tool life

Based on the experimental measurements from 3.4.4 and summarized in Table 17, inverse analysis is conducted through iterative gradient search of five process parameters including depth of cut d_a, feed per tooth f_z, cutting speed V_r, laser-tool distance L, and laser power P, to match the recorded tool life. Different initial guesses of X_0 are made in order to check the adaptability of proposed model. The time interval Δt is $0.25 min$ for laser-assisted milling and $0.5 min$ for conventional milling, and the average computation time is 90 to 110s per iteration. The process parameters in first and last iterations and comparison of tool life between experiments and inverse analysis are presented in Table 18. The predicted tool life in inverse analysis changes over iterations for laser-assisted milling is shown in Figure 44.

Table 17 Measured flank tool wear and tool life

		Flank tool wear at the beginning of steady wear region (μm)	Cutting time at the beginning of steady wear region (min)	Flank tool wear at tool life (μm)	Tool life (min)
Laser-assisted milling	Tool A	150	7.25	325	32
	Tool B	160	7.25	310	26
	Tool C	140	7.25	330	26
Conventional milling	Tool A	150	3	350	20
	Tool B	180	3	460	16.5
	Tool C	240	3	425	16.5

Table 18 Comparison of tool life from experiments and inverse analysis in first and final iterations

			Depth of cut (*mm*)	Feed rate (*mm/s*)	Cutting speed (*mm/s*)	Laser-tool distance (*mm*)	Laser power (*W*)	Tool life (*min*)		Percentage error (%)
								Experiment	Inverse analysis	
Laser-assisted milling	Tool A	Initial guess	0.18	0.13	550	2.9	593	32	50.75	58.59
		Final loop	0.169	0.123	517	2.782	557		30.75	3.91
	Tool B	Initial guess	0.18	0.13	550	2.9	593	26	30.25	16.35
		Final loop	0.174	0.126	530	2.848	572		27.25	4.81
	Tool C	Initial guess	0.21	0.12	533	2.96	590	26	37.75	45.19
		Final loop	0.199	0.114	504	2.855	558		24.25	6.73
Conventional milling	Tool A	Initial guess	0.2	0.1	500			20	36.5	82.50
		Final loop	0.194	0.094	485.979				19.5	2.50
	Tool B	Initial guess	0.199	0.096	495			16.5	11.5	30.30
		Final loop	0.19903	0.0962	495.04				19.5	18.18
	Tool C	Initial guess	0.21	0.11	517			16.5	38.5	133.33
		Final loop	0.205	0.104	504				19	15.15

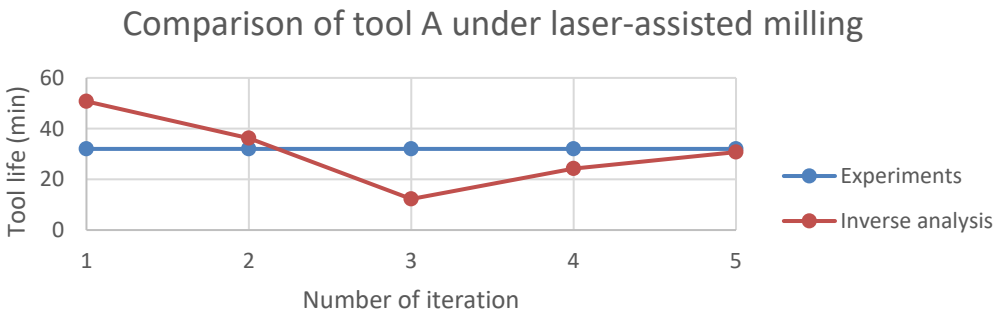

(a)

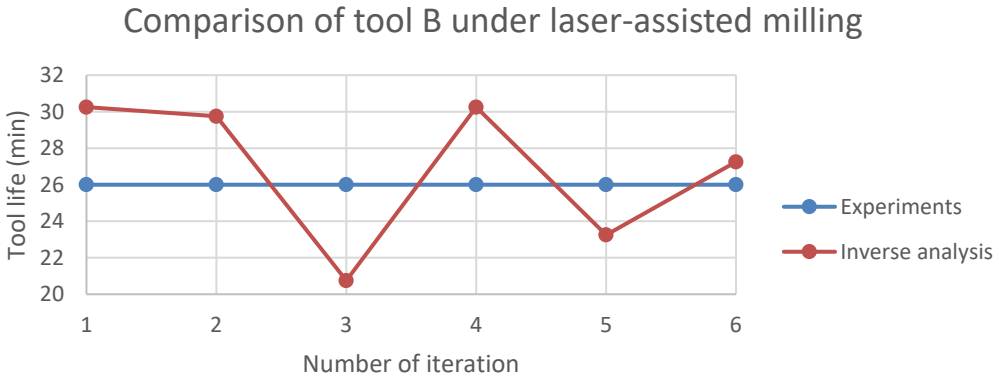

(b)

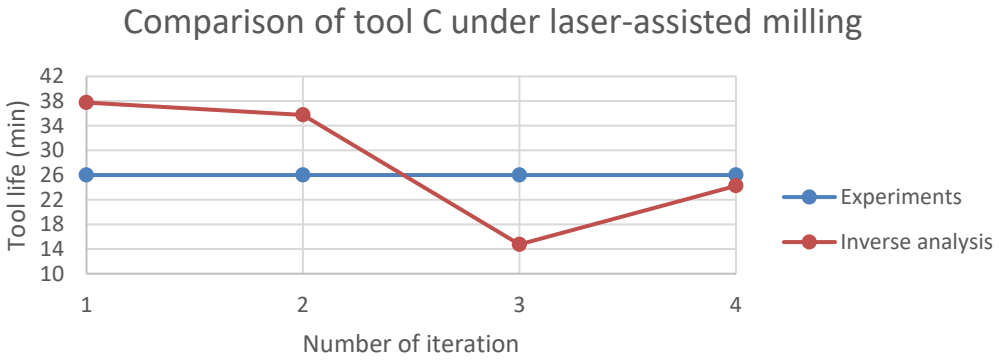

(c)

Figure 44 The comparison of tool life in laser-assisted milling of (a) tool A, (b) tool B, and (c) tool C between experimental measurements and predictions from inverse analysis

As shown in Table 17, the cutting time is shorter for conventional milling when the break-in period is complete with higher flank tool wear for tool B and tool C. The tool life is extended for all three tools when the laser is applied. For tool A, the flank wear increases from 150μm to 325μm in laser-assisted milling and from 150μm to 350μm in conventional milling. As shown in Figure 44(a), the predicted tool life based on initial guess has almost 60% error, while the error is reduced to less than 4% after five iterations and 533s computational time. All process parameters are changed within 7% of initial guesses which indicates that the algorithm is able to find a close match of target performance with process parameters around initial guesses. Three cutting parameters have same level of significance to tool life by changing around 6% over five iterations, while laser power has more significant influence of 6% change from 593 to 557W than laser-tool distance with 4% change, as shown in Figure 45(a). For conventional milling presented in Table 18, a close match of 2.5% difference is found.

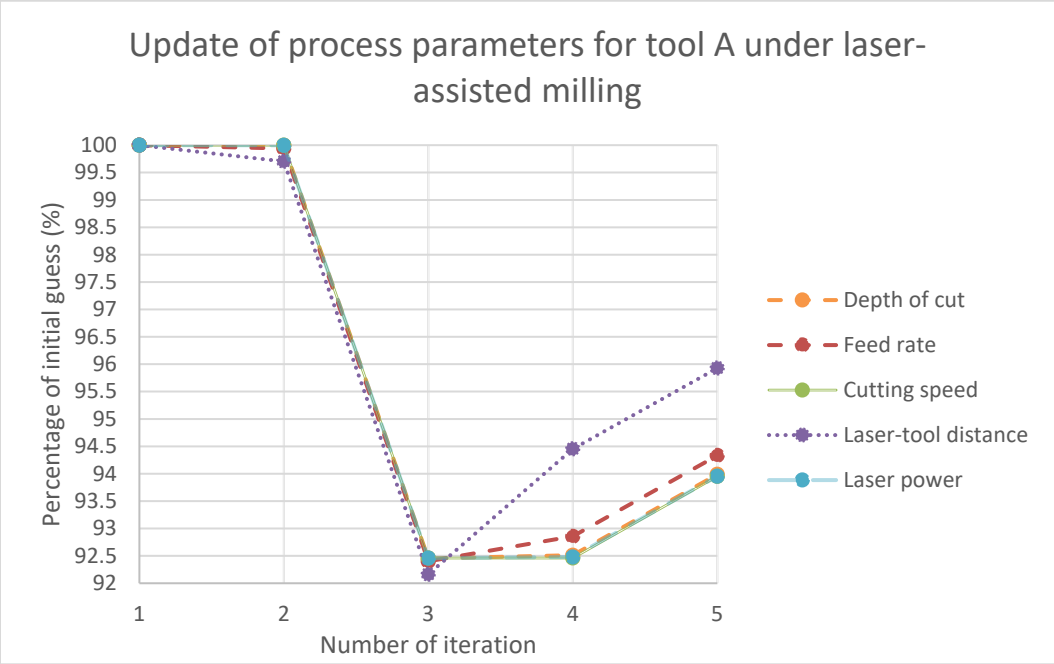

(a)

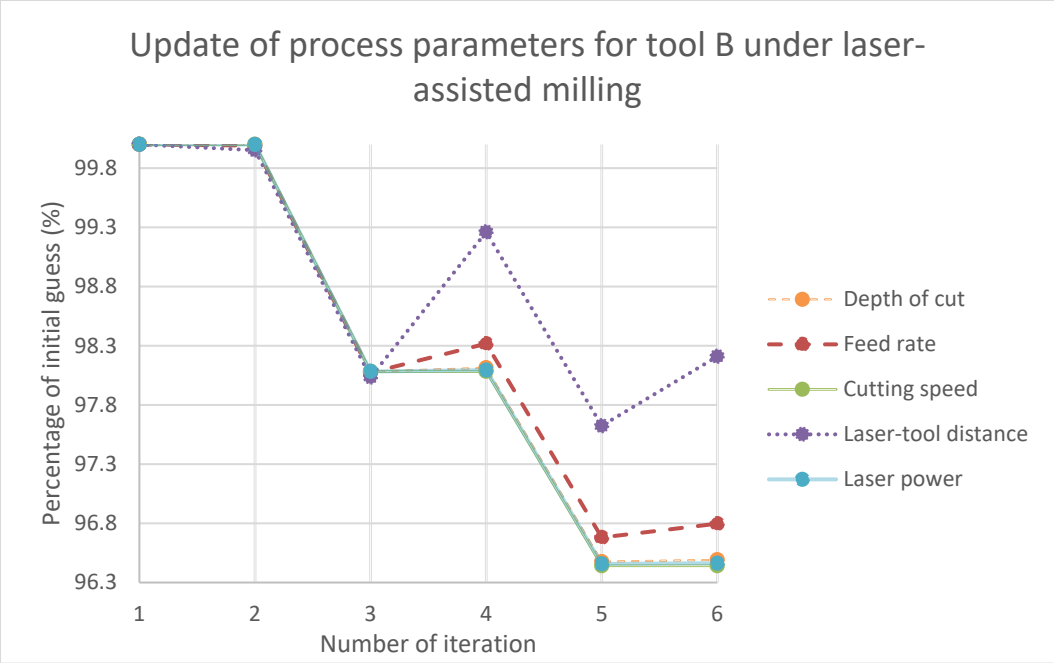

(b)

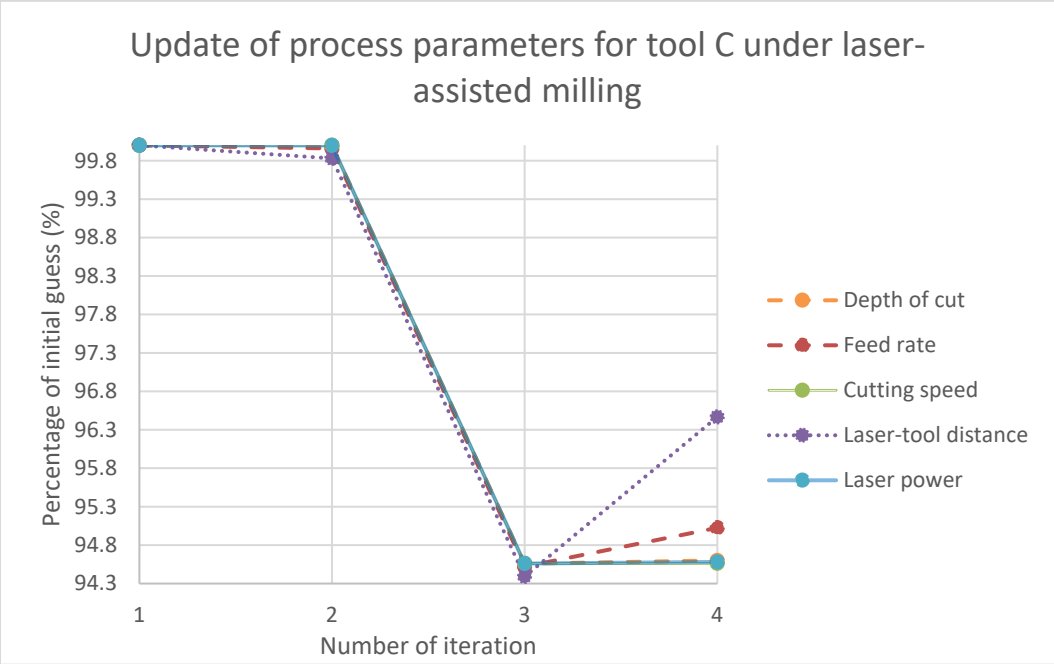

(c)

Figure 45 The update of depth of cut, feed rate, cutting speed, laser-tool distance, and laser power over iterations in laser-assisted milling of (a) tool A, (b) tool B, and (c) tool C

For tool B, the flank wear increases from 160μm to 310μm in laser-assisted milling and from 180μm to 460μm in conventional milling. As shown in Figure 44(b), the predicted tool life has 16.35% initial error, which is reduced to 4.81% after six iterations and 504s computational time. All process parameters are changed within 4% of initial guesses. In addition, laser power has more significant influence of 3.5% change comparing to laser-tool distance of 1.8% change from 2.9 to 2.848mm, as shown in Figure 45(b). The error also decreases from 30% to 18% in conventional milling. For tool C, the flank wear increases from 140μm to 330μm in laser-assisted milling and from 240μm to 425μm in conventional milling. As shown in Figure 44(c), the error of predicted tool life decreases from 45% to 6.7% after four iterations and 359s computational time. Again, the change of laser-tool distance is 3.5% between initial and final guesses, which is less significant than the 5.4% drop of laser power, as shown in Figure 45(c). For conventional milling, the error drops dramatically with the predicted tool life from 38.5 to 19min comparing with the measured 16.5min.

According to the experimental measurements and predictions from inverse analysis, it is concluded that the use of laser significantly extend the tool life, and the proposed iterative gradient search method for inverse analysis is able to match the measured tool life with high computation efficiency less than 540s and high accuracy of less than 7% difference in laser-assisted milling and 20% in conventional milling. The error is higher for conventional milling mainly because the two fewer process parameters limit the efficiency of gradient search. However, with more process parameters introduced in inverse analysis, multiple solutions may become an issue as the predicted process parameters are near initial guesses as long as the stopping criterion is met, while there are

possibly other combinations of process parameters that can also satisfy the required tool life. In addition, three cutting parameters have equal influences on tool life, while laser power has more significant impact than laser-tool distance between two laser parameters.

4.5 Surface roughness

The experimental data for the surface roughness for four milling depths and two feed rates are from 3.5.2 and summarized in Table 19. The results show that, for laser-assisted milling, an increase in the feed rate increases the value of surface roughness. This phenomenon is related to the higher feed speeds that create a larger gap in tool profiles between two revolutions. There is no significant correlation between the surface roughness and milling depth.

Table 19 Comparison between experimental measurement and inverse analysis of surface roughness

	Laser on			Laser off		
Experiment	Experimental measurement (μm)	Prediction from inverse analysis(μm)	Percentage error of target performance ($\%$)	Experimental measurement (μm)	Prediction from inverse analysis (μm)	Percentage error of target performance ($\%$)
A1	0.1822±0.1002	0.1827	0.296	0.1660±0.0137	0.1670	0.594
A2	0.1592±0.0531	0.1576	1.023	0.1100±0.0377	0.1092	0.743
A3	0.1667±0.0389	0.1676	0.566	0.2370±0.0792	0.2369	0.035
A4	0.1857±0.0546	0.1847	0.524			

B1	0.2229±0.0922	0.2239	0.434	0.1610±0.0259	0.1600	0.603
B2	0.2987±0.0919	0.2988	0.040	0.2950±0.0558	0.2954	0.124
B3	0.2371±0.0576	0.2379	0.340	0.2200±0.0078	0.2194	0.267

Table 19 also includes the predicted surface roughness and its percentage error. The algorithm predicts the surface roughness in laser-assisted milling on Inconel 718 from the estimation of feed per tooth, tool tip radius, minimum cutting thickness, and tool tip angle. The initial values of process parameters except t_1 were from experimental configuration. The initial minimum cutting thickness t_1 was assumed to be $0.4\mu m$ in experiments A1 to A4, and $0.2\mu m$ in experiments B1 to B3 when laser was on, and $0.7\mu m$ in all six experiments when laser was off [138]. The proposed variance-based recursive method matches the measurements perfectly in all cases with errors less than 1.1%. The algorithm is able to not only match the target performance, but also find the match within the certain ranges of process parameters. The average difference of process parameters is calculated between $X_n = (f_Z^n, r_t^n, t_{min}^n, \alpha_e^n)^T$ used in experiments or theory and actual $X_n = (f_Z^n, r_t^n, t_{min}^n, \alpha_e^n)^T$ in final iteration of the inverse analysis model. The difference is less than 5% for all cases, and the selection process is done in 50 loops within a minute. Measurement in experiment A2 is the only target performance not matched by $\left|Ra_R^{\exp} - Ra_R^n\right| < 0.001\mu m$ due to the large gap between target and initial guess. Alternative initial simulation covariance matrix P_0 in Equation (69) with larger expected variance range of α_e and smaller expected variance range of r_t was applied to give a close match of $0.1594\mu m$ with an error of 0.137%. But the average difference of process parameters increased to 8.62%. The previous P_0 was chosen

to avoid multiple solution issue. Overall, the proposed inverse analysis model is able to find the optimal combination of process parameters around the experimental settings to match the measured surface roughness with high accuracy within short computation time.

4.6 Conclusion

In CHAPTER 4, the inverse problem methodology is presented for force, residual stress, tool life, and surface roughness prediction in laser-assisted milling. The variance-based recursive method is applied to solve inverse problem and update process parameters to match the measurements. The following conclusions are summarized:

- For milling force, the proposed inverse analysis method is able to guide the process parameters and find an optimal solution in all experimentally validated cases with a maximum error between predicted forces and experimental measurements less than 8%
- For residual stress, the percentage difference between experiments and predictions is less than 5%, and the process is completed within 50 loops.
- For tool life, the proposed predictive model is able to match the measured tool life with high accuracy of less than 7% difference in laser-assisted milling and 20% in conventional milling, and high computation efficiency less than 540*s*. Depth of cut, feed per tooth, and cutting speed have equal influences on tool life, while laser power has more significant impact than laser-tool distance between two laser parameters, as the change of laser power is 1.7 to 2% more over the iterations.
- For surface roughness, the proposed model has high accuracy with average error less than 0.5%, and the average difference of process parameters is less than 5%.

The proposed inverse analysis model is adaptive to different initial guesses and measurements, highly accurate, and computationally efficient. The proposed method is valuable in terms of providing a fast, accurate and reliable reference for the selection of process parameters under certain performance requirements.

CHAPTER 5. FORWARD PROBLEM METHODOLOGY IN ULTRASONIC VIBRATION-ASSISTED MILLING

5.1 Tool-workpiece separation criteria

As shown in Figure 1, the tool-workpiece separation criteria are first checked in forward problem methodology. Kinematical analysis is conducted to calculate the exact trajectory of tool center as well as tip under ultrasonic vibration, tool rotation, and feed movement. According to the coordinate system in Figure 46, when the initial tool center position is chosen as origin, the tool center is described as a function of time as

$$\begin{aligned} x(t) &= A_x \sin(\omega_x t + \theta_x) - V_f t \\ y(t) &= A_y \sin(\omega_y t + \theta_y) \\ z(t) &= d_a + A_z \sin(\omega_z t + \theta_z) \end{aligned} \tag{71}$$

where V_f is the feed rate, d_a is axial depth of milling, ω_x, ω_y, and ω_z are the angular ultrasonic vibration frequency, θ_x, θ_y, and θ_z are the phase angle, A_x, A_y, and A_z are the vibration amplitude in each direction, which is zero when no vibration is applied in that direction.

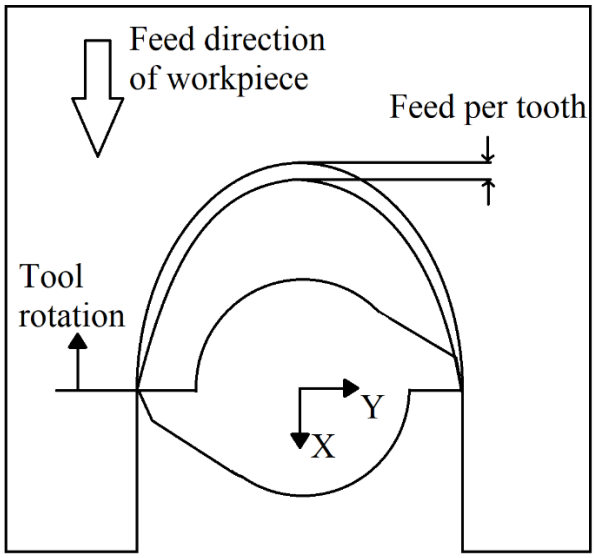

Figure 46 Coordinate system of cutting tool and workpiece

The tool center velocity is then calculated based on the derivative of Equation (71) as

$$\begin{aligned} x'(t) &= \omega_x A_x \cos(\omega_x t + \theta_x) - V_f \\ y'(t) &= \omega_y A_y \cos(\omega_y t + \theta_y) \\ z'(t) &= \omega_z A_z \cos(\omega_z t + \theta_z) \end{aligned} \tag{72}$$

In addition,

$$\begin{aligned} V_x(t) &= \omega_x A_x \cos(\omega_x t + \theta_x) - V_f - V_r \cos(\phi_r) \\ V_y(t) &= \omega_y A_y \cos(\omega_y t + \theta_y) + V_r \sin(\phi_r) \end{aligned} \tag{73}$$

describe the velocity of tool tip. V_r is the rotation speed dependent on spindle rotation frequency and cutter size, and ϕ_r is rotation angle.

There are three types of tool-workpiece separation criteria that decide whether there is contact between tool and workpiece at the instant. The first two types are described by Equations (71)-(73). Type I criterion is satisfied when the cutting direction component of the relative velocity between tool and workpiece is opposite to the tool rotation direction [49, 100]. As shown in Figure 47(a), $V_n = -V_x \cos(\phi_r) + V_y \sin(\phi_r)$ is the resultant cutting speed based on Equation (73), while $V_{ul} = z'(t)$ is the ultrasonic vibration velocity in axial direction, β is the helix angle. In Figure 47(b), the component along the transverse direction decides the type I intermittent effect at it is perpendicular to the uncut surface. When this component is negative, which is oppose to the tool rotation direction, there is no contact between tool and workpiece as described by

Type I criterion
$$V_n \cos(\beta) - V_{ul} \sin(\beta) < 0 \tag{74}$$

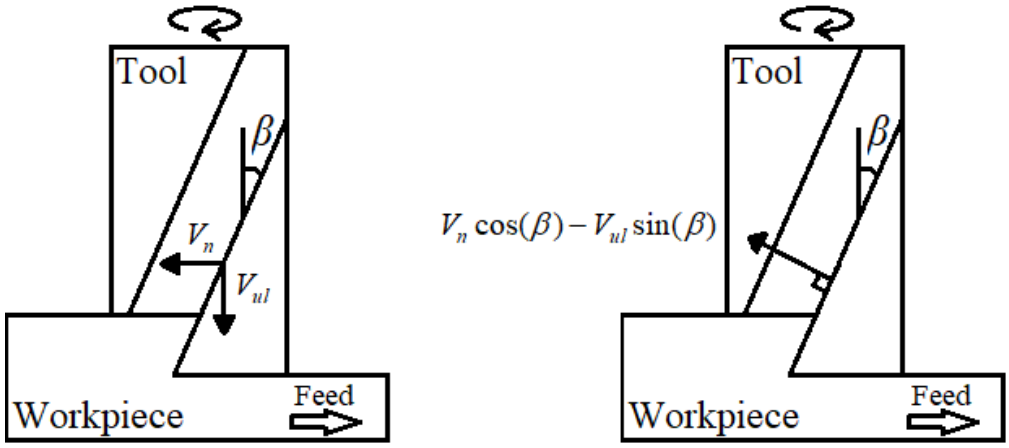

(a) (b)

Figure 47 Velocity at the tool tip due to tool rotation and ultrasonic vibration: (a) representation of V_n and V_{ul} at the cutting tip (b) resolved component at the tip

Type II criterion decides whether vibration displacement in the instantaneous cutting thickness direction (i.e., tool radial direction) is larger than the instantaneous uncut chip thickness. If the tool center is at a position where it is further away from the workpiece comparing to the initial position, tool and workpiece are separated even though Type I criterion is not satisfied. The criterion is mathematically expressed as

Type II criterion
$$x(t)\sin(\phi_r) + y(t)\cos(\phi_r) > t_{UVA,radial} \tag{75}$$

Type III criterion happens when the current tool path with vibration assistance overlaps in some regions with the surface contour left by previous cutting path(s). As shown in Figure 48(a), in conventional milling, the chip is continuous and has large thickness. While in ultrasonic vibration-assisted milling, much smaller and shorter chips are produced because of the overlaps between cutting paths as shown in Figure 48(b). Therefore, the chip thickness is recalculated considering the extra displacement from previous cutting path due to vibration as

Type III criterion
$$t_{UVA,radial} = t_c - \max\left[(A_x \sin(\phi_r)\sin(\omega_x t + \theta_x) + A_y \cos(\phi_r)\sin(\omega_y t + \theta_y)), 0\right] \tag{76}$$

where $t_{UVA,radial}$ and t_c are the instantaneous chip thickness with and without vibration.

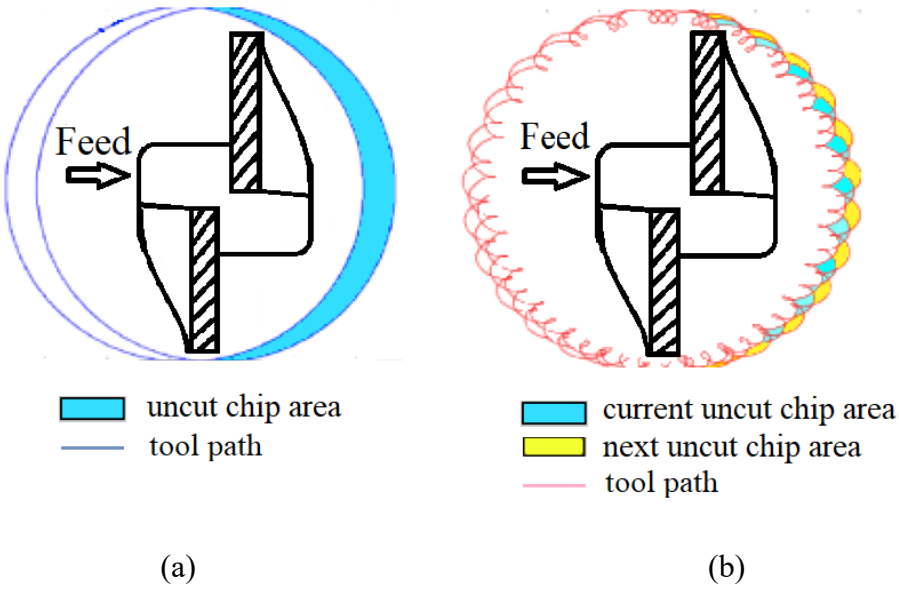

(a) (b)

Figure 48 Difference of chip thickness affecting cutting force reduction in (a) conventional and (b) vibration-assisted milling

Therefore, before the prediction of force, temperature, residual stress, tool wear rate, and surface roughness, the tool center trajectory is predicted, and the tool-workpiece separation criteria are checked. If there is no contact, the machining force, temperature rise, and tool wear rate are zero. If there is contact, the corresponding parameters are calculated based on instantaneous axial depth of milling $z(t)$, instantaneous feed rate $x'(t)$, and rotation speed V_r following the method introduced in CHAPTER 3.

5.2 Milling force

5.2.1 Experimental validation and results

The proposed predictive force model in ultrasonic vibration-assisted milling is validated through comparison to experimental measurements on Aluminum alloy 2A12 [140, 141]. The experiments are performed on five-axis high-speed CNC machining center. The ultrasonic generator and vibrator convert high-frequency oscillation electric energy

into workpiece vibration along the feed direction. The dynamic cutting force signals are gathered through dynamometer. The cutting tool is a two-flute end mill made of cemented carbide. The diameter is 2 mm, and the helix angle is 30°. The feed per tooth is 3 μm, the spindle rotation frequency is 1,000 r/min, and the axial depth of milling is 0.2 mm. For ultrasonic vibration, the vibration frequency is 19.58 kHz, and four slot-milling experiments are conducted with vibration amplitude of 0 (conventional milling), 4, 6, and 8 μm, respectively.

The machining forces in feed and cutting directions are calculated in analytical model between a rotation angle of 0° and 180°. If the tool-workpiece separation criterion is met, both forces are recorded as zero. Otherwise, the forces are calculated based on methodology described in section two. The original predicted force profiles are shown in Figure 49 with ten data points within one ultrasonic vibration period. The number of force data points predicted is later reduced to accommodate the number of measurements limited by the sampling frequency of dynamometer. The values of the parameters (A, B, C, m, and n) for the Aluminum alloy are 243.0, 618.8, 0.01, 1.6, and 0.2, respectively [142]. Figure 50 shows single-sided amplitude spectrums of measured as well as predicted F_x and F_y when vibration amplitude is 8 μm in half cutting cycle. The sampling frequency is 1,750 Hz for dynamometer. The fast Fourier transform of both experimental and predicted data shows presence of vibration around 1,750 Hz due to intermittent cutting effect under the sampling frequency. Another peak is observed at 0 Hz occurring due to tool engagement. The predicted spectrums in Figure 50(b) and (d) have more low frequency components since forces are considered zero when there is no contact between tool and workpiece, while measured force signals still have nonzero values at valleys. In addition, measured

spectrums in Figure 50(a) and (c) have more high frequency components as a result of noise such as tool chatter. Overall, the predicted force amplitude spectrums have good agreements with experimental measurements on both feed and cutting forces.

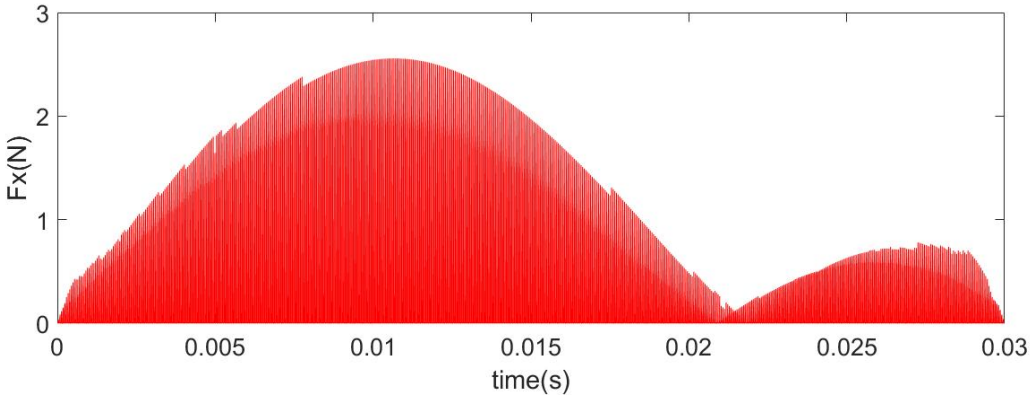

(a)

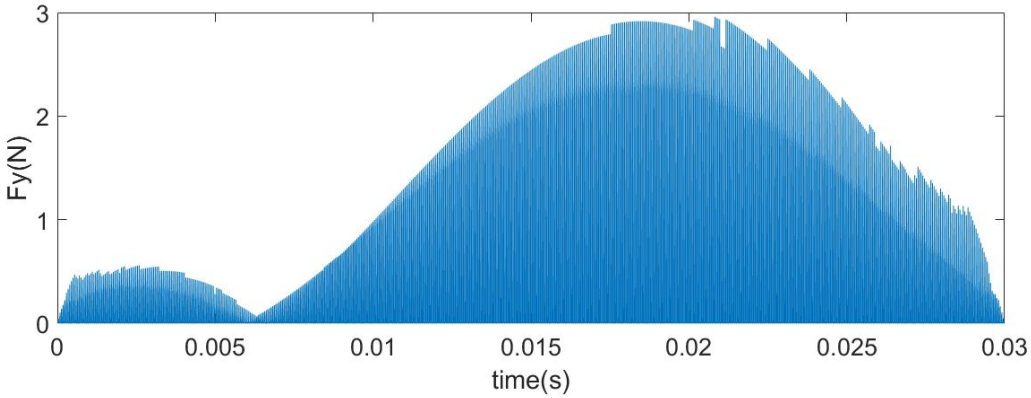

(b)

Figure 49 Predicted force profiles of (a) Fx and (b) Fy when vibration amplitude is 8 μm in half cutting cycle

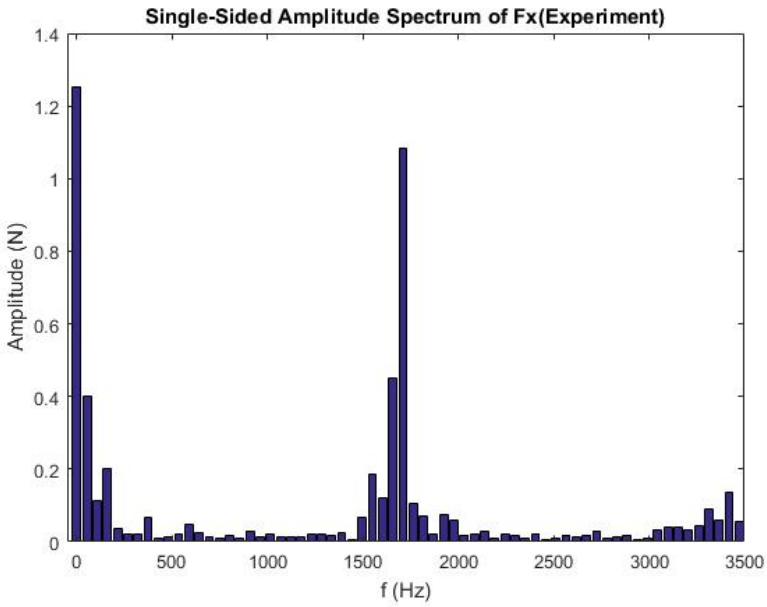
Single-Sided Amplitude Spectrum of Fx(Experiment)
Amplitude (N)
f (Hz)
0
0.2
0.4
0.6
0.8
1
1.2
1.4
0
500
1000
1500
2000
2500
3000
3500

(a)

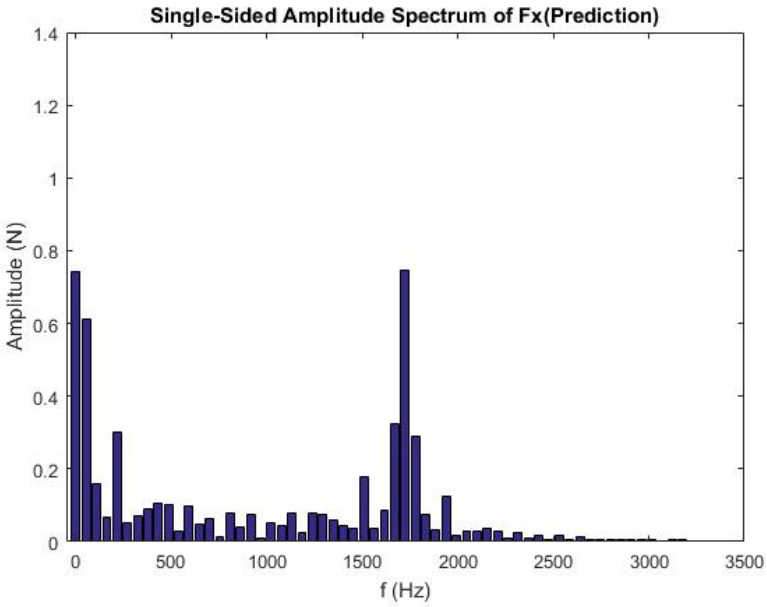
Single-Sided Amplitude Spectrum of Fx(Prediction)
Amplitude (N)
f (Hz)
0
0.2
0.4
0.6
0.8
1
1.2
1.4
0
500
1000
1500
2000
2500
3000
3500

(b)

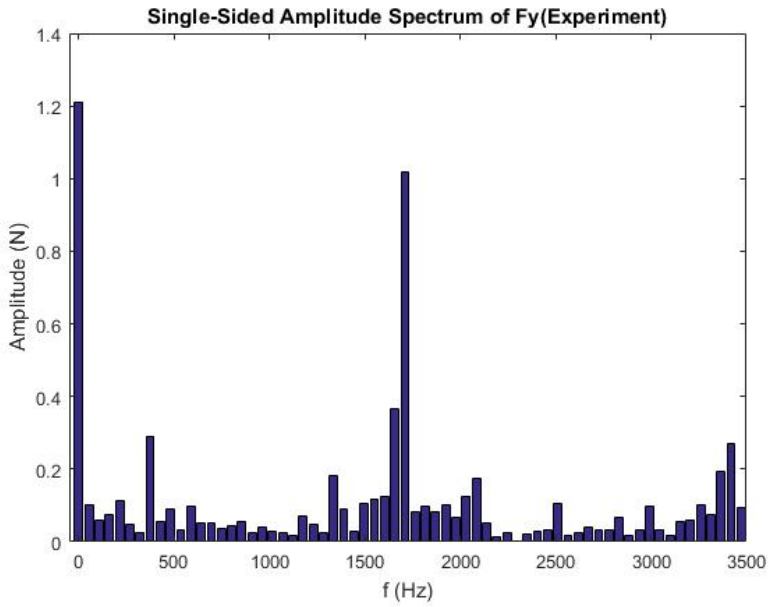

(c)

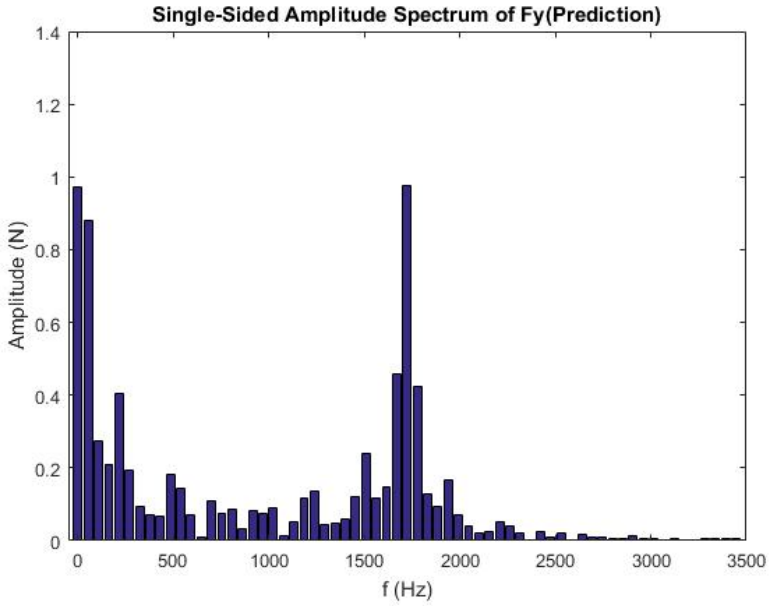

(d)

Figure 50 Comparison of single-sided amplitude spectrum of Fx between (a) experiment and (b) predictive model, Fy between (c) experiment and (d) predictive model, during ultrasonic vibration-assisted milling with 8 µm amplitude [141]

Figure 51 shows the average cutting forces from experiments and predictive model under four different vibration amplitudes. The average forces are 1.93 and 1.7 N for conventional milling in feed and cutting directions. With a vibration amplitude of 4 µm, the average forces in two directions are 1.17 and 1.1 N, respectively. The average values decrease by 39% in feed direction and 35% in cutting direction when the ultrasonic vibration is applied. In addition, the measured forces keep dropping gradually when the amplitude increases, since the tool-workpiece separation time is longer under higher vibration amplitude. The drop rate is approximately a constant as the average forces decrease linearly. The feed force is changing from 1.17 to 1.09 followed by 1.05 N as ultrasonic vibration amplitude increases from 4 to 6 and 8 µm. Similarly, the cutting force is changing from 1.1 to 1.05 followed by 0.98 N as ultrasonic vibration amplitude increases from 4 to 6 and 8 µm.

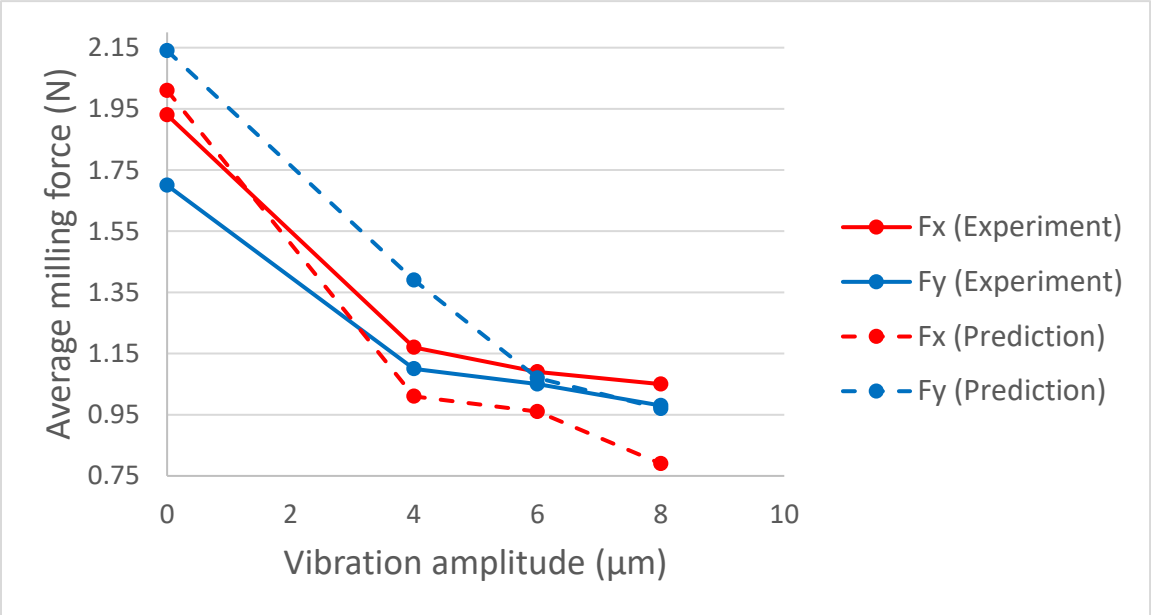

Figure 51 Comparison of average milling forces with different vibration amplitudes[141]

The predicted average forces are plotted as dashed lines in Figure 51. For conventional milling, both predicted forces are higher than measurements. In feed direction, the predicted value is 2.01 N which is 4.15% higher. In cutting direction, the prediction is 2.14 N and the error is 25.88% which is acceptable comparing with previous established conventional milling force predictive model [126]. When the ultrasonic vibration is applied, the average values decrease by 50% in feed direction and 35% in cutting direction. The feed force is changing from 1.01 to 0.96 followed by 0.79 N as ultrasonic vibration amplitude increases from 4 to 6 and 8 μm. Similarly, the cutting force is changing from 1.39 to 1.07 followed by 0.97 N as ultrasonic vibration amplitude increases from 4 to 6 and 8 μm. The maximum error in all cases is less than 27%. Overall, the proposed force prediction model is able to match the trend with average error of 13.6% in F_x and 13.8% in F_y.

5.2.2 Sensitivity analysis

In order to appreciate the proposed predictive model, sensitivity analysis is conducted to estimate average forces under the effects of different cutting and ultrasonic parameters including axial depth of milling, feed per tooth, ultrasonic frequency, and spindle rotation frequency. The ultrasonic vibration amplitude is fixed at 6 μm, and other parameters are the same as in 5.2.1. As shown in Figure 52(a), a higher axial depth of milling will significantly increase the milling forces in both directions. F_x and F_y are doubled from 0.96 and 1.07 N to 1.92 and 2.14 N when the axial depth of milling changes from 0.2 to 0.4 mm. The axial depth of milling decides the cutting width according to Equation (4). With the increase of cutting width, the contact area is also expanded resulting in higher forces under same flow stress. Similarly, a doubled feed per tooth from 3 to 6 μm

also approximately doubles F_x and F_y from 0.96 and 1.07 N to 1.88 and 2.20 N because of larger chip thickness according to Equation (1), as shown in Figure 52(b). On the other hand, when the ultrasonic vibration frequency increases, the cutting speed is higher, leading to decreased milling forces. F_x and F_y are 25.4% and 15.0% smaller when the ultrasonic vibration frequency increases by 28.6% as depicted in Figure 52(c). The spindle rotation frequency also decides cutting speed. F_x and F_y are 28.7% and 13.2% smaller when the spindle rotation frequency increases by 250% as depicted in Figure 52(d). The results of sensitivity analysis are in good agreement with conclusions from Verma *et al.* [90].

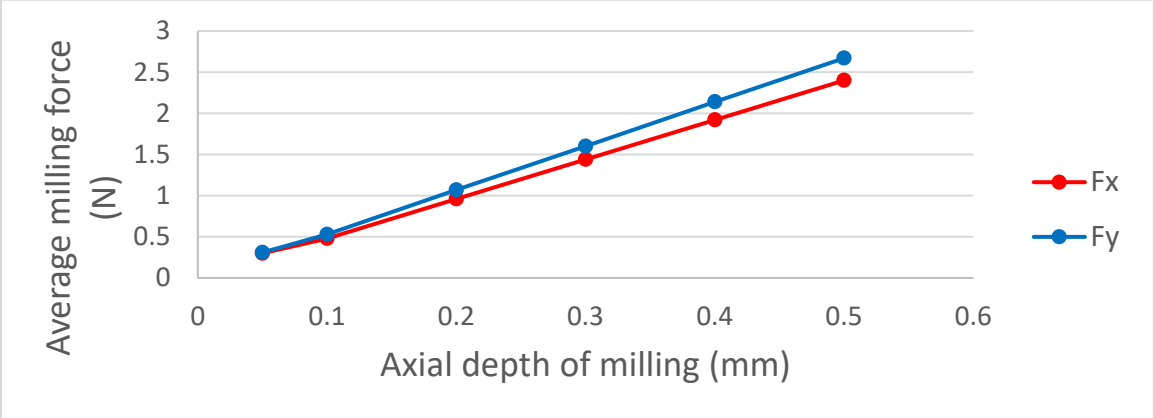

(a)

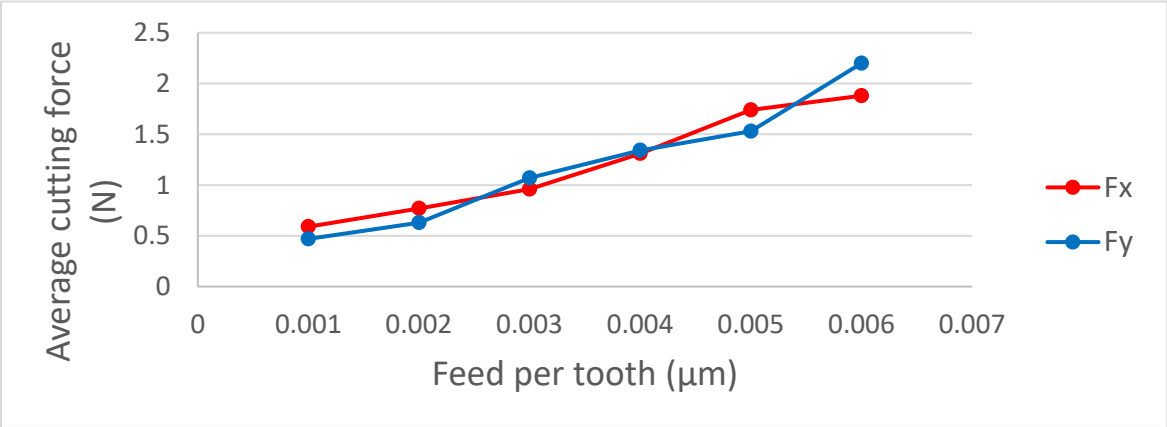

(b)

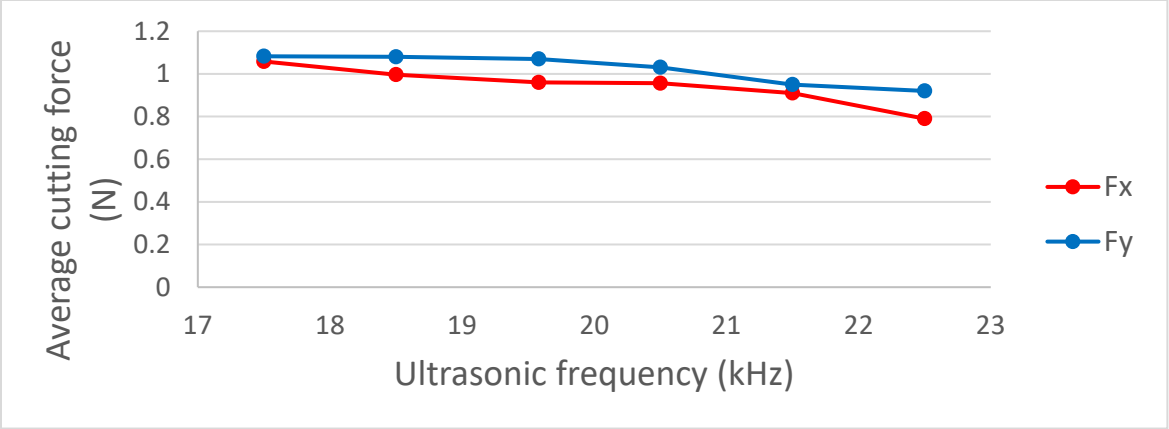

(c)

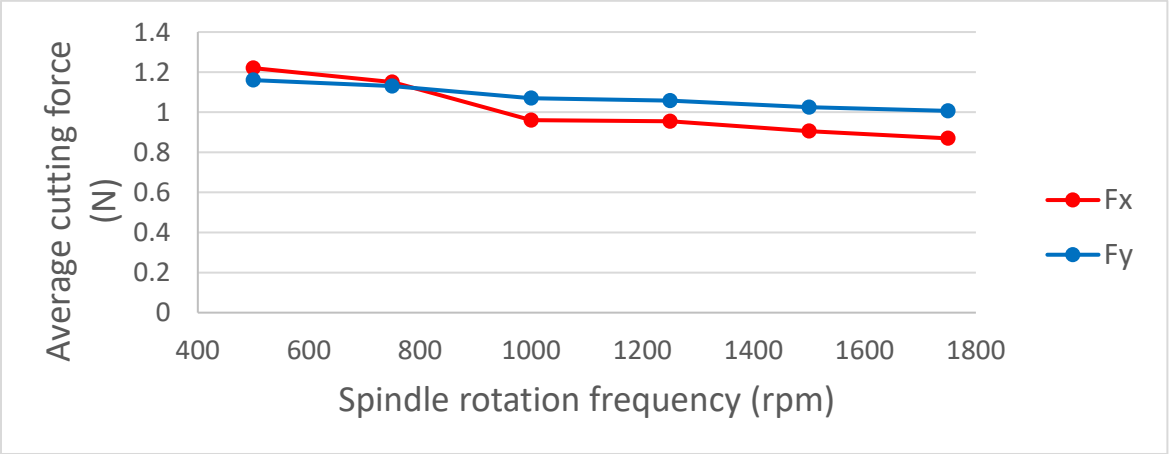

(d)

Figure 52 The change of predicted forces under the effect of different cutting and vibration parameters (a) axial depth of milling (b) feed per tooth (c) ultrasonic frequency (d) spindle rotation frequency

5.3 Temperature

5.3.1 Experimental validation and results

The proposed predictive temperature model in ultrasonic vibration-assisted milling is validated through comparison to experimental measurements on Al 6063 alloy [143]. The experiments are conducted on a CNC milling machine. The electric energy with high-frequency oscillation is converted into vibration of milling tool along the axial direction. The peak temperature is measured through K type thermocouple wire. A four-flute HSS

milling tool is used with a diameter of 3 mm, a rake angle of 10°, and a helix angle of 30°. The vibration frequency f_0 is 20 kHz for all experiments. Several slot-milling experiments are conducted under three levels of spindle rotation frequency (1590, 2650, and 3710 rpm), axial depth of milling (0.4, 0.8, and 1.2 mm), feed per tooth (0.01, 0.02, and 0.03 mm), and ultrasonic vibration amplitude (9, 15, and 20 μm), as shown in Figure 53.

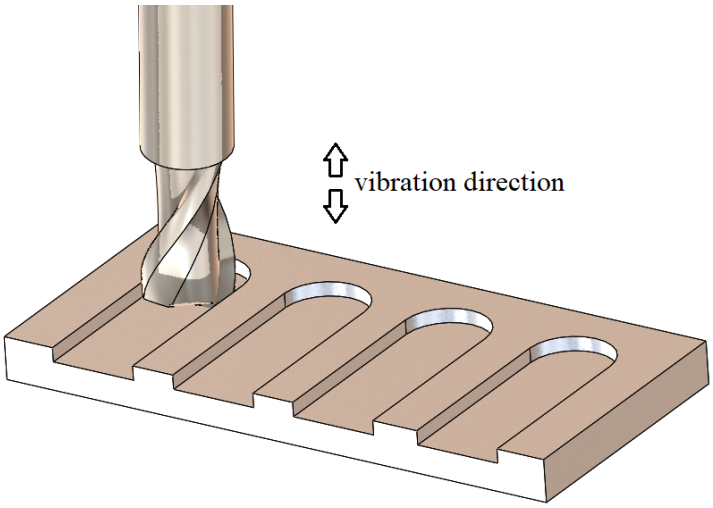

Figure 53 Schematic of slot-milling process

The peak temperature is recorded in analytical model at a rotation angle of 90°. If any tool-workpiece separation criterion is met, milling forces are zero, and no heat source will be present to raise the temperature. Otherwise, the temperature field is calculated based on methodology described in 3.2.2. The overall flow chart of predictive model is shown in Figure 54. The average forces within one ultrasonic vibration period around 90° rotation angle are used to calculate the temperature. Figure 55 shows the predicted temperature field under three different spindle rotation frequency, under an axial depth of milling of 0.8 mm, a feed per tooth of 0.02 mm, and an ultrasonic vibration amplitude of 15 μm. The peak temperature is recorded right in front of the tool tip and drops quickly to initial temperature for uncut workpiece surface. The machined workpiece surface remains high temperature due to rubbing heat source at tool-workpiece interface. It is observed from Figure 55(a) to (c) that the increased spindle rotation frequency will increase the peak temperature as the increased cutting speed will lead to higher heat source density as seen in Equations (20) and (22).

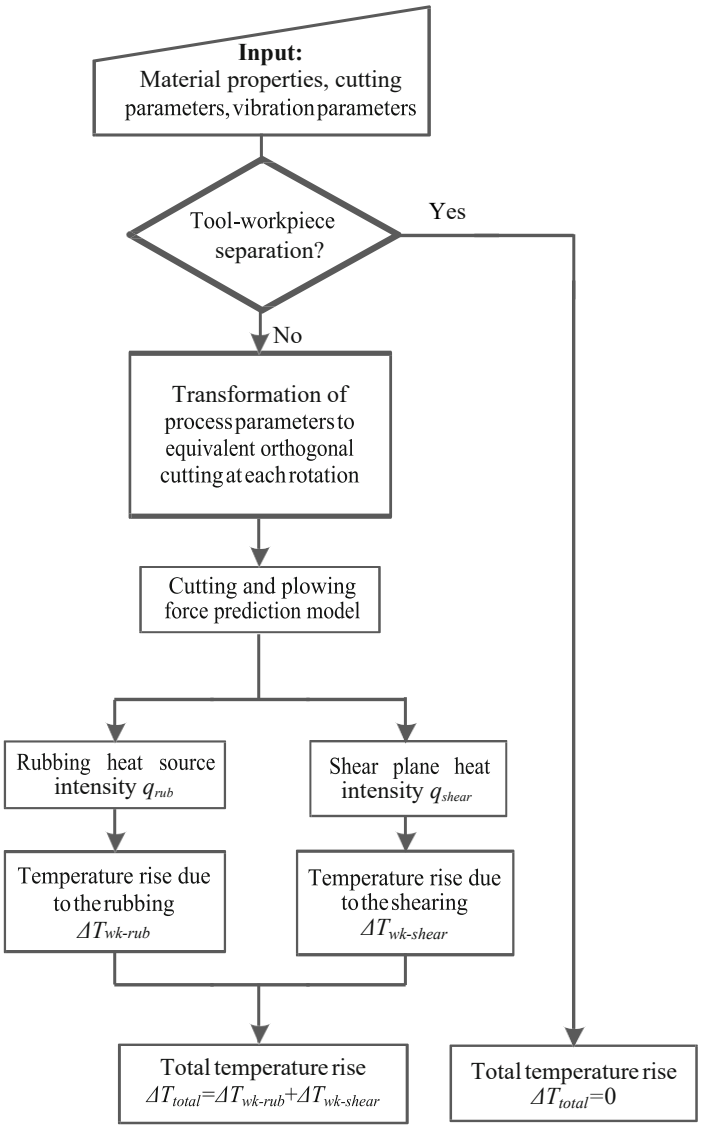

Figure 54 Overall flow chart of predictive model for temperature in ultrasonic vibration-assisted milling

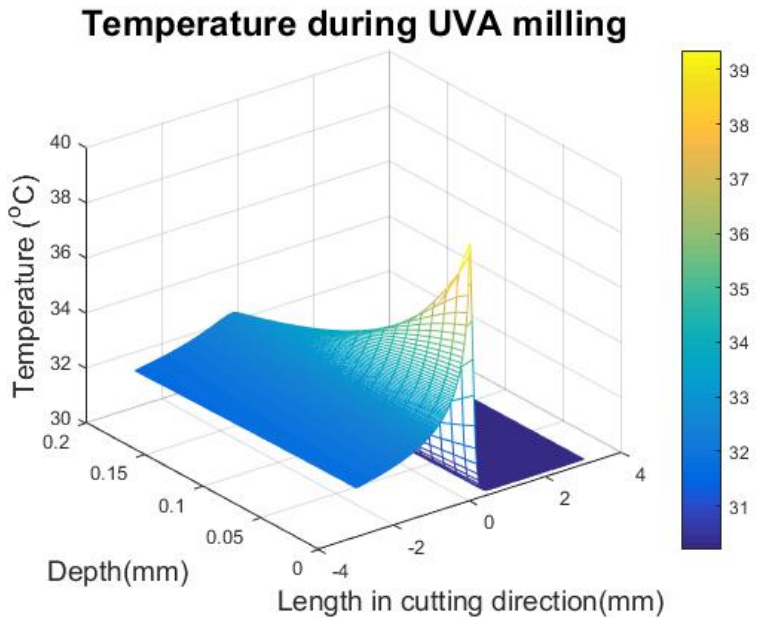
Temperature during UVA milling
Temperature (°C)
40
38
36
34
32
30
0.2
0.15
0.1
0.05
0
Depth(mm)
-4
-2
0
2
4
Length in cutting direction(mm)
39
38
37
36
35
34
33
32
31

(a)

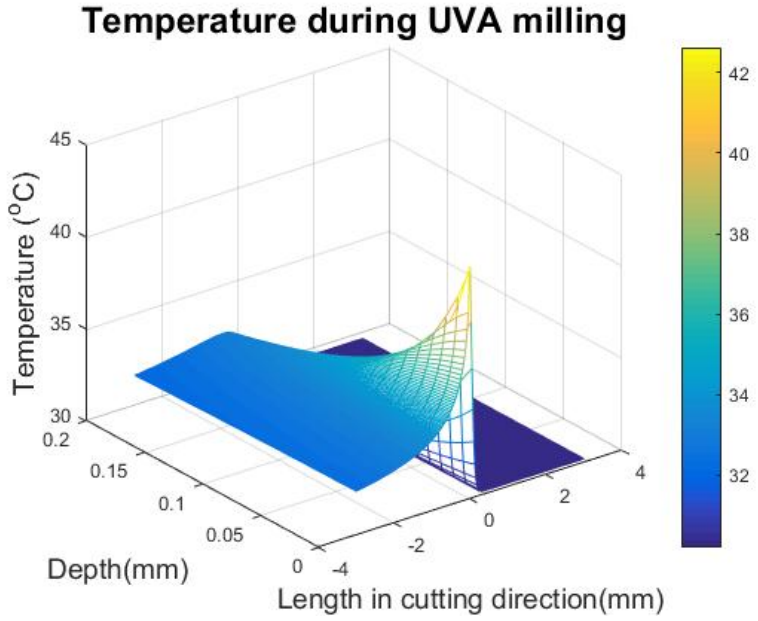
Temperature during UVA milling
Temperature (°C)
45
40
35
30
0.2
0.15
0.1
0.05
0
Depth(mm)
-4
-2
0
2
4
Length in cutting direction(mm)
42
40
38
36
34
32

(b)

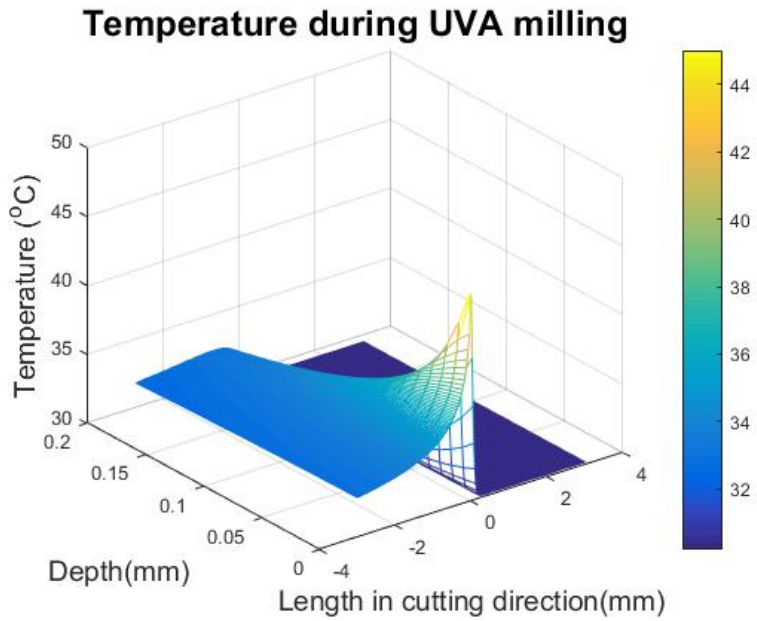

(c)

Figure 55 Predicted temperature field during ultrasonic vibration-assisted (UVA) milling at spindle rotation frequency of (a) 1590 rpm, (b) 2650 rpm, and (c) 3710 rpm

Figure 56 shows the comparison of peak temperature between experiments and predictive model under various cutting and vibration parameters. In Figure 56(a), the predicted highest temperatures based on Figure 55 are 39.4, 42.6, and 45.0 ℃, under spindle rotation frequency of 1590, 2650, and 3710 rpm, respectively. The corresponding measured temperatures are 40.3, 43, and 44.5 ℃. A close match is found with maximum error of 2.36% and average error of 1.46%. In Figure 56(b), three temperatures are measured at increasing axial depth of milling under a spindle rotation frequency of 2650 rpm, a feed per tooth of 0.02 mm, and an ultrasonic vibration amplitude of 15 μm. According to Equations (20) and (22), a larger axial depth of milling will increase both milling and plowing forces, which lead to higher heat source density. The analytical model is able to predict the peak temperature accurately with average error of 1.14% and

maximum error of 2.35%. As shown in Figure 56(c), similar to spindle rotation frequency, an increase of feed per tooth will also increase the cutting speed, which further results in higher heat source density. The measured temperatures are 41.6, 43, and 45.6 ℃ under feed per tooth of 0.01, 0.02, and 0.03 mm. The largest difference is found to be 5.22% between experiment and predictive model under high feed rate, while the average error is 3.05%. Lastly, as shown in Figure 56(d), the measured temperature is 45.8 ℃ at low ultrasonic vibration amplitude of 9 μm. The temperature drops to 41.5 ℃ as the amplitude increases to 20 μm. Under higher vibration amplitude, there is a higher chance for Type I or II tool-workpiece separation criterion to be triggered. Therefore, the effective cutting time within one ultrasonic vibration period is shorter which leads to lower peak temperature. Again, the predictive model is able to catch this trend with largest error of 3.49% and average error of 1.73%. Overall, the proposed temperature predictive model has high accuracy of 1.85% average error and 5.22% largest error among all cases.

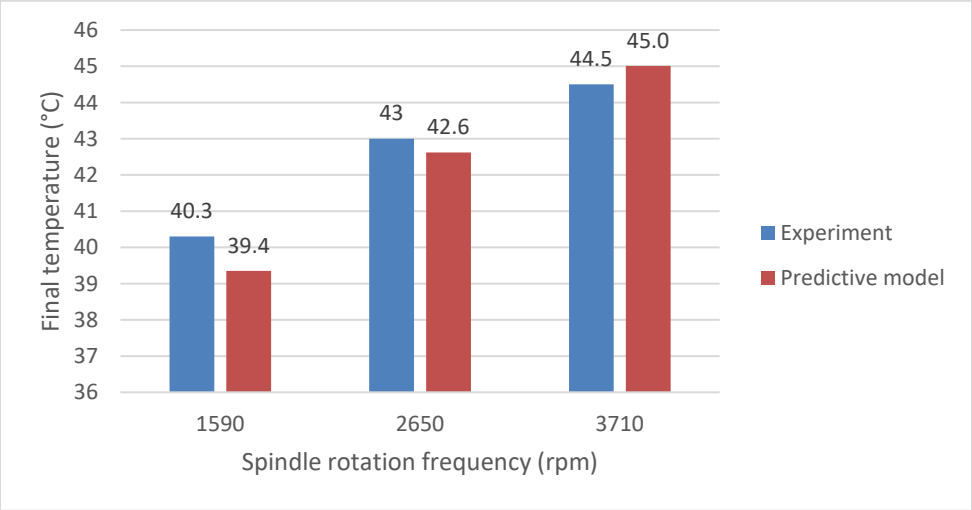

(a)

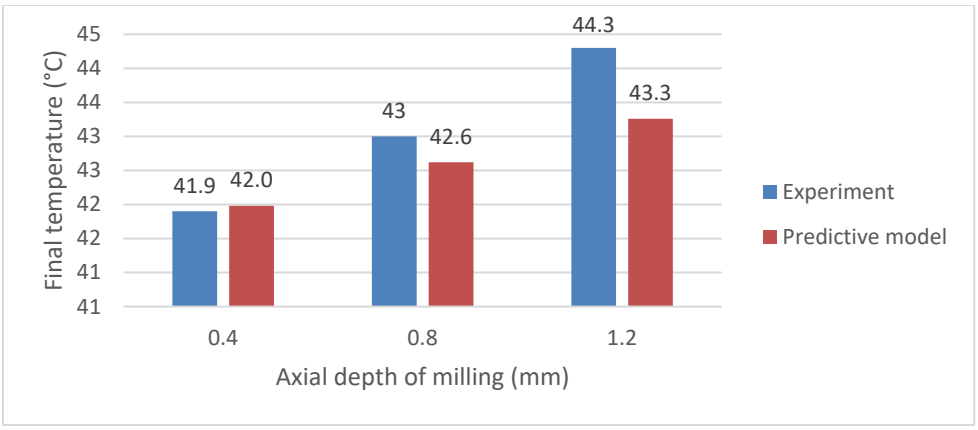

(b)

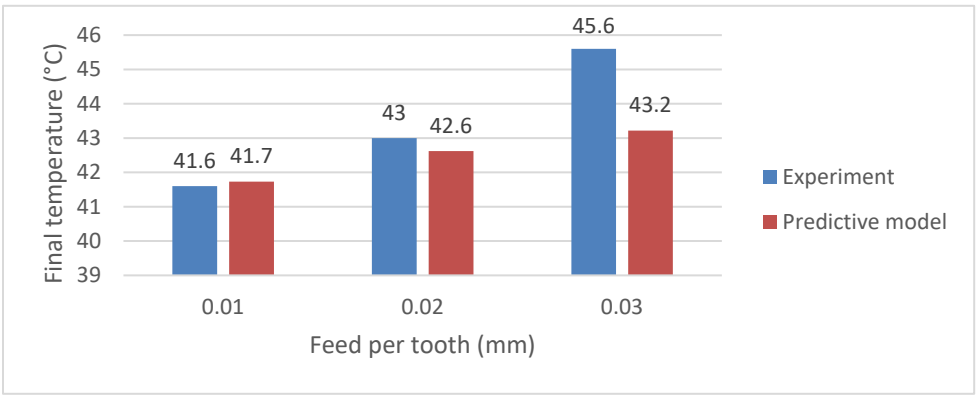

(c)

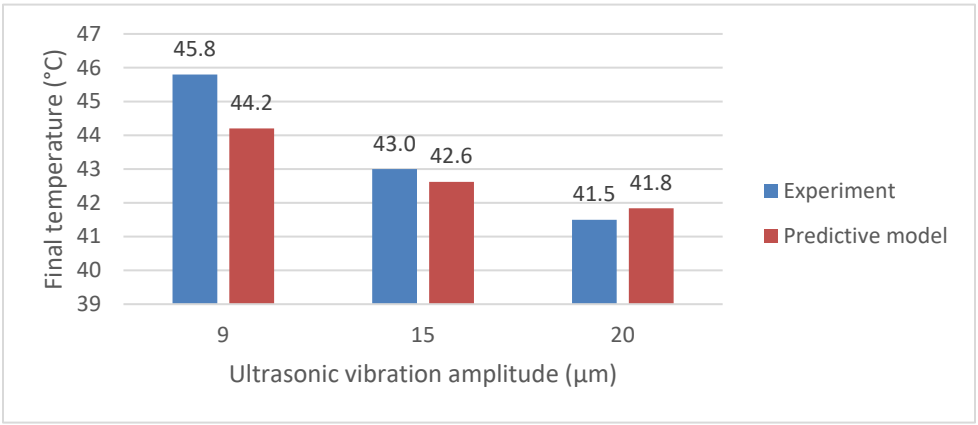

(d)

Figure 56 Comparison of peak temperature with different (a) spindle rotation frequency, (b) axial depth of milling, (c) feed per tooth, and (d) vibration amplitude [143]

5.3.2 Sensitivity analysis

In order to appreciate the proposed predictive model, sensitivity analysis is conducted to estimate peak temperature under the effects of different cutting and ultrasonic parameters including axial depth of milling, feed per tooth, spindle rotation frequency, ultrasonic vibration amplitude, and ultrasonic vibration frequency. All other parameters are the same as in Sec. three. As shown in Figure 57(a), a higher axial depth of milling from 0.2 to 1.4 mm will increase the temperature from 41.7 to 43.5 ℃. Similarly, under a feed per tooth of 0.005 mm, the predicted temperature is 40.6 ℃, while a larger feed of 0.035 mm per tooth results in higher temperature of 43.8 ℃, as shown in Figure 57(b). For axial depth of milling and feed per tooth, an increase of parameter by 700% will increase the temperature by 4.3% and 7.9%, respectively. Therefore, both factors have an approximate same levels of significance on temperature. In Figure 57(c), the spindle rotation frequency increases from 500 to 5000 rpm, and the temperature keeps increasing accordingly from 35.1 to 47.7 ℃, which is more than 35%. The influence of spindle rotation frequency is therefore more dominant on temperature comparing to two previous cutting parameters, which is the same as in conventional milling [144]. For vibration parameters, higher ultrasonic vibration amplitude will continuously lead to lower temperature as depicted in Figure 57(d). For ultrasonic vibration frequency, higher frequency will increase the cutting speed but lower the cutting forces, which results in lower peak temperature for Al 6063 alloy as shown in Figure 57(e).

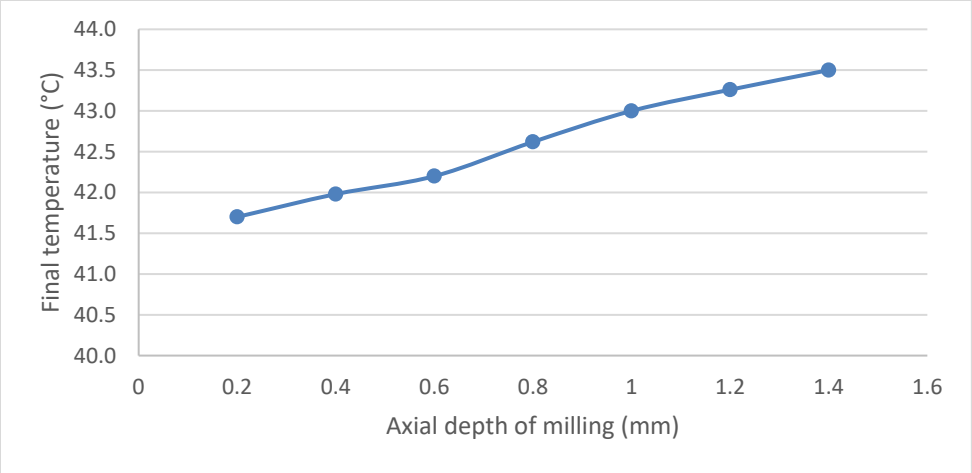
Final temperature (°C)
44.0
43.5
43.0
42.5
42.0
41.5
41.0
40.5
40.0
0
0.2
0.4
0.6
0.8
1
1.2
1.4
1.6
Axial depth of milling (mm)

(a)

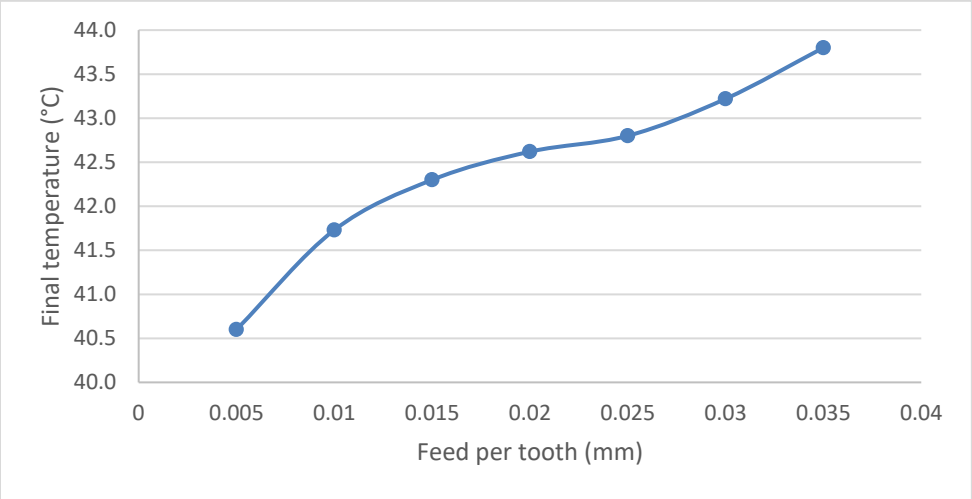
Final temperature (°C)
44.0
43.5
43.0
42.5
42.0
41.5
41.0
40.5
40.0
0
0.005
0.01
0.015
0.02
0.025
0.03
0.035
0.04
Feed per tooth (mm)

(b)

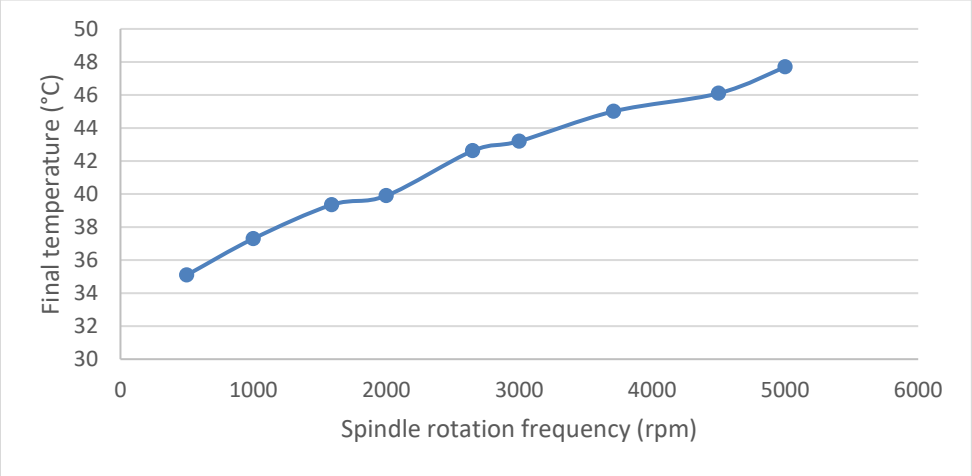
Final temperature (°C)
50
48
46
44
42
40
38
36
34
32
30
0
1000
2000
3000
4000
5000
6000
Spindle rotation frequency (rpm)

(c)

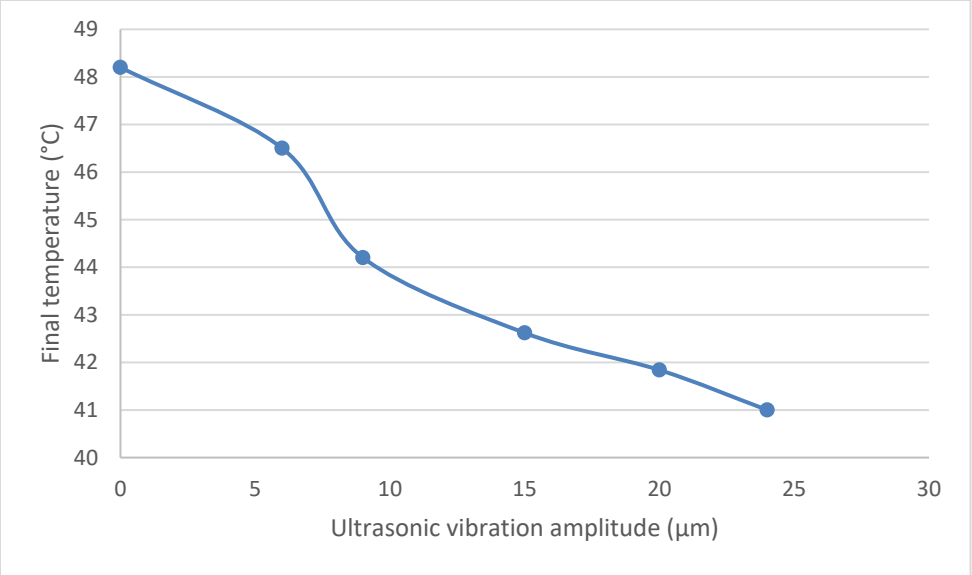

(d)

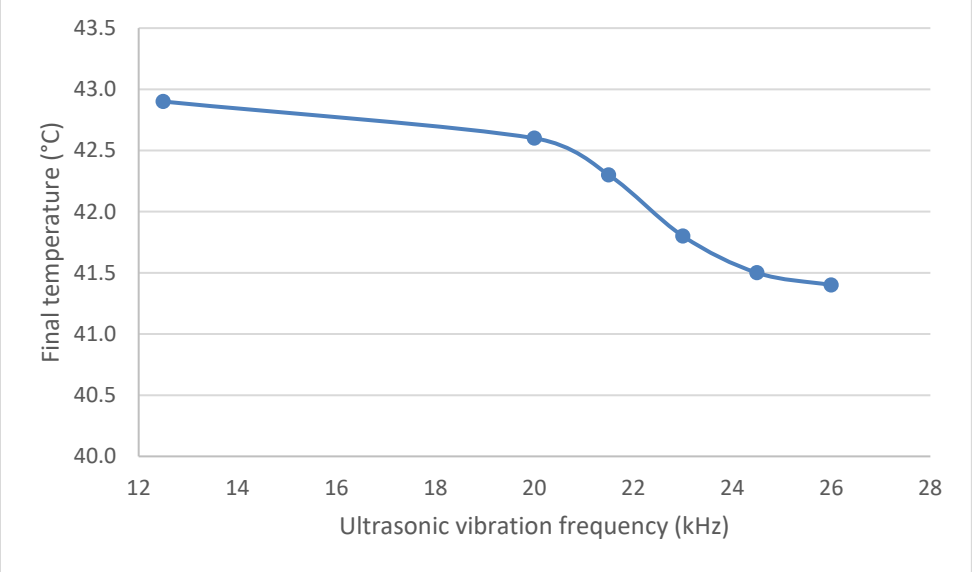

(e)

Figure 57 The change of predicted temperature under the effect of different cutting and vibration parameters (a) axial depth of milling, (b) feed per tooth, (c) spindle rotation frequency, (d) ultrasonic vibration amplitude, and (e) ultrasonic vibration frequency

5.4 Residual stress

5.4.1 Experimental validation and results

The proposed predictive residual stress model in ultrasonic vibration-assisted milling is validated through comparison to experimental measurements on AISI 316L alloy [145]. The experiments are performed on a 5-axis CNC milling machine. The spindle of the machine is monolithic and comprises the piezo-electric actuator, concentrating horn and tool holder. Vibration is generated by the actuator in a co-axial direction to the axis of the spindle. A cemented carbide tool is used with a diameter of 5 mm, a rake angle of 10.5°, with four flutes and TiAlN coating. Several slot-milling experiments are conducted as shown in Figure 53, with a spindle rotation frequency of 2,000 rpm, an axial depth of milling of 8 mm, and an ultrasonic vibration amplitude of 11 μm. Two key process parameters, feed per tooth and ultrasonic vibration frequency, are varied under different levels. Residual stress is measured under seven levels of feed per tooth (0.0066, 0.00825, 0.011, 0.0132, 0.0165, 0.0198, and 0.022 mm) and four levels of ultrasonic vibration frequency (0, 20, 40, and 60 kHz). Residual stress measurements are carried out on a Proto iXRD combo residual stress analyser.

Measured stresses are compressive for all test specimens, and the maximum surface residual stress is recorded as shown in Figure 58(a). The most compressive residual stress of 460 MPa is observed at the lowest feed per tooth of 0.0066 mm during conventional milling. The residual stress keeps moving toward tensile direction as the feed per tooth increases under all ultrasonic vibration frequencies. When the feed per tooth increases by 233% from 0.0066 to 0.022 mm, the residual stress decreases from 460 to 325 MPa during conventional and from 405 to 270 MPa when the frequency is 40 kHz. The decrease of residual stress is 32% in average. On the other hand, when the ultrasonic vibration is applied, the residual stress also becomes more tensile. The average residual stress is 397.1

MPa during conventional milling, while the value drops to 342.1 and 375.7 MPa when the frequency is 40 and 60 kHz, respectively. It is observed that the lowest average residual stress is measured at 40 kHz with 14.05% lower than that at 0 kHz frequency, while the residual stress becomes more compressive as the frequency keeps increasing to 60 kHz with only 5.5% lower average residual stress comparing to conventional milling.

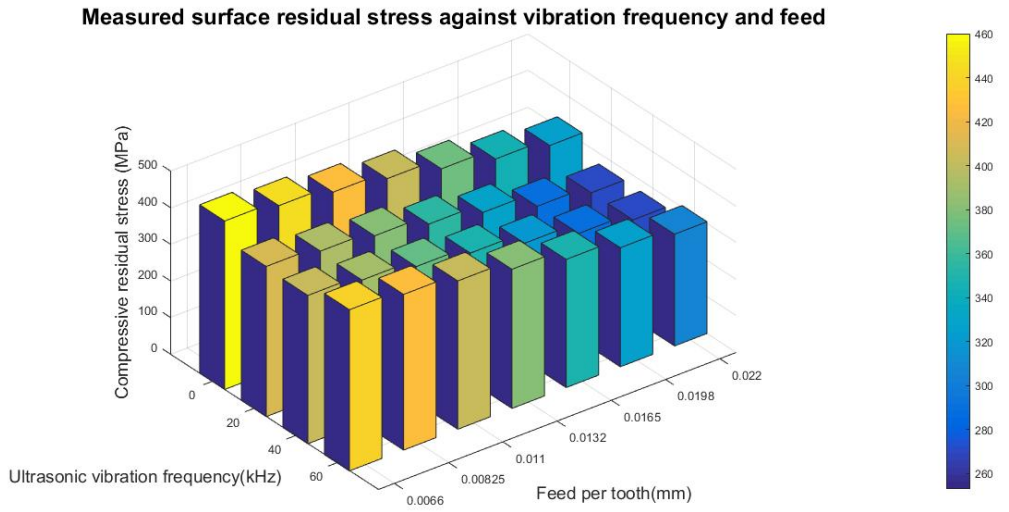

(a)

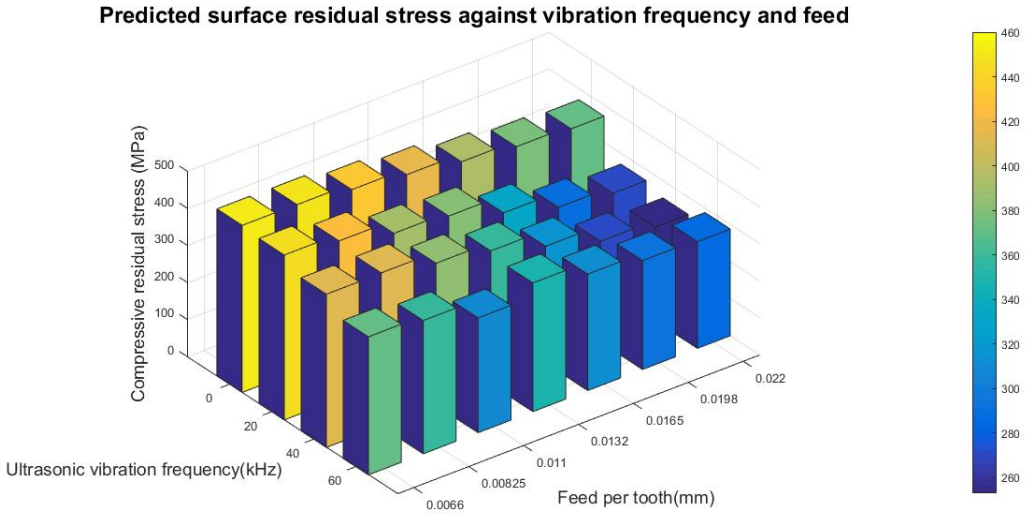

(b)

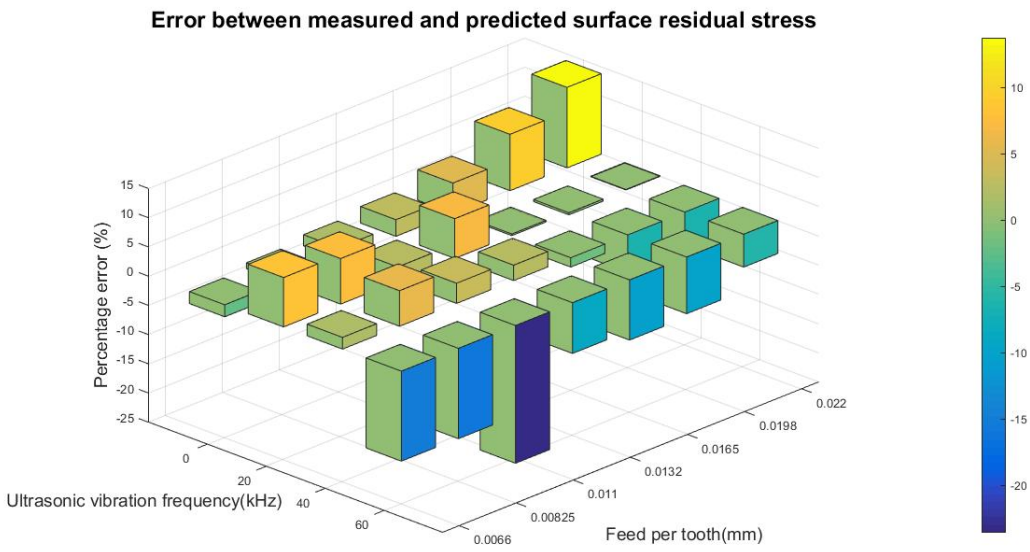

(c)

Figure 58 (a) Measured [145] and (b) predicted surface residual stress against vibration frequency and feed, and (c) comparison through error

The maximum surface residual stress is recorded in analytical model at a rotation angle of 90°. If any tool-workpiece separation criterion is met, milling forces are assumed as zero, and no heat source is present to raise the temperature. Therefore, both mechanical and thermal stresses are zero. Otherwise, the residual stress is calculated based on methodology described in section two. The average forces within one ultrasonic vibration period around 90° rotation angle are used to calculate mechanical stresses and temperature field for thermal stresses. Figure 58(b) shows the predicted maximum surface residual stress under same seven different feed per tooth and four different ultrasonic vibration frequency. The most compressive surface residual stress of 450.6 MPa is predicted at feed per tooth of 0.0066 mm and frequency of 0 kHz. The prediction follows the same trend as the measurement with a higher feed per tooth leading to less compressive residual stress. When the feed increases, the machining temperature becomes higher, which results in more

softening of the workpiece and less compressive residual stress. The average drop of residual stress is 29.6% when the feed per tooth increases from 0.0066 to 0.022 mm. Under same feed per tooth, the increase of ultrasonic vibration frequency will lead to both lower milling forces and temperature field. At low frequency from 0 to 40 kHz, force is the dominant factor for AISI 316L alloy as the less mechanical stress results in less hardening of the workpiece and less compressive residual stress. At high frequency from 40 to 60 kHz and high feed per tooth of 0.0198 and 0.022 mm, temperature effect becomes more significant, and lower temperature brings less softening of the workpiece and the predicted surface residual stress gets more compressive again. As shown in Figure 58(c), good agreements are found between predictions and measurements for all cases with an average error of 6.4% and maximum error of 23.6%.

5.4.2 Sensitivity analysis

In order to appreciate the proposed predictive model, sensitivity analysis is conducted to estimate maximum surface residual stress under the effects of different cutting and ultrasonic parameters including axial depth of milling, ultrasonic vibration amplitude, and spindle rotation frequency. All other parameters are the same as in section three with ultrasonic vibration frequency of 40 kHz and feed per tooth of 0.0132 mm. As shown in Figure 59(a), a higher axial depth of milling from 2 to 14 mm will decrease the residual stress from 413.4 to 353.9 MPa. A larger axial depth of milling will increase both milling and plowing forces, which lead to higher heat source density. Therefore, higher temperature will soften the material leading to more tensile residual stress. As shown in Figure 59(b), a higher ultrasonic vibration amplitude from 11 to 80 μm will increase the residual stress from 359.2 to 467.5 MPa. Under higher vibration amplitude, there is a higher

chance for either Type I or II tool-workpiece separation criterion to be triggered. Therefore, the effective cutting time within one ultrasonic vibration period is shorter which leads to lower temperature field and less softening of the workpiece. As shown in Figure 59(c), a higher spindle rotation frequency from 500 to 3500 rpm will increase the compressive residual stress from -9.7 to 419.6 MPa. A higher spindle rotation frequency will increase the cutting speed and lower milling forces, which lead to smaller heat source density. Therefore, decreased temperature field will soften the material less leading to more compressive residual stress.

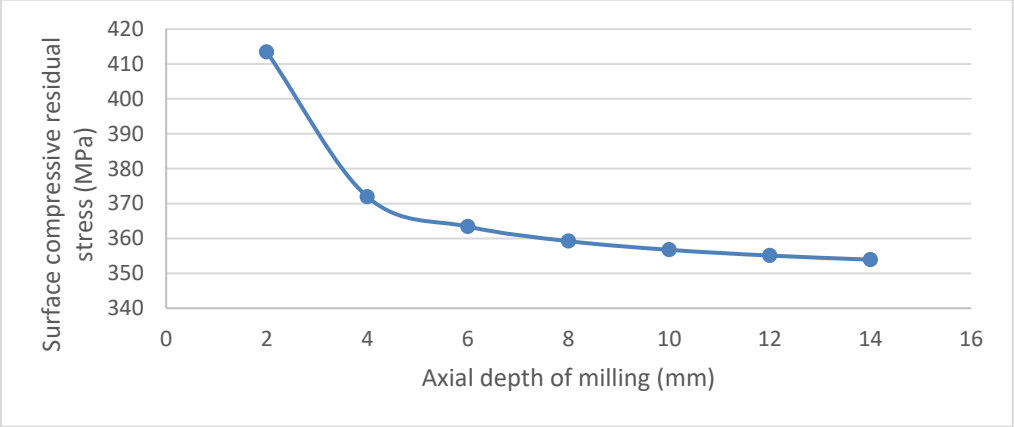

(a)

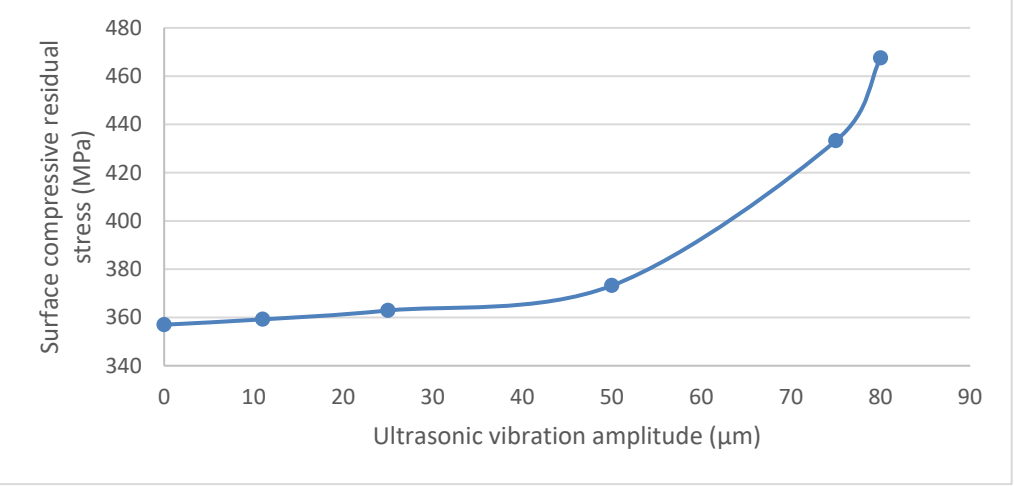

(b)

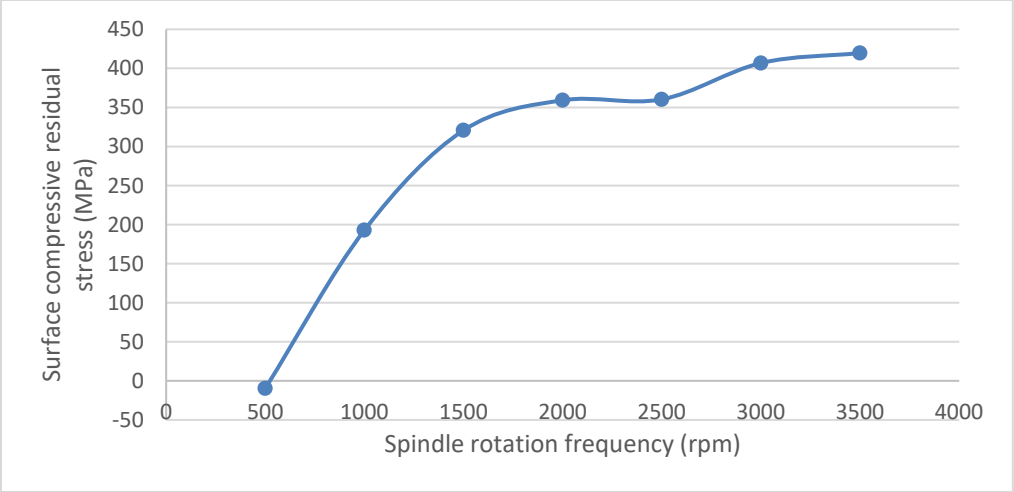

(c)

Figure 59 The variation of predicted surface residual stress with respect to different cutting and vibration parameters (a) axial depth of milling, (b) ultrasonic vibration amplitude, and (c) spindle rotation frequency

5.5 Tool flank wear rate

As shown in Figure 60(a), the predicted wear rate shows the intermittent contact between tool and workpiece, and the predicted tool wear grows gradually similar to a step graph as shown in Figure 60(b). In current study, all predicted tool wear rates are the average wear rate calculated within one tool rotation period.

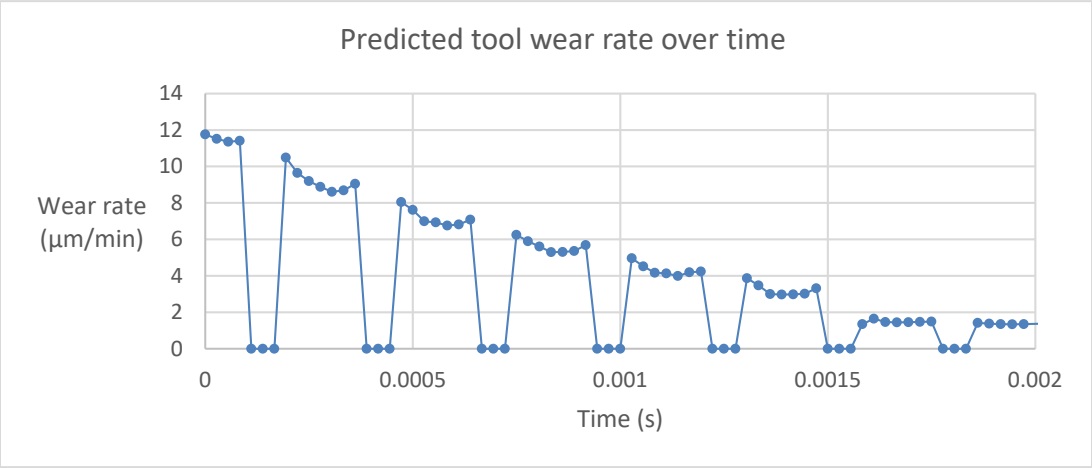

(a)

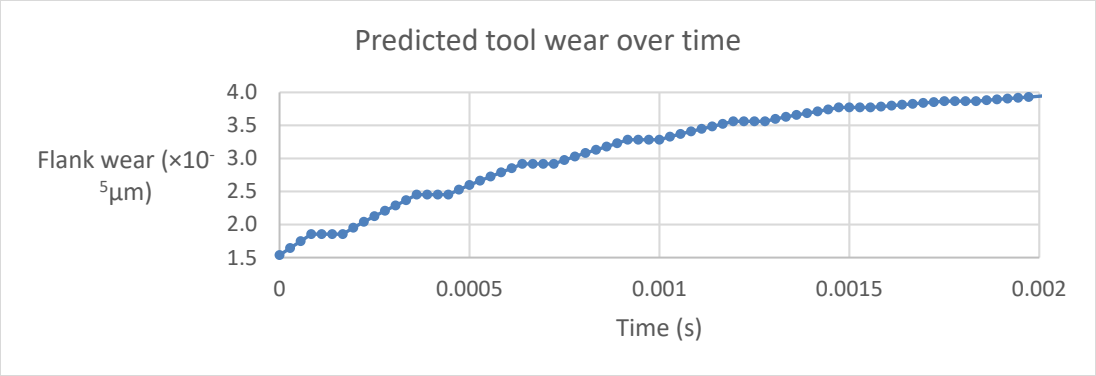

(b)

Figure 60 Predicted (a) tool wear rate and (b) tool wear over time

5.5.1 Experimental validation and results

The proposed predictive flank tool wear rate model in ultrasonic vibration-assisted milling is validated through comparison to experimental measurements on SKD 61 steel with uncoated carbide tool [146]. The experiments are performed on a DMG Ultrasonic 50 milling machine. The spindle unit provides vibrations in a co-axial direction to the axis of the spindle with a resonant frequency of 18.0 kHz and an amplitude of 2.0 µm. The uncoated carbide tools have diameters of 600 µm and helix angles of 35° with two flutes. Full slot-milling experiments are conducted as shown in Figure 53, with a spindle rotation frequency of 1,800, 3,600, and 5,400 rpm which corresponds to a cutting speed of 3.39, 6.79, and 10.18 m/min. For experiments with 3.39 m/min cutting speed, seven 24 mm length slots are cut with the same tool, so the measurements are collected at cutting lengths of 24, 48, 72, 96, 120, 144, and 168 mm. For cutting speed of 6.79 and 10.18 m/min, the cutting lengths are limited to 120 and 96 mm due to tool breakage. The axial depth of milling is 200 µm and the feed is 2 µm/rev. The flank wear land on the end face of tool is measured by a microscope after each slot-milling. The average flank wear is estimated by

averaging 10 values of the wear on the tool end face. The flank wear rate is calculated by the increase of flank wear between two measurements over the change of cutting time.

The measured tool flank wear after each slot under three different cutting speeds is shown in Figure 61(a). It can be observed that the tool wear rate is higher when the cutting speed increases. The cutting time is calculated based on the cutting length and the feed rate. And the wear rate at each measurement is calculated as the average of the slopes of two straight lines connecting the measurement as shown in Figure 61(b). The tool lasts much longer under a lower cutting speed. The measured tool flank wear is considered as the initial wear length for the input of predictive model.

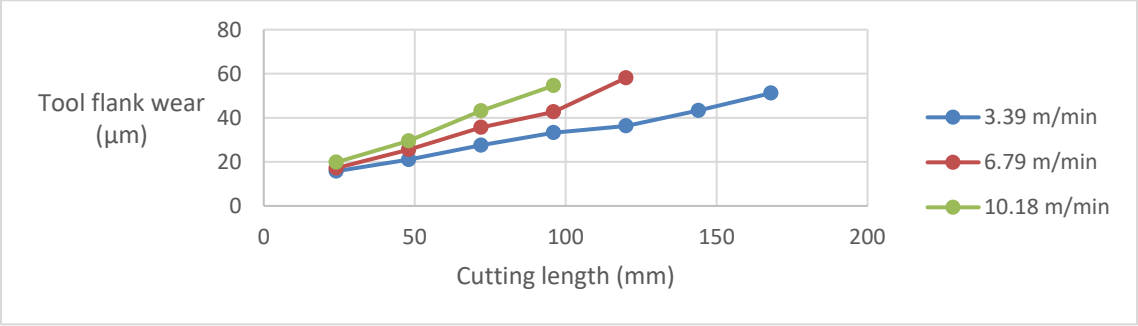

(a)

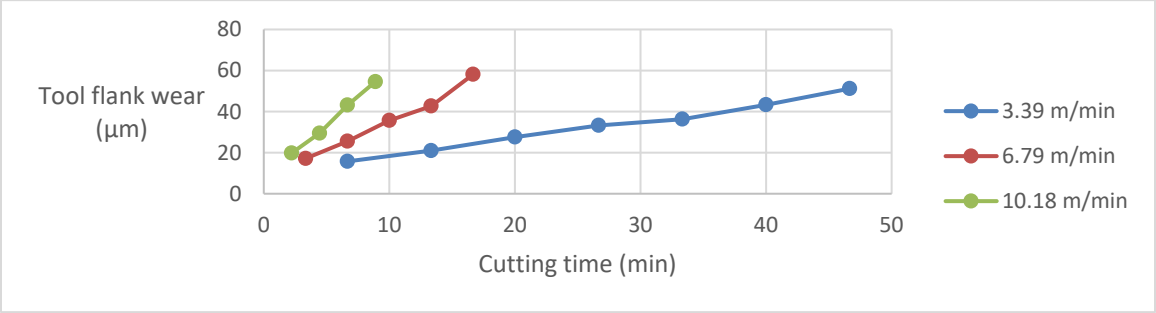

(b)

Figure 61 Measured tool flank wears vs. (a) cutting length and (b) cutting time for different cutting speeds [146]

The comparisons between calculated tool flank wear rate based on experimental measurements and predicted tool flank wear rate under three different cutting speeds are presented in Figure 62. As shown in Figure 60(a), if any tool-workpiece separation criterion is met, wear rate is assumed to be zero. Otherwise, the wear rate is calculated based on methodology described in section two, following the flow chart in Figure 63. In Figure 62, the predicted wear rate increases as the cutting time increases for all cases since a larger initial wear length is used. At a cutting speed of 3.39 m/min, the average wear rate over seven measurements is 0.90 μm/min, while the predicted value is 0.99 μm/min. Without two low wear rates from measurements around cutting time of 30 min, the predictions match the measurements in general. The average percentage error between measurements and predictions among seven data points is 15.4%. At a cutting speed of 6.79 m/min, the average wear rate over five measurements is 3.17 μm/min, while the predicted value is 3.04 μm/min. The average percentage error among five points is 10.2%, and the maximum percentage error is 23.3%. At a cutting speed of 10.18 m/min, the average wear rate over four measurements is 5.10 μm/min, while the predicted value is 5.44 μm/min. The average percentage error among four points is 7.1%, and the maximum percentage error is 20.1%. Overall, good agreements are found between predictions and measurements for all cases. Figure 62(a) also shows the reduction of measured wear rate in ultrasonic vibration-assisted milling comparing to conventional milling.

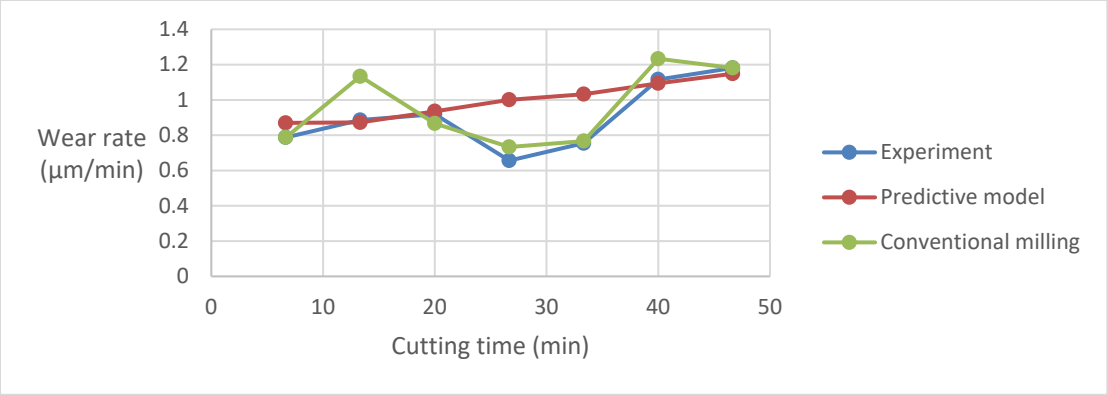

(a)

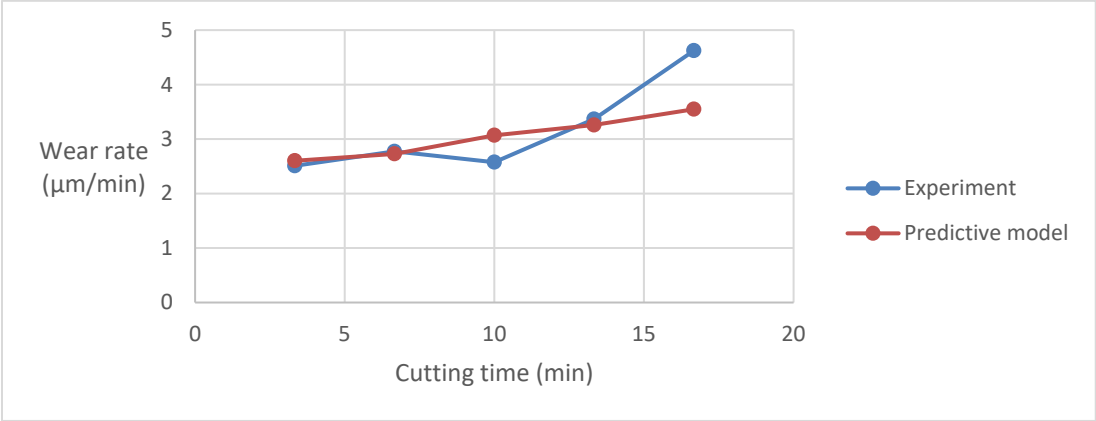

(b)

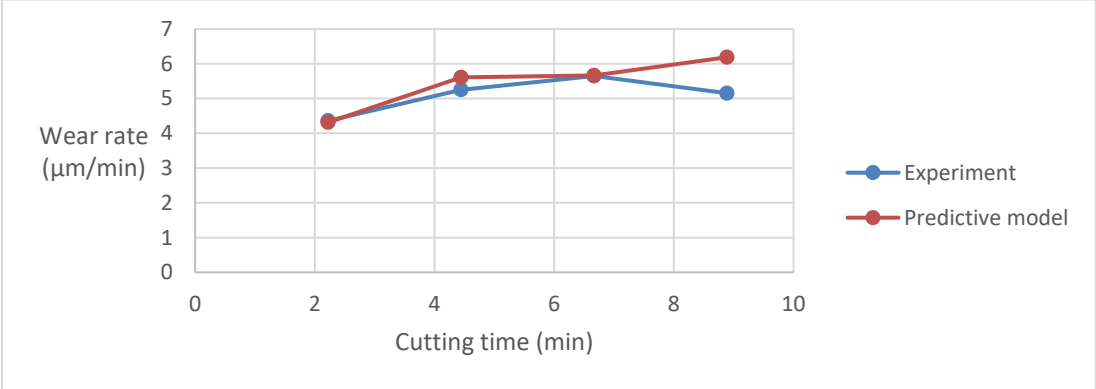

(c)

Figure 62 Comparison of wear rate between calculated value from experiment and predicted value from analytical model at a cutting speed of (a) 3.39, (b) 6.79, and (c) 10.18 m/min

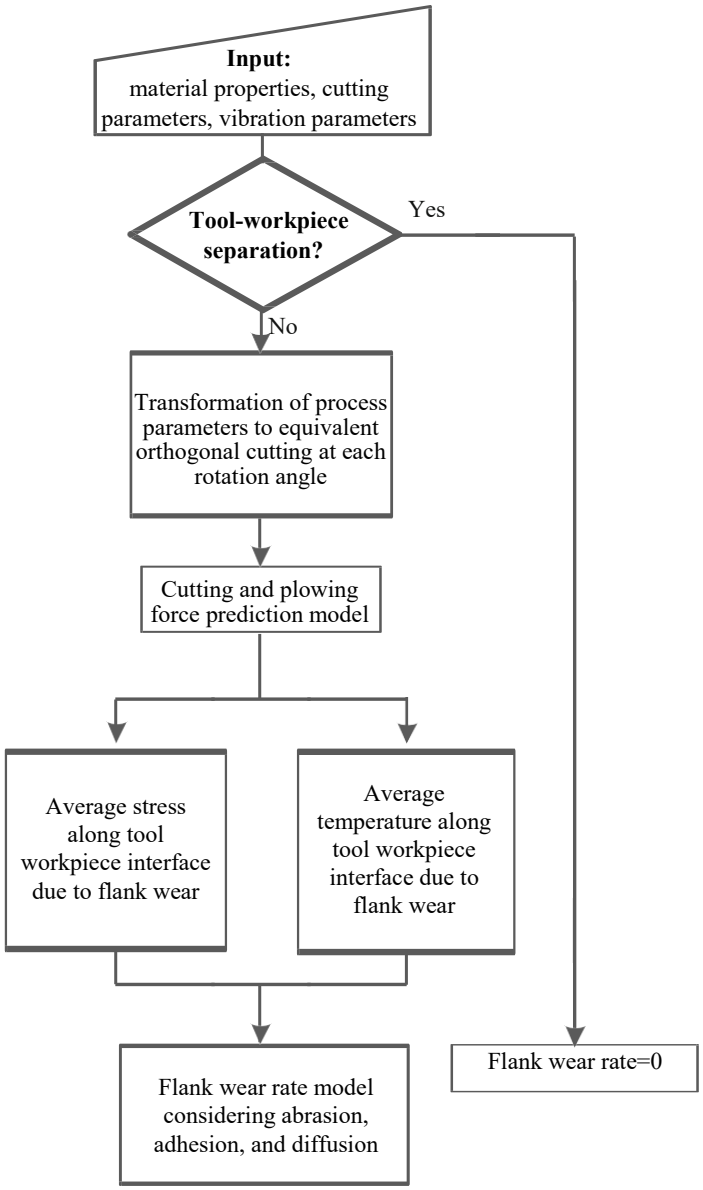

Figure 63 Overall flow chart of predictive model for flank wear rate in ultrasonic vibration-assisted milling

5.5.2 Sensitivity analysis

In order to appreciate the proposed predictive model, sensitivity analysis is conducted to estimate tool flank wear rate under the effects of different cutting and ultrasonic parameters including axial depth of milling, feed per tooth, ultrasonic vibration

amplitude, ultrasonic vibration frequency, and cutting speed. All other parameters are the same as in section three when one or two parameters are changing. As shown in Figure 64(a), the wear rate is predicted under three levels of axial depth of milling and seven levels of initial wear length from the measurements when cutting speed is 3.39 m/min. A higher flank wear will always lead to higher flank wear rate under all combinations of parameters in current study, since the continuous milling process will lead to eventual catastrophic tool failure. When the axial depth of milling increases, the effective cutting width w^* in orthogonal cutting also increases, leading to larger contact area and lower mechanical stress resulting in lower wear rate. However, the area affected by flank wear should be about the same or even larger, as the predicted flank wear rate is a one-dimensional linear rate in wear length direction. Figure 64(b) shows the predicted tool wear rate under four levels of feed per tooth. When the feed increases, both milling forces and machining temperature increases, leading to more severe abrasive, adhesive, and diffusive wears according to Equation (56). The effect of vibration amplitude on flank wear rate is shown in Figure 64(c). Within a wide range of amplitude from 2 μm to 20 mm, the change of wear rate is minimal. In current study, the vibration is applied only in z-direction. The Type II criterion is ignored as the vibration amplitude normally should be much smaller than axial depth of milling. In addition, the resultant planar velocity of the tool tip V_n has negligible effect on the Type I criterion. Therefore, the vibration amplitude has minimal influence on effective cutting time resulting in almost same wear rate. In reality, a much larger vibration amplitude should induce greater impact loading, which increases the wear rate. When an initial wear length of 33.25 μm is assumed, cutting speed has the most significant influence on flank wear rate as shown in Figure 64(d), as higher cutting zone temperature under

higher cutting speed results in severe thermal wear. Under low vibration frequency, the increase of frequency will lower wear rate as both milling forces and temperature are dropping. Under high vibration frequency and cutting speed, the increase of frequency will also increase wear rate due to greater impact loading.

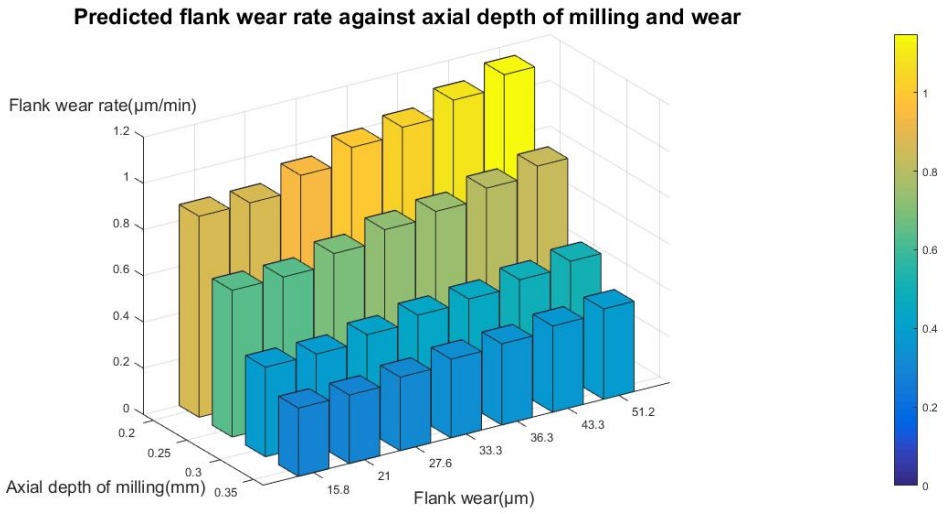

(a)

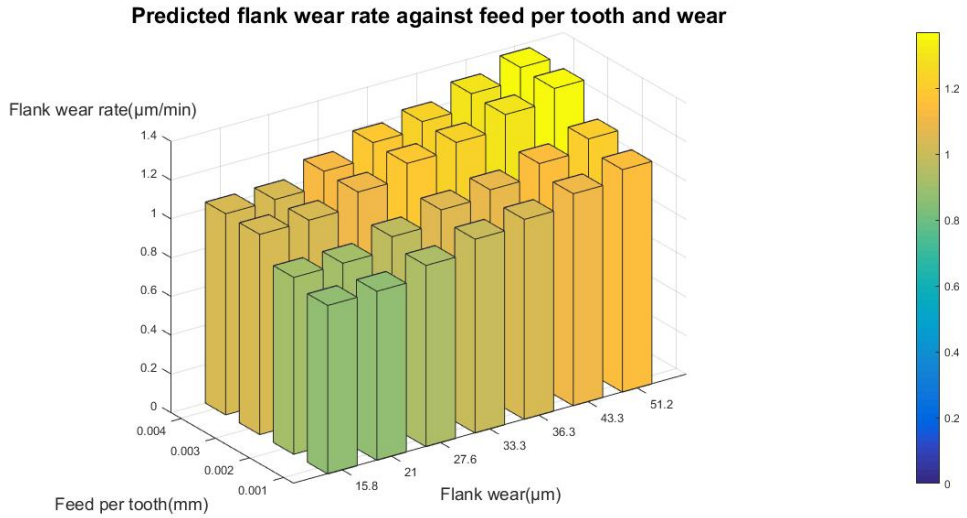

(b)

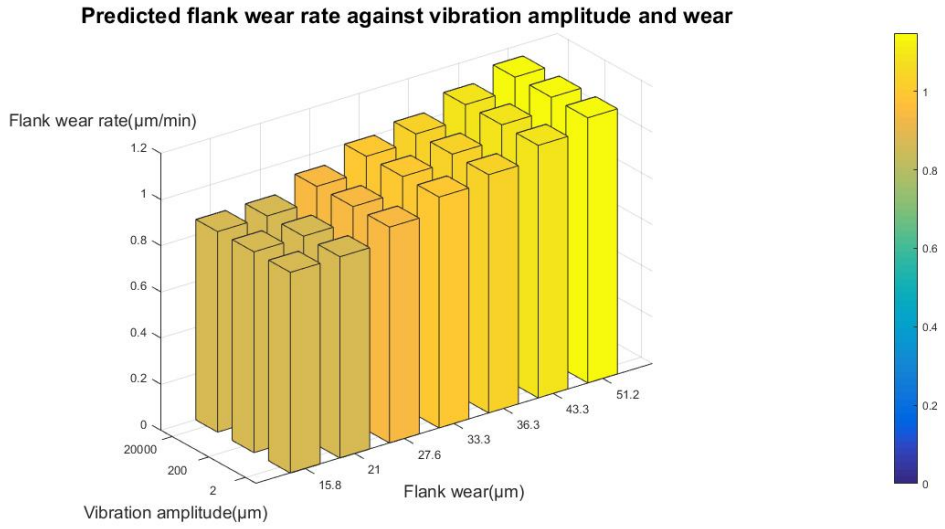

(c)

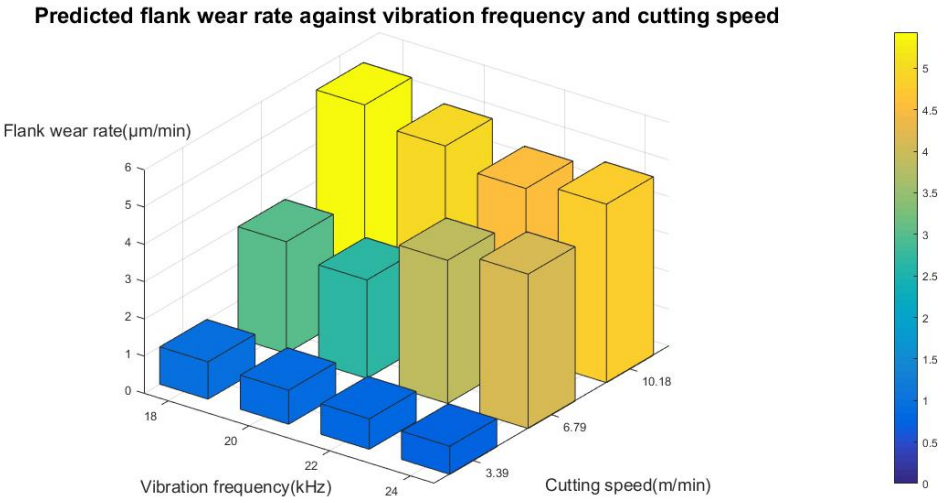

(d)

Figure 64 The variation of predicted tool flank wear rate with respect to different cutting and vibration parameters (a) axial depth of milling, (b) feed per tooth, (c) ultrasonic vibration amplitude, and (d) ultrasonic vibration frequency

5.6 Surface roughness

Analytical model of surface roughness on side wall in feed directional ultrasonic vibration-assisted milling is proposed. Since the ultrasonic vibration frequency is typically

much higher than tool rotation frequency, the tool movement under vibration is described as a translation in feed direction by $2A_x$ while other components remain the same.

5.6.1 Experimental validation

The experiments are conducted under a five-axis machining center by Shen *et al.* [147]. An ultrasonic vibrator drives the workpiece to vibrate along the feed direction with a frequency of 19.58 *kHz*. The workpiece material is Aluminum alloy 2A12. The milling tool is made of carbide with two flutes and diameter of 2 *mm*. The axial depth of milling is 0.5 *mm*. After the milling process, the workpiece is cut by wire electrical discharge machining to measure the surface roughness of side wall. Each surface is measured six times by optical interferometer, and the average value is recorded. For the first part of the experiments, both conventional and ultrasonic vibration-assisted milling with an amplitude of 4 μm are conducted. The comparisons are made under a feed per tooth of 2, 4, 6, and 8 μm, when the spindle speed is 5,000 *rpm*. In addition, under a constant feed per tooth of 4 μm, comparisons are made under spindle speed of 1,000, 5,000, 9,000, and 13,000 *rpm*. For the second part of the experiments, the effects of cutting and vibration parameters on surface roughness are analyzed. A total of 18 measurements are collected under spindle speed of 5,000, 9,000, and 13,000 *rpm*, feed per tooth of 4, 6, and 8 μm, and vibration amplitude of 4 and 7 μm.

5.6.2 Results

Figure 65 shows both experimental measurements and analytical predictions from proposed model when comparing surface roughness after conventional milling to surface roughness after ultrasonic vibration-assisted milling. Under the spindle speed of 5,000 *rpm*,

the surface finish has a huge improvement as the surface roughness drops 70% in average when the vibration is applied, as shown in Figure 65(a). When the spindle speed increases to 9,000 and 13,000 *rpm*, the benefit of ultrasonic vibration is less significant as the tool rotation frequency is getting closer to vibration frequency, but the decrease of surface roughness is still over 40%, as shown in Figure 65(b). The predicted R_a matches the measurements with an average percentage error of 3.6% and 13.4% for conventional and ultrasonic vibration-assisted milling, respectively, under a constant spindle speed. These two errors are 6.4% and 25.7% under an increasing spindle speed in Figure 65(b). The predictive model is less accurate in ultrasonic vibration-assisted milling or under a higher spindle speed as both higher vibration and tool rotation frequencies will bring more error sources such as tool chatter during the experiments, which are not accounted for in predictive model.

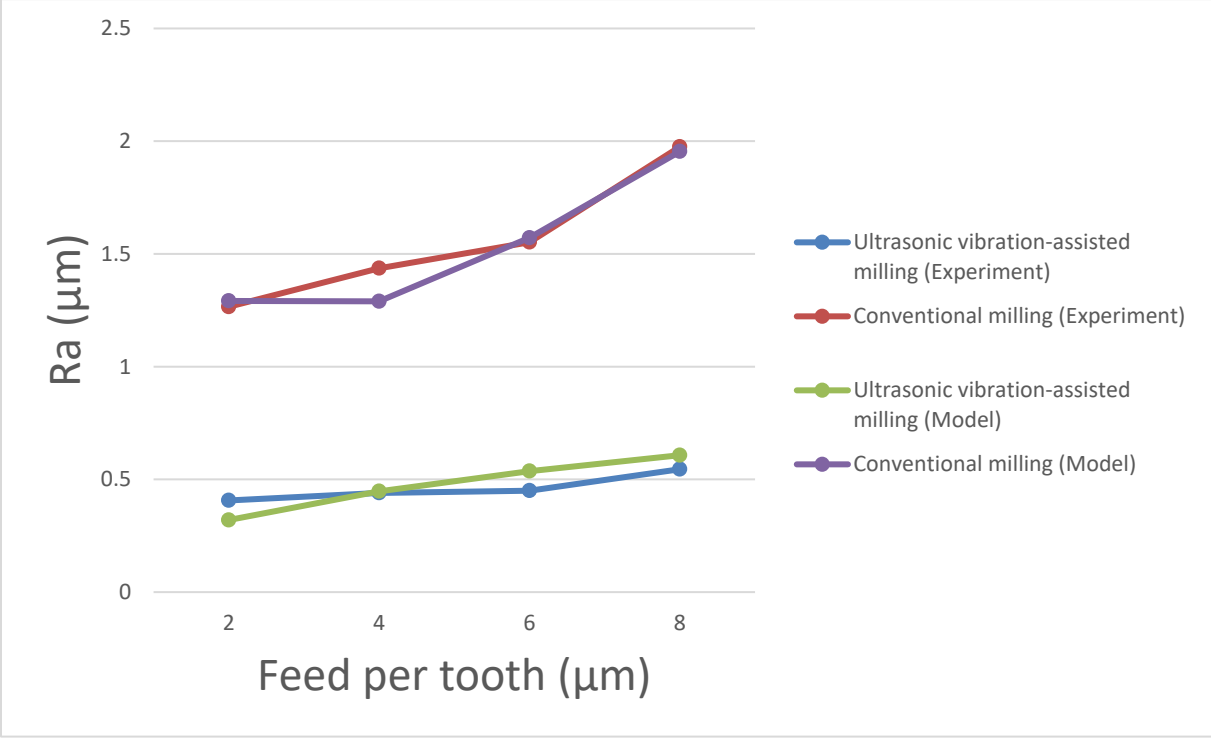

(a)

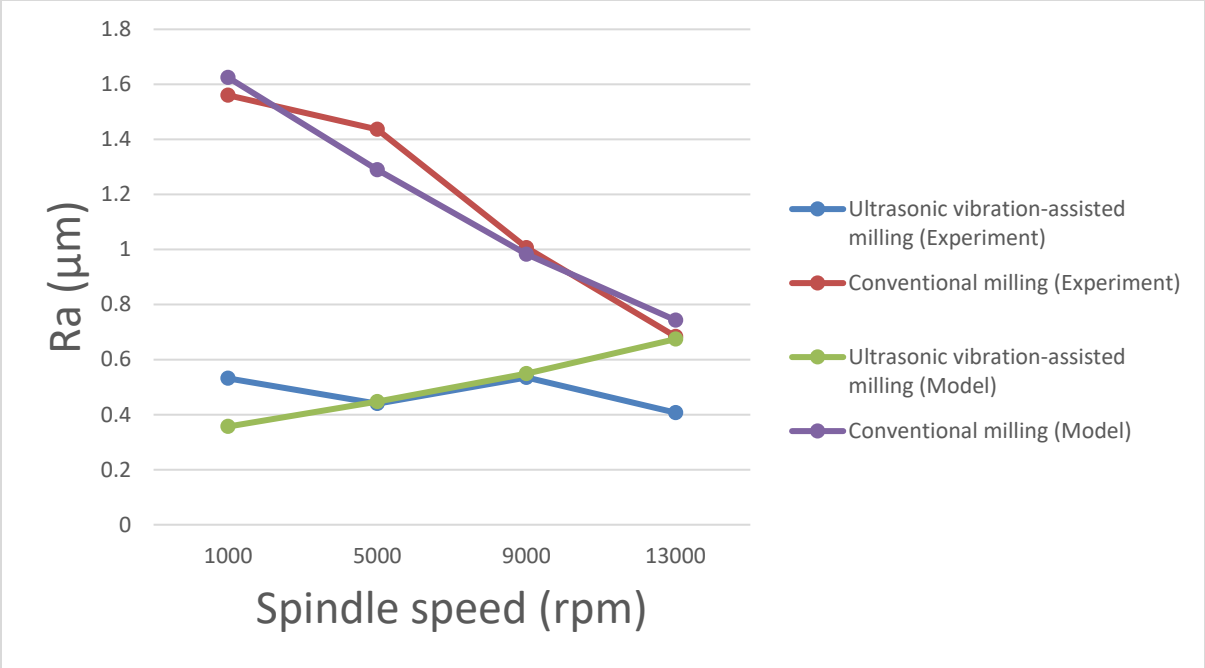

(b)

Figure 65 Comparison of surface roughness between conventional and ultrasonic vibration-assisted milling under various (a) feed per tooth and (b) spindle speed

Besides showing the benefits of feed directional ultrasonic vibration-assisted milling, the effects of feed per tooth, spindle speed, and vibration amplitude on surface roughness are reflected through additional experiments as summarized in Figure 66 and Figure 67. When the feed per tooth increases, the gap between two flutes on machined surface is larger, leading to higher surface roughness. For ultrasonic vibration-assisted milling, when the spindle speed increases, the increase of cutting speed results in larger deformation zone, which is considered as a larger $t_{\min}$ in predictive model, and the surface roughness becomes higher. When the vibration amplitude increases, the benefit of ultrasonic vibration is more significant, and the surface roughness gets lower. The proposed predictive model is able to match the trends in all cases. The average percentage error is 17.3% when the vibration

amplitude is 4 μm as shown in Figure 66. The average percentage error is 10.9% when the vibration amplitude is 7 μm as shown in Figure 67.

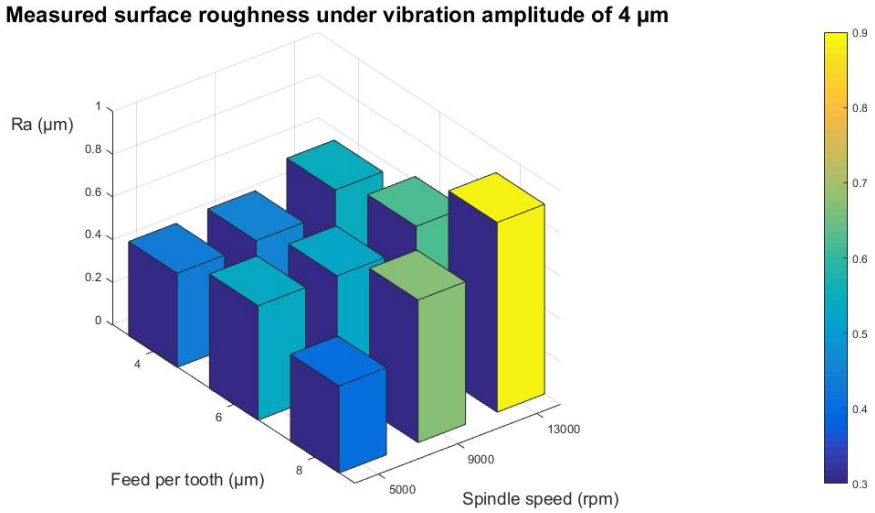

(a)

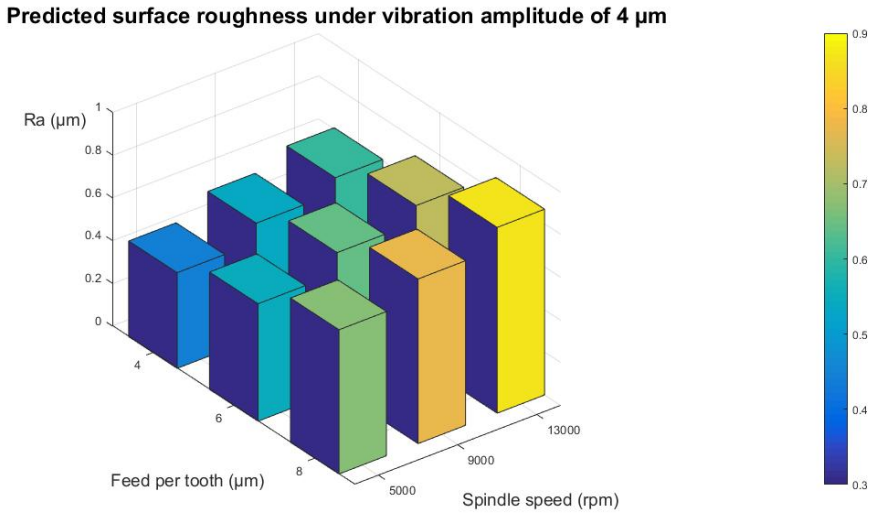

(b)

Figure 66 Comparison of surface roughness between (a) measurements and (b) predictions under vibration amplitude of 4 µm

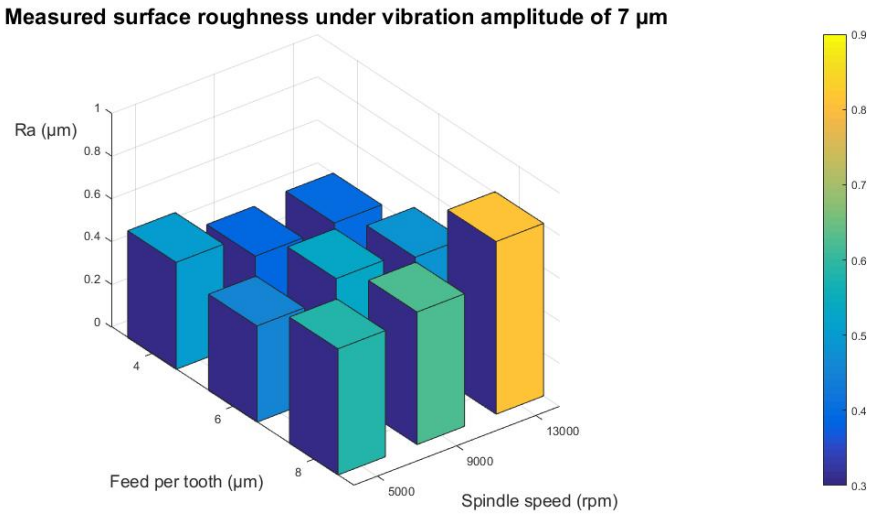

(a)

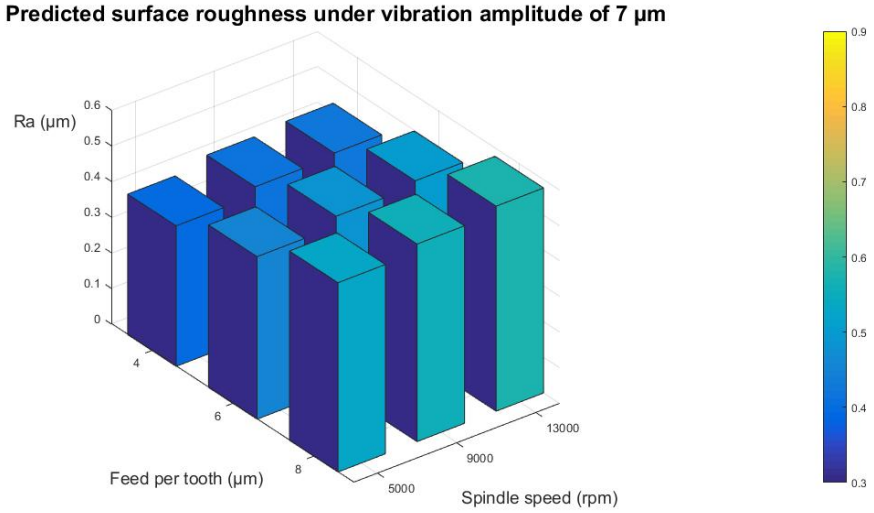

(b)

Figure 67 Comparison of surface roughness between (a) measurements and (b) predictions under vibration amplitude of 7 µm

The selection of minimum cutting thickness $t_{\min}$ is critical in current study in order to predict the machined surface profile with high accuracy. In current study, as the same combination of tool and workpiece is used throughout all experiments, $t_{\min}$ is only dependent on cutting parameters in conventional milling as

$$t_{\min} = 0.525 - 4.5\times10^{-5} n + 0.19 f_z + 0.035 f_z^2 \quad (77)$$

where n is the spindle speed. For ultrasonic vibration-assisted milling, $t_{\min}$ is also dependent on vibration amplitude as

$$t_{\min} = -2.7 + 10^{-4} n + 0.8 f_z + A_x \quad (78)$$

$t_{\min}$ is therefore accurately predicted and used as a boundary of shear-dominant and plowing-dominant processes in ultrasonic vibration-assisted milling, as the deflection of machined surface imparted by the tool is a combination of elastic and plastic deformation.

5.7 Conclusion

In CHAPTER 5, analytical predictive model on cutting force, temperature, residual stress, tool flank wear rate, and surface roughness in ultrasonic vibration-assisted milling is proposed. The three types of tool-workpiece criteria are considered based on the instantaneous position and velocity of tool. If there is contact, same procedure as in CHAPTER 3. The following conclusions are summarized. For force,

- The average forces in ultrasonic vibration-assisted milling are significantly lowered by over 35% comparing to conventional milling.
- The average forces keep decreasing as the vibration amplitude increases, since the tool-workpiece separation time is longer and the effective cutting time is shorter.
- The proposed predictive model is able to match the measured milling forces with high accuracy of average difference of 13.6% in feed direction and 13.8% in cutting direction.

- Based on the sensitivity analysis, a doubled axial depth of milling or feed per tooth will double the milling forces in both directions, while a higher ultrasonic vibration or spindle rotation frequency will result in lower milling forces.

For temperature,

- A higher spindle rotation frequency, axial depth of milling, or feed per tooth will all lead to higher temperature.
- The temperature keeps decreasing as the vibration amplitude increases, since the tool-workpiece separation time is longer and the effective cutting time is shorter.
- The proposed predictive model is able to match the measured temperature with high accuracy of 1.85% average error and 5.22% largest error among all cases.
- Based on the sensitivity analysis, the influence of spindle rotation frequency is more significant on temperature comparing to axial depth of milling and feed per tooth. In addition, higher ultrasonic vibration frequency will result in lower peak temperature for Al 6063 alloy.

For residual stress,

- A higher feed per tooth will lead to more tensile residual stress due to higher temperature field softening the workpiece.
- At ultrasonic vibration frequency below 40 kHz, residual stress becomes more tensile as the frequency increases due to less hardening of workpiece under smaller milling forces. At ultrasonic vibration frequency above 40 kHz, residual stress becomes more compressive as the frequency increases due to less softening of workpiece under lower temperature.

- The proposed predictive model is able to match the measured residual stress with high accuracy of 6.4% average error and 23.6% maximum error among all cases.
- Based on the sensitivity analysis, higher axial depth of milling will result in less compressive residual stress. In addition, both higher ultrasonic vibration amplitude and higher spindle rotation frequency will result in more compressive residual stress for AISI 316L alloy.

For tool flank wear rate,

- According to both experimental measurements and predictive model, the flank wear rate is higher under longer cutting length, cutting time, or wear length.
- The proposed predictive model is able to match the measured tool flank wear rate with high accuracy of 15.4%, 10.2%, and 7.1% average percentage error when cutting speed is 3.39, 6.79, and 10.18 m/min, respectively.
- Based on the sensitivity analysis, smaller axial depth of milling, larger feed per tooth, or higher cutting speed will result in higher flank wear rate. In addition, the effect of ultrasonic vibration amplitude is insignificant. And higher ultrasonic vibration frequency will result in lower wear rate at low frequency or cutting speed, and higher wear rate when both frequency and cutting speed are high.

For surface roughness,

- Under the spindle speed of 5,000 *rpm*, the surface finish has a huge improvement as the surface roughness drops 70% in average when the vibration is applied. When the spindle speed increases to 9,000 and 13,000 *rpm*, the benefit of ultrasonic vibration is less significant, but the decrease of surface roughness is still over 40%.

- For ultrasonic vibration-assisted milling, lower feed per tooth, lower spindle speed, or higher vibration amplitude will decrease the surface roughness.
- The proposed model has high accuracy in all cases. For the first group of experiments, the average percentage error is 13.4% under spindle speed of 5,000 *rpm*. The average percentage error is 25.7% under feed per tooth of 4 μm. For the second group of experiments, the average percentage error is 17.3% when the vibration amplitude is 4 μm. The average percentage error is 10.9% when the vibration amplitude is 7 μm.

The proposed analytical model is valuable for providing an accurate and reliable reference for the prediction of force, temperature, residual stress, flank wear rate, and surface roughness in ultrasonic vibration-assisted milling.

CHAPTER 6. CONCLUSION AND FUTURE WORK

6.1 Conclusion

Analytical performance analysis is conducted on two kinds of advanced milling technologies including forward problem methodology in laser-assisted milling, inverse problem methodology in laser-assisted milling, and forward problem methodology in ultrasonic vibration-assisted milling. The forward problem methodology is valuable in terms of providing an accurate and reliable reference for the prediction of milling forces, temperature, residual stress, tool wear, and surface roughness. The inverse problem methodology is valuable in terms of guiding the selection of process parameters based on desired target performances. The effects of laser preheating and grain growth are considered in laser-assisted milling, while the intermittent tool-workpiece separation is considered in ultrasonic vibration-assisted milling. All proposed models are validated through experiments with high accuracy, and the effect of each process parameter on the target performance is presented through the sensitivity analysis. A computing platform is built to incorporate all algorithms consisting of several graphical user interfaces (GUI) as shown in APPENDIX A. GRAPHICAL USER INTERFACE. The current work is able to evaluate the performance of advanced milling process from different aspects, and guide the process based on different requirements.

6.2 Future work

As shown in Figure 68, there is one part missing in the computing platform for lubrication condition. For the current study, all predictive models are based on dry

machining condition. However, the use of cutting fluids is very common as it is able to reduce the cutting force and temperature. Minimum quantity lubrication (MQL) machining refers to the use of a small amount of cutting fluid, which was sprayed to the cutting zone with the compressed air. Compared with the conventional flood cooling machining, MQL machining reduces the costs of cutting fluids and its ancillary equipment, and also alleviates the environment pollution. Up to now, analytical predictive model has not been proposed for MQL milling. And the use of MQL can be combined with laser-assisted or ultrasonic vibration-assisted milling, which requires the future work to incorporate these factors into the analytical performance analysis.

On the other hand, the measurements of temperature, residual stress, and tool wear in laser-assisted milling and all measurements in ultrasonic vibration-assisted milling are from experiments in references under different workpiece and process parameter combinations. Good agreement is found for each individual target performance, but the overall accuracy of the model including all five performances has not been validated under same condition. Therefore, future work is needed to conduct more experiments and measure force, temperature, residual stress, tool wear, and surface roughness under same cutting, laser, and vibration conditions to verify the effectiveness of the computing platform.

APPENDIX A. GRAPHICAL USER INTERFACE

As shown in Figure 68, the main interface allows the user to select whether the milling is conducted under conventional, laser-assisted, or ultrasonic vibration-assisted condition. Each button is linked to an input interface where the user defines the parameters or material properties, and clicking the 'Run' button will execute algorithms in forward problem methodology for performance analysis. An example of input interface for tool geometry and material definition is shown in Figure 69, and the output interface in Figure 70 displays predicted cutting force, temperature, residual stress, surface roughness, and tool life, with corresponding graphics.

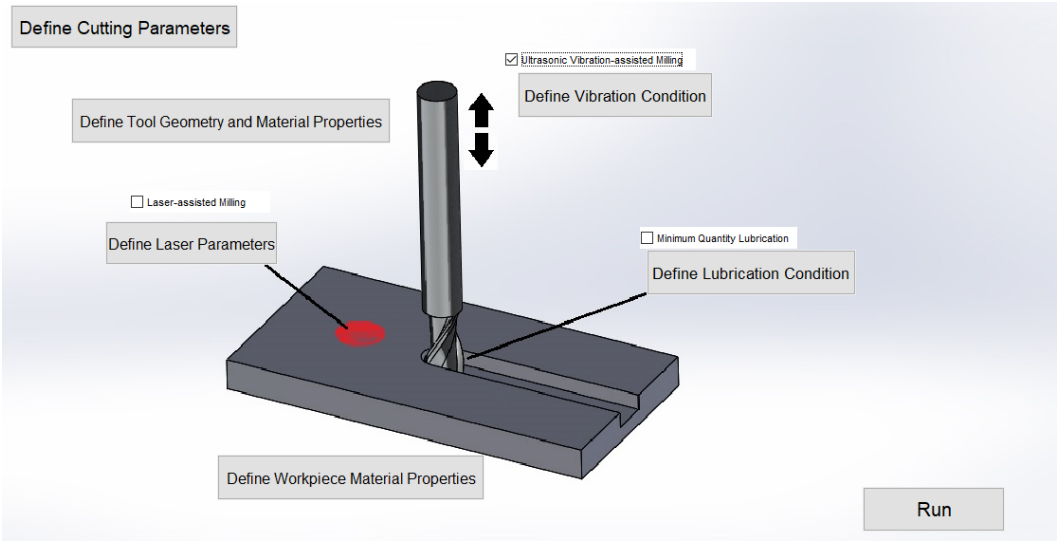

Figure 68 Main interface for process selection

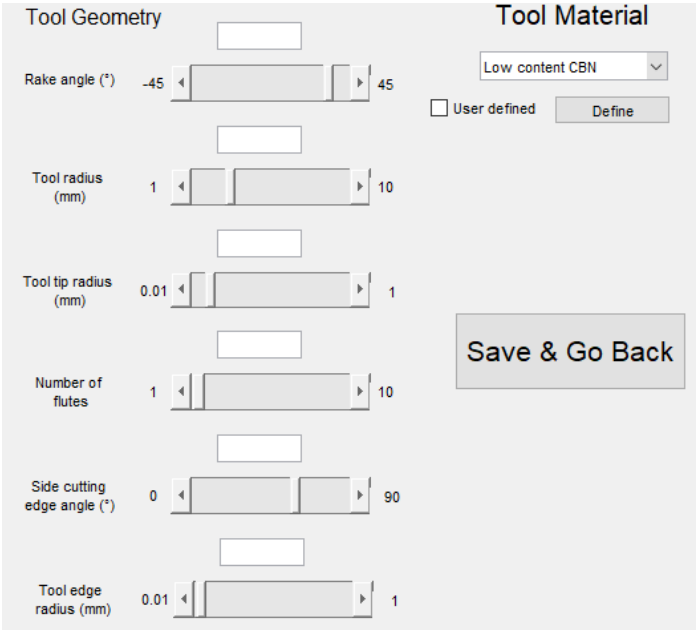

Figure 69 Input interface

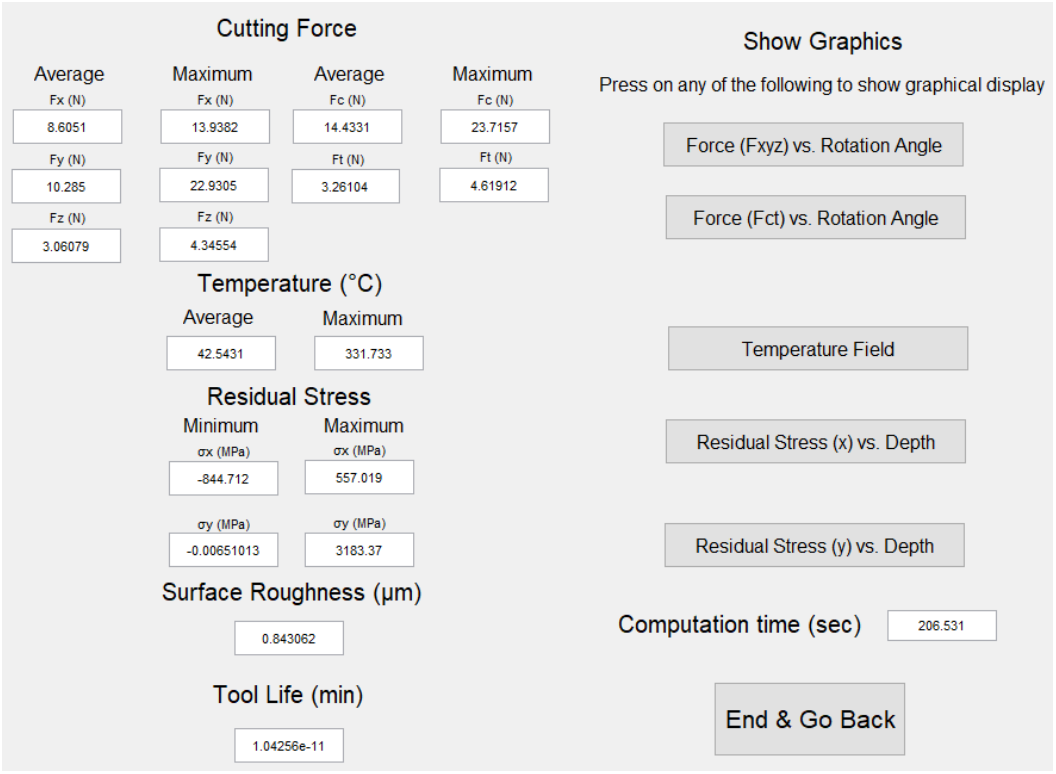

Figure 70 Output interface

A computing platform is also built for inverse analysis. As shown in Figure 71(a), the platform is able to find optimal combination of spindle speed, feed rate, and axial depth of milling, based on target performance of maximum material removal rate, maximal tool life, or minimum peak force. And the top three recommended parameters and corresponding material removal rate, tool life, and peak force are displayed in output interface of Figure 71(b).

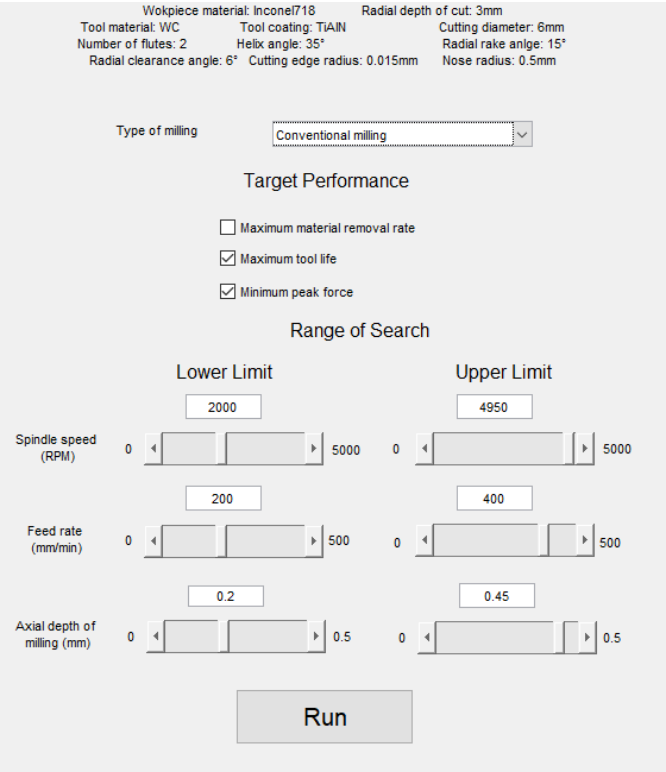

(a)

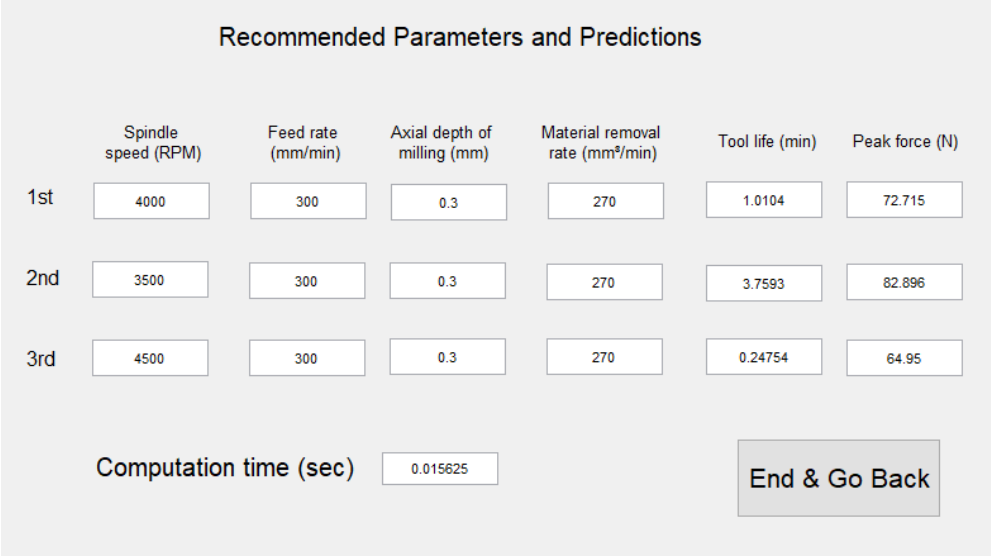

(b)

Figure 71 GUI for Inverse analysis

REFERENCES

1. Bermingham, M.J., et al., *Tool life and wear mechanisms in laser assisted milling Ti–6Al–4V.* Wear, 2015. **322-323**: p. 151-163.

2. Halim, N.F.H.A., H. Ascroft, and S. Barnes, *Analysis of Tool Wear, Cutting Force, Surface Roughness and Machining Temperature During Finishing Operation of Ultrasonic Assisted Milling (UAM) of Carbon Fibre Reinforced Plastic (CFRP).* Procedia Engineering, 2017. **184**: p. 185-191.

3. Azarbarmas, M.A.-K., M. Cabrera, J. M. Calvo, J., *Dynamic recrystallization mechanisms and twining evolution during hot deformation of Inconel 718.* Materials Science and Engineering: A, 2016. **678**: p. 137-152.

4. Thakur, D.G., B. Ramamoorthy, and L. Vijayaraghavan, *Machinability investigation of Inconel 718 in high-speed turning.* The International Journal of Advanced Manufacturing Technology, 2009. **45**(5-6): p. 421-429.

5. Manshadi, S.T., *Laser Assisted Machining of Inconel 718 Super Alloy*, in *Department of Mechanical Engineering*. 2009, McGill University: Montréal, Québec. p. 124.

6. Lonikar, K.V., *Laser Assisted Machining (LAM) of Inconel 718 with Thermal Modeling and Analysis of Process Parameters.* International Journal of Engineering Research & Technology, 2015. **4**(7): p. 308-312.

7. S.C. Medeiros, Y.V.R.K.P., W.G. Frazier, R. Srinivasan, *Microstructural modeling of metadynamic recrystallization in hot working of IN 718 superalloy.* Materials Science and Engineering, 2000. **293**: p. 198–207.

8. B. Marty, J.Y.G., P. Gergaud, J.L. Lebrun, *RECRYSTALLIZATION AND WORK-HARDENING PREDICTION DURING FORGING PROCESS OF INCONEL 7 18.* The Minerals, Metals & Materials Society, 1997: p. 331-342.

9. Robert P. Guest, S.T., *THE DYNAMIC AND METADYNAMIC RECRYSTALLISATION OF IN 718.* 2005: p. 373-383.

10. Robert P. Guest, S.T., *MODELLING MICROSTRUCTURAL TRANSFORMATIONS OF NICKEL BASE SUPERALLOY IN 718 DURING HOT DEFORMATION.* The Minerals, Metals & Materials Society, 2005: p. 385-397.

11. Wang, Y., et al., *Investigation on Dynamic Recrystallization Behavior in Hot Deformed Superalloy Inconel 718.* Materials Science Forum, 2007. **546-549**: p. 1297-1300.

12. Zhao, X., et al., *Modelling hot deformation of Inconel 718 using state variables.* Materials Science and Technology, 2013. **20**(11): p. 1414-1420.

13. Shi, B., et al., *NUMERICAL AND EXPERIMENTAL INVESTIGATION OF LASER-ASSISTED MACHINING OF INCONEL 718.* Machining Science and Technology, 2008. **12**(4): p. 498-513.

14. Tian, Y., et al., *Laser-Assisted Milling of Silicon Nitride Ceramics and Inconel 718.* Journal of Manufacturing Science and Engineering, 2008. **130**(3): p. 031013.

15. Woo, W.-S. and C.-M. Lee, *A study of the machining characteristics of AISI 1045 steel and Inconel 718 with a cylindrical shape in laser-assisted milling.* Applied Thermal Engineering, 2015. **91**: p. 33-42.

16. Garcí, et al., *Mechanisms involved in the improvement of Inconel 718 machinability by laser assisted machining (LAM).* International Journal of Machine Tools and Manufacture, 2013. **74**: p. 19-28.

17. Özel;, T. and T. Altan;, *Process simulation using finite element method — prediction of cutting forces, tool stresses and temperatures in highspeed flat end milling.* International Journal of Machine Tools & Manufacture, 2000. **40**: p. 713-738.

18. Abukhshim, N.A., P.T. Mativenga, and M.A. Sheikh, *Heat generation and temperature prediction in metal cutting: A review and implications for high speed machining.* International Journal of Machine Tools and Manufacture, 2006. **46**(7-8): p. 782-800.

19. Lu, X., et al., *Coupled thermal and mechanical analyses of micro-milling Inconel 718.* Proceedings of the Institution of Mechanical Engineers, Part B: Journal of Engineering Manufacture, 2018: p. 095440541877458.

20. Schlauer, C., R.L. Peng, and M. Odén, *Residual Stresses in a Nickel-Based Superalloy Introduced by Turning.* Materials Science Forum, 2002. **404-407**: p. 173-178.

21. Dudzinski, D., et al., *A review of developments towards dry and high speed machining of Inconel 718 alloy.* International Journal of Machine Tools & Manufacture, 2004. **44**: p. 439-456.

22. Sharman, A.R.C., J.I. Hughes, and K. Ridgway, *An analysis of the residual stresses generated in Inconel 718™ when turning.* Journal of Materials Processing Technology, 2006. **173**(3): p. 359-367.

23. Madariaga, A., et al., *Analysis of residual stress and work-hardened profiles on Inconel 718 when face turning with large-nose radius tools.* The International Journal of Advanced Manufacturing Technology, 2014. **71**(9-12): p. 1587-1598.

24. Outeiro, J.C., et al., *Analysis of residual stresses induced by dry turning of difficult-to-machine materials.* CIRP Annals - Manufacturing Technology, 2008. **57**(1): p. 77-80.

25. Le Coz, G., et al., *Residual stresses after dry Machining of Inconel 718, experimental results and numerical simulation.* 2010.

26. Ulutan, D., B. Erdem Alaca, and I. Lazoglu, *Analytical modelling of residual stresses in machining.* Journal of Materials Processing Technology, 2007. **183**(1): p. 77-87.

27. Fergani, O., et al., *Analytical modeling of residual stress and the induced deflection of a milled thin plate.* The International Journal of Advanced Manufacturing Technology, 2014. **75**(1-4): p. 455-463.

28. Peng, F.Y., et al., *Analytical modeling and experimental validation of residual stress in micro-end-milling.* The International Journal of Advanced Manufacturing Technology, 2016. **87**(9-12): p. 3411-3424.

29. Zhou, R. and W. Yang, *Analytical modeling of residual stress in helical end milling of nickel-aluminum bronze.* The International Journal of Advanced Manufacturing Technology, 2016. **89**(1-4): p. 987-996.

30. Huang, X., X. Zhang, and H. Ding, *An Enhanced Analytical Model of Residual Stress for Peripheral Milling.* Procedia CIRP, 2017. **58**: p. 387-392.

31. Ma, Q., Z.-q. Lin, and Z.-q. Yu, *Prediction of deformation behavior and microstructure evolution in heavy forging by FEM.* The International Journal of Advanced Manufacturing Technology, 2009. **40**(3-4): p. 253-260.

32. Huang, D., et al., *Computer Simulation of Microstructure Evolution during Hot Forging of Waspaloy and Nickel Alloy 718.* 2001.

33. Furrer, D., R. Goetz, and G. Shen, *Modeling and Simulation of Alloy 718 Microstructure and Mechanical Properties*, in *7th International Symposium on Superalloy 718 & Derivatives*. 2010, The Minerals,Metals&Materials Society: Pittsburgh, Pennsylvania.

34. Arunachalam, R.M., M.A. Mannan, and A.C. Spowage, *Residual stress and surface roughness when facing age hardened Inconel 718 with CBN and ceramic cutting tools.* International Journal of Machine Tools and Manufacture, 2004. **44**(9): p. 879-887.

35. Ning, F., et al., *Chip morphology and surface roughness in high-speed milling of nickel-based superalloy Inconel 718.* International Journal of Machining and Machinability of Materials, 2014. **15**(3/4): p. 285.

36. D'Addona, D.M., S.J. Raykar, and M.M. Narke, *High Speed Machining of Inconel 718: Tool Wear and Surface Roughness Analysis.* Procedia CIRP, 2017. **62**: p. 269-274.

37. Alauddin, M., M.A. E1 Baradie, and H. M.S.J., *OPTIMIZATION OF SURFACE FINISH IN END MILLING INCONEL 718.* Journal of Materials Processing Technology, 1996. **56**: p. 54-65.

38. Lu, X., et al., *A surface roughness prediction model using response surface methodology in micro-milling Inconel 718* International Journal of Machining and Machinability of Materials, 2017. **19**(3): p. 230–245.

39. Kasim, M.S., et al., *Prediction Surface Roughness in High-Speed Milling of Inconel 718 under Mql Using Rsm Method.* Middle-East Journal of Scientific Research, 2013. **13**(3): p. 264-272.

40. dos Santos Schlüter, M., H.B. Hübner, and A.J. de Souza, *Optimization of Cutting Parameters for Face Milling of Cast Iron by Reducing Specific Cutting Energy and Machined Surface Roughness.* Applied Mechanics and Materials, 2015. **727-728**: p. 339-344.

41. Lu, X., et al., *Surface roughness prediction model of micro-milling Inconel 718 with consideration of tool wear.* International Journal of Nanomanufacturing, 2016. **12**(1): p. 93-108.

42. N, S.S., V. H.V., and T. D.G., *A comparative study of cutting force, feed force, surface roughness and tool wear in machining of Inconel 718 with uncoated and coated tungsten carbide inserts.* Int. Journal of Applied Sciences and Engineering Research, 2016. **5**(1): p. 30-38.

43. Babur, O., O. Hasan, and K. Hasan, *Optimum surface roughness in end milling Inconel 718 by coupling neural network model and genetic algorithm.* The International Journal of Advanced Manufacturing Technology, 2005. **27**(3-4): p. 234-241.

44. Jafarian, F., et al., *Experimental Investigation to Optimize Tool Life and Surface Roughness in Inconel 718 Machining.* Materials and Manufacturing Processes, 2015. **31**(13): p. 1683-1691.

45. Tebassi, H., et al., *On the Modeling of Surface Roughness and Cutting Force when Turning of Inconel 718 Using Artificial Neural Network and Response Surface Methodology: Accuracy and Benefit.* Periodica Polytechnica Mechanical Engineering, 2017. **61**(1): p. 1-11.

46. Muñoz-Escalona, P. and P.G. Maropoulos, *A geometrical model for surface roughness prediction when face milling Al 7075-T7351 with square insert tools.* Journal of Manufacturing Systems, 2015. **36**: p. 216-223.

47. Hao, Y. and Y. Liu, *Analysis of milling surface roughness prediction for thin-walled parts with curved surface.* The International Journal of Advanced Manufacturing Technology, 2017. **93**(5-8): p. 2289-2297.

48. Lu, X., et al., *Model for the prediction of 3D surface topography and surface roughness in micro-milling Inconel 718.* The International Journal of Advanced Manufacturing Technology, 2017.

49. Chen, W., et al., *State-of-the-art review on vibration-assisted milling: principle, system design, and application.* The International Journal of Advanced Manufacturing Technology, 2018. **97**(5-8): p. 2033-2049.

50. Yuan, Z.J., M. Zhou, and S. Dong, *Effect of diamond tool sharpness on minimum cutting thickness and cutting surface integrity in ultraprecision machining.* Journal of Materials Processing Technology, 1996. **62**: p. 327-330.

51. Son, S.M., H.S. Lim, and J.H. Ahn, *Effects of the friction coefficient on the minimum cutting thickness in micro cutting.* International Journal of Machine Tools and Manufacture, 2005. **45**(4-5): p. 529-535.

52. Wu, J.H. and Z.Q. Liu, *Modeling the Minimum Chip Thickness in Orthogonal Micro-Cutting Based on Plastic Strain Gradient.* Advanced Materials Research, 2009. **69-70**: p. 203-208.

53. Zhanqiang, L., S. Zhenyu, and W. Yi, *Definition and determination of the minimum uncut chip thickness of microcutting.* The International Journal of Advanced Manufacturing Technology, 2013. **69**(5-8): p. 1219-1232.

54. Wang, X.B., et al., *The Minimum Cutting Thickness in Milling Process Simulation Analysis.* Materials Science Forum, 2014. **800-801**: p. 264-268.

55. Huang, Y., *PREDICTIVE MODELING OF TOOL WEAR RATE WITH APPLICATION TO CBN HARD TURNING*. 2002, Georgia Institute of Technology.

56. Li, H.Z., H. Zeng, and X.Q. Chen, *An experimental study of tool wear and cutting force variation in the end milling of Inconel 718 with coated carbide inserts.* Journal of Materials Processing Technology, 2006. **180**(1-3): p. 296-304.

57. Brecher, C., et al., *Laser-assisted Milling of Advanced Materials.* Physics Procedia, 2011. **12**: p. 599-606.

58. Zhang, S., J.F. Li, and Y.W. Wang, *Tool life and cutting forces in end milling Inconel 718 under dry and minimum quantity cooling lubrication cutting conditions.* Journal of Cleaner Production, 2012. **32**: p. 81-87.

59. Yazid, M.Z.A., et al., *Tool Wear when Finish Turning Inconel 718 under Dry Conditions.* International Journal of Science Engineering and Technology, 2009. **2**(3): p. 53 - 57.

60. Khan, S.A., et al., *Tool wear/life evaluation when finish turning Inconel 718 using PCBN tooling.* Procedia CIRP, 2012. **1**: p. 283-288.

61. Xavior, M.A., et al., *Tool Wear Assessment During Machining of Inconel 718.* Procedia Engineering, 2017. **174**: p. 1000-1008.

62. Attanasio, A., E. Ceretti, and C. Giardini, *Analytical Models for Tool Wear Prediction During AISI 1045 Turning Operations.* Procedia CIRP, 2013. **8**: p. 218-223.

63. Ojolo, S.J. and O. Ogunkomaiya, *A Study of Effects of Machining Parameters on Tool Life.* International Journal of Materials Science and Applications, 2014. **3**(5): p. 183.

64. Salvatore, F., S. Saad, and H. Hamdi, *Modeling and Simulation of Tool Wear During the Cutting Process.* Procedia CIRP, 2013. **8**: p. 305-310.

65. Zhang, G. and C. Guo, *Modeling Flank Wear Progression Based on Cutting Force and Energy Prediction in Turning Process.* Procedia Manufacturing, 2016. **5**: p. 536-545.

66. Huang, Y. and S.Y. Liang, *Modeling of CBN Tool Flank Wear Progression in Finish Hard Turning.* Journal of Manufacturing Science and Engineering, 2004. **126**(1): p. 98.

67. Huang, Y., Y.K. Chou, and S.Y. Liang, *CBN tool wear in hard turning: a survey on research progresses.* The International Journal of Advanced Manufacturing Technology, 2007. **35**(5-6): p. 443-453.

68. Lorph`evre, E.R.e., E. Filippi, and P. Dehombreux, *INVERSE METHOD FOR CUTTING FORCES PARAMETERS EVALUATION.* Engineering MECHANICS, 2007. **14**(5): p. 1-13.

69. Carvalho, S.R.D., et al., *Comparison of inverse methods in the determination of heat flux and temperature in cutting tool during a machining process.* High Temperatures-High Pressures, 2009. **38**: p. 119–136.

70. Santos, M.R.d., et al., *Analyses of Effects of Cutting Parameters on Cutting Edge Temperature Using Inverse Heat Conduction Technique.* Mathematical Problems in Engineering, 2014. **2014**: p. 1-11.

71. Pujana, J., et al., *Analysis of the inverse identification of constitutive equations applied in orthogonal cutting process.* International Journal of Machine Tools and Manufacture, 2007. **47**(14): p. 2153-2161.

72. Agmell, M., A. Ahadi, and J.-E. Ståhl, *Identification of plasticity constants from orthogonal cutting and inverse analysis.* Mechanics of Materials, 2014. **77**: p. 43-51.

73. Franchi, R., et al., *Inverse Analysis Procedure to Determine Flow Stress and Friction Data for Metal Cutting Finite Element Modeling.* Key Engineering Materials, 2015. **651-653**: p. 1345-1350.

74. Laakso, S.V. and E. Niemi, *Using FEM Simulations of Cutting for Evaluating the Performance of different Johnson-Cook parameter sets acquired with inverse methods*, in *Chike F. Oduoza. Proceedings of the 25th International Conference on Flexible Automation and Intelligent Manufacturing, Designing for Advanced, High Value Manufacturing and Intelligent Systems for the 21st Century, FAIM 2015*. 2015, The Choir Press: Wolverhampton, United Kingdom. p. 172-180.

75. Denkena, B., et al., *Inverse Determination of Constitutive Equations and Cutting Force Modelling for Complex Tools Using Oxley's Predictive Machining Theory.* Procedia CIRP, 2015. **31**: p. 405-410.

76. Bäker, M., *A New Method to Determine Material Parameters from Machining Simulations Using Inverse Identification.* Procedia CIRP, 2015. **31**: p. 399-404.

77. Chen, X., et al., *Determining Al6063 constitutive model for cutting simulation by inverse identification method.* The International Journal of Advanced Manufacturing Technology, 2017: p. 1-8.

78. Cui, M., W.-w. Duan, and X.-w. Gao, *A new inverse analysis method based on a relaxation factor optimization technique for solving transient nonlinear inverse heat conduction problems.* International Journal of Heat and Mass Transfer, 2015. **90**: p. 491-498.

79. Xie, T., et al., *An inverse analysis to estimate the endothermic reaction parameters and physical properties of aerogel insulating material.* Applied Thermal Engineering, 2015. **87**: p. 214-224.

80. Mohebbi, F. and M. Sellier, *Estimation of thermal conductivity, heat transfer coefficient, and heat flux using a three dimensional inverse analysis.* International Journal of Thermal Sciences, 2016. **99**: p. 258-270.

81. De Bono, D.M., et al., *A robust inverse analysis method to estimate the local tensile properties of heterogeneous materials from nano-indentation data.* International Journal of Mechanical Sciences, 2017. **123**: p. 162-176.

82. Ning, J., et al., *Inverse determination of Johnson–Cook model constants of ultra-fine-grained titanium based on chip formation model and iterative gradient search.* The International Journal of Advanced Manufacturing Technology, 2018. **99**: p. 1131–1140.

83. Mirkoohi, E., P. Bocchini, and S.Y. Liang, *An analytical modeling for process parameter planning in the machining of Ti-6Al-4V for force specifications using an inverse analysis.* The International Journal of Advanced Manufacturing Technology, 2018. **98**(9): p. 2347-2355.

84. Song, X., et al., *Numerical Comparison of Iterative Ensemble Kalman Filters for Unsaturated Flow Inverse Modeling.* Vadose Zone J., 2013.

85. Gua, Y., et al., *Micro-indentation and inverse analysis to characterize elastic-plastic graded materials.* Materials Science and Engineering, 2003. **A345**: p. 223-233.

86. Cuellar, K.J.Q. and J.L.L. Silveira, *Analysis of Torque in Friction Stir Welding of Aluminum Alloy 5052 by Inverse Problem Method.* Journal of Manufacturing Science and Engineering, 2017. **139**.

87. Xu, W.-X. and L.-C. Zhang, *Ultrasonic vibration-assisted machining: principle, design and application.* Advances in Manufacturing, 2015. **3**(3): p. 173-192.

88. Hsu, C.Y., et al., *A Study on Ultrasonic Vibration Milling of Inconel 718.* Key Engineering Materials, 2009. **419-420**: p. 373-377.

89. Rasidi, I., et al., *A performance of 2 dimensional ultrasonic vivration assisted milling in cutting froce reduction, on Aluminium AL6061* ARPN Journal of Engineering and Applied Sciences, 2016. **11**(18).

90. Verma, G.C., P.M. Pandey, and U.S. Dixit, *Modeling of static machining force in axial ultrasonic-vibration assisted milling considering acoustic softening.* International Journal of Mechanical Sciences, 2018. **136**: p. 1-16.

91. Abbasi, N., M. Razfar, and M. Khajehzadeh, *Experimental Investigation and Finite Difference Modeling of Cutting Tool Temperature Distribution During Ultrasonically Assisted Turning.* Amirkabir Journal of Mechanical Engineering, 2018. **50**(3): p. 657-670.

92. Overcash, J.L. and J.F. Cuttino, *In-process modeling of dynamic tool-tip temperatures of a tunable vibration turning device operating at ultrasonic frequencies.* Precision Engineering, 2009. **33**(4): p. 505-515.

93. Khajehzadeh, M. and M.R. Razfar, *Theoretical modeling of tool mean temperature during ultrasonically assisted turning.* Proceedings of the Institution of Mechanical Engineers, Part B: Journal of Engineering Manufacture, 2014. **230**(4): p. 675-693.

94. Nestler, A. and A. Schubert, *Surface Properties in Ultrasonic Vibration Assisted Turning of Particle Reinforced Aluminium Matrix Composites.* Procedia CIRP, 2014. **13**: p. 125-130.

95. Sharma, V. and P.M. Pandey, *Recent advances in ultrasonic assisted turning: A step towards sustainability.* Cogent Engineering, 2016. **3**(1).

96. Xiangyu, Z., et al., *Surface Quality and Residual Stress Study of High-speed Ultrasonic Vibration Turning Ti-6Al-4V Alloys.* Procedia CIRP, 2018. **71**: p. 79-82.

97. Lu, Z., et al., *Study on residual stresses in ultrasonic torsional vibration assisted micro-milling.* 2010. **7657**: p. 76571F.

98. Hu, H.J., Y.Z. Sun, and Z.S. Lu, *Simulation of Residual Stress in Ultrasonic Vibration Assisted Micro-Milling.* Advanced Materials Research, 2011. **188**: p. 381-384.

99. Ren, W., et al., *Research on Homogenization and Surface Integrity of Ti-6Al-4V Alloy by Longitudinal-Torsional Coupled Ultrasonic Vibration Ball-End Milling.* Preprints, 2018(2018090032).

100. Abdur-Rasheed, A., *A Fundamental Study of Vibration Assisted Machining.* Advanced Materials Research, 2011. **264-265**: p. 1702-1707.

101. Razfar, M.R., P. Sarvi, and M.M.A. Zarchi, *Experimental investigation of the surface roughness in ultrasonic-assisted milling.* Proceedings of the Institution of Mechanical Engineers, Part B: Journal of Engineering Manufacture, 2011. **225**(9): p. 1615-1620.

102. Xiao, M., et al., *The effect of tool nose radius in ultrasonic vibration cutting of hard metal.* International Journal of Machine Tools and Manufacture, 2003. **43**(13): p. 1375-1382.

103. Ko, J.H., et al., *The Effect of One Directional Ultrasonic Vibration Assistance in High Speed Meso-Scale Milling Process.* Key Engineering Materials, 2010. **447-448**: p. 41-45.

104. Ko, J.H., et al., *Cusp error reduction under high speed micro/meso- scale milling with ultrasonic vibration assistance.* International Journal of Precision Engineering and Manufacturing, 2011. **12**(1): p. 15-20.

105. Gao, Y. and R.L. Sun. *Modelling of Theoretical Surface Roughness for Two-Dimensional Vibration-Assisted Machining*. in *International Conference on Computer Information Systems and Industrial Applications*. 2015. Atlantis Press.

106. Nath, C., M. Rahman, and S.S.K. Andrew, *A study on ultrasonic vibration cutting of low alloy steel.* Journal of Materials Processing Technology, 2007. **192-193**: p. 159-165.

107. Li, C.P., et al. *The effects of ultrasonic vibration on surface finish and tool wear in end-milling machining*. in *2012 International Conference on Manipulation, Manufacturing and Measurement on the Nanoscale (3M-NANO)*. 2012.

108. Yuan, H.L., et al., *An Experimental Investigation of Cutting Temperature and Tool Wear in 2 Dimensional Ultrasonic Vibrations Assisted Micro-Milling.* MATEC Web of Conferences, 2017. **95**: p. 07005.

109. Sharma, V., P.M. Pandey, and S. Dubey, *Recent advances in ultrasonic assisted turning: A step towards sustainability.* Cogent Engineering, 2016. **3**(1).

110. Tsai, M., C. Chang, and J. Ho, *The Machining of Hard Mold Steel by Ultrasonic Assisted End Milling.* Applied Sciences, 2016. **6**(11): p. 373.

111. Hafiz, M.S.A., et al., *A review on feasibility study of ultrasonic assisted machining on aircraft component manufacturing.* IOP Conference Series: Materials Science and Engineering, 2017. **270**: p. 012034.

112. Feng, Y., et al., *Residual stress prediction in laser-assisted milling considering recrystallization effects.* The International Journal of Advanced Manufacturing Technology, 2019. **102**(1): p. 393-402.

113. P.L.B.Oxley, *Mechanics of Machining, an analytical approach to assessing machinability*. 1989: ELLIS HORWOOD LIMITED. 242.

114. Zhipeng Pan, S.Y.L., Hamid Garmestani,Donald S. Shih, *Prediction of machining-induced phase transformation and grain growth of Ti-6Al-4 V alloy.* Int J Adv Manuf Technol, 2016. **87**: p. 859–866.

115. F.Jafarian, M.I., D.Umbrello, P.J.Arrazola, L.Filice, H.Amirabadi, *Finite element simulation of machining Inconel 718 alloy including microstructure changes.* International Journal of Mechanical Sciences, 2014. **88**: p. 110-121.

116. D. Huang, W.T.W., D. Lambert, S.L. Semiatin, *Computer Simulation of Microstructure Evolution during Hot Forging of Waspaloy and Nickel Alloy 718.* The Minerals, Metals & Materials Society, 2001: p. 137-146.

117. L.A. Reyes, P.P.r., A. Salas Zamarripa, M. de la Garza, and M.P. Guerrero-Mata, *Influence of Processing Parameters on Grain Size Evolution of a Forged Superalloy.* Journal of Materials Engineering and Performance, 2016. **25**(1): p. 179-187.

118. A. Loyda, G.M.H.n.-M.o., L.A. Reyes, and P. Zambrano-Robledo, *Microstructure Modeling of a Ni-Fe-Based Superalloy During the Rotary Forging Process.* Journal of Materials Engineering and Performance, 2016. **25**(6): p. 2128–2137.

119. Pan, Z., et al., *Heat affected zone in the laser-assisted milling of Inconel 718.* Journal of Manufacturing Processes, 2017. **30**: p. 141-147.

120. Feng, Y., Z. Pan, and S.Y. Liang, *Temperature prediction in Inconel 718 milling with microstructure evolution.* The International Journal of Advanced Manufacturing Technology, 2018. **95**(9): p. 4607-4621.

121. Shen, X. and S. Lei, *Experimental study on operating temperature in laser-assisted milling of silicon nitride ceramics.* The International Journal of Advanced Manufacturing Technology, 2010. **52**(1-4): p. 143-154.

122. Sun, S., et al., *Experimental investigation of cutting forces and tool wear during laser-assisted milling of Ti-6Al-4V alloy.* Proceedings of the Institution of Mechanical Engineers, Part B: Journal of Engineering Manufacture, 2011. **225**(9): p. 1512-1527.

123. Tian, Y. and Y.C. Shin, *Multiscale Finite Element Modeling of Silicon Nitride Ceramics Undergoing Laser-Assisted Machining.* Journal of Manufacturing Science and Engineering, 2007. **129**(2): p. 287.

124. Pan, Z., Y. Feng, and S.Y. Liang, *Material microstructure affected machining: a review.* Manufacturing Review, 2017. **4**: p. 5.

125. Pan, Z., et al., *Microstructure-sensitive flow stress modeling for force prediction in laser assisted milling of Inconel 718.* Manufacturing Review, 2017. **4**: p. 6.

126. Pan, Z., et al., *Force modeling of Inconel 718 laser-assisted end milling under recrystallization effects.* The International Journal of Advanced Manufacturing Technology, 2017. **92**(5): p. 2965-2974.

127. Feng, Y., et al., *Inverse analysis of the cutting force in laser-assisted milling on Inconel 718.* The International Journal of Advanced Manufacturing Technology, 2018.

128. Pan, Z., et al., *Turning induced residual stress prediction of AISI 4130 considering dynamic recrystallization.* Machining Science and Technology, 2017. **22**(3): p. 507-521.

129. Hedberg, G.K., *Laser assisted milling of difficult to machine materials*. 2013, Purdue University.

130. Hedberg, G.K. and Y.C. Shin, *Laser Assisted Milling of Ti-6Al-4V ELI with the Analysis of Surface Integrity and its Economics.* Lasers in Manufacturing and Materials Processing, 2015. **2**(3): p. 164-185.

131. Karpat, Y.i. and T.r. Özel, *Predictive Analytical and Thermal Modeling of Orthogonal Cutting Process—Part II: Effect of Tool Flank Wear on Tool Forces, Stresses, and Temperature Distributions.* Journal of Manufacturing Science and Engineering, 2006. **128**(2): p. 445.

132. Kong, X., et al., *Cutting performance and coated tool wear mechanisms in laser-assisted milling K24 nickel-based superalloy.* The International Journal of Advanced Manufacturing Technology, 2014. **77**(9-12): p. 2151-2163.

133. Pan, Z., et al., *Turning Force Prediction of AISI 4130 Considering Dynamic Recrystallization.* 2017(50725): p. V001T02A040.

134. Kumar, M.P., et al., *Study on Tool Life and its Failure Mechanisms.* International Journal for Innovative Research in Science & Technology, 2015. **2**(4).

135. Rahim, E.A., et al., *A prediction of laser spot-to-cutting tool distance in laser assisted micro milling Inconel 718.* Advances in Materials and Processing Technologies, 2015. **1**(3-4): p. 529-541.

136. Pan, Z., et al., *Force modeling of Inconel 718 laser-assisted end milling under recrystallization effects.* The International Journal of Advanced Manufacturing Technology, 2017. **92**(5-8): p. 2965–2974

137. Dunn, K.J. and F.P. Bundy, *The stress-strain curves for cemented tungsten carbide and sintered diamond compact.* Journal of Applied Physics, 1978. **49**(12): p. 5865-5870.

138. Lu, X., et al., *Floor surface roughness model considering tool vibration in the process of micro-milling.* The International Journal of Advanced Manufacturing Technology, 2017.

139. Feng, Y., et al., *Residual stress prediction in laser-assisted milling considering recrystallization effects.* The International Journal of Advanced Manufacturing Technology, 2019.

140. Shen, X.-H. and G.-F. Xu, *Study of milling force variation in ultrasonic vibration-assisted end milling.* Materials and Manufacturing Processes, 2017. **33**(6): p. 644-650.

141. Shen, X.-H., et al., *Ultrasonic vibration-assisted milling of aluminum alloy.* The International Journal of Advanced Manufacturing Technology, 2012. **63**(1-4): p. 41-49.

142. Zhang, X., et al., *Microstructure investigation and mechanical property analysis in electromagnetic riveting.* The International Journal of Advanced Manufacturing Technology, 2014. **78**(1-4): p. 613-623.

143. Verma, G.C., P.M. Pandey, and U.S. Dixit, *Estimation of workpiece-temperature during ultrasonic-vibration assisted milling considering acoustic softening.* International Journal of Mechanical Sciences, 2018. **140**: p. 547-556.

144. Lu, X., et al., *Effects of cutting parameters on temperature and temperature prediction in micro-milling of Inconel 718.* International Journal of Nanomanufacturing, 2018. **14**(4): p. 377-386.

145. Maurotto, A. and C.T. Wickramarachchi, *Experimental investigations on effects of frequency in ultrasonically-assisted end-milling of AISI 316L: A feasibility study.* Ultrasonics, 2016. **65**: p. 113-20.

146. Li, K.-M. and S.-L. Wang, *Effect of tool wear in ultrasonic vibration-assisted micro-milling.* Proceedings of the Institution of Mechanical Engineers, Part B: Journal of Engineering Manufacture, 2013. **228**(6): p. 847-855.

147. Shen, X.-H., et al., *A study of surface roughness variation in ultrasonic vibration-assisted milling.* The International Journal of Advanced Manufacturing Technology, 2011. **58**(5-8): p. 553-561.